Sviluppo di metodi fotochimici per la sintesi di particelle Janus con specifiche proprietà e capacità di auto-assemblaggio


ScuDo
Scuola di Dottorato ~ Doctoral School
WHAT YOU ARE, TAKES YOU FAR

Doctoral Dissertation
Doctoral Program in Material Science and Technology (31th Cycle)

# Photogenerated Janus-like surface heterogeneity to design particle properties and assembly

Nicolò Razza

---

**Supervisor:**

- Prof. Marco Sangermano - Politecnico di Torino, Department of Applied Science and Technology (Torino, Italy).

**Referees:**

- Prof. Sandra Schlögl - Polymer Competence Center Leoben, (Leoben, Austria).
- Dr. Paula Bosch - Spanish National Research Council, Institute of Polymer Science and Technology (Madrid, Spain)

---

Politecnico di Torino
2019

# Declaration

I hereby declare that, the contents and organisation of this dissertation constitute my own original work and does not compromise in any way the rights of third parties, including those relating to the security of personal data.

* This dissertation is presented in partial fulfilment of the requirements for Ph.D. degree in the Graduate School of Politecnico di Torino (ScuDo).

Nicolò Razza
Torino, 2019

# Acknowledgments

I would like to express my deepest gratitude to Prof. M. Sangermano for his guidance and - not least - patience over these years. He gave me support and freedom when facing complicated and unclear crossroads and useful career advice close to the end of this journey. I appreciate the responsibility he feels for each single member of the research group, which very often goes beyond an ordinary professional duty.

I would like to express my appreciation to Dr. G. Rizza who hosted me in his labs at l'*X* and for introducing me to the stunning world of liquid phase electron microscopy. I believe that his contribution was key for my career development and for the quality of my research. Thank you very much also for all the invitations at art-related events which allowed me to see Paris under a different light.

I want to thank the other LSI/CEA people, especially Dr. G. Fadda and Dr. D. Lairez for the fundamental help with scattering techniques and for sharing with me their knowledge in biophysics.

I would like to thank Dr. A. Synytska for hosting me in her labs in Dresden and to Prof. B. Voit for the fruitful discussion and guidance.

I would like to thank Dr. P. Bosch and Prof. S. Schlögl for finding time in their busy schedule for reviewing this manuscript.

I take this opportunity to thank all my buddies in Torino, starting with my former office mates Marco (annoying health aware guy) and Farrukh (membrane expert and politician) for the daily dialogues and open-mindedness (a particular thank to Marco for supporting my picky needs all around the world at international conferences). Thanks to Luigi (argumentative Latinist) and Graziano (the respectful misanthrope) for all the dinners and beers after work and for your friendship. Thanks to those who joined later such as Fiora (the *Crocettista*), Duccio (neurotic but beautiful) Angelo (the geopolitical expert), Camilla (the sweet but touchy secretary), Simone (the cross-contaminant guy) Andrea A. (the Lemures' guy) and all the others. I want also to thank all my buddies in Paris, starting with my acquired brother Giuseppe (the handyman), Rashmi (my best French friend), Tal (the theoretical cook), Pier (the actor), Annalisa (the documentary passionate), and all the others.

Finally, I'd like to thank Carlos for being so supportive over these years and for encouraging me to challenge myself in everything I did and in all the decisions I've taken. Thanks for being so close even when we were thousands mile apart.

# Abstract

Heterogeneity introduces complexity: when it is compartmentalized - which means spatially-distinct within a single object - novel properties and functions can arise. This type of heterogeneity is generally indicated as Janus-like heterogeneity, named after the bi-faced roman god *Janus*.

The research findings, herein reported, represent the outcome of efforts in the direction of filling the research gaps in the synthesis of reliable synthetic routes of general validity to generate Janus-like heterogeneity at the micro and nanoscale. The central idea of this manuscript is developed around photochemical concepts to allow the generation of Janus-like heterogeneity by exploiting the spatial and temporal control of light-induced reactions. This enables the introduction of Janus character, to a given system, without the constrains of thermodynamically driven approaches (e.g. built upon phase segregation or heterogeneous nucleation), and thus paving the way for more complex systems with the possibility of broad material combinations. To do so, the Janus character is introduced, in all cases, in terms of Janus-like surface heterogeneity.

In this work, a tool-set of light-driven strategies to generate a variety of Janus-like surfaces at both micro and nanoscale has been developed. Thanks to their photochemical nature, the use of heat and/or metal catalysts is not required, whereas it is generally necessary to drive other available surface modification approaches. As a consequence, the photogeneration of Janus-like surfaces, while remaining efficient, can be potentially extended to systems requiring milder conditions.

For each experimental contribution, a different photochemical approach has been developed and investigated. Both organic and inorganic, soft and hard surface modifications have been exploited. In parallel to the specific synthetic protocol, we explored the properties arising from the surface modifications reactions by adopting techniques allowing near-realistic-condition investigations.

In the first experimental contribution, a UV-light induced photochemical approach to generated Janus-like hybrid surfaces is reported for micrometric particles (silica cores of 500 nm in average radius). By using surface-anchored organothiols, the technique combines hard structuration with *in situ* photogenerated metal nanoparticles and soft structuration with polymer brushes via

*photografting-from* methods. By playing on the hard-structuration-conditions, we demonstrated how it is possible generate Janus-like hybrid with tailorable optical properties in terms of metal nanoparticle size and, in turn, wavelength of optical absorption. In the second experimental section, we reported a long-wavelength photochemical approach to generated soft Janus-like amphiphiles from small silica cores (below 25 nm in average radius). Janus nanoparticles with hydrophilic and lipophilic hairy compartments were synthetized via two-step toposelective *grafting-from* reactions. This is done by taking advantage of a surface anchored Norrish I photoinitiator and a reversible electrostatic particle immobilization technique. Because of their amphiphilicity, the so-synthetized particles show precise self-assembly patterns in water. Since the self-assembly behaviour is driven by hydrophobic directional forces occurring in water, we investigated the assembly process in liquid environment by employing small angle X-ray scattering and optical scattering techniques to get statistically relevant data. The assembly patters were also directly visualized in near-realistic condition by using *in situ* liquid phase transmission electron microscopy and confirmed by means of other direct and indirect techniques. In the last experimental section, starting from photoactive silica nanoparticles (below 20 nm in average radius), we reported a photochemical approach combining long-wavelength *grafting-from* and click chemistry to generate amphiphilic nanoparticles with a pH-tailorable cationic charge (from tertiary amine groups) and amphiphilic Janus-like surface properties. We investigate also the ability of these amphiphilic nanoparticles to controllably interact with cell membrane models. Since the so-synthetized hairy nanoparticles possess two distinct domains, a lipophilic cell-adhesive and a hydrophilic cell-non-adhesive, membrane-anchoring properties are likely to follow. The interaction behaviours were investigated at different pH values in order promote or depress the protonation of amine groups of the hairy corona and, in turn, to question the effect of the nanoparticle-borne surface charge on the interaction patterns. This was determined by probing the interaction from impedance measurements of the cell membrane via electrophysiology of planar lipid membrane (as cell membrane model). To further corroborate the electrophysiology findings, along with conventional techniques, *in situ* liquid phase transmission electron microscopy was used to unravel the interaction dynamic in near-realistic conditions.

*"I am among those who think that science has great beauty. A scientist in his laboratory is not only a technician: he is also a child placed before natural phenomena which impress him like a fairy tale. We should not allow it to be believed that all scientific progress can be reduced to mechanisms, machines, gearings, even though such machinery also has its beauty. Neither do I believe that the spirit of adventure runs any risk of disappearing in our world. If I see anything vital around me, it is precisely that spirit of adventure, which seems indestructible and is akin to curiosity."*

Madame Curie: A Biography - by
Eve Curie Labouisse (1937)

# Contents

# 1.

# Introduction

## 1.1 Symmetry and asymmetry

Whether it's about flower in full bloom, facial features, or architecture, humans have been always visually attracted by symmetry from cultures across the globe and throughout time. Researchers have tried to explain it in terms of perceptual bias by suggesting that human visual system may be strongly biased toward axes of global symmetry.[1] Other studies suggested that, evolutionary advantage aspects play also a role since symmetry is, generally, an indicator of good health in an individual or good genetic quality in a mate.[2] However, beyond human perception, is nature preferring symmetry? The answer is no. Indeed, asymmetry represents a way to express complexity and it is an essential aspect of development. [3] Nature offers several examples on that. It's the case of the morphologically asymmetric rightward bent of the wrybill plover beak (Figure 1.1a), whose advantage is still today objet of debate. Another example is presented by the asymmetric growth of some trees (Figure 1.1.b) which has been related to adaptation, in order to maximise photosynthesis by growing in response to gaps and neighbours or incoming solar radiation.[4] Asymmetry is present also at a much smaller level. For example, the presence of an asymmetric carbon centre is one of the structural features that induce chirality in organic molecules. Scientists reported that the asymmetry presented by chiral compounds (Figure 1.1c), such as amino acids and carbohydrates, has even played a role in the origin of life and it still does it in many biological functions. [5,6] A reasonable question may have hit the reader: can asymmetry be introduced in man-made systems to bring added complexity and therefore novel functions? For example, what if asymmetry is

added to micro and nano objects (Figure 1.1d) not necessarily in terms of morphology but properties as well?

### 1.1.1 The power of asymmetry: the concept of Janus

The French scientist and Noble Prize Laureate, Pierre-Gilles de Gennes, aroused interest in similar questions. In his Noble lecture entitled "Soft Matter" he said:

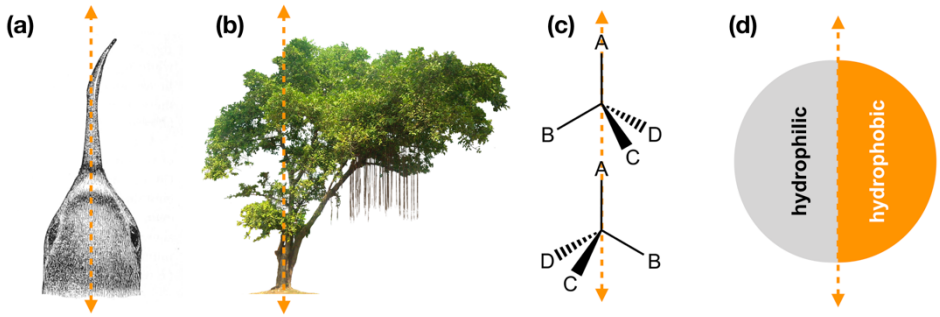


**Figure 1.1**: (a) rightward bent of the wrybill plover (*Anarhynchus frontalis*) beak; (b) example of asymmetric tree growth; (c) asymmetric carbon generating chiral molecules, dextrorotatory for the top and laevorotatory for the bottom; (d) example of asymmetric particle with amphiphilic properties showing, so called, Janus character.

"*Let me quote still another new animal: the Janus grains, first made by C. Casagrande and M. Veyssié. The god Janus had two faces. The grains have two sides: one apolar, and the other polar. Thus, they have certain features in common with surfactants. But there is an interesting difference if we consider the films which they make, for instance at a water/air interface. A dense film of a conventional surfactant is quite impermeable. On the other hand, a dense film of Janus grains always has some interstices between the grains, and allows for chemical exchange between the two sides; "the skin can breathe". This may possibly be of some practical interest.* [7]"

These mentioned particles present physical and/or chemical anisotropy within a single particle and therefore they are asymmetric in properties. They were named after *Janus,* god of beginnings and endings, in roman mythology. The broken symmetry offers efficient and distinctive means to target complexity and achieve properties inconceivable for homogeneous particles. From the initial conceptual ideas, different particle architectures have been experimentally attained so far: from simple spherical, to different kinds of dumbbell shapes, to vesicles/capsules and highly anisotropic architectures, such as cylinders or disks (Figure 1.2 (a-h)).

Experimental as well as theoretical and computational studies have elucidated the unusual and sometimes surprising behavior of Janus particle, especially in terms of interaction and self-assembly. Just to name few, JPs have shown to be

able to interrogate cellular function [8-12] by spatially-controlled affinity with cell membranes, to thermodynamically stabilize emulsions by acting as solid amphiphiles, [13,14] and to study aggregations and self-organization phenomena. [15-18]

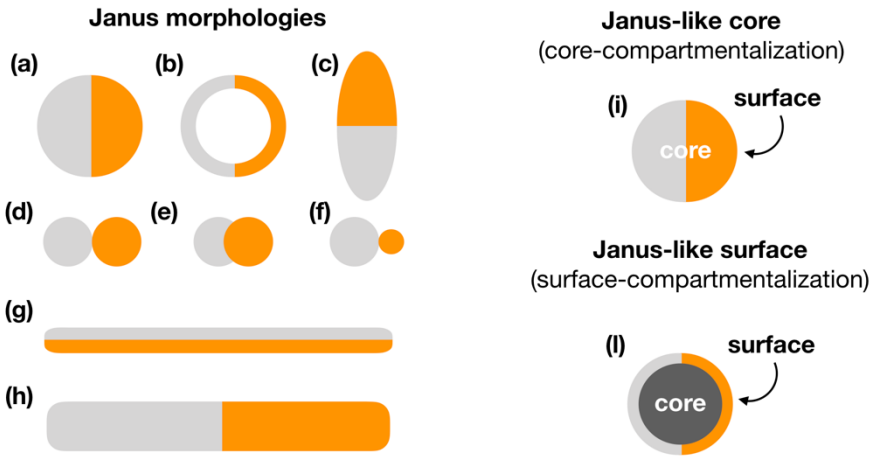


**Figure 1.2**: Janus morphologies and architectures for two materials/properties (in orange and light grey): spherical (a), capsules or vesicles (b), and ellipsoidal (c) geometries. (d-f) Various kinds of dumbbell-shaped Janus particles with symmetric appearance (d), attached nodes (e) or snowman character (f). Disk shaped (g) and cylindrical (h) Janus particles. Janus character from core-compartmentalization (i) and from surface-compartmentalization (l).

## 1.12 Janus nature from the particle surface: Janus-like surfaces heterogeneity

For a given material composition, interaction between objects encounter tremendous and drastic changes when going from macroscopic dimensions to micro/nanoscale dimensions. [19] When the particle size decreases, the total surface area, in parallel, increases (as $1/d^2$). Just to give an idea of this, if a cube of 1 cm in size is powdered in small cubes with a size of 10 nm, the total surface area increases of 1 million times. However, it is not only matter of total surface area. Indeed, when the size decreases, most of the atoms/molecules are accounting for the surface rather than for the bulk. For instance, in a particle of 30 nm size, about 10% of its molecules are accounting for the surface, whereas at 10 and 3 nm size the ratios increase to 20% and 50%, respectively. Because the number of atoms/molecules on the surface of the particle may determine the material reactivity, this is key to defining the chemical and biological properties of particles. That's why, for small particles, the physio-chemical properties of the surface play one of the main roles in particle behaviors, and it's there that the efforts should be targeted to tailor specific proprieties. For example, it has been known for more than a century that, the stability of a micro and nanoparticles dispersed in a liquid (colloidal dispersion) is affected by surface properties such solvent-philicity and surface charge, and not only by size and shape.[20] In more

recent time, surface properties of particle systems have been matter of discussion also in understanding particle-cell interactions,[21] particle toxicity [22] and even to predict the formation of protein coronas at particle surfaces in biological media.[23]

It goes without saying that the by changing the surface properties of a particle system, its behaviour can be drastically changed. In this regard, if the chemical and/or physical asymmetry mentioned in the previous section (defined as compartmentalization or Janus nature) is applied to the surface of a micro/nano particles, Janus-like surface heterogeneity is created (case (l) in Figure 1.2). In other words, Janus particles are generated with the asymmetry coming from the surface while keeping (in most of the cases) unchanged the particle-core features. However, most of JPs, synthetized up to now, present a core-compartmentalization (case (i) in Figure 1.2). These particles are sometime called heterodimers or heterostructures because consist of the physical junction or segregation of two different (and often dissimilar) materials. Synthetic routes and morphologies for particles with Janus-like cores are regulated by the limited possibility of material combination. On the other hand, Janus-like surface heterogeneity can be applied, ideally, to any core with any morphology and composition. Furthermore, it is possible to design either hard (inorganic) or soft (organic) Janus-like surface. Indeed, since the fabrication methodologies rely on surface modification techniques, Janus-like surfaces offer larger versatility, paving the way for more complex and smarter micro and nano systems.

## 1.2 Research gap and thesis motivation

From the first paper in 1989[24] year by year the number of publications on asymmetric particles has increased as illustrated Figure 1.3, reaching today more that 2000 publications with an average citation of 26, which indicates a remarkable scientific activity in the field. Many synthetic strategies for the fabrication of asymmetric micrometric particles have been reported for both Janus-like core and surface. [18] On the on the other hand, when going to truly nanometric systems (1 - 100 nm in size), almost all the works, are about nanoparticles with Janus-like cores. Indeed, as it will be explained in the detail in the Chapter 2, the fabrication of Janus-like surfaces requires the ability to control and confine the modification step on the surface of a sub-100nm object. That's not a trivial task, for sure!

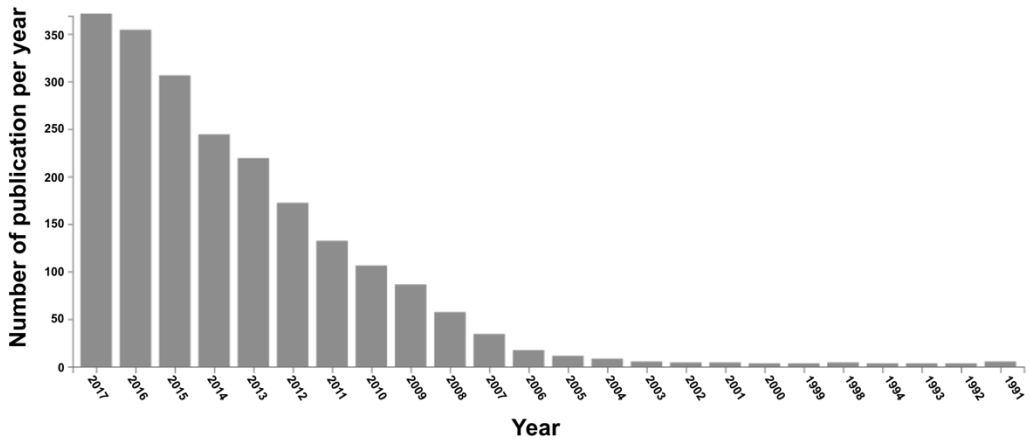


**Figure 1.3**: Number of articles published in peer-reviewed journals each year in the field of "Janus Particles" from 1991 to 2017. The data were obtained from the citation indexing service Web of Science®.

## 1.2.1 Synthetic protocols: enabling spatio-temporal control by using light-induced reactions

The key aspect in almost all the strategies to generate particles with a Janus-like surface heterogeneity is the control and the confinement of the modification reactions on a specific region of the particle surface. In other terms, the modification must be toposelective (from ancient Greek τόπος or *tópos*, "place"). In doing so, the synthetic protocols - nearly always - make use of thermal energy to activate/initiate the surface modification reactions. [25,26.] However, thermal energy cannot be directed toward a specific surface region. Conversely, if light is used as source of energy to activate the surface modification reactions, it is possible to gain temporal and spatial control over the whole modification process. [27,28] Indeed, photochemical approaches allow to arrest the modification process on-demand by rapidly turning off the light source. Additionally, because light can be directed and oriented: by shining light on a given surface portion and by keeping in shadow the remaining surface, Janus-like surfaces with truly-nanometric features can be easily generated (similarly to photolithography processes).

The fully spatio-temporal control of the modification process, possessed by light-induced approaches, is not the only remarkable feature. For instance, since heat is not required, the photogeneration of Janus-like surface heterogeneity is a very mild process and it is also applicable to heat-sensitive substrates. Even when this feature is not needed, the absence of heat makes the surface modification process very energy efficient and environmentally friendly. [29,30]

Throughout the following chapters, we will demonstrate how photochemical methods can be used to generate Janus-like surfaces in order to obtain nanomaterials with unprecedented properties. The project was started with silica cores of 500 nm in radius. We demonstrated the feasibility of Janus-like hybrid

surface modification by combining a hard structuration with photogenerated metal nanoparticles and a soft structuration with polymer brushes via *grafting-from* methods, both induced by UV-light (Chapter 4). After verifying the feasibility of our ideas with the first proof of concept, the project was carried out by following more challenging synthetic routes. We switched to cores with radius below 25 nm, designing a soft structuration via *grafting-from* approach to generate small nanoparticles with amphiphilic behaviour. In doing so, we adopted a more efficient photo-initiating system able to absorb longer wavelength of light irradiation (Chapter 5). Finally, this soft approach was combined with post-polymerization functionalizations via photo-click chemistry to generate amphiphilic nanoparticles with pH-responsive behaviour to design interaction with cell membranes (Chapter 6).

### 1.2.2 Investigation protocols: Providing characterization tools in near-realistic conditions

The complexity introduced by the Janus-like asymmetry allows to tailor and design properties and behaviours, otherwise impossible to obtain for a particle system. The newly introduced set of properties strongly depend of the type of Janus-like asymmetry. Focusing on systems with asymmetric-in-properties (i.e. compartments with dissimilar properties), it is possible to introduce self-assembly capabilities. In classical terms, self-assembly is defined as a spontaneous and reversible organization of system units into structures with a specific patter by noncovalent interactions. These assembly can occur (i) in bulk fluids (e.g. organization of particles in dimers, trimers, …, suprastructure in liquid) or (ii) at interfaces (e.g. particles at liquid-liquid or liquid-air interfaces, as well as biological interfaces such as cell membrane). The unique self-assembly properties can give access to new hierarchical nanomaterials, drug-delivery systems, emulsion stabilizers, interfacial catalysis, display technology and many others. However, while theoretical and computational basis are already established, experimental evidences of these assembly properties are often limited by the available investigation tools. This is especially true when dealing with small nanoparticles for which a direct visualization of their behaviour is not easily accessible.

Aware of those limits, in parallel to the establishment of novel synthetic routes, we tried to adopt proper characterization tools to openly disclose the unique behaviours of asymmetric particles. Indeed, when investigating self-assembly behaviours, it is important to adopt investigation tools that do not introduce any artefact. Otherwise, the spontaneous nature of self-assembly is lost and we can only talk of assembly induce by external stimuli. For instance, although electron miscopy has a suitable resolution to investigate self-assembly at the nanoscale, conventional techniques requires dry specimens. In other words, the colloidal suspension must be dried prior the analysis. However, sample drying may introduce artefacts and, in turn, it would not be possible to distinguish

between self-assembly and evaporation-induced assembly. In this regards, the emerging technique of liquid phase transmission electron microscopy (LP-TEM) allow to investigate *in situ* the self-assembly in liquid environment. LP-TEM allowed us to apply the powerful capabilities of the electron microscopy to the direct visualization and analysis of nanoparticles in liquid. With this technique, we could examine behaviours occurring in liquid that are traditionally inaccessible to electron microscopy (needs of dry specimens) and to optical microscopy (low resolution). Besides their direct visualization, self-assembly behaviours were investigated using other non-destructive *in situ* technique such as X-ray scattering. This technique gives access to nanoparticles pattern of assembly in liquid environment from a statistically-relevant number of particles. In the last experimental section, we aimed to probe the self-assembly of nanoparticles on unsupported lipid membrane. We developed a non-destructive membrane electrophysiology method bases on complex impedance measurements which allowed us to detect very small impedance variation due to particle-membrane interactions.

# 2.

# State-of-the-art and background of the synthetic routes

## 2.1 Syntheses of Janus particles

In this section an overview on the main scientific contributions on the synthesis and the application of Janus particles is presented. The literature has been divided in two main categories: (i) Janus-like core, whenever the compartmentalization occurs at a core-level; (ii) Janus-like surfaces, whenever the compartmentalization occurs at a surface-level. Additionally, pursuing the scope of this manuscript, greater emphasis has been placed on organic systems. On top of that, among the giant Pandora of synthetic routes, only the techniques suitable for the nanometric (1 – 100 nm) or sub-micrometric (100 – 1000 nm) particles were considered.

### 2.1.1 Janus-like cores

### Inorganic structures with core-compartmentalization

In addition to the intrinsic functionalities of the single inorganic components (e.g., combination of optical, magnetic and electrical properties), extrinsic characteristics such as efficient charge separation,[31] magnetic interaction,[32] or spin-polarization transfer [33] arise when the anisotropy from the combination of two inorganic phases exploited. To date different material combination have been shown: (i) metal - metal oxide, such as Pt-$Fe_3O_4$,[34] Pd-$Fe_3O_4$,[35] Au-$Fe_3O_4$,[36.] Ag-$Fe_3O_4$,[37] Cu-$Fe_3O_4$,[38] FePt-MnO,[32] Au-MnO,[39], and Co-$Fe_2O_3$;[40] (ii) metal - semiconductor, such as Au–PbS, Au– PbSe,

Au–CdSe, Au–Si, and FePt–CdS;[41-43] (ii) metal oxide – semiconductor, such as $Fe_3O_4$–CdS, $Fe_3O_4$–HgS,[41,42] and $Fe_2O_3$–ZnS;[44] (iv) semiconductor-semiconductor, such as PbSe-CdSe.[45] An example of each class of Janus heterostructures is reported in Figure 2.1 from (a) - (d).

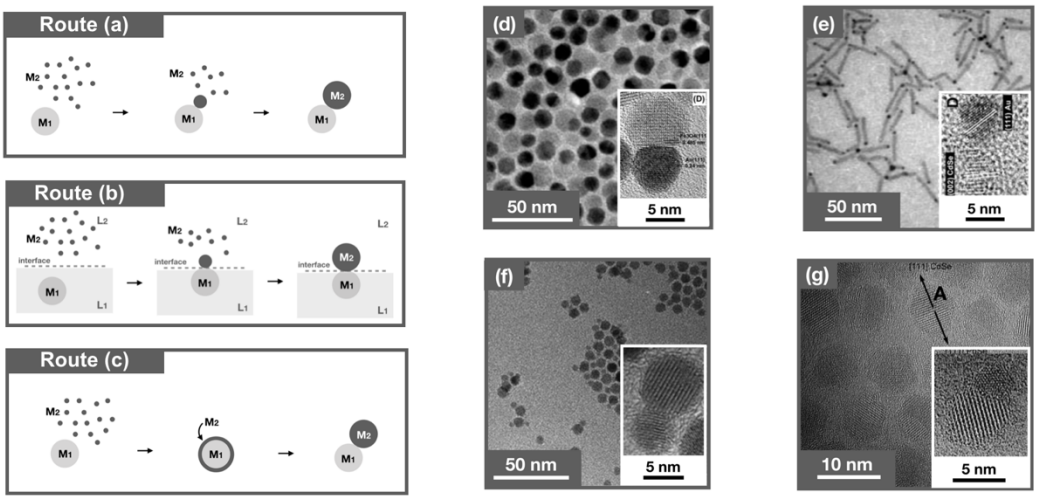


**Figure 2.1**: Common synthetic routes for the synthesis inorganic Janus heterostructures composed of a combination of two materials (indicated as $M_1$ and $M_2$) via (a) heterogeneous nucleation, (b) synthesis at liquid-liquid interface, (c) decomposition of an initial core-shell structure into dumbbell-structure. Example of different material combination such as: (d) metal - metal oxide Au-$Fe_3O_4$, (e) metal – semiconductor Au-CdSe, (f) metal oxide – semiconductor $Fe_2O_3$-ZnS, (g) semiconductor – semiconductor CdSe-PbSe. Adapted from the references [44-47].

Most of these inorganic Janus structure have a dumbbell shape with different architectures such as attached nodes, eccentric encapsulation, snowman-shape and rod-shape. These particles generally rely on a common synthetic strategy: the synthesis starts from a first type of nanoparticle (seed) onto which a second particle is grown leading to the formation of a dumbbell structure with different architecture. The second particles can be grown in different ways: heterogeneous nucleation, [36,46,48.] asymmetric modification at liquid/liquid interface [49] just to name few. Following a similar approach, Chen and co-workers proposed another strategy based on the segregated ligand coordination on a gold surface to direct anisotropic silica deposition and generate Janus nanoparticles. [50] A different fabrication protocol reported the synthesis of inorganic Janus particles from core-shell structure followed by a thermally induced atomic reconstruction of the system in a Janus structure.[45]

The available fabrication strategies for inorganic dumbbell-shaped Janus particles allow the synthesis of very small nanoparticles (below 100 nm) since they are well-controlled bottom-up approaches. On the other hand, there are several experimental constrains. Indeed, it is decisive to suppress homogeneous nucleation of the second growing component because it is a competitive reaction

to the desired heterogeneous nucleation on the preformed or in situ formed seeds. Additionally, the added term of Gibbs free energy for the adhesion at the interface between the seed and the growing particle must be negative. [42,46] Therefore, because of all these constrains the possibilities of material combination are severely limited.

## Organic structure with core-compartmentalization

Most of the techniques to synthetize nanometric or sub-micrometric organic Janus structure make use of phase-inversion combined with mini-emulsion techniques. Indeed, the incompatibility of two homopolymers in polymer blends induces a powerful driving force for the phase-separation with typical characteristic lengths in the micrometric-scale. Therefore, if a mixture of homopolymers is confined inside an object with a size below the length-scale of phase separation, a complete phase separation in two phases can occur, which leads to the formation of particles with Janus character. The spatial-confinement of the phase-separation is typically achieved using mini-emulsions and classical emulsions techniques. For instance, Shimomura, Higuchi, and Yabu developed a synthetic strategy to fabricate such systems. [51,52] In their (mini)emulsion methodology, they used a solvent for solubilisation of the two homopolymers that is miscible with water (THF). With the evaporation of the organic solvent, the polymer particles grow via nucleation, growth, and precipitation. The size of the generated particles mostly depends on the initial concentration and the ratio of water to organic solvents. Although, this approach typically leads to particles with sizes in the region of several micrometres, particles with nanometric dimensions have been reported by playing on the preparation conditions. For example, the same group fabricated nanometric well defined biphasic JPs by using a mixture of poly(styrene) (PS) and poly(isoprene) (PI),[53] in which the volume ratios of the individual compartments followed the feed ratio of the two polymers as illustrated in Figure 2.2a.

A variation of the same approach has been proposed using block copolymers instead of a mixture of two homopolymers. [54-56] Higuchi and colleagues developed a phase diagram of the accessible morphologies for PS-b-PI diblock-copolymer (Figure 2.2b). Depending on the molecular weight ($M_n$) and on the ratio between the particle diameter (D) and the period of the lamellar-forming block copolymer ($L_0$). Because the length scale of phase separation in block copolymers $L_0$ is mainly a function of the molecular weight, a characteristic transition is observed when a block copolymer is confined within droplets of a certain diameter, D. For ratios of $D/L_0$ larger than two, multi-lamellar structures were observed, in which the number of lamellas increased with increasing $D/L_0$. Conversely, for $D/L_0$ below the unity, the phase-separation resulted in particles with Janus character. However, because of experimental limitations for the

synthesis of high molecular weight block-copolymers, Janus character is typically obtained only for particles in the range of 20–150 nm. On top of that, other experimental constrains arises from the fact that those sizes are generally problematic to achieve (with a fair polydispersity) through mini-emulsion.

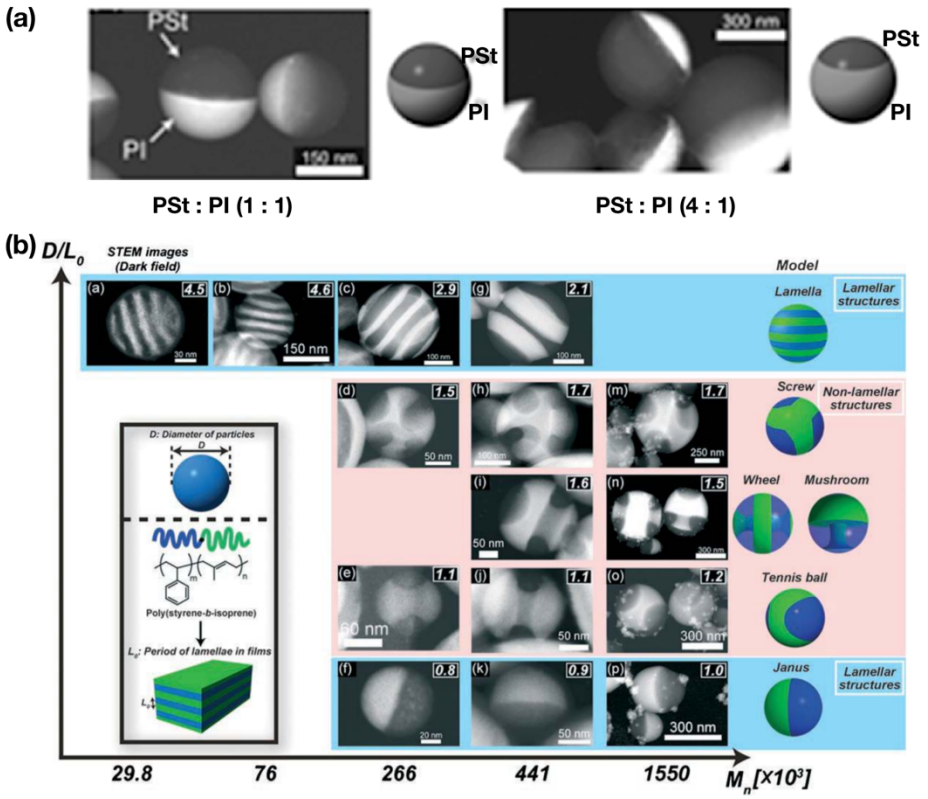


**Figure 2.1**: Phase inversion for the preparation of organic Janus particles made from poly(styrene) and poly(isoprene) with a volume ratio of both sides depends on the polymer feed composition (a). Preparation of nanoparticles via phase-separation of block-copolymers. Evolution of the structures as function of molecular weight and the $D/L_0$ ratio, where D and $L_0$ correspond to the particle diameter and the period of lamellar structure (b). Adapted from the references [53, 54].

## 2.1.2 Janus-like surfaces

### Inorganic surface structuration

The pathways belonging to this section make use of desymmetrization tools to achieve a toposelective surface modification. The simplest way to do that involves the use of planar substrate to immobilize the particles during the surface modification reactions. In most of the cases, the Janus particles fabricated using planar substrates have sizes of several microns and therefore they have not been included in this manuscript. Some examples can be found at the reference [18].

When dealing with CVD (psychical vapour deposition) modification techniques, a simple monolayer or sub-monolayer deposition of micro/nanoparticles on planar substrates is enough for the toposelective surface

modification. For example, Le and co-workers, fabricated Janus particles with a partial gold coating by thermal evaporation deposition. Initially, sub-monolayers of aminated silica nanoparticles (100 nm) were deposited on hydrophilic glass microscope slides from an ethanolic suspension and dried under gentle air steam. Subsequently, a layer of 5 nm of chromium was deposited on the silica nanoparticles followed by a thicker gold layer of 25 nm. Le *et al*. also reported the possibility of further functionalize the gold hemi-cups with hydrophobic ligands via thiol-gold interaction.[57] A similar approach was adopted by Sanchez's research group to fabricate mesoporous silica nanoparticles (40, 65 and 90 nm) with different inorganic Janus coatings. After nanoparticle deposition on planar substrate, a layer of platinum (2 nm), gold (2 nm) or silica (4 nm) was deposited via e-beam evaporation system onto the unprotected side of the deposited particles.[58]

However, a simple planar deposition is not adequate for wet surface modifications because more reliable particle immobilizations are required. In this regard, thanks to the development of strategies allowing tighter particle attachment, more recently, wet methods have been employed for the fabrication of sub-micrometric Janus particles. For example, a very simple and accurate way to immobilize silica nano and sub-micrometric particles was introduced by Yang and colleagues.[59] They observed that amine-modified silica particles can be covalently immobilized on poly(styrene-ran-acrylic acid) P(S-r-AA) copolymer film surfaces via active ester-mediated amidation reactions. When the particles are deposited onto the copolymer film, they sank into it during the amidation reactions. Therefore, it is possible to control the immersion depth and consequently the Janus balance of the colloids by simply following and controlling the amidation reaction (Figure 2.3a). This concept was applied to silica particles with diameters of 106, 230, and 460 nm. Upon immersion into the copolymer film, the unmasked surface was modified with acid-functionalized gold NPs via electrostatic interactions in water. This process generated a patchy coverage (i.e. distinct gold nanoparticles) of the exposed particle surface, which could be transformed into a continuous gold hemishell via gold/palladium co-sputtering and subsequent annealing.

An extension of the abovementioned approach was proposed by using electrospun fiber mats to immobilize sub-micrometric silica.[60, 61] Specifically, asymmetric Janus and triphasic silica particles with a diameter of 450 nm were fabricated via a particles embedding into PMMA/P4VP nanofibers and subsequent surface modification processes as illustrated in Figure 2.3b. [60] The authors demonstrated that it is possible to tailor the Janus balance by manipulating the temperature and time of the embedding process on the fiber mats. After the physical immobilization on the fiber mats the particle surface can be partially modified by using a chemical vapor deposition of silanes. Subsequently the treated surface can be labeled with gold nanoparticles. A

statistical analysis revealed the reliability and uniformity of the immobilization process resulting in Janus particles with a modification yield above 80%.

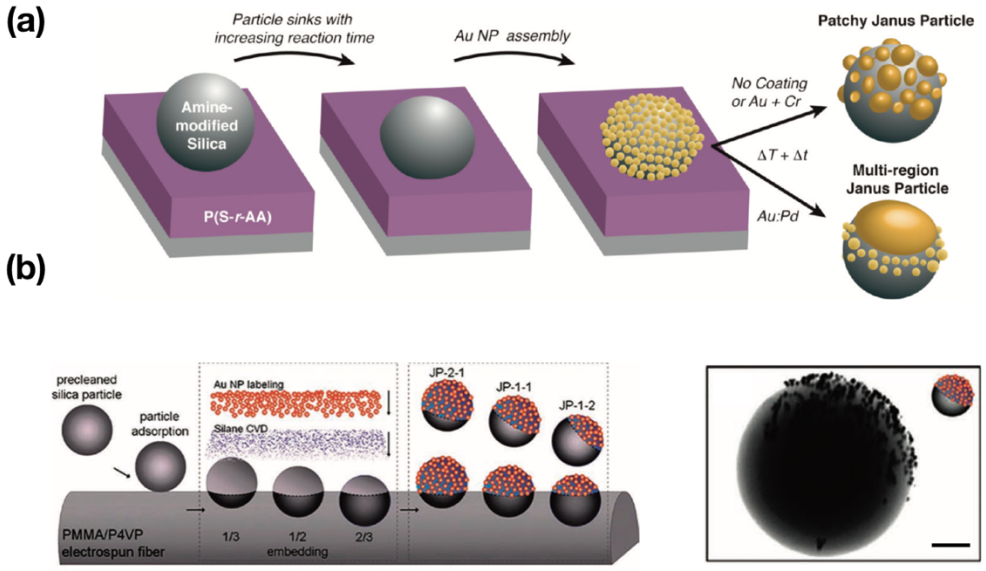


**Figure 2.3**: Schematic representation of Janus particles fabrication via particles immobilization by controlled sinking in P(S-r-AA), gold nanoparticles self-assembly and thermal annealing (a). Janus particles fabrication through particle physical entrapment in polymeric fiber mats and toposelective nanoparticles labelling, scale bar is 100 nm(b).[59, 60]

However, all the immobilization strategies relying on planar substrate suffer largely from the fact that the resulting particle yield is extremely low due to the very limited interface. This limit is even more constraining when the particle size decreases. These restrictions have called for novel immobilization concepts to replace the limited 2D interfaces by systems with higher internal interfaces such as in dispersions. Among these, the utilization of Pickering emulsion as immobilization strategy has received great interest and has largely promoted the development of new fabrication routes for particles with Janus-like surface heterogeneity. Indeed, besides the larger yields, the Pickering approach is scalable, often easy to control, and economically interesting since inexpensive materials are required. A Pickering emulsion is a two-phase oil/water emulsion stabilized by solid particles through just physical interactions. The experimental formation and theoretical background of this type of emulsions has been reported by Pieranski,[62] who derived the expression for the desorption energy ($E$) of a homogeneous particle, P.

$$E = \pi R^2 \gamma(OW)(1 - |\cos\beta|)^2 \quad (1)$$

$$\cos\beta = |\gamma(PO) - \gamma(PW)|/\gamma(OW) \quad (2)$$

Where, γ(PO), γ(PW), and γ(OW) are the interfacial tensions of the particle (P) with oil (O) and water (W), and between the two phases (oil and water), respectively. The maximum of the desorption energy, *E*, can be reached if γ(PO) – γ(PW) < γ(OW). The Equation 1 clearly expresses that the formation of Pickering emulsions is strongly favored with increasing particle size. This explains why the formation of Pickering emulsions becomes more challenging when the particle size decreases. However, most of the Pickering-based strategies do not rely only on the desorption energy to immobilize the particles. Indeed, tighter anchorages of particles is especially important for smaller particles to suppress particle rotation or desorption processes which would not allow a defined toposelective surface modification. In this regard, Granick's research group reported groundbreaking contributions for the fabrication of Janus particle via Pickering emulsion with wax as oil phase.[63] The strategy is the following: The oil in water emulsion is formed at high temperature (when the wax is liquid) allowing the particles to stabilize the w/o interface. Once the Pickering emulsion is formed, the emulsion is cooled, the wax becomes solid, and by doing so the particles remain entrapped at the interface with a fully restricted rotational motion. In a following step, the collected solid wax droplets with particles at the surface (colloidosomes) can be chemically modified so that only the unprotected particle surface will be affected by the surface modification procedure.

The use of Pickering-based immobilization strategies has been exploited by Panwar, Jassal and Agrawal to perform toposelective inorganic Janus-like surface modifications. They showed that aminated sub-micrometric silica particles can be partially modified with small silver nanoparticles (3 nm) upon particle entrapping in wax colloidosomes. In their strategy, silver nanoparticles were generated *in situ* from silver ions ($AgNO_3$) as precursor. The ion clusters associated with the amino groups on the exposed silica surface were reduced to silver nanoparticles via chemical reduction by using $NaBH_4$.[64, 65] In a similar approach, the same group reported a partial surface modification of sub-micrometric silica particles with $TiO_2$. After entrapping aminated silica particles in wax colloidosomes, the exposed surface was partial modified via hydrolysis and condensation reactions of tetrabutyl orthotitanate as precursor in the presence of ethanol and hydroxyethyl cellulose.[66]

## Phase-segregated corona from self-assembled structures of block copolymers

The strategies belonging to this section have been classified as Janus-like surface because the Janus character is coming from a phase-segregated corona. However, contrarily to other methodologies, these strategies do not rely on surface modification reactions but requires transformation at both core and

surface-level to generate the Janus structure. Systems generated by using the methodologies of this section are generally defined as Janus micelles.

The most common strategies can be divided in two main classes: (i) self-assembly of mixture of two diblock-copolymers; (ii) direct self-assembly of triblock-copolymers. In both strategies, one (or two) block forms the core of a micellar structure and the other two blocks generate the corona. The Janus nature arises from the phase segregation of the two block which build up the corona thanks to their mutual incompatibility.[18] Because of their architectures, these Janus particles generated from block-copolymers are usually defined as Janus micelle

When diblock-copolymers are used, a widely adopted self-assembly strategy involve a combination of AB and BC diblock-copolymers in which the B blocks are not soluble in a given solvent and will form the core of the micelle. In this case, if blocks A and C possess a very high incompatibility, there is a high probability of forming individual AB and BC micelle populations with only a minor fraction of Janus co-micelles. In this regard, Halperin and Potemkin suggested that the co-micellization of AB and BC diblock-copolymers into Janus co-micelles can only be expected for two sufficiently compatible corona blocks (still with a certain degree of incompatibility).[67-70]

Additional improvements came from Han and Jiang thanks to Monte Carlo simulations. [69] They suggested that co-micelles with Janus character can be formed by balancing incompatibility of the corona blocks (A and C) with the use of diblock-copolymers AB′ and B″C with B′ and B″ which can interact via hydrogen bonding. This suggestion was adopted experimentally by Hu and Liu, who introduced adenine and thymine into the B' and B" segments of two diblock copolymers leading to an enhanced mixing of both chains in mixed micelles due to hydrogen bonding of the nucleic acid pairs.[71]

A different approach by using AB and BC diblock-copolymers was proposed by Cheng *et al*. They transformed mixed shell micelles formed by a mixture of PEO-b-PAA and PAA (P2VN-b-PAA) (with PEO (poly-(ethylene oxide)), PAA (poly-(acrylic acid)) and P2VN (poly(2-vinyl naphthalene))) diblock-copolymers into Janus micelles by exploiting the different solubility characteristics of the blocks, as well as crosslinking reactions.[72] The procedure is illustrated in Figure 2.4. As a first step, mixed shell micelles were formed in DMF via non-covalent crosslinking of diamine molecules with the PAA segments. This crosslinking prevented dissolution when changing the solvent to neutral water. When dispersed in water, the hydrophobic P2VN domains collapsed onto the non-covalently crosslinked micelles-core, and the overall structure remained stabilized by the PEO arms. Subsequently, by reducing the pH to 3.1, PEO/PAA complex formation was induced with liberation of small diamine molecules. This process led to a rearrangement of the structure and, in turn, to the formation of Janus micelles.

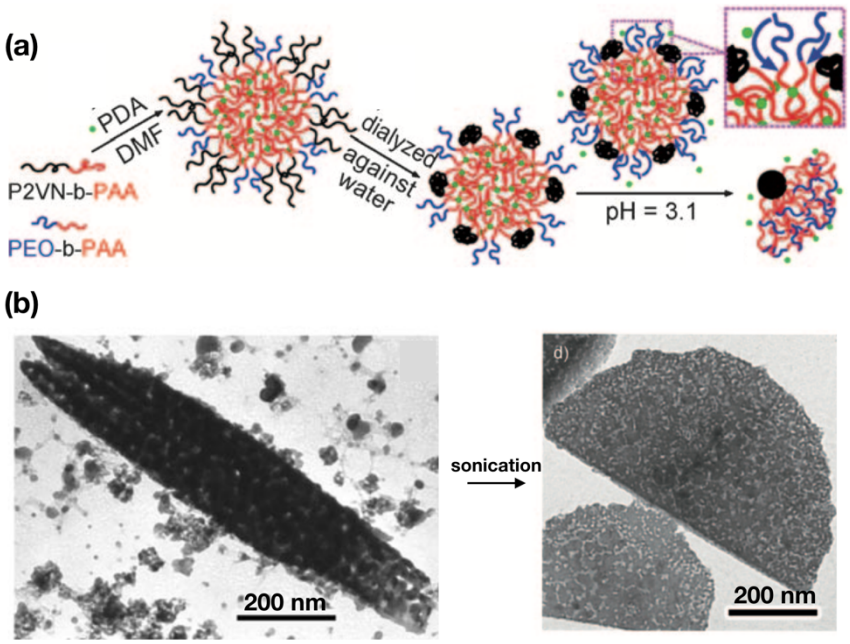


**Figure 2.4**: Organic Janus micelles via stepwise transformation of mixed shell micelles of two diblock-copolymers AB and BC. Chemical transformation scheme (a) and the resulting Janus micelles self-assemble into tubular structures, which, upon sonication, disassembly into half-discs (b). Adapted from reference [72].

Another route for the self-assembly of two diblock-copolymers mixture relies on the use of a combination of AB and CD diblock-copolymers, instead of relying in a common B segment. In this case, the blocks B and D show mutual attractive interaction which results in a forced co-assembly of the two blocks. Voets *et al.* reported pioneering contributions by using the mentioned approach. They reported comprehensive studies on Janus micelles using the forced co-assembly of two oppositely charged diblock copolymers (AB + CD) into a complex-core micelle with PEO and PAAm (poly- (acrylamide)) as corona-forming blocks, whereas the core was formed by an inter-polyelectrolyte complex of B (made of P2MVP, poly(N-methyl- 2-vinylpyridinium iodide)) and C (made of PAA).[73-76]

As mentioned at the beginning of the section, the self-assembly of triblock-copolymers can be also adopted for the synthesis of organic Janus micelles. As for diblock-copolymers, the segregation of the corona-forming blocks must be addressed upon self-assembly of the structure to generate micelles with Janus character. Also in this case, the process is ruled by the thermodynamic interplay of enthalpy and entropy. Hereof the parameters necessary to induce morphological transitions of the corona from mixed to phase-segregated were assessed by Charlaganov *et al.* through a self-consistent field theory (SCFT).[68] Theoretically speaking, the main parameter determining the extent of corona phase separation are the incompatibility of the two types of polymers as expressed by the Flory–Huggins interaction parameter, $\chi$. Charlaganov and collegues found for the case of $A_{100}B_{70}C_{100}$ triblock-copolymers, (subscripts denoting the average degrees of polymerization) a transition from mixed to phase-separated micelles starts at $\chi_{AC} = 0.5$ with the presence of Janus micelles at $\chi_{AC} = 1$. However, in real

experimental systems, an interaction parameter of $\chi_{AC}$ = 1 between two highly swollen corona blocks is challenging to attain.

More reliable systems have been developed using thermo-responsive segments in triblock-copolymers. For example, Walther *et al.* assessed the effect of the length of a thermo-responsive segment on the behaviour and phase-segregation of micelles based on ABC triblock-copolymers with two different outer hydrophilic blocks, PEO- b-PnBuA-b-PNIPAAm (where PnBuA is poly(n-butyl acrylate) and PNIPAAm is poly(N-isopropylacrylamide)).[77,78] The thermo-responsive behaviour of PNIPAAm blocks was used to induce its collapse onto the central core of PnBuA through a heating step (above the lower critical solution temperature, LCST, the block is hydrophobic). By doing so, the solvent is excluded from the PNIPAAm domains, and the incompatibilities between the corona blocks (PEO/PNIPAAm) and between the PnBuA-core and PNIPAAm domains are increased which force the phase segregation of the corona. They showed that the extent of phase separation can be amplified for repeated heating cycles; however, independently of the length of the thermo-responsive block, a full transition to Janus micelles could not be observed. This lack of complete segregation in a Janus morphology was attributed to energetic penalties in the core (packing constraints) and the very minor energetic differences between a partially demixed and completely demixed (Janus) corona, which cannot compensate the entropic penalty of a complete segregation.

Another improvement came from Gröschel *et al.*[79] They designed a flexible and simple route toward large amounts of Janus micelles based on selective crosslinking of multi-compartment micelles (MCMs) (Figure 2.5). These MCMs have the shape of a "hamburger" or "clover" and typically consist of an A core with different amount of B patches and a C corona. After crosslinking of block B within its distinct compartments in the MCMs, the conformation and connectivity of the other blocks A (core) and C (corona) are chemically frozen on the B core which acts as a knot. Subsequently, Janus micelles are released after dissolution the crosslinked MCMs in a good solvent for both corona hemispheres (A and C). This concept was successfully applied for a wide range of triblock-copolymers and for different MCM architectures.

Triblock-copolymers have found applicability in the synthesis of organic Janus particles via local immobilization of self-assembled bulk structure. This approach is based on the fact that triblock-copolymers can form highly defined self-assembled phase-segregated structures in the solid state.[80] An example of the structure which can be obtained for ABC triblock-copolymer is reported in Figure 2.6 (left) as phase diagram for polystyrene-b -polybutadiene-b -poly(methyl methacrylate), known as SBM. Within the many morphological variation of the SBM, the research group of Ishizu and Müller, identified the suitable bulk morphologies for the generation of spherical Janus.[81-83] This methodology has been, later, followed by Müller's group to extend the fabrication of Janus particles to cylinders, discs and sheets shapes.[84-89]

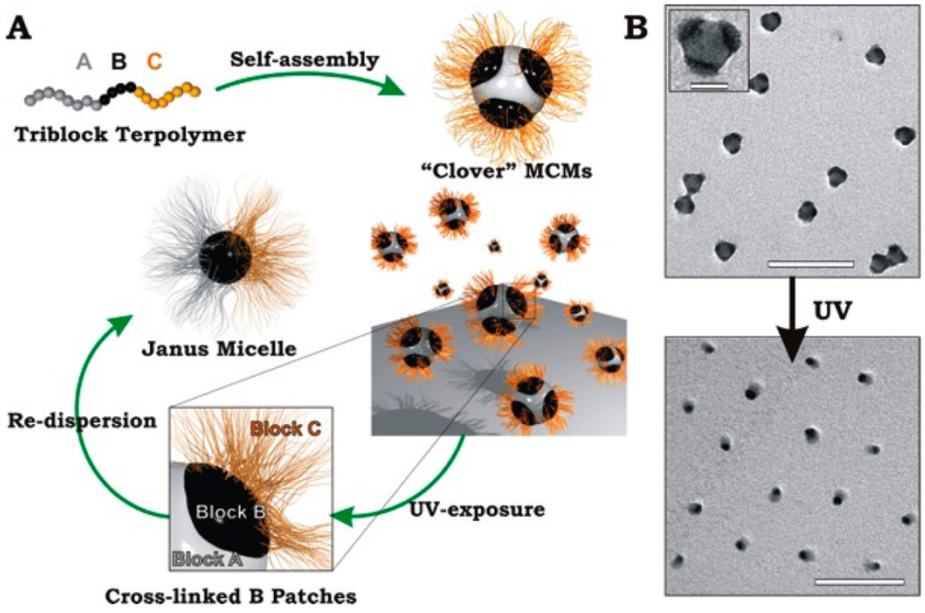


**Figure 2.5**: Synthesis of organic Janus particles via crosslinking of the B block-assembly (black) within multi-compartment micelle (MCM) based on ABC triblock-copolymers. (A) Directed self-assembly of ABC triblock-copolymer into clover-shaped MCMs with three B knots. Scheme of crosslinking of the micelles and Janus particles formation after redispersion in a good solvent for block A and C. (B) TEM images of "clover" MCMs structure (top) and organic Janus particles after crosslinking and redispersion (bottom) after stain with $OsO_4$ (scale bars are 200 and 25 nm in inset). Adapted from reference [79].

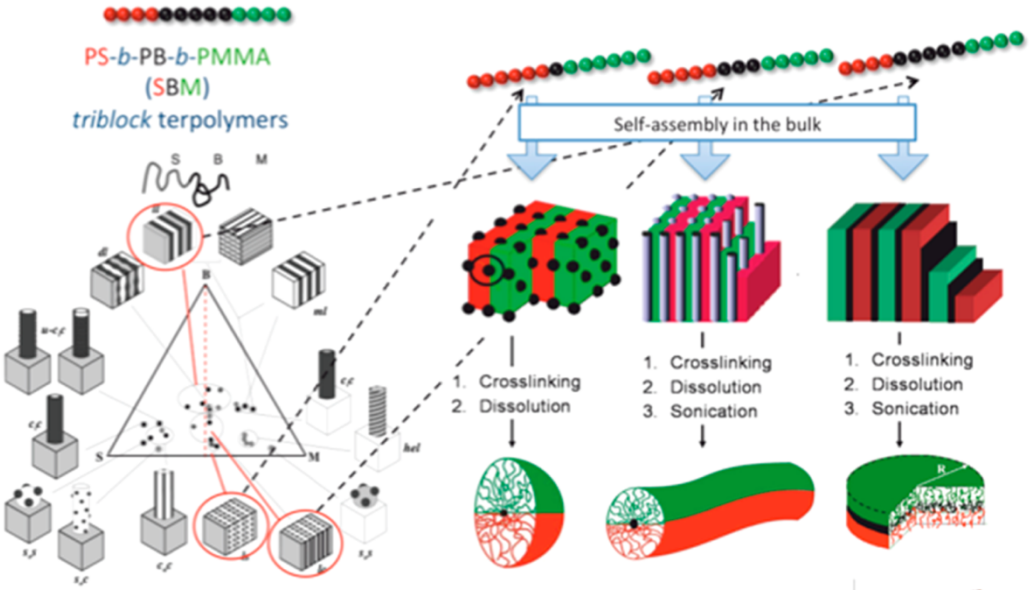


**Figure 2.6**: Synthesis of organic Janus particles with different architectures prepared via the selective crosslinking of the middle block of polybutadiene of triblock-copolymer (polystyrene-b -polybutadiene-b -poly(methyl methacrylate), SBM) assembled in microphase-segregated bulk structure and subsequent dissolution. On the left: Phase diagram of SBM. On the right: Synthetic protocols to target Janus micelles, Janus cylinders, or Janus discs. Adapted from [82, 84, 88].

Regardless the specific morphology, the underlying principle relies on the fact that once a specific microphase-segregated morphology has been obtained, the non-centrosymmetric orientation of the terminal blocks, A and C, can be frozen via the crosslinking of the inner block, B. This leads, in turn, to a preservation of the compartmentalization.

All the reported strategies of this section allow the synthesis of very small organic particles with Janus-like surface heterogeneity. However, since the fabrication methodologies rely on a synergic energy balance between attractive and repulsive interactions of di or tri-block copolymers, the composition freedom of the segregated polymer corona is severely restricted by thermodynamic constrains. Additionally, the theoretical predictions of the obtainable structures are met only if the copolymers can be experimentally synthetized with reasonably high fidelity and reproducibility.

## Segregated ligands on particle surface

The synthetic strategies belonging to this section exploit the use of self-assembled monolayers (SAMs) of thiolated ligands on gold surface, whose anchoring is driven by the formation of sulphur-gold bonds.[90] It has been demonstrated that ligand-exchange reactions can be employed to functionalize the surface of gold nanoparticles.[91-95] Pradhan and colleagues demonstrated that if these ligand-exchange reactions are limited to an air/water interface, nanoparticles with Janus-like surface morphology are produced by replacing hydrophobic hexanethiolate with hydrophilic mercaptopropanediol (MPD).[96] More specifically, a close-packed monolayer of alkanethiolate-protected gold nanoparticles (2 nm) was formed by Langmuir technique. Subsequently, MPD ligands were injected in the water subphase and a mechanical pressure was applied to the nanoparticles monolayer for several hours in order to limit the interfacial mobility by ligand intercalation between adjacent nanoparticles. An extension of the mentioned approach was later proposed by Bishop's group by using liquid/liquid interefaces rather than air/liquid. [97] They showed how gold nanoparticles (9 nm) stabilized with weakly bound dodecylamine (DDA) ligands can undergo to ligands exchange reactions at toluene/water interfaces in the presence of hydrophilic and hydrophobic thiolated ligands. Indeed, a simultaneous addition of an equal number of two competing ligands, one hydrophobic (dodecanethiol, DDT), the other hydrophilic (mercaptoundecanoic acid, MUA) will lead to the formation of amphiphilic nanoparticles because of a thermodynamic drive to reduce the interfacial energy (Figure 2.7a). Additionally, in the same work, they extended the synthetic protocol to the synthesis of amphiphilic iron oxide nanoparticles (10 nm) by adopting a similar ligands combination: 1,2-decanediol (DCD) as hydrophobic ligand and dihydrocinnamic acid (DCA) as hydrophilic ligand (Figure 2.7b)

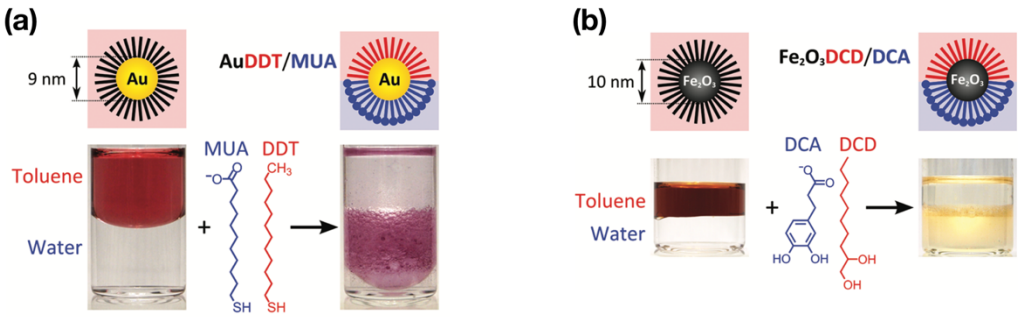


**Figure 2.7**: Schematic representation of the preparation of Janus gold (a) and iron oxide nanoparticles (b) with amphiphilic character by ligand-exchange at toluene/water interface. Reproduced and adapted from reference [97].

Studies have demonstrated that that two different ligands self-assembled in monolayers can re-organize into nanoscale patchy, or striped domains on planar surfaces. [98, 99] Consequently, a segregation of the ligands onto NPs seems to possibly lead to the formation of Janus-like corona shells. This could be possible by carefully selecting the ligands and the appropriate size of the nanoparticles. The size of the NPs has a pivotal role on the appearance of a Janus character. Indeed, the available surface area must provide a confinement below the characteristic length scale of phase separation of the respective mixed self-assemble monolayers on planar substrate. Therefore, it is obvious that a fully segregated ligand shell is formed only for very small nanoparticle core. On the other hand, for bigger cores, the segregated ligand shell may arrange into patchy or striped morphology. In this regard, modeling investigations of mixed ligand shell systems allowed to gain a better understanding over the phase-segregation process. For instance, Glotzer *et al.* thanks to atomistic and mesoscale simulations on mixed ligand shell systems, investigated the surface patterns with respect to the ligand structure, their mixing ratios, and in relation to the size of the nanoparticle core. They concluded that the conformational entropy plays the main role. For example, the conformational entropy can provide an additional energy gain when long ligands are mixed with shorter ones (Figure 2.8a). Moreover, the creation of additional interfaces between the two incompatible ligands can induces a transition from a Janus to a striped surface due to additional space provided at the interface between long and bulky surfactants versus short ones. The entropy gain depends on different parameters such as: (i) the length of both ligands, (ii) their length mismatch as well as (iii) the bulkiness of the end groups. Additional influences on the segregated ligand morphology arise from the nanoparticle size (or more precisely the surface curvature). The ligand shell morphology goes from a fully demixed (Janus character) into a partially demixed (striped character) when increasing the particles sizes (Figure 2.8b). From the investigations of Glotzer and co-workers, it is possible to conclude that ligand shells segregated in a Janus morphology are preferred for pairs of immiscible ligands with short lengths, small

length differences and limited bulkiness. Additionally, a given ligand pair, smaller nanoparticle sizes facilitates the formation of segregated Janus-like shells. Stellacci (one of the author of Glotzer's study) and his co-workers reported the experimental feasibility of the spontaneous phase-segregation of mixed ligands predicted by Glotzer's work for the synthesis of Janus gold nanoparticles.[100] To do so, they adopted a comparative approach synthesizing particles of different sizes, (2.0 nm and 4.5 nm, respectively) with an identical ligand shell composition. The authors demonstrated that ligand phase-segregate occurs in a Janus fashion when the nanoparticle core diameter is smaller than 1.5 nm (Figure 2.8d). On the other hand, nanoparticles bigger than 3 nm did not form fully demixed shells with Janus character but mainly stripe-like morphologies (Figure 2.8c). Interestingly, a transition between Janus and striped morphologies happens between 1.5– 3.0 nm core sizes. Although these findings clearly showed the possibility to generate Janus gold nanoparticle, they also highlighted how the spontaneous ligand segregation in with Janus-like shell is strongly limited by the nanoparticle size.

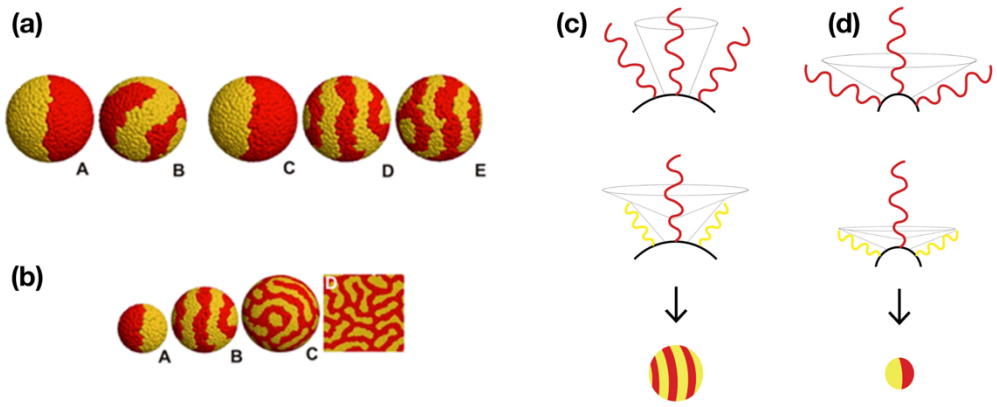


**Figure 2.8**: Mesoscale simulations of nanoparticles coated with different mixtures of two immiscible ligands. In (a) effect of different ligand structures at a constant sphere radius: (A) Length ratio 4:4, equal bulkiness. (B) Length ratio 6:6 with one ligand (yellow) having a bulkier tail group. (C–E) Length ratios 4:6, 4:7, and 4:13, respectively, with equal bulkiness of the tail. In (b) Effect of surface curvature from high to zero (A–D) for a ligand pair with length ratio of 4:7. In (c-d) schematic illustration of how the presence of shorter ligands allows longer ones to have a larger free volume; and hence, gain conformational entropy. The free volume is indicated as cone structure for the longer ligand. Two sub-cones can be identified: one whose angle is determined by the packing of the molecules and the other due to this interfacial free volume. As the radius of curvature decreases, the first cone becomes the dominant, and make the second one irrelevant which is related to the formation of a Janus-like segregation. Reproduced and adapted from [100, 101].

More recently, Percebom and co-workers proposed a way to overcome the size limitation by adopting segregated polymer shells. In their work, prepared Janus-like shells were generated by simply adding citrate-capped gold nanoparticles (23 nm) to a dilute solution of two incompatible thiol-terminated

polymers in a common solvent. The concentration of the two polymers in solution was maintained low enough to dissolve them but high enough to be in excess with respect to the available gold nanoparticle surface. In these conditions, the thiol groups spontaneously bind to the gold surface, forming a polymer shell. Moreover, because of the high local polymer concentration at the nanoparticle surface, a segregation of the two thiol-terminated polymers occurs leading to the formation of a segregate shell with a Janus-like morphology.

Although the intense study in this field, segregation of ligands to introduce Janus-like surface heterogeneity is still limited by composition and size of the core and ligands combination. That is why segregation of ligands has been mainly applied to the synthesis of amphiphilic nanoparticles with mixed shell composition and not segregated in a Janus-like fashion.

## Polymer-grafted (hairy) particles

The approaches discussed so far for the synthesis of organic Janus-like cores/surfaces rely on thermodynamic driving forces (e.g. ligands segregation and phase-separation phenomena) which impose severe experimental constrains in the exploitable fabrication strategies. A more general and flexible way is represented by polymer-grafted Janus particles, also known as hairy particles. These systems embody a link between colloidal chemistry and polymer chemistry by having surface-anchored polymeric chains onto, ideally, any type of core. In a similar fashion to what was reported in the section 2.1.2.1, the Janus anisotropy is introduce by exploiting the use of masking/immobilization tools during the surface modification reactions (e.g. polymer grating). There is a large variety of techniques to anchor polymers on a surface: these includes either (i) *grafting-to* approaches in which preformed polymeric chains are covalently anchored onto a surface via chemical reaction between surface-functionalities and polymer end-functionalities; or (ii) *grafting-from* techniques in which polymeric chain are grown from surface-bound initiator molecules via a surface-initiated polymerization reaction. Generally, the two approaches are combined in the synthesis of polymer-grafted Janus particles.

For example, Yang group proposed an approach based on the simultaneous biphasic polymer grafting on the two sided of silica particles at water/toluene Pickering emulsion.[102] Silica particles (450 nm) were modified with (4 -(chloro-methyl) phenyl) trichlorosilane to modify their lipophilicity and subsequently stabilize water-in-oil (W/O) Pickering emulsions. The available -$CH_2Cl$ groups were used for the atomic transfer radical polymerization (ATRP) initiated from the surface of poly (styrene) and poly (acrylamide), respectively in the toluene and water phases. The key aspect of this approach lies on the fact that when the two grafting reactions start the rotation of the particles is constrained by the developed amphiphilic character of the colloid. The authors clearly showed the asymmetry of

the grafting process by labeling the PAAm domain with Au, Ag or $Fe_3O_4$ nanoparticles

Zhao group used a similar method for the synthesis of amphiphilic Janus hairy particles. In their case, instead of using water-in-oil Pickering emulsion, they adopted an oil-in-water Pickering emulsion in which the oil-phase consists of the hydrophobic monomer (styrene) while the water-phase is a solution containing the hydrophilic monomer (sodium methacrylate). They demonstrated that amphiphilic particles could be generated via two simultaneous free radical *grafting-from* processes performed from silica nanoparticles (150 nm) at the w/o interface. In this case, the rotation of the particles was limited by the generated free homopolymer in the oil-phase, which increased the liquid viscosity and, in turn, limited the particle rotation at the interface.[103] The same research group, adopted a conceptually similar desymmetrisation strategy to generate Janus particles via two-step grafting-to processes by exploiting azide-alkyne cycloaddition click reactions. In this case, oil-in-water Pickering emulsion was prepared by using azide-modified silica nanoparticles (120-180 nm) and a solution of PS in toluene as oil-phase. The rotation of the particles was prevented by evaporating the toluene from the oil-phase and leaving the nanoparticles trapped at the surface of solid PS droplets. Finally, biotin moieties and poly (ethylene oxide) (PEO) chains were anchored onto the surfaces of the silica nanoparticles by two sequential step click reaction.[104]

Berger and co-workers reported a pioneering work on the synthesis of polymer-grafted Janus particles with a sub-micrometric size through a wax/water Pickering emulsion approach initially introduced by Granick's group. [105] As reported in Figure 2.9, ATRP-initiator functionalities were anchored onto the available particle side via amidation reaction after having immobilized aminated silica particles (800 nm) at the surface of wax colloidosomes. By doing so, the ATRP-initiator (partially covering the particle surface) was used to graft-from the surface either poly(*N*-isopropyl acrylamide) PNIPAm or poly(*tert*-butyl acrylate) PtBA. In a second step, the remaining amino functionalities were used in a grafting-to process to anchor carboxy-terminated poly(2-vinyl pyridine) P2VP by exploiting the use of the end-groups. With the mentioned synthetic strategy, the authors demonstrated that the synthetized Janus particles have a sharp interface between the two polymer hairy compartments and that can hierarchically self-assemble in suprastructures in a certain pH range. Synytska and colleagues extented the mentioned synthetic protocol to fabricate Janus particle with different polymer compositions, particle size and shapes. [106-109]

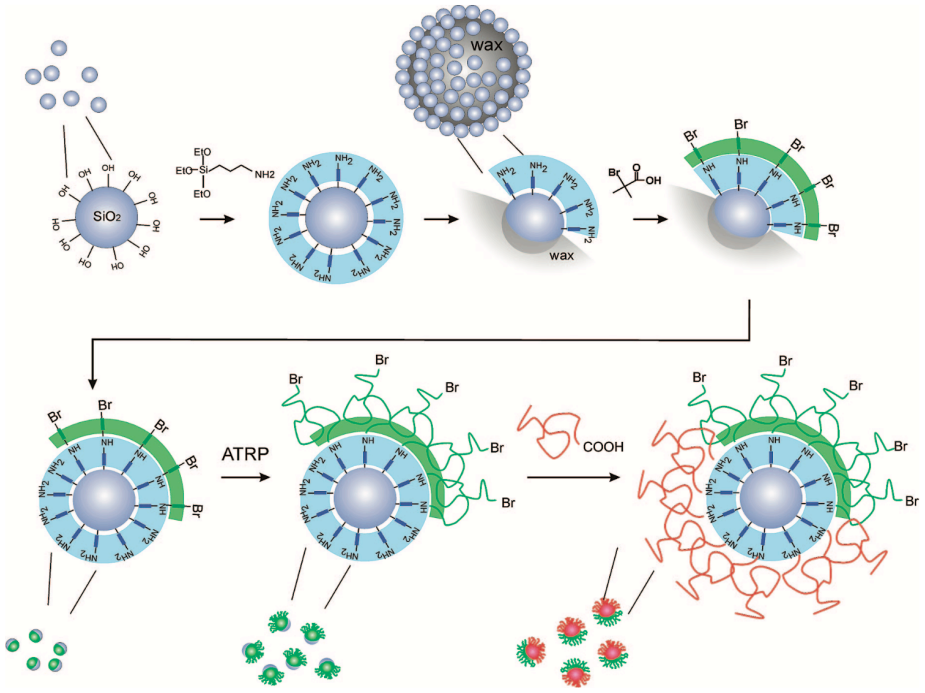


**Figure 2.9**: Schematic representation of the synthesis of polymer-grafted stimuli-responsive Janus particles by combining *grafting-from* and grafting-to approaches in the following order: (i) modification of silica particles with organo-amine functionalities; (ii) toposelective modification of such functionalities into ATRP-initiator functionalities on the surface of particles immobilized at wax colloidosomes; (iii) *Grafting-from* via ATRP process and grafting-to by using carboxyl-terminated polymers. Reproduced from the reference [105].

When dealing with truly nanometric sizes (i.e. below 100 nn), Pickering emulsion is not a reliable strategy for particle immobilization. In those cases, researchers have often opted for solid substrate as immobilization tool to generate the asymmetric polymer grafting. For example, Vasquez and colleagues electrostatically immobilized aminated iron oxide nanoparticles (50 nm) on negatively charged mica surfaces (Figure 2.10a) and modified the unprotected nanoparticle surface with ATRP-initiator (Figure 2.10b). Under this condition, PNIPAm brushes were grown from the exposed nanoparticle (Figure 2.10c) hemispheres followed by nanoparticle release by decreasing the pH (Figure 2.10d). ATRP-initiator moieties were again immobilized on the nanoparticles thanks to the availability of $-NH_2$ groups on both the PNIPAm brushed and the unmodified nanoparticle hemisphere. Therefore, in a second *grafting-from* step, poly (methacrylic acid) PMAA chains were grown from NPs resulting in the formation of bicompartmental polymer-grafted magnetic NPs (Figure 2.10f).[197]

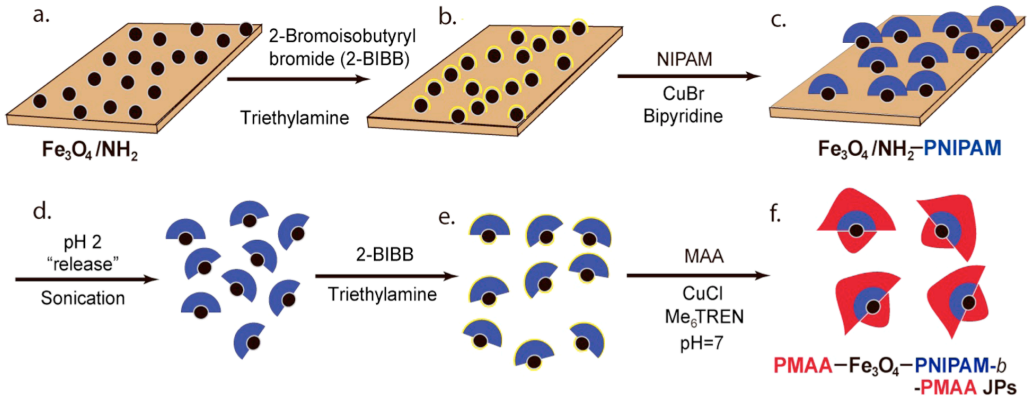


**Figure 2.10**: Schematic representation of the synthesis of polymer-grafted magnetic nanoparticles: (a) electrostatic immobilization of aminated nanoparticles onto mica substrates; (b) toposelective modification of amino functionalities to ATRP-initiator groups; (c) partial *grafting-from* of PNIPAm from the nanoparticle exposed surface; (d) nanoparticle release; (e) modification of available amino functionalities to ATRP-initiator groups; (f) *grafting-from* of PMAA. Reproduced from the reference [197].

Hatton and Lattuada used a similar approach to fabricate Janus magnetic nanoparticles (20 nm of core size).[110] They started with homogenously grafted NPs with poly(acrylic acid) PAA which were immobilized onto the surface of aminated microparticles via electrostatic interaction. The Janus-like surface heterogeneity was generated by modifying the immobilized NPs with preformed polymeric chains with $-NH_2$ end-groups via amidation reaction between carboxylic acid and amine functionalities.

Li and co-workers proposed a conceptually different immobilization strategy lying on the use of polymer single crystal acting as both protective desymmetrization tool and polymer-source for *solid-state grafting-to* modification reactions. More precisely, as reported in Figure 2.11, they used single crystals of thiol-terminated PEO to immobilize gold nanoparticles (6 – 15 nm). In a second step, the available nanoparticle surface was activated with ATRP-initiator molecules and followed by a toposelective *grafting-from* of PMMA, PtBA or PAA. After polymer grafting, the immobilization crystal was dissolved leading to the formation of Janus gold nanoparticles with PMMA/PtBA brushes on one side and PEO chains on the other one.[111, 112] The same group extended this strategy to other nanoparticle materials. Therein, silica nanoparticles (40-50 nm) were immobilized by using polymer single crystal of alkoxysilane-terminated poly (ε-caprolactone) and subsequently partially grafted with PNIPAm via surface-initial polymerization. [113]

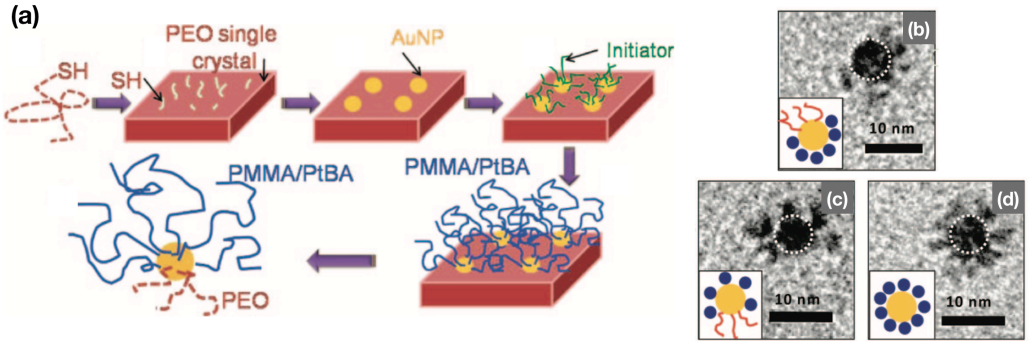


**Figure 2.11**: Schematic representation of the synthesis of polymer-grafted gold Janus nanoparticles via a combination of *grafting-from* and solid-state grafting-to (a). TEM images of the polymer-grafted nanoparticles (b-d) with asymmetric morphology identified by labelling the grafted PAA domain (grown via *grafting-from*) with platinum nanoparticles (yellow – AuNPs, blue - Pt NPs, red - PEO). Reproduced and adapted from the reference [111].

More recently, Yao and colleagues proposed another simple protocol to fabricate amphiphilic Janus particles by combining grafting-to and *grafting-from* strategies.[198] As reported in Figure 2.12, a single chain of anionic terminated PS with relatively high molecular weight was grafted onto each particle of chloromethylphenyl-capped iron oxide via rapid elimination of the Cl from the NP surface promoted by the Li anion of the single chain. The still available NP surface was then modified with PNIPAm brushes through *grafting-from* method.

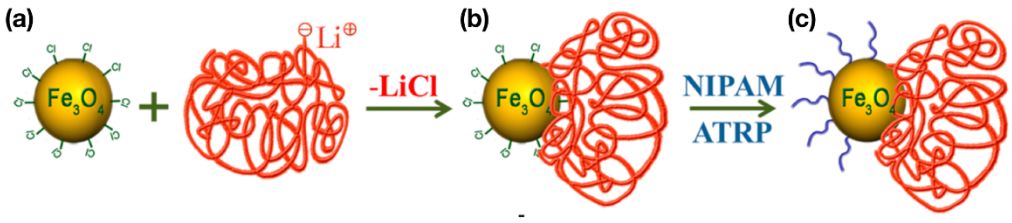


**Figure 2.12**: Schematic representation of polymer-grafted Janus nanoparticles via grafting from and grafting-to of single chain: (a) grafting-to of single chain of anionic polystyrene onto the surface of chloromethylphenyl-capped nanoparticles by a rapid elimination of Cl from the NP surface with Li anion of the polymer (b); *grafting-from* of PNIPAm on the remaining particle surface (c). Reproduced from the reference [198].

The studies reported in this section demonstrated how polymer grafting techniques are a more flexible and versatile modification strategy to synthetize particles with Janus-like surface heterogeneity. Nevertheless, all the available studies make use of heat and/or metal catalyst in the polymer grafting reactions.

## 2.2 Self-Assembly of Janus particles

Self-assembly can be defined as an autonomous organization of system components into patterns or structures in a spontaneous way i.e. without any human intervention but determined by naturally occurring forces.[114] Self-

assembling is common at any scale: from small system, such as that of nucleic acid double helix driven by hydrogen bonding at the level of the base pair,[115] to much bigger systems such as those of galaxy in which planets and stars are assembled as a consequence of gravitational forces.[116]

Among the unusual behaviours of asymmetric Janus particles, self-assembly is surely the one to have received the greatest scientific interest, as well as one of the most studied.[18] In general terms, self-assembly of Janus particles occurs spontaneously and it is driven by solvophobic and/or electrostatic attraction/repulsion, although other external stimuli can play a role in some cases.[48, 117-123] Particle self-assembly can be referred either to (i) assembly between particles in a bulk liquid or to the (ii) assembly at interface as simple as air/liquid and liquid/liquid interfaces or to more complex biointerfaces such as lipid membranes. In the following subsection, some examples of the above-mentioned assembly behaviours are reported from experimental and computational perspectives.

### 2.2.1 Self-assembly in a bulk liquid

In this section, we highlighted the differences between self-assembly behaviours of Janus particles depending on the character of the two particle domains. Indeed, it is the character of the single domain that governs the balance of forces responsible of driving the self-assembly process. Additionally, it will be shown how the volume or surface ratio between the two domains, affects the geometry of the suprastructure obtained from the particle self-assembly. We reported only theoretical and experimental contributions related to the self-assembly of amphiphilic Janus particles and we intentionally omitted the behaviour of dipolar Janus particles (i.e. with opposite charge in the two compartments) because it is out of the scope of this manuscript. Indeed, the self-assembly of this last class of Janus particles should be treated differently because they require interaction potentials whose sign depends on the interplay between two particle domains and cannot be simply assigned as attractive or repulsive for a given particle domain. For more details on the self-assembly of dipolar Janus systems see references [105, 124-126].

#### Amphiphilic with solvophilic / solvophobic domains

In the simplest case, amphiphilic Janus particles possess two domains: one solvophobic and the other one solvophilic. These properties can be simply referred to hydrophilicity and hydrophobicity whenever the solvent under consideration is water. In water, the interactions between amphiphilic Janus particles are dominated by hydrophobic attraction and therefore when the hydrophobic domains face each other they will be attracted to minimize the hydrophobic domain / water interactions. Because the hydrophobicity is confined to a spatially-

limited domain, the hydrophobic interactions are directional (i.e. ascribed by an anisotropic attractive potential) and they will lead to the formation of self-assembled superstructures with precise geometries. On the other hand, when the hydrophobic character is isotropic (homogeneous particles), the attractive forces are not directional and therefore huge agglomerate will be formed without any geometric motif as a consequence of the isotropic attractive potential.

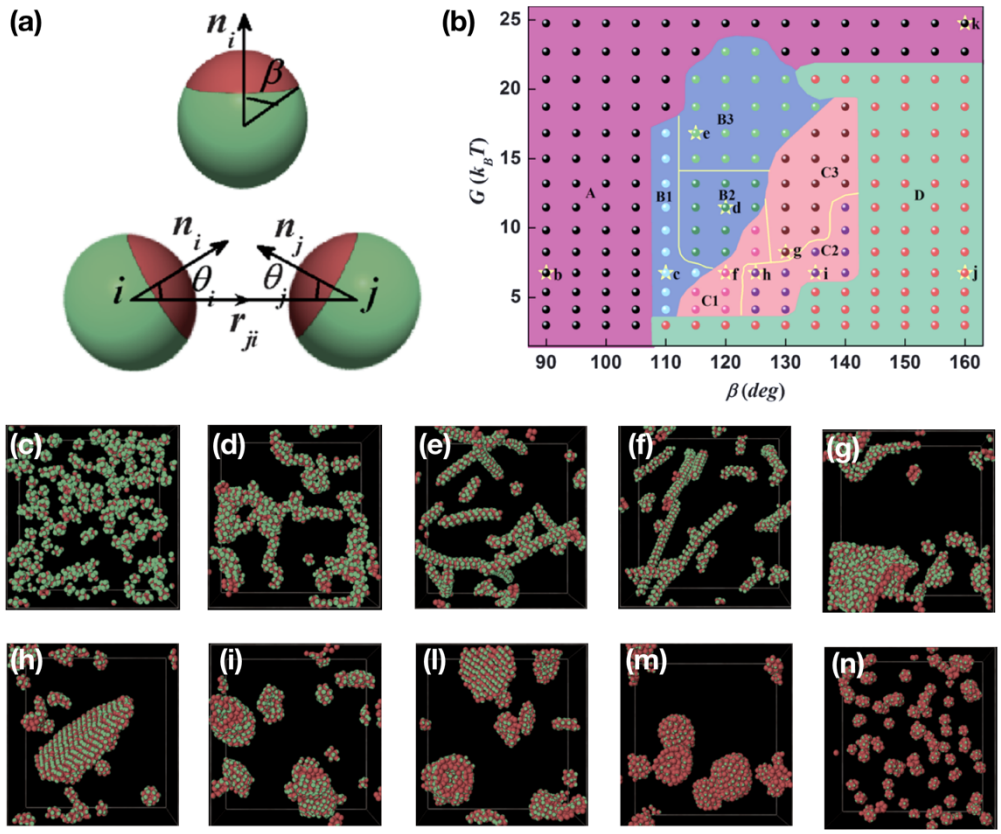


**Figure 2.13**: Mesoscale simulations for the self-assembly of soft amphiphilic Janus particles. (a) structure of the soft Janus particles; (b) Phase diagram of soft Janus particles in the G– $\beta$ plane. Snapshots of typical equilibrium self-assembled structures (marked by star symbols in the phase diagram) (c-n). Reproduced and adapted from the reference [285].

A detailed theoretical study on the self-assembly of soft (i.e. deformable) amphiphilic Janus particles was proposed by Li *et al.*[285] They provided a mesoscale model able to predict the self-assembly scenario depending on experimentally measurable particle properties as reported in Figure 2.13a. In their model, attractive interactions refer to solvophobic interaction between deformable domains which could be traced back to polymer-based Janus systems. They showed that by varying the Janus balance $\beta$ and the strength of attraction of two solvophobic domains, expressed as adhesion energy, G, it is possible to compute a phase diagram of the soft Janus particle from a series of simulated scenarios

(Figure 2.13b). The results demonstrate that proper tuning of the Janus balance and adhesion strength leads to reversible self-assembly into several hierarchical superstructures in liquid, such as micelles, wormlike strings, single helices, double helices, bilayers, tetragonal bilayers, and complex supermicelles (Figure 2.13c-n); superstructure that in many cases are yet to be discovered experimentally.

A more complex case of Janus amphiphiles occurs when repulsive interactions exist between the particles (e.g. electrostatic repulsion) along with the attractive interactions between the hydrophobic domains mentioned above. This is a very common scenario and, in most of the cases, it is more realistic than a system only driven by hydrophobic interactions. As a matter of fact, in presence of polar solvents such as water, the particle surface is generally charged. This is also the case for many polymers which possess functional groups that can be protonated or deprotonated in specific pH range, leading to a net surface charge (e.g. PAA, PNIPAm, PDMAEMA, etc). In the case of amphiphilic Janus particles with electrostatic repulsion between the hydrophilic domains, the self-assembly depends on the balance between the attractive hydrophobic interactions and the electrostatic repulsion. For these systems, we can distinguish two cases: (i) isotropic electrostatic repulsive potential (e.g. the electrostatic repulsion affect the whole particle) or (ii) anisotropic electrostatic repulsive potential (e.g. the electrostatic repulsion affect only the hydrophilic domain of the particle). The first case (i) is a common example when there is a surface charge all over the particle, affecting both hydrophilic and hydrophobic domains. In this situation, the isotropic repulsive potential has the effect of partially or completely screen the anisotropic attractive potential, depending on the respective strength of interactions. In total, the amphiphilic particle owns a repulsive potential for the hydrophilic domain and a screened attractive potential for the hydrophobic domain. The second case (ii), instead, is common whenever only the hydrophilic domain possess a surface charge. In this case, both attractive and repulsive potentials are anisotropic by possessing a directionality in their action. Granick and coworkers included the electrostatic repulsive potential in their theoretical and experimental study on the self-assembly of Janus colloids.[16] In their study, both ranges of electrostatic interactions (expressed in terms of Debye screening length) and of hydrophobic interactions are significantly less as compared to the particle dimension. This case is experimentally applicable to Janus particles with size from several hundreds of nanometers to few microns. They observed that, in pure water, the Janus particles were stable with no sign of assembly due to sufficiently strong electrostatic repulsion (Figure 2.14a). When the electrostatic screening length was adjusted below 10 nm upon salt addition (1 mM of $KNO_3$), the Janus particles started assembling into small clusters and then into chain-like structure by further increasing the salt concentration (5 mM $KNO_3$) as schematically illustrated in Figure 2.14b. In following study, the same research group was able to give new insight in the kinetic of self-assembly by using Monte

Carlo simulations.[127] It was found that several type of clusters occur overtime. As reported in Figure 2.14c, these can evolve following different reaction pathways: (i) monomer addition which is a step-by-step addition of single particles (red arrows), (ii) cluster fusion of small cluster into larger one (black arrows) and (iii) isomerization for example from capped trigonal pyramid shape into a more symmetric octahedral shape (blue arrows). These different pathways highlighted a remarkable orientation freedom possessed by the individual particles within the clusters. Interestingly, unlike micelles formed by molecular surfactant, the rigid shape of these Janus particles allows them to rotate without change in position, making possible, in turn, the fusion of clusters from their ends. Furthermore, in contrast with molecular surfactant, many long-lived shapes of kinetic origin are possible because of the lack of fluidity, which does not make possible a rapid shape equilibration. Because of this, upon a suitable screening of the electrostatic repulsion, it is possible to generate unique non-equilibrium helical Boerdijk-Coxeter shapes, which are generally not formed in other colloidal systems. However, the deep insights provided by the studies of Granick group do not provide adequate answer for amphiphilic particles with nanoscopic size. In these cases, indeed, the length of interaction is comparable with the particle size and, therefore, the self-assembly of such systems should be handled differently. In this regard, Sciortino and colleagues provided a model for Janus particles self-assembly with two distinct hemisphere, one solvophobic and attractive and the other solvophilic and repulsive.[128] The interactions were considered in terms of a square-well potential with a range equal to the particle radius. The study allowed to draw a phase diagram for the modelled Janus particles as reported in Figure 2.14d. The phase diagram, reported either in temperature–density or pressure-temperature, showed the existence of a colloidal-poor region (gas) with particles assembled in micelles or vesicles, and a colloidal-rich region (liquid) interpreted as an infinite size aggregate. Additionally, they clearly identified a gas-liquid coexistence region in which the two colloidal-rich and colloidal-poor phases compete between micelles formation and phase separation.

In experimental terms, the observed self-assembly behaviors of amphiphilic Janus particles do not cover, yet, the whole spectrum of possible geometrical configurations. Additionally, experimental systems not always follow the predictions from the mentioned phase diagrams, which are calculated under simplifications more or less severe. As a matter of fact, the theoretical predictive models proposed by Granick and Sciortino consider the surface of the amphiphilic Janus particles as an undeformable solid. Therefore, deformable and flexible surfaces such as hairy polymer coronas are far from being properly described by those models. Although the theoretical model developed by Li and coworkers included the flexibility of the surface, in their model the interactions were considered purely attractive and the existence of electrostatic repellence was neglected. Consequently, unpredicted cluster arrangements and behaviors are very

often observed in experimental systems. For instance, Groschel at al. investigate the self-assembly of amphiphilic hairy Janus nanoparticles providing new finding regarding the effect of the Janus balance and the solvent-induced swelling of the hairy corona.[79] Perfectly symmetric Janus particles with solvophobic/solvophilic domains are expected to form the same equilibrium superstructures when changing from a solvent selectively good for one domain to another selectively good for the other. On the other hand, when the Janus balance is changed, different behaviors should be observed when changing solvent. To demonstrate this hypothesis, poly(styrene)-core-poly(methacrylic acid) amphiphiles were prepared. In a good solvent for both domains (e.g. THF) the Janus particles remained as unimers resulting in a bigger corona for the PS domain and a smaller one for the PMAA. As it schematically illustrated in Figure 2.15a, when the nanoparticles are dispersed in alkaline water, the PS chains are collapsed while the PMAA chains are swollen. Consequentially, the Janus nanoparticles self-assemble

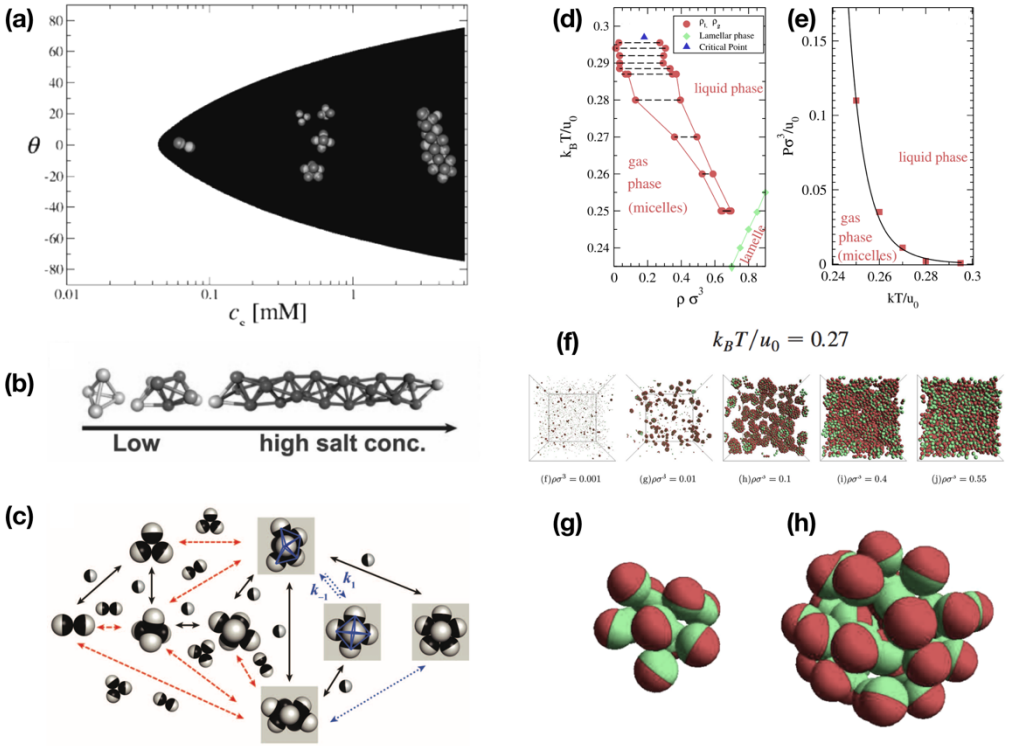


**Figure 2.14**: Simulation of Self-assembly of amphiphilic particles with uncharged hydrophobic domain on one side and charged hydrophilic domain on the other. Results from Granick group: (a) Region of permitted tilt angles between two charged hemispheres plotted as a function of the concentration of a monovalent salt. (b) Geometric representation of helix growth by face-sharing tetrahedral as the salt concentration increases. (c) Observed reaction pathways and kinetics of cluster formation of amphiphilic Janus particles at low salt concentration. Results from Sciortino *et al.*: Phase diagram in the temperature – density (d) and pressure - temperature (e) planes. Snapshot of an equilibrium typical configuration for a 5000 particles system (f). Typical shape of particle aggregates as micelles (g) and vesicles (h). Reproduced and adapted from references [16, 127-128].

in multimers superstructure via solvophobic attractive interactions. A progressive increase of the cluster size was observed when increasing the concentration from 0.05 to 5 g/L (Figure 2.15b). On the other hand, when the Janus balance was inverted by transferring the nanoparticles into chloroform, the picture was quite different. In this case, the nanoparticles self-assembled in dimers and trimers with a behavior almost independent from the concentration (Figure 2.15c). In chloroform, the collapsed PMAA domain is protected by the larger swollen PS domain, which causes weaker solvophobic interactions between the PMAA domains. As a consequence, only near-equilibrium self-assemblies (such as dimers and trimers) are formed.

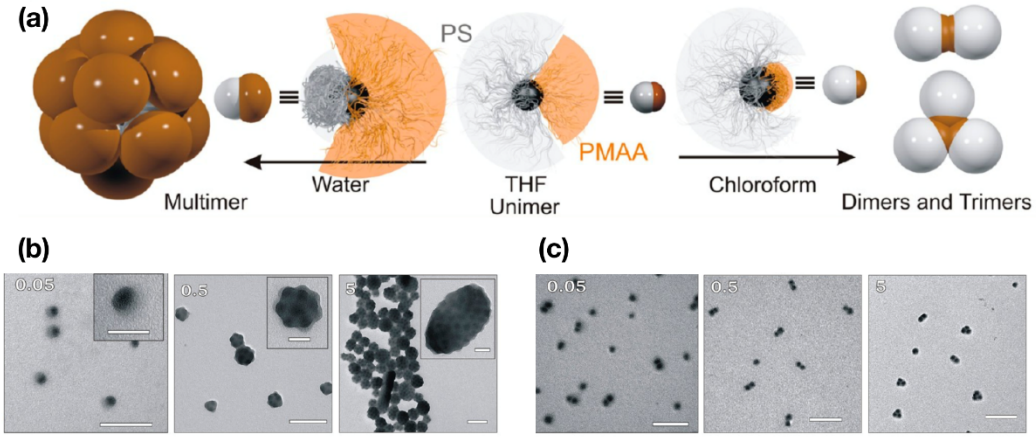


**Figure 2.15**: Schematic clustering of amphiphilic Janus particles (Janus-like surface) in dependence of the corona size in chloroform and water at pH 10 (a). Here also, PS is gray, PMAA is orange and the sore is black. TEM images of nanoparticle self-assembly at concentration of 0.05, 0.5 and 5 g/L in alkaline water (b) and chloroform (c). Images collected after stain with OsO4. Scale bars are 100 and 50 nm in insets. Reproduced and adapted from reference [79].

In another study, Hatton and Lattuada investigated the self-assembly of polymer-grafted nanoparticles with a hydrophilic negatively charged domain of poly (sodium-4-styrene sulfonate) PSSNa and a PAA domain with a pH-responsive character[110]. The carboxylic functionalities of the PAA can be deprotonated at high pH leading to a negative surface charge. The self-assembly was investigated in terms of cluster size from DLS measurements by changing the pH and the molecular weight of PSSNa domain (from 18.3 to 158 kDa). As reported in Figure 2.16a, at high pH both domains possess a negative charge and consequently repulsive interactions occur between the nanoparticles. In this condition, the nanoparticle surface is fully hydrophilic and therefore the system is well stabilized in as for the homogeneous nanoparticles only grafted with PAA. When the pH decreases below 5, the PAA is protonated and loses its charge. Therefore, hydrophobic attractive interactions arise between the PAA domains, which are translated in a self-assembly behavior which is strongly dependent on the average molecular weight of the PSSNa chains. An example of the geometry

of the self-assembled clusters is reported in Figure 2.16b from cryo-TEM study on a system with 90.8 kDa and at a pH of 2. The elongated shape of the self-assemblies (confirmed through Monte Carlo simulations, Figure 2.16c) was found to be a consequence of the small percentage of hydrophobic surface. The explanation for these cluster morphologies is that the steric hindrance between the PSSNa domains do not allow more than three hydrophobic domains to meet. In the case of very low hydrophobic surface extension (i.e. below 10%), most of the cluster formed are dimers or trimers. This was experimentally found for PSSNa with a molecular weight of 18.3 KDa, which correspond to an extension of the hydrophobic surface of 8.6%. In confirmation of that, the hydrodynamic size of the cluster was found to be 1.5 times bigger than that of a single particle.

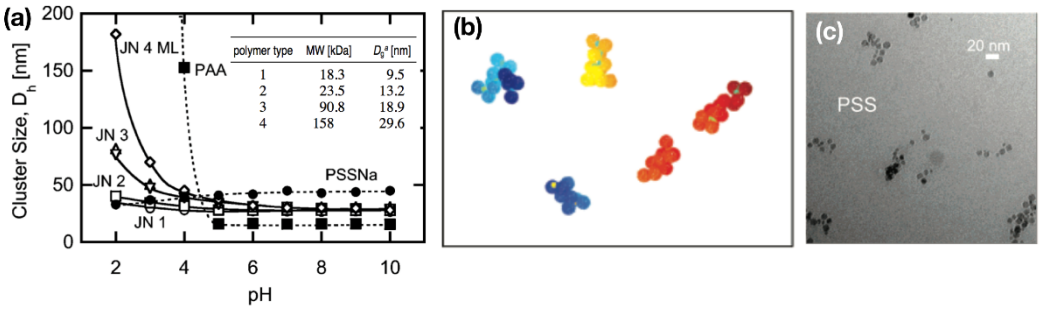


**Figure 2.16:** Effect of pH on the cluster/particles size in terms of average hydrodynamic diameter of PAA/PSSNa Janus particles (indicated with JN, with different polymer types as reported in the enclosed table) as compared to uniformly grafted nanoparticles with PAA or PSSNa (a). Monte Carlo simulation based on a hydrophobic surface equal to 14.9% at a pH of 2 (b). Cryo-TEM of Janus nanoparticle (JN3) with 90.8kDa PSSNa molecular weight (c). Reproduced and adapted from reference [110]

A different example of self-assembly behavior was investigated for Janus gold nanoparticles with two hairy compartments, one of PMMA and the other one of PEO chains.[129] The amphiphilic nanoparticles were stable when disperse in acetone. However, when dioxane was added to the system, the polarity of the liquid medium progressively changed, leading the PEO chain to collapse onto the nanoparticles surface (Figure 2.17a). Consequently, solvophobic interactions appear and the nanoparticles begin to self-assembly initially in small clusters (Figure 2.17b-c). Overtime, the size of clusters increases becoming anisotropic with the formation of worm-like structures (Figure 2.17d) and after 35 minutes, branches start forming (Figure 2.17e-f). The overall cluster structure evolves to minimize the free energy of the system because of the decreased solubility of the PEO chains in the liquid medium. Interestingly, it is not merely the presence of the PEO chain to cause the self-assembly process, but it is related to the distribution of the PEO chains in an asymmetric Janus morphology. Indeed, (Figure 2.17a, bottom) when the liquid polarity decreases, the dispersed uniformly grafted nanoparticle remain stable because, although the PEO chains collapse, the stretched and uniformly distributed PMMA chains stabilize the system. This was

experimentally confirmed by looking at the distribution of uniform nanoparticles after 180 minutes of incubation in acetone-dioxane liquid medium (Figure 2.17g).

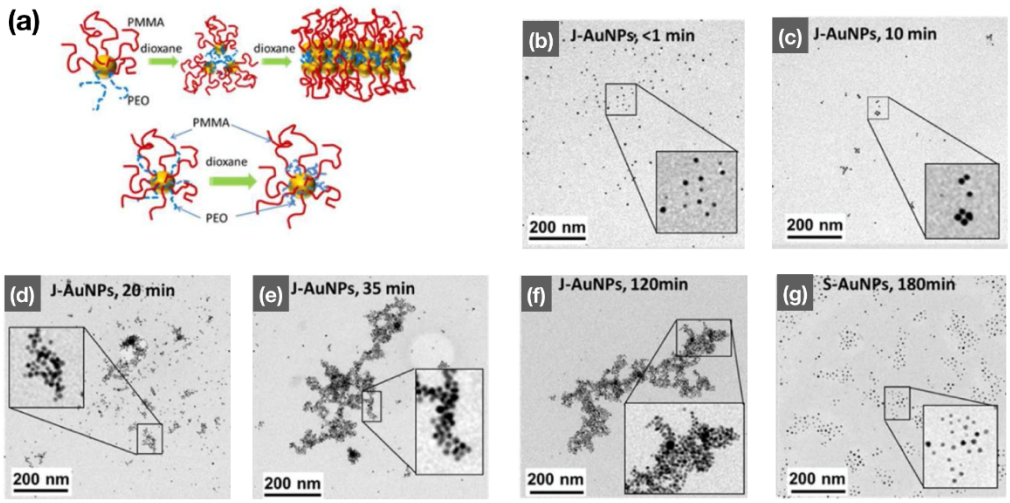


**Figure 2.17**: Self-assembly of polymer-grafted PMMA/PEO Janus nanoparticles (Janus-like surface) in acetone-dioxane solvent solution: (a) Schematic representation of the clustering phenomena for Janus (top) and mixed (bottom) morphology. TEM micrographs of polymer-grafted particles with Janus (b–f) and mixed (g) morphology in dioxane after various incubation times. Reproduced and adapted from reference [129].

## 2.2.2 Self-assembly at interfaces

Fluid-fluid interfaces are characterized by having an imbalance in cohesive interactions, which is translated in a tension that minimize the interfacial area between the two fluids. This tendency is described in terms of interfacial tension $\gamma$, which is a surface energy per unit area. Particles are known to be able to move from the bulk phase to the liquid-liquid interface where they assembly to minimize the interfacial tension. Since the process of assembly is spontaneous, it can be denoted as self-assembly at the interface. A similar particle self-assembly can occur at more complex interface such as those of biological systems. Cell membraned, which consist mainly of a double layer of phospholipids, are a common example of biointerface. The inherent complexity of these systems is reflected in the complexity of the interaction between them and nanoparticles. That's why, the self-assembly of Janus nanoparticle at lipid membrane has been treated in a separate subsection.

### Behavior at fluid-fluid interfaces

We have already discussed that homogeneous particles can self-assemble at fluid-fluid interface. Indeed, it is because of this ability that it is possible to generate Pickering emulsion. However, if the particles have an amphiphilic

character coming from asymmetric Janus-like surface properties, the behaviour at interfaces is different. As a matter of fact, amphiphilic Janus particles can lower the surface tension between two liquids, for instance, by orienting their hydrophilic domain facing the water phase, and the hydrophobic domain facing the oil phase.[130] As a consequence, amphiphilic Janus particles are able to effectively stabilize water-oil emulsions, not only kinetically (as for conventional Pickering emulsion) but also thermodynamically.[14]

The reasons behind their unique interfacial behaviour lie on the adsorption/desorption of a single Janus particle at a fluid-fluid interface. The expression derived for the desorption energy of a homogeneous particles at a fluid-fluid interface (see subsection 2.1.2.1) can be extended for an amphiphilic Janus particle. Binks and colleagues, starting from the surface free energy of the interface between two immiscible liquids, proposed the following equation: [131]

$$E_{interface} = 2\pi R^2 \left[\gamma(JP_O O)(1+\cos\alpha) + \gamma(JP_w O)(\cos\beta - \cos\alpha) + \gamma(JP_w W)(1-\cos\beta) - \frac{1}{2}\gamma(OW)(sin^2\,\beta)\right] \; for\; \beta \leq \alpha \qquad (3)$$

Where, $\beta$ is the angle related to immersion depth of the particle at the interface; $\alpha$ is the angle related to the Janus balance ($\alpha$ = 90°, Janus particle with symmetric hemispheres); R is the radius of the particle, $\gamma(JP_O O)$, $\gamma(JP_w O)$ and $\gamma(JP_w W)$ are the interfacial tension between the hydrophilic or hydrophobic particle domain and the water or oil phase; $\gamma(OW)$is the interfacial tension between the water and oil phases. It is important to note that the Equation 3 was derived for a planar interface. For Janus particles at curved interfaces, Hirose and co-workers proposed a different theory.[132] The desorption energy of a Janus particles can calculated as the energy necessary to transfer the particle from the interface (Equation 3) to one of the bulk phases ($E_w$ - $E_{interface}$ or $E_o$ - $E_{interface}$). If the Janus particle has two perfectly symmetric hemispheres ($\alpha$ = 90°), it is located perfectly at the middle of the interface ($\beta$ = 90°) and that the interfacial tensions $\gamma(JP_O O)$ and $\gamma(JP_w W)$ are negligible, the desorption energy for a Janus particles can be written as follow:

$$E_{Janus-des} = 2\pi R^2\gamma(OW) + \pi R^2\gamma(OW) = 3\pi R^2\gamma(OW) \qquad (4)$$

Similarly, we can estimate the maximum desorption energy for a homogeneous particle by rewriting the Equation 1 from Pieranski when $|\gamma(PO) - \gamma(PW)| \ll \gamma(OW)$ and reads as:

$$E_{homo-des} = \pi R^2\gamma(OW) \qquad (5)$$

Therefore, from the comparison between the Equations 4 and 5, the adsorption strength is clearly greater for a Janus particle than a homogeneous particle of the same size. In this regard, Glaser *et al.* published a pioneering experimental study

on the interfacial activity of Janus nanoparticles. They verified the higher interfacial activity of Au-$Fe_3O_4$ amphiphilic Janus nanoparticles in comparison to the respective homogeneous particles of the same size. [199] The self-assembly at the water/hexane interface was followed in terms of interfacial tension measurements by pendant drop tensiometry. The authors investigated the effect of the amphiphilicity on the interfacial activity. To do so, the gold domains were modified with hydrophobic ligands, which resulted in an increase of amphiphilicity. They showed that the increase of amphiphilicity caused an increase of interfacial activity as reported in Figure 2.18a by the decrease of water/hexane interfacial tension. Furthermore, it was observed that, by increasing the length of the alkyl chains (from C12 to C18), it is possible to further decrease the interfacial tension.

More recently, investigations demonstrated that nanoparticles with a Janus hairy polymer surface possess other unique self-assembly behaviours at interface because of the additional configurational changes made possible by chain entanglement. Jiang *et al.* showed that the self-assembly of PS-PMMA hairy Janus particles can effectively reduce the interfacial tension between toluene and water (Figure 2.18b).[200] It was observed an increased energy gain for locating the nanoparticles at the interface when increasing the nanoparticle concentration. When self-assembled at interface, unlike hard particles, Janus hairy particles showed the ability to entangle the polymer chains causing the nanoparticle to form a solid-like interfacial assembly. The entanglement of PMMA chains led to a reduction of the interfacial area. Consequently, the interfacial area reduction caused a compression of the interface and, as a result, wrinkles were formed as illustrated in Figure 2.18c.

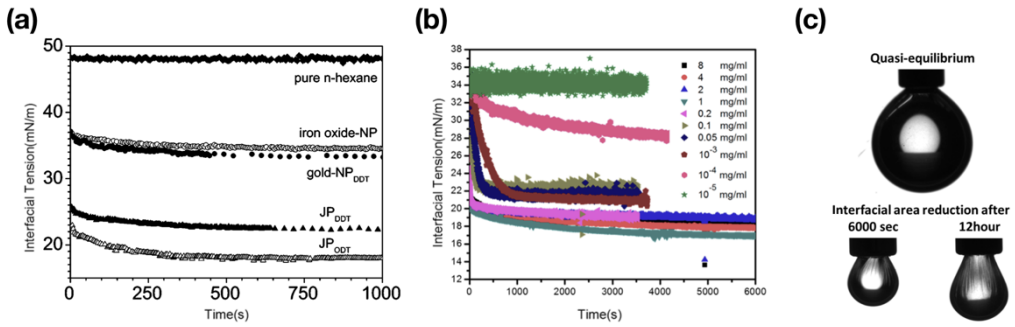


**Figure 2.18**: Surface activity of Janus nanoparticles: (a) Interfacial tension isotherms (hexane/water interface) for the adsorption of pristine $Fe_3O_4$ nanoparticles and DDT-coated Au nanoparticles in comparison to dumbbell Au/$Fe_3O_4$ Janus nanoparticles (Janus-like core), in which the Au-domain is coated with different thiols, DDT and ODT. (b) Interfacial tension isotherms of deionized water against PS/PMMA Janus particles (Janus-like surface) in toluene solution at different concentrations. (c) Droplet after the interfacial tension reaches quasi-equilibrium and droplets with interfacial area reduction with wrinkling formation at aging time of 6000 sec and 12 hours. Reproduced from references [199, 200].

## Behavior at lipid membranes

The interaction between particles and membrane can be mediated by different adhesion mechanisms. In this work, we focused our attention to nonspecific adhesion mechanisms, which are based on interactions that do not involve specific cell receptors.[133] Indeed, nonspecific adhesion is based only on molecular interactions mediated by the chemistry of particle surface and lipid bilayer. In a general sense, because of the complex nature and uncertainty in the structure of lipid bilayers[134-136] along with the intrinsic complexity of asymmetric particles, the derivation of unified theories describing the interaction between lipid membrane and Janus particles is far from being accomplished. For instance, Ding *et al.* investigated the interaction and the translocation dynamics of Janus particle and lipid membrane by using dissipative particle dynamics simulations.[137] The same approach was adopted later by Arai and colleagues to study the collision of homogeneous or Janus particles with lipid vesicles.[138] Alexeev *et al.* used coarse-grained numerical simulations to design membranes with controllable pores by using Janus particles.[139] However, for all the mentioned works, hard particles (i.e. not deformable) with a size comparable to the membrane thickness were taken into consideration. More recently, Agudo-Canalejo and Lipowsky derived an analytical model describing the interaction between lipid vesicles and particles with a homogeneous or Janus-like surface (i.e. particles with membrane adhesive and non-adhesive domains).[140] For their studies, they treated the membrane as a smooth surface with a given curvature and characterized by a bending free energy value. The interaction with nanoparticles was studied in terms of energy landscapes and curvature-induced forces caused by the attractive interaction between the membrane and the particles. In general, depending on the local curvature of the lipid membrane, the particle can have different fates: (i) in can maintain its freedom, (ii) it can become partially engulfed (i.e. anchored at the membrane), (iii) it can be completely engulfed or (iv) it can display a bistability between free and completely engulfed. In a previous work, they derived the energetic stability conditions for the occurrence of a defined fate.[141] These depends on the particle size, material properties, adhesiveness and even local curvature of the membrane. Among the different fates, a particle is partially engulfed when it is bound to the membrane surface but it is not fully covered by the membrane, i.e. it is self-assembled at the lipid membrane. This situation is very interesting for its potentially useful applications in biomedical imaging or drug-delivery. Nevertheless, nanoparticles with homogeneous surface chemistry can be partially engulfed only if size and adhesiveness are finely tuned.[141, 142] On the other hand, based on the hypotheses of the model of Agudo-Canalejo and Lipowsky, Janus particles are always partially engulfed and, therefore, subject to curvature induced forces. In their work, the curvature-induced forces experimented by Janus particles were derived when in contact with vesicles of

different shapes. Interestingly, they observed that these forces are conceptually similar to capillary forces for particle at fluid interfaces.[143, 144]

Even though theoretical and computational studies have foreseen an interesting prospective for the use of Janus particles to tailor particle-membrane interactions in biological systems, the few experimental works available are limited to micrometric systems making use of immunoglobulin G (IgG) antibody–antigen interactions, [8-12] in other terms specific interactions. Only one work has been very recently published on nanometric Janus particles interacting with lipid membrane via nonspecific interactions. In their study, Yu group demonstrated that the spatial segregation of hydrophobic ligands on silica nanoparticles (100 nm in diameter) remarkably change the interaction with lipid membranes. They observed that amphiphilic Janus nanoparticles disrupt supported membrane of zwitterionic lipids at pM concentrations. From these findings, it was speculated that the hydrophobicity of the ligand-coated domain is responsible of extracting the lipids from the supported membrane creating holes. Furthermore, the surface charge on the hydrophilic domain seemed also to play a role in the interaction. Positive charged systems appeared to disrupt lipid membrane more effectively than the anionic counterparts did. Interestingly, it was observed that nanoparticles with uniformly mixed surface functionalities were not able to induce the disruption of the supported membranes.[57] The mentioned work showed only destructive particle-membrane interactions in terms of microscopic defects after several dozen minutes of interaction. However, they lacked of providing information regarding the initial stages of the interaction in order to tailor non-destructive self-assembly of nanoparticles at the interface.

# 3

# Tools to photogenerate Janus-like surface heterogeneity

Besides the thermodynamically driven processes, two foundations are generally required to generate Janus-like surfaces: a masking/immobilization strategy and a surface modification tool. The first one must be tailored depending on particle size, material chemistry and surface modification conditions. On the other hand, the surface modification steps are designed depending on the type of surface that is required. So far, several approaches have been reported for the synthesis of particles with Janus-like surface, as it was discussed in the first section of Chapter 2. However, all chemical surface modification methods, available in literature, are thermal and/or catalysed approaches. Herein, we proposed novel approaches to generate Janus-like surfaces based on light-induced reactions. We did so with the aim of gaining temporal and spatial control over the surface modification process (see subsection 1.2.1), and to have access to more flexible, milder fabrication protocols that could be performed efficiently at room temperature. This Chapter is intended to overview the available light-induces methodologies for the modification of surfaces.

## 3.1 How to use light to initiate chemical reactions

Light-induced reactions are not a human invention. Indeed, plans, algae and even some bacteria can use light to trigger reactions such as those involved in photosynthesis. Photosynthesis is a good example of photo-controlled chemistry in which light is absorbed by light-harvesting systems called reaction centres (i.e.

light-absorbing molecules such as chlorophyll, phaeophytin and quinones) and transferred via electron transfer steps, which eventually lead to the synthesis of chemical energy (i.e. adenosine triphosphate, ATP) [145]

In a similar way, light can be used to induce chemical reactions but, in this case, photoinitiator molecules (PIs) represent the reaction centres. Upon light exposure, PIs are exited and generate reactive species (e.g. free radicals, anion or cations), which will induce chemical reactions. In our case, the interest laid at radical photoinitiator, which can be used to promote polymer *photografting-to* and *photografting-from* or to photoreduction of metal ions. In general, as illustrated in Figure 3.1 by following the photoinitiator Jablonski diagram, upon light excitation, the molecule is promoted to its first excited singlet state, and then converted into its triplet state via a fast intersystem crossing.

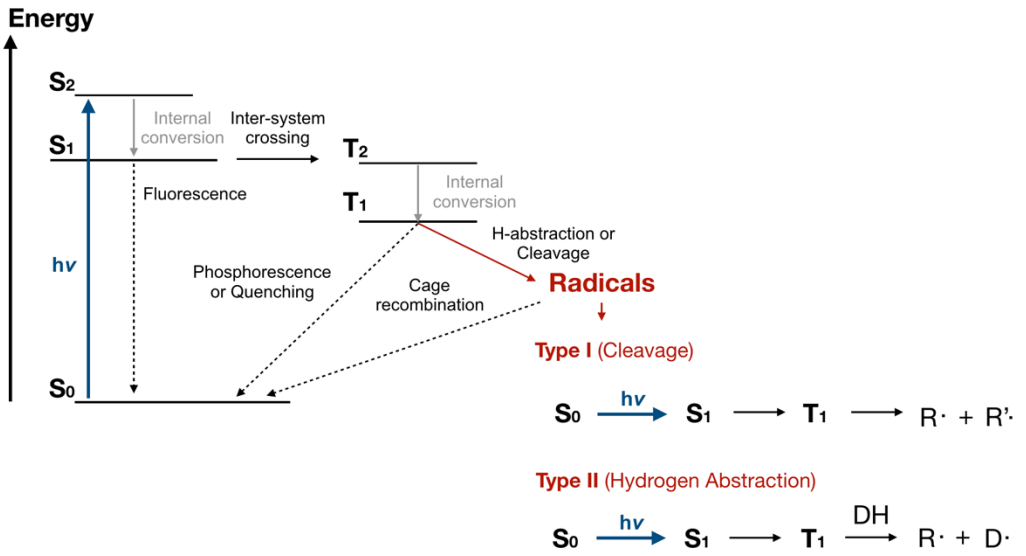


**Figure 3.1**: Electronic states and transitions between them represented as Jablonski diagram for a photoinitiator molecule. Radical formation pathways for type I and II photoinitiators from the excited triplet following a cleavage process and hydrogen abstraction, respectively.

The excited triplet state may be deactivated through several processes such as quenching by oxygen, non-radiative or radiative products, and reaction with other molecules. If not deactivated, the transient triplet state yields the reactive radicals R•, which are used to induce the chemical reaction. The reactive radical can be generated mainly in two way, which represent two different class of radical photoinitiators.[146]

(i) Cleavage process (Type I initiators): unimolecular photochemical cleavage or homolysis of the initiator molecule into two free radical intermediates.

(ii) Hydrogen abstraction reaction (Type II photoinitiators): generally photochemical bimolecular reaction where the excited triplet of the

photoinitiator interacts with a second molecule (a donor) abstracting a hydrogen to generate free radicals.

In type I photoinitiators, free radicals are generated from a direct fragmentation of the PI molecules. On the contrary, type II PIs (e.g. benzophenone, thioxantone and benzyl derivatives) work only through electron transfer: the amine-derived radical formed are considered as the initiating species; ketyl structures (inactive for the initiation, are simultaneously generated.[147] Therefore, it is clear the greater simplicity and flexibility of type I initiating systems. Most type I photoinitiators are based on the benzoyl chromophore. Adequate substitution and modification of the benzoyl chromophore lead to a wide variety of radical photoinitiators with different reactivity and wavelength of absorption as reported in Figure 3.2.

The photogenerated radicals can initiate a large variety of chemical reactions, as reported in the following subsections for those employed in this work.

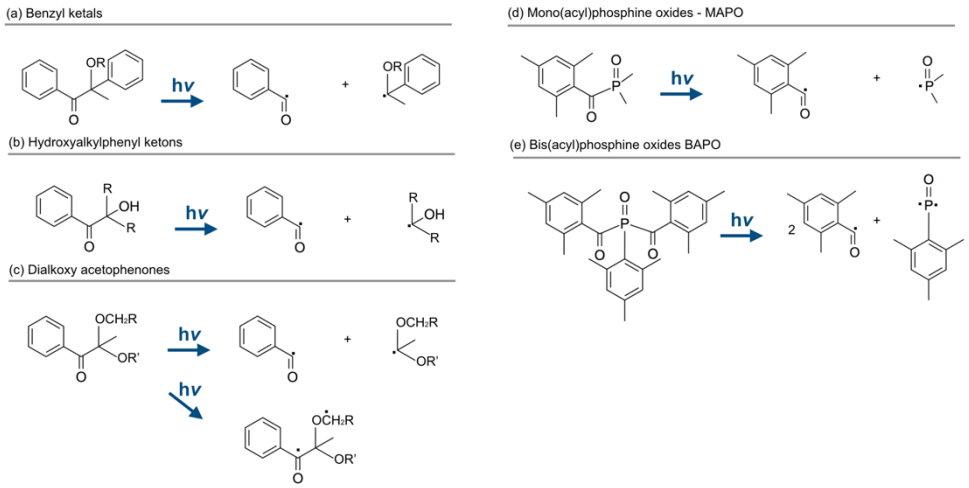


**Figure 3.2**: Photoscission following an α-cleavage of benzyl chromophore derivatives (type I) for different substitution scenario: (a) benzyl ketals, (b) hydroxyalkyl phenyl ketones, (c) dialkoxy acetophenones, (d) mono(acyl)phosphine oxides, (e) bis(acyl)phosphine oxides.

## 3.2 Soft Surface Modification: Polymeric surfaces

A polymeric surface is generated when polymeric chains are chemically or physically anchored to a surface. Although, physical adsorption of polymer chain on a surface (e.g. via electrostatic interactions) is a rather simple strategy, it generates surfaces with poor thermal stability, unable to withstand high shear forces and easily displaceable by other chemicals/proteins. On the other hand, chemical anchoring (known as grafting) generates very stable surfaces because of the formation of chemical bonds between polymer chains and surface. The chemical anchoring process can follow to main pathways: (i) *grafting-to* strategy, where preformed polymer chains are surface grafted, usually, via chemical reaction

between surface-bound functionalities and polymer-end groups (Figure 3.3a); (ii) *grafting-from* strategy, where the polymer chains are directly grown from the surface in a process known as surface-initiated polymerization (Figure 3.3b). Between the two strategies, the *grafting-from* method is commonly preferred because it gives access to higher grafting density and film thickness. Indeed, besides its greater simplicity, the grafting-to method owns intrinsic limitations due to the inevitable steric hindrance among the chains going to be grafted, which makes problematic to tether end-chains at short intermolecular distances. Interestingly, the grafting density plays a fundamental role in the final conformation acquired by polymer chains and in turn remarkably affect the properties of the polymeric surface. Indeed, we can distinguish three different regimes depending on the polymer grafting density, or more precisely on the

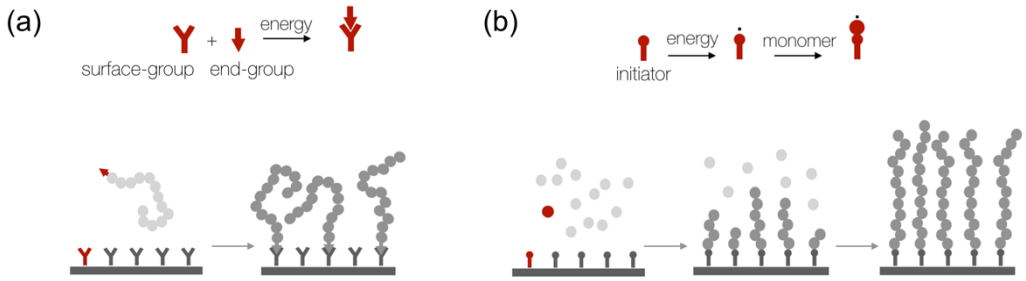


**Figure 3.3**: Generation of polymeric surface via grafting-to approach (a), i.e. reaction between surface-bound group and end-group from preformed polymer chain, and *grafting-from* approach (b), i.e. surface-initiated polymerization from a monomer. The initial stages of the grafting processes are reported in red.

distance between two tethered chains in comparison to the radius of gyration $R_g$ of a free chain. For neutral polymers, the film thickness $h$ is scaling following the relation $h \sim N (\sigma)^{v}$. Here, N is the degree of polymerization, which is related to the molecular weight of the grafted polymer; σ is the grating density, which is expressed as number of chains per surface area; $v$ is the scaling factor, which is related to the polymer conformation on the surface.[148-150] The variation of grafting density leads to three different regimes as illustrated in Figure 3.4:

(i) Low grafting density (mushroom regime): the conformation is that of the free polymer and, therefore, the thickness is mainly related to the polymer molecular weight, the scaling factor $v$ is 0 (Figure 3.4a);

(ii) Medium grafting density (semi-dilute brush regime): the chain-chain interaction starts affecting the polymer conformation, the scaling faction is equal to 1/3 (Figure 3.4b);

(iii) High grafting density (concentrated brush regime): the chain-chain interaction dominates the polymer conformation, the scaling factor is higher than 1/3 (Figure 3.4c).

Semi-dilute and concentrated brush regimes can be archived achieved only by using *grafting-from* strategies. For these regimes, scaling laws, similar to those mentioned above as function of the grafting density, have been derived depending on the solvent quality. The power law dependence of the film thickness can be described with a scaling factor increasing from 1/3 to 1/2 to 1 as the solvent quality decreases from good solvent to $\theta$-solvent to bad solvent.[151, 152]

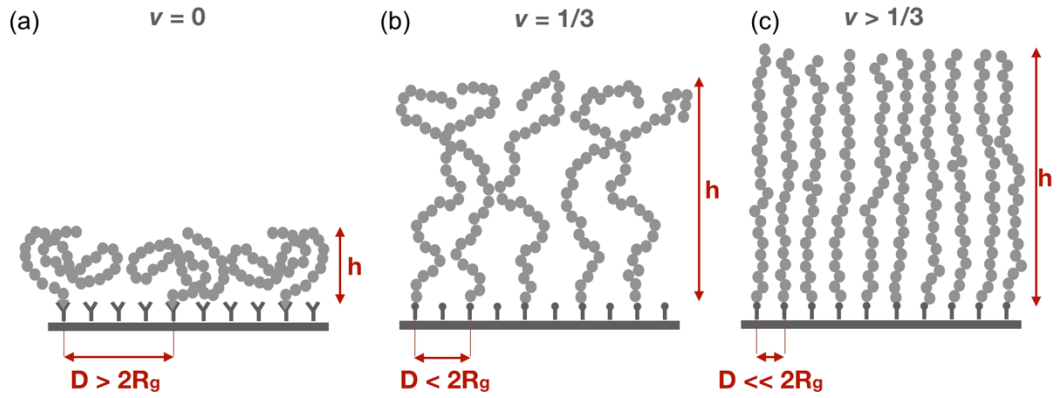


**Figure 3.4**: Representation of scaling laws for different regimes of neutral polymer surfaces. Scenarios at different grafting densities are reported in terms of distance between two chain, D and radius of gyration of the free polymer, Rg. (a) Low grafting density (D > 2Rg), mushroom regime. (b) Medium grafting density (D < Rg), semi-diluted brush regime. (c) High grafting density (D << Rg), concentrated brush regime.

### 3.2.1 Light-induced *grafting-from*

In the fabrication of polymer surfaces through a *grafting-from* method, surface-bound radicals must be generated from the initiator molecules anchored onto the surface. If light is used to generate such radicals, the process is defined as *photografting-from* approach. In the following pages, we reported a brief overview of the currently available *photografting-from* methods. Part of this work has been already published and it is available in a review article at the ref [28]. The different literature contributions are presented focusing on the photoinitiating system: starting from type I then type II initiating systems and finally reporting few examples of self-initiating approaches.

## Norrish Type I photoinitiating systems

Regarding Norrish type I initiating systems, derivatives of the widely used 2,2-azobis- (isobutyronitrile) (AIBN) initiator have been also adapted in surface modification via light-induced *grafting-from*[153, 154]. However, these azo initiators show a relatively low absorbency and long half-life [155] and consequently, long polymerization times are needed. Additionally, the photoactivation of AIBN derivatives produces two radicals with the same reactivity, only one of which is tethered to the surface. The unanchored radical diffuses into solution and initiates polymerization in the bulk. The so produced bulk polymer intercalates into the grafted brush and requires a time-demanding purification for complete removal.

A more reliable and promising photoinitiating system is represented by bis-(acylphosphane) oxides (BAPO) derivatives with functional groups that allow surface-anchoring. In this field, the Grützmacher group reported a large toolbox of BAPO-derivatives which can be used for surface modification of different substrates[156]. BAPO-derivative photoinitiators offer several exceptional advantages such as: (i) Photolysis yields a total of up to four radicals (see Figure 3.2e), with the phosphinoyl radical about 1000 times more reactive than the acyl radicals. (ii) Light in the visible region is absorbed by BAPOs ($\lambda$ = 360 – 440 nm), but the cleavage products are transparent. (iii) BAPOs show a relatively high thermal stability (> 100 °C) and can be easily stored[157, 158].

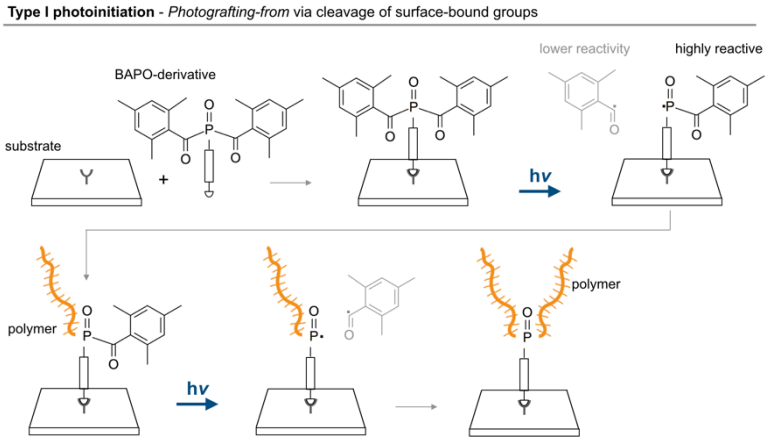


**Figure 3.5**: *Photografting-from* via type I initiating system. Immobilization of BAPO-derivative on a given substrate (this step depends on the available surface functionalities). Photoscission of the anchored initiator with generation of one acyl radical (low reactive), released in the medium and a surface-anchored phosphoryl radical (highly reactive). Polymerization initiation from the phosphoryl radical and subsequent photoscission of the remaining acyl group. Polymerization initiation from the freshly generated phosphoryl radical. Note that the photogeneration of phosphoryl radicals has been reported in two separate steps for clarity. However, depending on the irradiation condition, the two steps can be virtually simultaneous.

When a BAPO-derivative is surface-anchored, the above-mentioned advantages apply to the *photografting-from* process. As illustrated in Figure 3.5, from the photo-cleavage, two phosphinoyl radicals are generated and, ideally, two polymer chains could be grown from a single photoinitiator anchoring site, making this system ideal for polymer brushes. In each of these steps, an acyl radical is likewise generated but these are significantly less reactive and the homopolymers generated as side-products by these as initiators are easily removed.

For instance, Wang et. al. proposed the synthesis of a surface-anchored bis-(acylphosphane) oxides (BAPO) via a stable bis(mesitoyl) phosphane intermediate.[159] The functionalized BAPO was attached on the nanocellulose particles and poly(methyl methacrylate) chains were grown by the light-triggered grafting onto the surface. In another work from the same group, a tri(methoxy)silyl-substituted BAPO derivative was attached on the cotton surface and fluorinated acrylates were photografting onto cotton fabrics.[156] Alkoxy functionalized BAPO was also proposed for the glass surface modification, obtaining a photoactive surface. By spreading the monomer on the functionalized substrate and by UV irradiation in the presence of either a partially fluorinated acrylate or a specifically synthesized polysiloxane containing polymerizable acrylate functions allowed the generation of polymer chains which grew from the surface in an efficient radical polymerization process (*grafting-from* procedure). Durable hydrophobic surfaces were prepared characterized by contact angles between 93° and 95°.[160]

Another strategy to photograft polymers on different substrate is to anchor on the surface thiol groups, by a simply silanization of the surface with alkoxy-functionalized organo-thiols. Indeed, under UV-light, thiyl radicals are generated from the thiol groups and these radicals can initiate free-radical chain growth polymerization form the surface. This approach has been used by Mostegel and colleagues to photopattern planar surfaces with poly (ethylene glycol) brushes and biomolecules. When thiol functionalities are exposed to UV-light in presence of oxygen, UV-induced photo-oxidation of the thiol occurs which yields to sulfonate groups. These sulfonic acid groups were used for immobilization of amino-functionalized biomolecules while the intact thiol groups were used to induce a photografting polymerization of poly (ethylene glycol) [161] The group of Bowman reported the use of thiol-surface functionalities to photoactivate the formation of PEG-brushes. The photogenerated thiyl radical adds across the carbon–carbon bond of the PEGMA to form a carbon–sulphur bond and carbon radical. The just formed carbon radical can add to another PEGMA molecule and propagate leading to the formation of PEG-brushes.[162-164] Similarly, some ketones and aldehydes were reported to undergo hydrogen abstraction from substrate upon UV-irradiation. So, these compounds could be used to promote *photografting-from* process, where the monomer is added on the radical generated on the surface.[165]

## Norrish Type II photoinitiating systems

Although surface-anchored type I initiator offers many advantages, so far, the most commonly reported surface modification strategies via *photografting-from* make use of benzophenone (BP) type II photoinitiating system.[166, 167] As illustrated in Figure 3.6, when light-irradiated, BP or BP-based molecules are excited to a singlet state and then jump to a triplet state by intersystem crossing. Several studies have demonstrated that BP and its derivatives in a triplet state $[BP]^T$ undergo hydrogen-abstracting reactions from substrates, consequently providing surface radicals (R•) capable of initiating surface graft polymerization. The resulting benzopinacol radicals (BP–OH•) are relatively less reactive and not prone to promote free radical polymerization, but tend to participate in termination by coupling reaction.

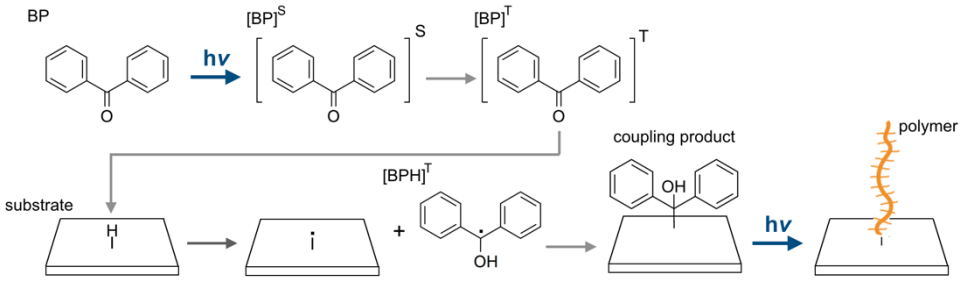


**Figure 3.6**: *Photografting-from* via type II initiating system. Schematic representation of the BP excitation process, leading to the formation of BP molecules in their excited triplet $[BP]^T$. Abstraction by $[BP]^T$ of hydrogens available on the substrate surface with rapidly radical coupling of the surface radical and the generated semipinacol $[BPH]^T$. Upon subsequent light-exposure, the surface radicals, formed from the coupling products, initiate a polymerization from the surface.

Different substrates have been treated with BP in a first step, and subsequently photoactivated to promote radical chain-grow polymerization on the surface. Some authors photografted polyacrylamide onto cotton fabrics by linking photo-active moiety benzophenone chromophoric groups.[168] Ma et. al proposed a two-step process to photografting polypropylene membranes [169] in the first step irradiated BP abstracts hydrogen from poly(propylene) substrate, the photogenerated radicals on the surface quickly combine with semipinacol radicals. In the second step, the monomer solution is added to the active substrate and the surface initiators initiate the graft polymerization under UV irradiation. Roppolo et. al followed a similar concept to photograft graphene oxide (GO).[170] By dispersing GO in the presence of BP, under irradiation the semipinacol radical can recombine with remaining radicals on the GO sheets creating a covalent bond. In the second step, during UV-irradiation, a homolitical break the bond between the semipinacol group and the GO surface is induced, generating an initiating point on the GO surface, so a radical chain grown polymerization is

promoted in the presence of a suitable monomer. Luan *et al.* modified the surface of biomedical elastomers poly (styrene-b- (ethylene-co-butylene)-b-styrene) (SEBS). Oxygen plasma process was used as pre-treatment to form polar onto the surface of SEBS film. This treatment improved the wetting properties of both hydrophilic monomer and ethanol solution of BP initiator on the plasma-treated substrate, thus facilitating the uniform distribution of grafted chains on the surface. In the UV-induced graft polymerization process, SEBS films in BP solution were exposed to UV irradiation which caused BP initiator abstracted hydrogen from the SEBS backbones to form surface free radicals, and further initiated the surface graft polymerization of N-vinyl pyrrolidone (NVP) monomer. After the surface photografting with NVP, the water contact angle decreased to about 40° and protein adsorption and platelet adhesion were significantly inhibited.[171] Sugiura and co-workers reported that the surface of polydimethylsiloxane (PDMS) can be micropatterned with poly(ethylene glycol) (PEGDA) in one step photografting process by using a reaction mixture of monomer and BP.[172] Schneider and colleagues accurately investigated the process parameters for the photografting of the inner channel of polydimethylsiloxane microfluidic devices with poly(acrylic acid), PPA, even for very complex geometry. A solution of BP in acetone when applied inside the microfluidic channels diffuses into the PDMS matrix. After washing, the channels filled with acrylic acid (PA) can be exposed to UV-light to generate the photografted PPA surface.[173] Benzophenone as photoinitiator have also been employed in PDMS materials to photograft methacrylate monomer bearing a phosphorylcholine moiety prior photogeneration of semipinacols. It was shown that it is possible to tailor protein repellency and lubrication property by playing on the grafting density.[174] Feng *et al.* anchored BP molecules onto poly (carbonate urethane) surfaces and, by using UV-light, induced the polymerization of poly(ethylene glycol) monomers with different molecular weight to improve hemocompatibility and increment hydrophilicity. They showed that monomer molecular weight affects platelet adsorption and hemocompatibility, which might be explained with an optimum balance between poly(ethylene glycol) grafting density and chain length.[175] Also other, type II initiating system has been proposed. For example, Yin and co-workers proposed another strategy involving surface-anchored dendric thioxanthone (TX) photoinitiators. In this approach, in the presence of amino groups as co-initiators, light-irradiation leads to the formation of a ketyl radical from the thioxanthone and another radical coming from the hydrogen donor amine. In the presence of a suitable monomer, the polymerization is initiated by the amino radicals while the ketyl radical are generally very less reactive because of the steric hindrance. This approach has been adopted on both planar surfaces[176] to grow poly(N-isopropylacrylamide) brushes and on microparticle surfaces[177] to grow poly(methyl methacrylate) brushes.

## Self-initiating systems

Some research groups reported *photografting-from* processes via self-initiated photopolymerization without the use of added photoinitiating molecules. There are some monomers, such as Maleic anhydride (MAH) which can undergo in a photografting polymerization even in the absence of any photoinitiator. In fact, under UV-irradiation, MAH molecules produce excimers that are able to abstract hydrogen from the backbones of the substrate and form surface free radicals which could consequently initiate graft polymerization and homopolymerization of MAH as well as other monomers.[178] With LDPE as the substrate and after UV irradiation, the conversion percentage and grafting efficiency of MAH can reach nearly 80 and 70%, respectively.

Another example of self-initiated photografting was shown by irradiating poly(ether sulfone) ultrafiltration membrane in the presence of N-vinyl-2-pyrrolidinone . The resulting grafted membrane showed a severe loss of protein rejection.[179] The *grafting-from* method is activated due to the use of very low wavelength, where poly(ether sulfone) is absorbing generating free-radicals on its surface.[180] Jordan's group reported in several work the photogeneration of polymer brushes by direct self-initiated photografting. This occurs by hydrogen abstraction by a radical mechanism under the UV- illumination via from glassy carbon[181, 182] and silicon carbide[183] substrates. They demonstrated that the presence of C-OH functionalities onto the surface is a crucial parameter for the hydrogen abstraction. Similarly, Steenackers and colleagues demonstrated that uniform of patterned polymer brushed can be grown from graphene without the use of any initiator and by simply UV-irradiation. They proved that photopolymerization occurs at existing defect sites. Polymerizations were performed with a wide range of monomers (including styrene, methyl methacrylate (MMA), N,N-dimethylaminoethyl methacrylate (MAEMA), methacrylatoethyl trimethyl ammonium chloride (METAC), and 4-vinyl pyridine). Additionally, they demonstrated there is non-detectable disruption of the basal plane conjugation of graphene after the photografting.[184] Shiojima and colleagues reported a methodology for preparing a poly(2-methacryloyloxyethyl phosphorylcholine) layer on the surface of poly(ether ether ketone) (PEEK) by photoinduced and self-initiated graft polymerization. Indeed, PEEK has diphenylketone unit in the main chain which is similar to the structure of benzophenone. Therefore, when photoirradiated, activation of diphenylketone units in the PEEK chain is induced and semibenzopinacol radicals are formed. These radicals can initiate polymerization of surrounding monomers at the PEEK interface. In the study, the effects of inorganic salt addition (LiCl, NaCl and KCl) was evaluated in terms of increase in polymerization rate. These findings can be explained considering the ionic hydration of the 2-methacryloyloxyethyl phosphorylcholine monomer which is translated in a monomer concentrating effect.[185] A mussel-inspired photografting on colloidal spheres was reported from

Jia's lab. Monodispersed silica spheres with an average diameter of 220 nm were coated with a thin layer of polydopamine. They demonstrated that surface-initiated polymerization reactions can be carried out on polydopamine (PDA)-coated surfaces via a simple surface modification approach. based on a photopolymerization without adding any photoinitiator or any photosensitizer. In their study, thermally-responsive poly(2-(dimethylamino) ethyl methacrylate) polymer were grown from the polydopamine layer.[186] The same group, in a similar approach, reported the fabrication of self-induced photografting after depositing a thin layer of green tea polyphenols (TP). Indeed, the UV-irradiated generates on the TP surface, surface-bound radicals which can be used for a photoinduced polymerization. When compared with polydopamine-coated surfaces, green tea polyphenol layers were typically colourless instead of dark-black which can be a plus in some applications.[187]

## 3.3 Hard Surface Modification: Metal Nanostructuration

A nanostructured surface can be imagined as a layer of anchored/immobilized metal nanoparticles onto the surface. These type of surfaces own the advantage of bringing nanoscale features of metal nanoparticles to macroscopic or micrometric surfaces. To nanostructure a surface, two components are required: (i) surface-groups that allow the immobilization of the nanoparticles onto the surface support (ii) *in situ* synthetized or already synthetized nanoparticles. Several surface functionalities are adequate, such as thiols and amines, for the nanoparticle immobilization. Similarly, there are many synthetic pathways for the *in situ* generation of nanoparticles (i.e. synthesis in the presence of the support), which in most of the cases rely of chemical reduction of a metal precursor by using a reduction agent (e.g. sodium borohydride, sodium citrate, etc).[188, 189] However, being committed to the aim of this work, we focused on the pathways which make use of light-irradiation to generate reducing agents and, in turn, synthetize metal nanoparticles from their metal ions.

### 3.3.1 Light-induced photoreduction of metal ions

Ketyl radicals have demonstrated to be able to reduce a large variety of metal ions to metal nanoparticles.[190] Indeed, ketyl radical can be viewed as a caged electron, which can be delivered whenever an appropriate electron and proton acceptors is available, such as a metal ion and a hydrogen bond accepting solvent. During the photoreduction, the metal ions $M^{n+}$ are reduced to $M^0$ which progressively assemble in metal cluster and eventually to nanoparticles (Figure 3.7a). Ketyl radicals can be photogenerated by $\alpha$-cleavage of type I photoinitiators. However, not every type of hydroxyalkylphenyl ketone

photoinitiator (i.e. ketyl radical-forming initiator) is valid. The reason behind that is related to the reducing properties of the radicals and not only to its photochemistry. In fact, the excited state (which eventually generates radicals) is frequently a triplet and therefore it can be rapidly quenched by transition metal ion such as those from silver, gold and copper.[191, 192] Generally, the shorter the triplet lifetime, the lower is the percentage of triplets that will be quenched. The radicals survived from the quenching are available to reduce the metal ions. At this point, the lifetime of generated radicals come into place. The higher the radical lifetime, the higher the probability of metal ion reduction. Because of these two aspects, a photoinitiator, to be effectively used as reducing agent, should possess short triplet lifetime and long ketyl radical lifetime. That is why the most commonly used photoinitiator for metal nanoparticle synthesis is the Irgacure-2959 (2-Hydroxy-1-[4-(2-hydroxyethoxy)phenyl]-2-methylpropan-1-one), which is characterized by short triplet lifetime (10 ns) and relatively long ketyl radical lifetime (order of ms). [190, 193] As reported in Figure 3.7b, the photodecomposition of the I-2959 leads to the generation of a benzoyl and a ketyl radical. Interestingly, as it has been clearly showed by Scaiano group, it is beneficial to conduct the photogeneration in air. Indeed, by doing so the benzoyl radicals are oxidized to a substituted benzoic acid (Figure 3.7c), which contributes significantly to nanoparticle stability.[190]

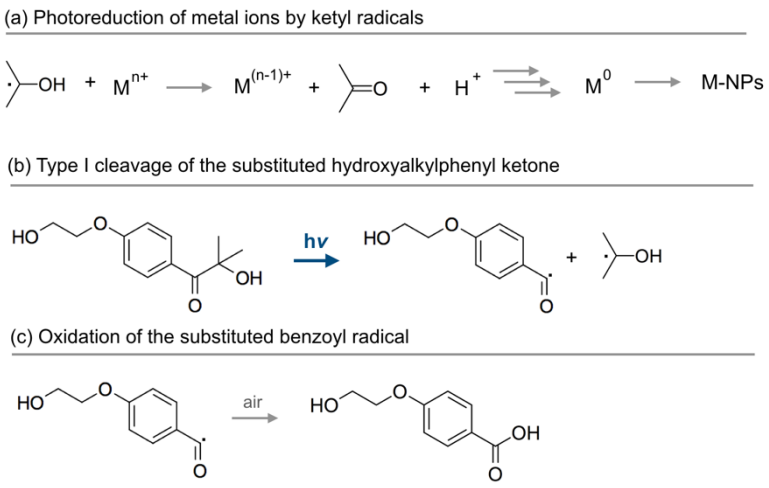


**Figure 3.7**: (a) Reduction of metal ions by ketyl radicals leading to the formation of metal nanoparticles, acetone and protons. (b) Photoscission process via α-cleavage of I-2959 (type I initiator) with formation of a ketyl radical and a benzoyl radical. (c) Air induced oxidation of benzoyl radical to the corresponding substituted benzoic acid.

Ketyl radicals are not the only options, indeed other radicals, such as $\alpha$-aminoalkyl radicals, are even better electron donors. [194, 195] A photochemical source of those radical is the initiator Irgacure-907 (2-Methyl-4'-(methylthio)-2-morpholinopropiophenone). Although the better reducing characteristics of the radical derived from I-907 system, the preference for I-2959 has remained. The

reason for that lies on presence of sulphur and nitrogen in the I-907, which can lead to chemical rubbish that coats the nanoparticle surface. [196] On the other hand, for I-2959, only acetone (which is rapidly removed because of its volatility) and a substituted benzoic acid (useful for the nanoparticle stabilization) are produced.

# 4

# Hybrid microparticles with Janus-like surface and tunable optical properties

## 4.1 Motivation and specific introduction

Surface plasmon resonance of gold nanoparticles (Au NPs) consists of collective oscillations of free electrons (i.e. plasmons) that are generated as effect of an excitation by the external electromagnetic radiation, causing displacements of the conduction electrons (considered as a polarizable electron gas) with respect to their equilibrium position around positively charged ions. Plasmons in NPs with size much smaller than photon wavelength are called localized surface plasmons, because the resulting plasmon oscillation is distributed over the whole particle volume (Figure 4.1a). The localized surface plasmon resonance is translated in a strong adsorption peak in the visible range [201]

Nanostructuring a surface with Au NPs is of considerable significance because it allows to impart the mentioned nanoscale features to micro and macro objects. For instance, nanostructured surfaces (Figure 4.1b) possess highly tunable optical properties with a structure-dependent localized surface plasmon resonance,[202] which makes them relevant for a range of photonic, optoelectronic, and biomedical applications.[203-205] Interestingly, the structure-dependent optical properties of the nanostructured microscopic object depend on both (i) gold nanoparticle size and (ii) their distribution onto the surface. More recently, we observed an increasing interest in the fabrication of particles with a Janus-like surface nanostructuration, meaning with asymmetric nanostructuration (Figure 4.1c). On top of the conventional properties, a partial surface nanostructuration can disclose novel features and behaviours. For instance, Composto's group

provided detailed insights on the influence of the structuration morphologies on

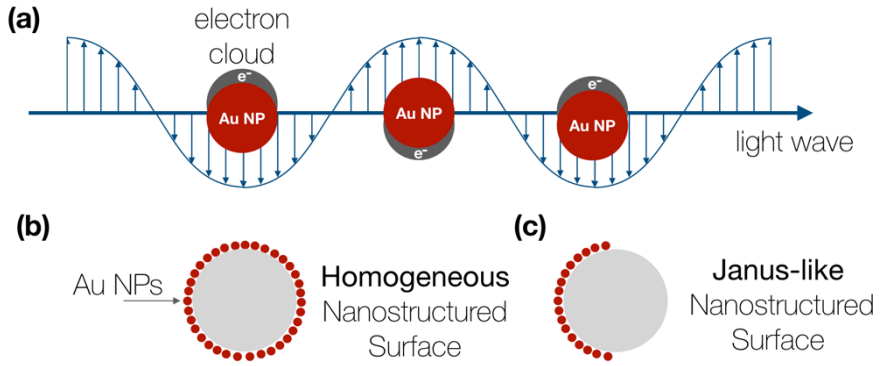


**Figure 4.1**: (a) Graphical illustration of localized surface plasmons in gold nanoparticles excited by light propagating in free space. Schematic representation of a cross section of (sub)-micrometric particle (b) homogeneously and (c) asymmetrically nanostructured with Au NPs.

the optical properties of Janus-like nanostructured sub-micrometric silica particles.[59] Additionally, because of the localized plasmon resonance, Au NPs behave as optical antennas and therefore partial nanostructured particles can be used as probes that enhance molecular spectral information with techniques like surface-enhanced Raman spectroscopy (SERS). Several groups have been reported on the use of Janus-like nanostructured particles as SERS probes.[206-207] Furthermore, a partial nanostructuration, if coupled with fluorescence, can provide information about the rotational dynamics of the particles. These hybrid systems show intensity fluctuation (blinking) because of their rotational Brownian motion. If molecules are anchored onto their surface, because of their restricted rotation dynamics (coming from the molecular interactions), the intensity fluctuations are consequently modulated. Therefore, it is possible to probe interactions at a molecular level by using the Janus-like nanostructuration.[208]

Although the notable scientific and technological interest for Janus-like nanostructured particles, the available fabrication route are yet limited. As it has been reported in the section 2.1.2.1, the existing methods for Au-nanostructuration with Janus-like character rely either on the (i) use of prefabricated nanoparticles, [59-60] or (ii) the more flexible *in situ* generation of nanostructures in the presence of the surface to be coated. [209-212] However, the available *in situ* methods employ chemical reduction of gold precursor to generate Janus-like surface nanostructurations.

In this chapter, we report a novel approach to generate Janus-like gold nanostructuration by using a photochemical *in situ* synthesis. More specifically, starting with a surface activation with organothiols of a support of our choice (500 nm in radius silica particles), we generated *in situ* gold nanostructures by photochemical reduction of gold precursor promoted by acetone ketyl radicals.

Additionally, we showed the possibility of using the same surface-anchored organothiols to generate thiyl radicals and initiate a *photografting-from* process. This allows the fabrication of a hairy polymer domain. The spatial-control over the surface-modification reactions was ensured by an emulsion-assisted particles masking. Part of this work has been already published and it is available at the reference [213].

## 4.2 Materials

Silicon(IV) oxide particles (99.9%, 1.0 micron of diameter, SMPs) were purchased from Alfa Aesar. Deionized pure water was produced by Millipore water system. Poly (ethylene glycol) methyl ether methacrylate (average Mn 950, PEGMA), ethyl alcohol (96%, EtOH), (3-mercapto-propyl) trimethoxysilane (95%, MP-TMESI), hexadecane, Gold(III) chloride trihydrate (ACS reagent, 49.0%) and Hydrogen peroxide solution ($H_2O_2$, 30%) were purchased from Sigma Aldrich. Ammonium hydroxide ($NH_4OH$, 28–30% solution) was purchased from Acros Organics. The radical photoinitiator, 2-hydroxy-4-(2-hydroxyethoxy) -2-methylpropiophenone (Irgacure 2959) was received from BASF. If not specified otherwise, all the chemicals were used as received without further purification.

## 4.3 Experimental procedures

### 4.3.1 Surface activation with organothiols

The surface of SMPs was activated by using a alkoxy silane bearing a short organothiols (MP-TMESI) via hydrolysis and condensation reactions with the silanols of silica surface. In order to remove any organic contaminant and to maximize the availability of surface silanols, the silica microparticles were cleaned with wet chemical treatment (RCA-SC1) as follow: silica microparticles (1 g) were added to 100 ml hydrogen peroxide (30%), 100 ml ammonia hydroxide (28-30%) and 100 ml deionize water. The mixture was first sonicated and then stirred for 1 hour at 70 °C in an open round-bottom flask. The particles were then collected by centrifugation and washed 5 times with ethanol by centrifugation/redispersion cycles. Once the cleaning process was concluded, 1 g of SMPs were added to 400 ml water/ethanol solution (1:3 v/v). The colloidal suspension was sonicated for 5 min and then added to a 500-ml two-neck round-bottom flask. The flask was connected to a reflux apparatus to avoid solvent evaporation. The system was heated to 80 °C under inert conditions. Once the temperature was reached, 5 g of MP-TMESI were poured in the mixture. The silanization was carried out in these conditions under stirring (750 rpm) for 4 h to promote hydrolysis and condensation reactions. Then, the mixture was filtered by vacuum filtration and washed several times with ethanol. The collected particles (SH-SMPs) were dried at 80 °C overnight under reduced pressure.

### 4.3.2 Emulsion-assisted particle immobilization

The activated SH-MPs were partially immobilized by using wax-in-water Pickering emulsion. The emulsion was prepared by adding 100 mg of SH-MPs to 500 mg of melted paraffin wax under magnetic stirring for 10 min. After the complete dispersion of the silica particles in the wax phase, 5 mL of deionized water were added. The system was stirred at 1500 rpm at 85 °C for 1 h. The so-obtained emulsion was cooled down to room temperature and filtered to collect the wax colloidosomes with SH-MPs trapped at their surface.

### 4.3.3 Partial *photografting-from* of PEGMA

The exposed surface of the immobilized SH-MPs in the colloidosome structures were grafted with poly (ethylene glycol) brushes by using UV light. The previously fabricated colloidosomes (100 mg of SH-MPs and 500 mg of paraffin wax) were added in 50 mL of deionized water. A monomer solution (1 g of PEGMA solubilized in10 ml of water) was subsequently added after few minutes of sonication. Subsequently, the colloidosomes/PEGMA system was then transferred in a lab-made photoreactor. It consists of a round-bottom flask covered with aluminium foil, equipped with three necks for nitrogen/argon inlet and outlet and optical fiber connection through the main neck. The optical fiber was connected to a light source (LC8 Lightning cure, Hamamatsu Photonics, Hamamatsu, Japan equipped with a Mercury-Xenon lamp with a spectral range distribution from a wavelength of 185 nm to visible light), and the height between the fiber-end and the level of the liquid was adjusted in order to achieve a light intensity of 70 $mWcm^{-2}$ in the UVA range. The photografting reaction was conducted for 30 min under nitrogen and gentle stirring to favour a homogeneous grafting while avoiding particles detachment from the colloidosomes. The photografing was carried out without the use of any photoinitiator in order to promote the formation of surface-bound thiyl radicals only. This allows to limit homopolymerization phenomenon in the bulk liquid which would derive from the use of a photoinitiator and the consequent release of reactive radicals in liquid (these, besides promoting the generation of thiyl radicals, would initiate the polymerization in the liquid phase). After the UV irradiation, the colloidosomes were filtered and washed several times to remove any traces of unreacted monomer and homopolymerized monomers. Eventually, the wax mask was completely removed by using hexadecane followed by filtration and washing steps with acetone.

### 4.3.4 Surface nanostructuration with gold nanoparticles

Gold nanoparticles (Au NPs) were generated in situ by photoreduction of $HAuCl_4$ by using a Norrish I photoinitiator (I-2959). The available organothiols (previously protected in the wax phase) act as both nucleation site and bridging

groups for the photogenerated Au NPs. In this step, 100 mg of partially grafted Janus microparticles PEG-JMPs, were dispersed in 10 ml of ethanol (96 vol%). Two different concentration of $HAuCl_4$ were used: in a first batch, 10 mg of $HAuCl_4$ (10:1 PEG-JMPs : $HAuCl_4$ mass ratio) and 3 mg of Irgacure 2959 were used. In a second batch 30 mg of HAuCl4 (10:3 PEG-JMPs : $HAuCl_4$ mass ratio) and 9 mg of Irgacure 2959 were used. The mixtures were then transferred in 25-ml balloon covered with aluminum foil and subsequently exposed to UV radiation under stirring (750 rpm). The photoreaction was performed in air by using the abovementioned UV lamp with the same light intensity. After 10 min of irradiation, the colloidal suspension was let stirring in dark for other 20 min. The AuNP/PEG-JMPs were then collected by vacuum filtration and washed several times with ethanol.

## 4.4 Characterization techniques

### 4.4.1 Morphological investigation

Electron microscopy techniques were adopted throughout this work to investigate the morphologies at micro and nanoscale. Because the dimensions of interest of the work included in this chapter were relatively high (from several microns to some nanometric details), the morphologies and assemblies were investigated by using scanning electron microscopy (SEM) This technique provide high resolution topographical images of the specimen surface as an effect of the signals generated from the interactions between a scanning focused electron beam and the specimen. The electron beam is focused and scanned by means of several electron lenses. When the focused primary beam penetrates the specimen surface, it scatters electrons within the specimen at different depths. Some scattered electrons, created by inelastic collisions, escape close to the specimen surface. These are kwon as secondary electrons (SE) and have typically energies between 0.5 and 5.0 eV. Secondary electrons can be detected by a suitable electron detector and converted to photons (generally by means of a scintillator and a photomultiplier) to generate the topographical image of the specimen surface. [214] In this work, we used a MERLIN field-emission scanning electron microscope (FE-SEM) from Carl Zeiss in which a finely focused electron beam is produced from thermionic emission. The microscope was equipped with a GEMINI II column and an in-lens SE detector for the surface imaging. In a typical analysis, a probe current of 120 pA and an accelerating voltage between 3.00 and 5.00 kV were used to analyse the specimens without prior metallization. When evaluating dimensions with SEM, the size distributions were obtained from the micrographs by estimating the equivalent spherical particle diameters. This was calculated from few hundreds particle by using ImageJ image analysis software.

To better investigate the surface nanostructurations, the morphological analyses were coupled with elemental analyses by energy dispersive X-ray spectroscopy (EDS). Indeed, the electron beam can excite electrons from the specimen, and, because of their return to the ground state, X-rays are emitted. The emitted X-rays have energies which depend on the specific electron transition (e.g. from K or L electron shells) and on the specific element. The emitted X-rays energies are translated into peaks in an EDS spectrum and allow the elemental analysis of the investigated area.[215]

### 4.4.2 Chemical analysis

Spectroscopic techniques were used to confirm the activation of the surface with organothiols, the photografting with poly (ethylene glycol) brushes and the tangible photoreduction of gold ions (III) to metallic gold (0). Although infrared spectroscopy (FTIR) is very straightforward, it does not provide information about the oxidation states of elements, because its working principle relies on the absorption characteristics of the sample due to molecular vibrations. [216] Therefore, X-ray photoelectron spectroscopy (XPS) was selected since it gives direct access to the orbitals energetics and thus it is suitable for our characterization requirements. The basic principle of photoelectron spectroscopy technique implicates the ionization of the sample atom or molecule by a monoenergetic photon beam, in which the sample loses an electron (photoelectron). Only the photoelectrons generated near the surface can escape the sample and, in turn, be detected. This means that the technique is surface sensitive. From an experimental point of view, the kinetics energy of the ejected photoelectrons is the parameter to be measured. By knowing the initial photon energy and the resulting kinetic energy of the ejected photoelectron, it is possible to evaluate the binding energy of a specific electron. The result of this process is a XPS spectrum reporting the number of electron detected (counts) for a specific binding energy (i.e. kinetic energy). Each element generates a characteristic peak with a specific binding energy which depends both on the element and the electron configuration of the photoelectron (i.e. 1s, 2s, 3p, 3s, etc.). The photoelectron spectrum can be collected in two different modes: (i) wide-scan or survey and (ii) high-resolution. From the first one, it is possible to identify all the elements present in the sample. On the other hand, the high-resolution spectrum allows the precise evaluation of binding energies. In most of the cases, a high-resolution spectrum, for a given electron configuration of an element, appears as an ensemble of peaks rather than a single peak. The ensemble can be deconvoluted by curve-fitting techniques which allow to identify the different shifts in binding energy. These energy shifts correspond to the chemical states of that element, meaning the bonding environment of the given element. Therefore, the chemical shifts of a given element allow to determine its oxidation state, the

nearest neighbor-atom and the hybridization of the bond between the element and the nearest neighbor-atom.[217]

For our experiments, a PHI 5000 Versaprobe Scanning X-ray photoelectron spectrometer (monochromatic Al K-α X-ray source with 1486.6 eV energy) was employed. A spot size of 100 μm was used to collect the photoelectron signal for both the high resolution (HR) and the survey spectra. Different pass energy values were exploited: 187.85 eV for survey spectra and 23.5 eV for HR peaks. All samples were analyzed with a combined electron and Argon ion gun neutralizer system to reduce the charging effect during the measurements. All core-level peak energies were referred to C1s peak at 284.5 eV, and the background contribution in high-resolution scans was subtracted by means of a Shirley function. Spectra were analyzed using Mutipak 9.6 dedicated software.

### 4.4.3 Optical analysis

The optical properties of the gold nanostructured systems were evaluated by means of ultraviolet-visible spectroscopy. For these measurements, an optical spectrometer records the wavelength at which absorption from the sample occurs. The resulting spectrum is reported in terms of absorbance as function of the wavelength. UV–Vis absorption spectrums of the $HAuCl_4$ - Irgacure 2959 solution (before UV-light exposure) and of the nanostructured Janus AuNP/PEG-MPs were recorded by using double-beam UNICAM UV2 (ATI Unicam, Cambridge, UK) spectrophotometer in a spectral range of 400–900 nm.

## 4.5 Results and discussion

An activated surface with organothiols can be exploited for different photochemical surface modification reactions. These different modification strategies can be performed toposelectively on a single particle by physically limiting the available thiolated surface for each modification step. The physical protection of the particle surface was achieved by using an emulsion-assisted masking. Indeed, as it was reported in the section 2.1.2.1, solid particles can stabilize oil-in-water emulsion by locating themselves at the interface between the two fluids in a so-called Pickering emulsion. We prepared Pickering emulsions stabilized by the particles (activated with organothiols) and using melted wax as the oil phase. Once the emulsion was prepared, it was cooled down to room temperature. This resulted in the solidification of the wax and therefore in the physical immobilization of the particles in a colloidosome structure (Figure 4.2a). In this condition, the surface of the physically-locked particles present an unprotected domain. Therefore, the organothiols of this unprotected surface area can be used for a first surface modification step in a toposelective fashion. If the colloidosomes are exposed to UV-light, thiyl radicals are generated from the

exposed thiols (Figure 4.2, step I). Indeed, homolytic cleavage of the S-H bonds can be induced by light irradiation. More specifically, thiols absorb at very low wavelength with a maximum of absorbance around 200 nm (note that irradiation above 300 nm is rather inefficient to generate a substantial amount of thiyl radicals).[218] Anyhow, by using a suitable source of light-irradiation, it is possible to generate thiyl radical on the exposed surface of the particles. These radicals can add to a suitable monomer (in our case a monofunctional methacrylic monomer with a poly (ethylene glycol) side chain) and initiate a free radical chain-growth polymerization initiated from the surface (i.e. *photografting-from* approach).

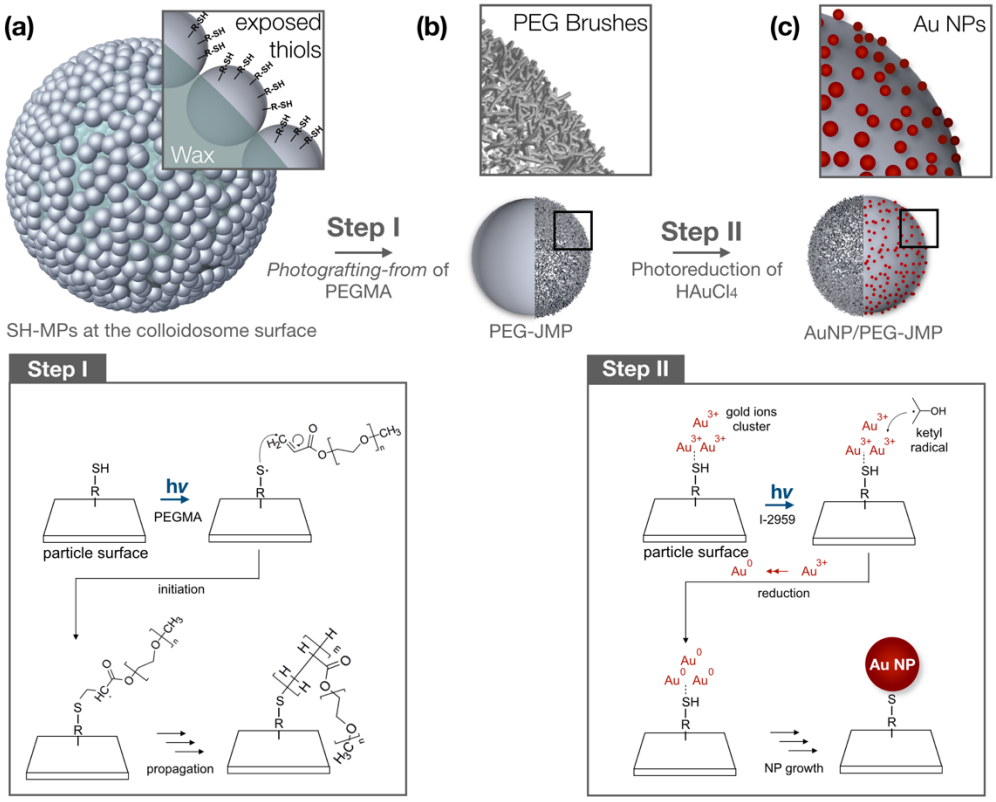


**Figure 4.2**: (a) Graphical illustration of a colloidosome structure with thiolated particles immobilized and partially masked by the solidified wax. (b) Partially grafted particle with PEG brushes resulting from the *photografting-from* process. (c) Final particle consisting of two distinct domains: one with polymer brushes and the other nanostructured with photogenerated Au NPs. (Step I) Scheme of the *photografting-from* process from the surface-bound thiyl radical generated upon UV exposure. (Step II) Scheme of the gold nanostructuration through gold ions photoreduction process by ketyl radicals. Note that, for the sake of simplicity, in the step II the photogeneration of thiyl radicals was omitted.

Consequently, polymer brushes are photogenerated on the exposed particle surface. After the first modification step, the physical-immobilization can be easily removed by solubilizing the wax. At this point, the partially grafted particles (PEG-JMPs in Figure 4.2b) possess a surface-domain with unreacted thiols. In a second modification step (Figure 4.2, step II), the available organothiols are

exploited for the nanostructuration with gold nanoparticles. As illustrated schematically in the step II of Figure 4.2, gold ions $Au^{3+}$ coming from chloroauric acid ($HAuCl_4$, as gold precursor), coordinate the organothiols. Under this conditions, consequently to the photocleavage of the type I photoinitiator I-2959, acetone ketyl radicals are generated. These radicals reduce the gold ions to metallic gold, leading to the formation of gold clusters, which will grow into gold nanoparticles upon further ion photoreduction (step II in Figure 4.2). This second surface modification step allow the fabrication of the final particles with PEG polymer brushes and Au NPs in a Janus-like surface distribution (AuNP/PEG-JMPs).

## 4.5.1 Effective surface activation with organothiols

The feasibility of the whole photochemical approach to the synthesis of Janus-like nanostructured/grafted surfaces was investigated step by step. Starting from the activation of the silica surface with organothiols, the presence of thiols was evaluated by XPS analysis. In Figure 4.3a, the survey spectrum of the particles modified with organothiols (SH-MPs) is reported. The survey shows all the elements present and their chemical states, whereas the atomic percentages are reported in Table 1.

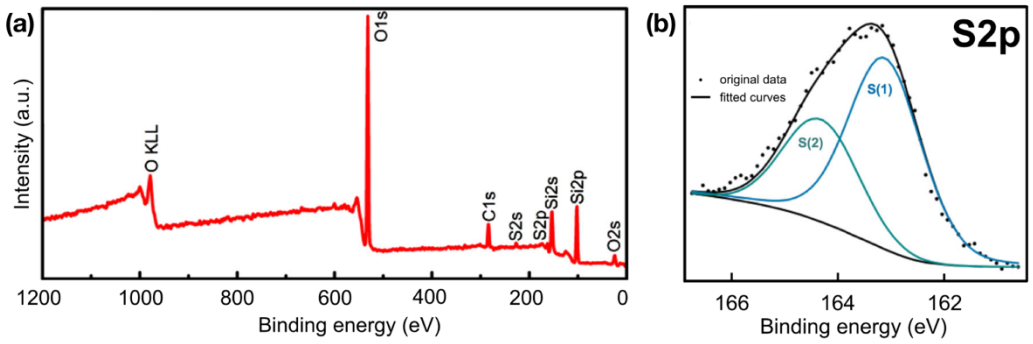


**Figure 4.3**: Survey (a) and S2p high-resolution XPS spectra (b) of organothiol-modified silica particles (SH-MPs). The high-resolution spectrum reports original (filled circle) and fitted (–) data along with peaks deconvolutions S(1) and S(2).

As expected, silicon and oxygen were detected from the thiolated silicon dioxide particles. The main evidence of the actual organothiols surface activation is shown by the Sulphur (S2p) with 1.6% as relative atomic percentage. A better understanding was attained from the high-resolution S2p peak (Figure 4.3b). The S2p spectrum can be fitted with two differed peaks S(1) and S(2). The main peak S(1) is located at 163.11 eV, followed by a second peak S(2) shifted toward higher energies by 1.18 eV. These can be attributed to thiol groups $S2p_{1/2}$ and $S2p_{3/2}$ involved in –C–SH bond as it has been reported in previous works.[219-220]

The carbon reported in the survey spectrum (Figure 4.3a) most likely comes from the propyl groups of the MP-TMESI molecules. Little amount of carbon, coming from not fully hydrolysed MP-TMESI, could also reasonably affect the total C1s atomic percentage. As a matter of fact, the mentioned XPS results clearly corroborate the surface activation of the silica particles with organothiols.

**Table 1**: Atomic concentration (%) from the X-Ray photoelectron spectroscopy survey spectra for thiol-modified silica microparticles (SH-MPs) and Janus silica microparticles with polyethylene(glycol) brushes and Au nanoparticles (AuNP/PEG-JMPs)

| | Atomic percentage for each spectrum peak, % | | | | |
|---|---|---|---|---|---|
| **Particle system** | **O 1s** | **Si 2p** | **C 1s** | **S 2p** | **Au 4f** |
| SH-MPs | 58.7 | 28.7 | 13.9 | 1.6 | - |
| AuNP/PEG-JMPs | 43.4 | 18.5 | 35.0 | - | 3.1 |

## 4.5.2 Toposelective grafting and nanostructuration through emulsion-assistance

The silica particle activated with organothiols showed to be very effective in the preparation of Pickering emulsions. Indeed, although native silica particles are not very effective in stabilizing emulsion, [221-222] organothiol-modified silica particles work much better because of the decreased surface hydrophilicity. As it was reported in the Equation 1 of section 2.1.2.1, the energy needed for the desorption of a particle at a water/oil interface is related to the surface hydrophilicity/hydrophobicity. More specifically, the desorption energy is maximum (i.e. the emulsion stability is maximized), when $|\gamma(PO) - \gamma(PW)|$ is close to zero. Considering that, the surface modification with organothiol leads to a reduction of $\gamma$ (PO) and an increase of $\gamma$ (PW),[223] it leads, consequently, to an increase of the emulsion stability. Once the Pickering emulsion is formed it can be cooled down to room temperature allowing the wax to solidify. The so generated colloidosomes were investigated by FE-SEM. Representative images of colloidosomes are reported in Figure 4.4a-c. The diameter of the collected colloidosomes was between 15 and 200 μm. The micrographs clearly show a partial masking of the SH-MPs physically immobilized in the solidified wax.

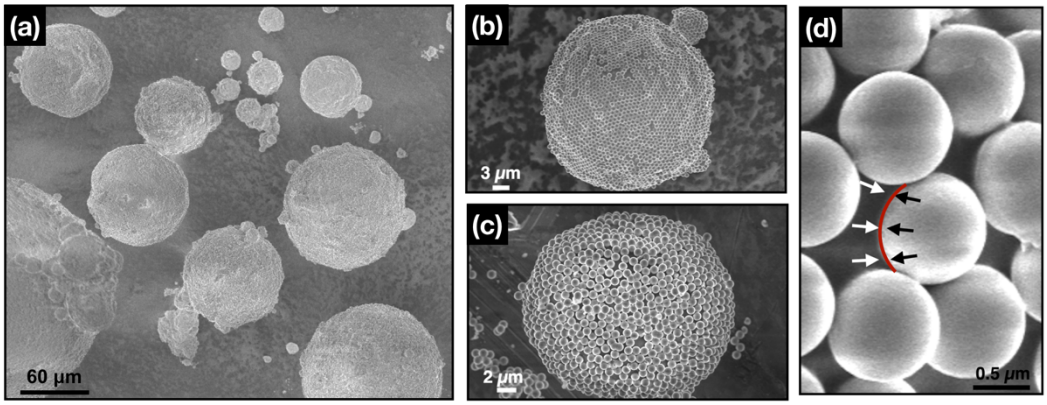


**Figure 4.4**: Representative FE-SEM micrographs of the emulsion-assisted masking. (a) Overall view of the collected wax droplets stabilized by thiolated particles after wax solidification (colloidosomes) (b)-(c) Magnification of colloidosome of different size. (d) Magnification of the colloidosome surface highlighting the masking balance. The black arrows are pointing toward the protected side.

Interestingly, the magnification of the colloidosome surface (Figure 4.4d) showed a symmetric masking balance between the protected and the exposed sides of the particles. Indeed, this is an effect of the maximization of the Pickering emulsion stability because of the particle hydrophobization from organothiols. The symmetric masking balance will be translated in a symmetric modification balance (also known as Janus balance) between the grafted and nanostructured domains. As mentioned in the previous section, the first surface modification to be performed was the *photografting-from* of PEGMA with the SH-MPs physically immobilized in the colloidosome structures. Furthermore, because of the non-thermally activated nature of the *photografting-from* process, issues related to the partial or total melting of the wax-colloidosomes during the surface modification are avoided. Indeed, despite the exothermic nature of the polymerization, no notable changes in temperature were observed since the particles were dispersed in a relatively large volume of water. After the masking removal, the grafting step was followed by the *in situ* photoreduction of gold nanoparticles, which led to the formation of the final product AuNP/PEG-JMPs. With the aim of proving that organothiols act as both bridging-group (via Au-S bond) and nucleation sites, the nanostructuration with Au NPs was performed by using two different mass ration between the gold precursor and the partially grafted particles $HAuCl_4$ : PEG-JMPs. Two different ratios were used, 10:1 and 10:3 while keeping the ratio $HAuCl_4$ : I-2959 always equimolar. By doing so, the source of reducing ketyl radials was kept constant. The only parameter to be changed was the number of organothiols available (related to the quantity of PEG-JMPs ) for a given quantity of gold precursor. Both photochemical surface modification steps were investigated in detail by X-ray photoelectron spectroscopy.

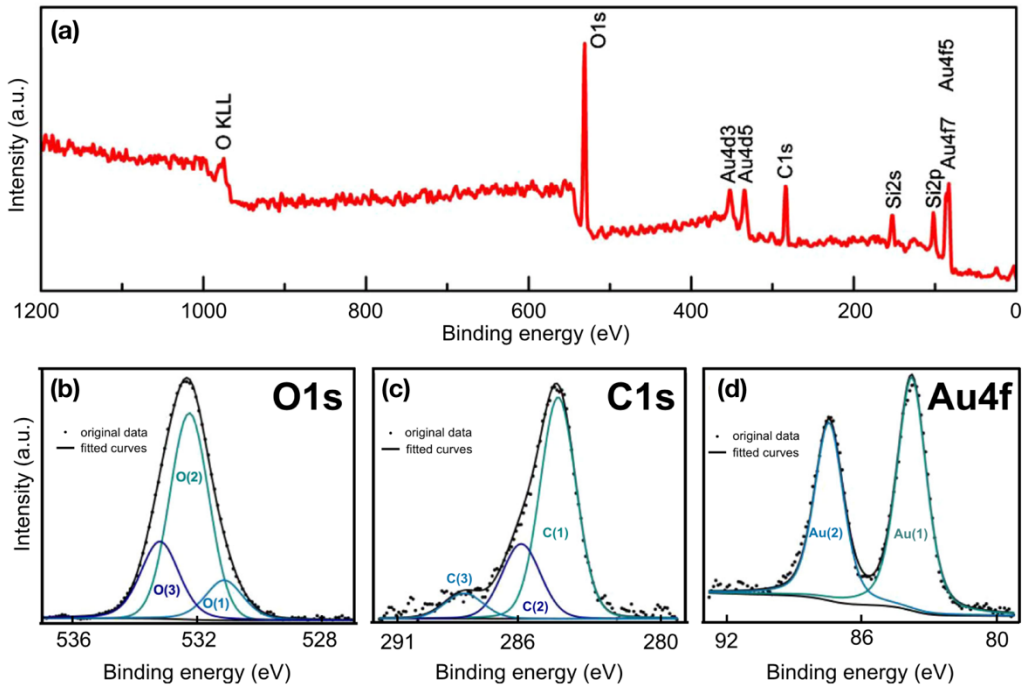


**Figure 4.5**: Survey (a) and O1s (b), C1s (c) and Au4f (d) high-resolution XPS spectra of PEG grafted and Au nanostructured Janus microparticles (AuNP/PEG-JMPs synthetized with a PEG-JMPs : $HAuCl_4$ ratio of 10:1). The high-resolution spectra report original (filled circle) and fitted (–) data along with peaks deconvolutions.

In Figure 4.5a, the survey spectrum for photogenerated AuNP/PEG-JMPs is reported. The survey spectrum clearly shows peaks for oxygen (O 1s) and carbon (C 1s). It is important to note that oxygen and carbon were detected also for the thiol- modified silica, but in this regard, two observations need to be pointed out. From Table 1, the atomic ratio of silicon to oxygen is 1:2.34, which is much higher in oxygen than the atomic ratio in plain silica (1:2) and in thiol-modified silica (1:2.04). This indicates that oxygen content in PEGylated JPs is higher. Additionally, the same logic can be applied for the carbon (C1s) atomic percent. In fact, the carbon percentage PEGylated JPs is higher than the carbon percent in thiol-modified silica. Therefore, both oxygen and carbon concentrations in Figure 4.5a evidently indicate the presence of poly (ethylene glycol). The presence of such brushes is better elucidated by the high-resolution spectrum for oxygen and carbon (Figure 4.5b and 4.5c, respectively). The XPS O1s high-resolution spectrum can be fitted with three peaks O(1), O(2), O(3). The main peak O(1), located at 531.17 eV, can be attributed to carbonyl C=O groups. The O(3) peak, which is shifted of 2.06 eV from the O(1), can be assigned to C–O–(C,H). Both O(1) and O(3) are well-known features of PEG-brushes. The central O(2) peak, located at 532.29 eV, comes from the oxygen of the silica core of the JPs. A further proof of the PEGylation can be found looking at the high-resolution spectrum for the carbon. The XPS C1s high-resolution spectra (Figure 4.5c) can be fitted with three peaks C(1), C(2), C(3). The main peak C(1), placed at 284.34

eV, can be recognized as carbon involved in C–C bond. It comes from both ethyl groups of the PEG backbone and propyl group of MP-TMESI (less relevant because of the escape depth of photoelectron). Most importantly, the C(2) and C(3) - shifted by 1.54 and 3.92 eV, respectively - revealed carbon involved in C–O–(C,H) and C=O. Therefore, the XPS C1s high-resolution spectrum undoubtedly shows the presence of PEG brushes. [223] The photoreduction of gold ions in Au NPs was validated by XPS analysis. The XPS survey spectrum (Figure 4.5a) reports several peaks which can be attributed to gold. More in detail (Table 1), from the survey spectrum, it was possible to identify 3.1% of gold (Au4f). Furthermore, the high-resolution spectrum of gold core levels (Figure 4.5d) showed a main peak, Au(1), located at 83.80 eV and a second peak Au(2) shifted by 3.67 eV from the main peak. These two peaks can be attributed to $Au4f_{7/2}$ (Au(1)) and $Au4f_{5/2}$ (Au(2)). This doublet clearly indicates that the oxidation state of Au is zero in the AuNP/PEG-JMPs , i.e., metallic gold. [225]

The morphology of the AuNP/PEG-JMPs was investigated by FE-SEM as reported in Figure 4.6. The micrographs showed a high yield of JPs production by UV light and a remarkable neat division between the two domains (PEG/AuNPs) of the Janus particles. Different particles size distributions of Au NPs were obtained by using 10:1(Figure 4.6a-b) and 10:3 (Figure 4.6c-d) mass ratio of partially PEGylated particles and gold precursor (PEG-JMPs : $HAuCl_4$). The coverage density was similar in both cases, probably because it is related to the thiol-groups density on the surface (which is the same in both cases). On the other hand, when 10:1 mass ratio was used, gold nanoparticles with an average diameter of 12.7 nm and a standard deviation (SD) of 3.7 nm were obtained. When 10:3 was used as mass ratio, bigger particles were synthetized and specifically with an average diameter of 22.5 nm with a SD of 9.8 nm. These results indicate that Au NPs with a bigger size in average are obtained by using higher amount of gold precursor for a given quantity of thiol-modified particles. On the other hand, a higher amount of gold precursor leads to a more broaden particle population. The Au NP size distribution for 10:1 and for 10:3 can be fitted with log-normal distributions as reported in Figure 4.6b and 4.6d, respectively. It is important to note the reducing agent concentration (i.e., ketyl radicals from Irgacure 2959 in this case) has a strong effect on the particle size distribution. [226] However, in this case the reducing agent was kept constant with respect of the gold precursor. Therefore, the only parameter playing a role on the nanoparticle size is the concentration of thiols. When going from 10:1 to 10:3 PEG-JMPs : $HAuCl_4$, the availability of nucleation sites (i.e. organothiols), for a given amount of gold ions, is reduced. The higher amount of nucleation sites for the ratio 10:1 explains the smaller particles size obtained in this case.

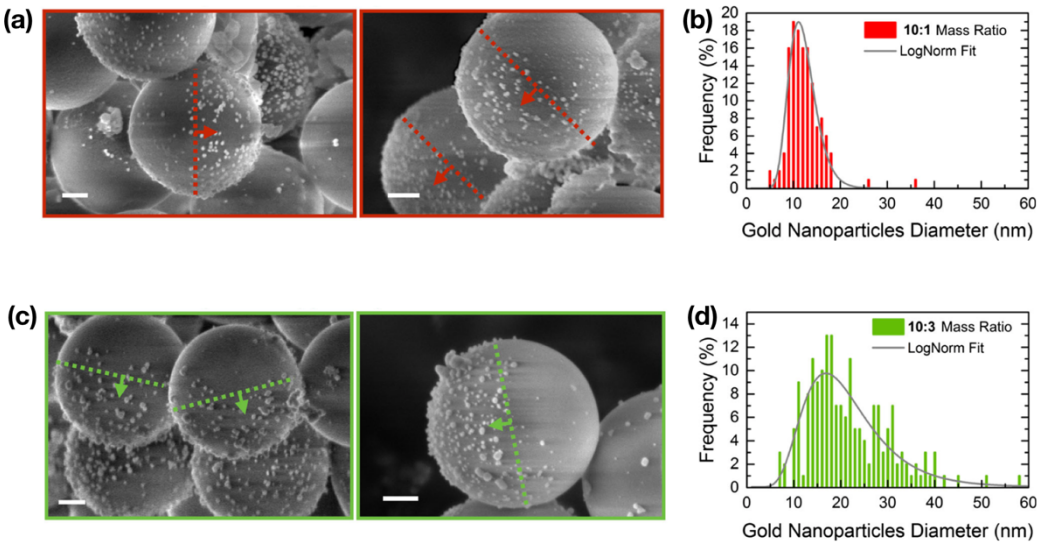


**Figure 4.6**: Representative FE-SEM micrographs of AuNP/PEG-JMPs fabricated by photochemical route. The dashed lines show the division between the two domains of each particles. The arrows are pointing toward the gold nanostructured sides of the Janus particles. Systems synthetized by using a PEG-JMPs : $HAuCl_4$ mass ratio of either 10:1 (a) or 10:1 (c) along with their respective size distributions (b) and (d). All the scale bars are 200 nm

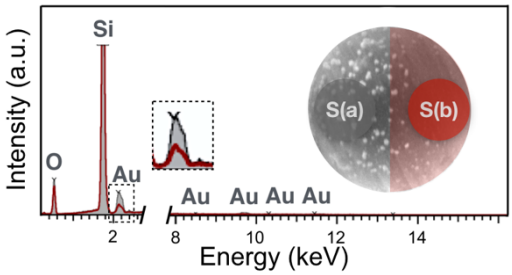


| Atomic percentage, % | | | |
|---|---|---|---|
| | Silicon | Oxygen | Gold |
| S(a) | 50.98 | 45.60 | 3.42 |
| S(b) | 57.98 | 40.50 | 1.52 |

**Figure 4.7**: Energy-dispersive X-ray spectroscopy for particle surface area centred in the Au nanostructured domain (spectrum S(a)) and in the polymer-grafted domain (spectrum S(b)) for AuNP/PEG-JMPs synthesized by using a PEG-JMPs : $HAuCl_4$ mass ratio of 10:1. On the left panel the atomic percentages for silicon, oxygen and gold are reported.

The actual anisotropy of the Janus-like surface modification for AuNP/PEG-JMPs was proved by evaluating the elemental concentration of gold by EDS in two different particle regions (Figure 4.7). The results show an atomic percentage of gold of 3.43% for a spectrum (a) cantered in the AuNPs decorated side (against 45.60 at.% of O and 50.97 at.% of Si). The spectrum (b) on the other side (grafted with polymer chains) showed an atomic percentage of 1.52% (against 40.50 at.% of O and 57.98 at.% of Si) which clearly indicates a lower concentration than the other side. It is important to note that, these percentage values can be interpreted on qualitatively as a yardstick to compare the two particle domains. Although the beam probe is smaller than a single particles domain, because of the beam broadening inside the material, the emission of characteristic X-ray comes from a much larger volume. This inevitably affects the

resolution of the technique, preventing in most of the cases quantitative analysis with EDS in SEM.

As briefly described in the introduction, the nanostructuration with Au NPs introduce localized surface plasmons. Consequently, the nanostructured systems begin absorbing in the visible range. The changes in optical properties subsequently to the nanostructurations were evaluated by ultraviolet–visible spectroscopy from 400 to 900 nm (Figure 4.8). As expected, the gold ions solution before UV irradiation did not show any notable absorption in the visible wavelength range. Dissimilarly, the colloids of AuNP/PEG-JMPs showed a remarkable absorption with a maximum around 550 and 565 nm for the 10:1 and 10:3 systems, respectively. Interestingly, the bathochromic shift, observed from 10:1 to 10:3, is in good agreement with the increase in Au nanoparticle size between the two systems.

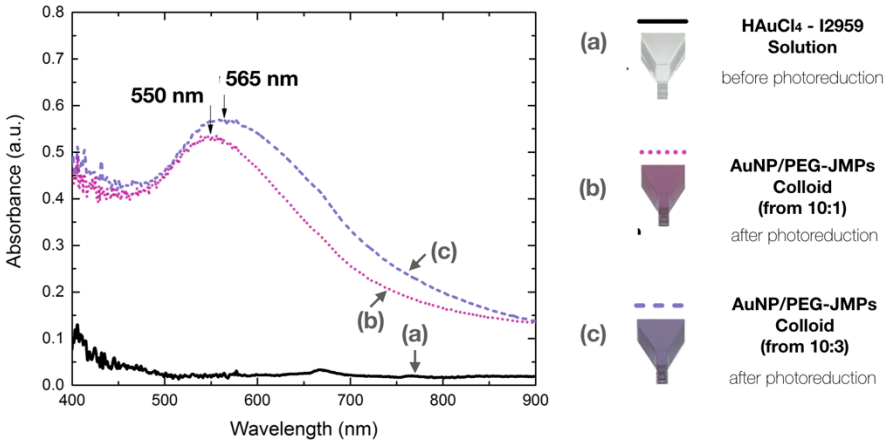


**Figure 4.8**: Absorbance from UV-Visible spectroscopy of (a) gold precursor photoinitiator solution before irradiation (i.e. gold ions $Au^{3+}$) and of colloid of Janus AuNP/PEG-JMPs after gold ions photoreduction by using either a PEG-JMPs : $HAuCl_4$ mass ratio of 10:1 (b) or 10:3 (c). On the left panel, the optical appearances of the solutions/colloids are reported.

Because the gold nanoparticles did not closely pack on the silica surface, the absorption peaks (for a specific Au NPs size) do not show any remarkable red shift in comparison to the free NPs (phenomenon which would result from plasmon coupling of adjacent NPs). Therefore, the optical behaviour of the of AuNP/PEG-JMPs in terms of wavelength of absorption peaks was comparable with that of free Au nanoparticles in solution. [227]

## 4.6 Conclusion

In this chapter, we demonstrated that the surface-modification of micrometric particles (1 µm) with organothiols allows, upon UV exposure: (i) the

*photografting-from* of polymer brushes via photogeneration of surface-bound thiyl radicals which initiate a polymerization from the surface and (ii) the surface nanostructuration with Au NPs via photoreduction of gold ions promoted by photogenerated ketyl radical. The possibility to partially protect the surface of silica particles was shown by physically immobilizing them in solidified wax/water Pickering emulsions. The physical immobilization allowed to perform the *photografting-from* and gold nanostructuration in a toposelective way, which resulted in Janus-like surface with distinct domains within a single particle.

This synthetic protocol led to the production of AuNP/PEG-JMPs with one surface-domain consisting of PEG brushes and another one consisting of surface anchored Au NPs. It was observed that the size of gold nanoparticles could be tuned by playing on the ratio between gold ions and thiol-modified microparticles (note that thiols act as preferential sites for the nucleation of Au NPs). It was observed that by going from 10:1 to 10:3, of PEG-JMPs : $HAuCl_4$ mass ratio, the average diameter of nanostructuring Au NPs went from 12.7 ± 3.7 nm to 22.5 ± 9.8 nm. The nanostructuration with Au NPs introduced light absorption in the visible range (between 550-565 nm) as a consequence of the localized plasmon resonance from the nanometric gold structure. The absorption peaks highlighted an optical behaviour typical of free Au NPs, excluding effect from plasmon coupling of adjacent nanoparticles.

This work was the first example of photochemical synthesis of hybrid Janus particles. Surface-anchored thiols and UV-light have demonstrated to be a winning combination, since both organic and inorganic surface-modification reaction have been successfully performed with fast reaction times (dozens of minutes). Although, PEGMA was used for the photogeneration of polymer brushed, ideally, any monomer able to polymerize via a radical mechanism can be used (e.g. other acrylic and methacrylic monomers [29,164]). Finally, it is noteworthy that the herein proposed method belongs to the surface modification strategy. Thus, the use of 1 μm silica particles is a mere practical choice, since the method is applicable to any particle size able to stabilize a Pickering emulsion (any sub-micrometric/micrometric size [62,63]).

# 5

# Soft hairy nanoparticles with Janus-like surface heterogeneity for controlled self-assembly behaviour

## 5.1 Motivation and specific introduction

Hairy particles are the bridge between colloids and macromolecules, where physical chemistry meets the polymer chemistry paving the way for materials with unprecedented properties. [26,228] These polymer-grafted particles are covered with surface-anchored polymer chains forming a hairy corona. In the section 3.2, the fabrication of hairy polymeric surfaces was presented placing emphasis on the two fabrication approaches: (i) *grafting-to* and (ii) *grafting-from*. Because in the *grafting-from* strategy the polymer chains are grown from the surface, it is possible to achieve greater grafting densities and thicknesses. When *grafting-from* strategies are applied to highly curved surfaces such as those of nanoparticles with sizes below 100 nm, fascinatingly, unusual features arise. Indeed, at this scale, the thickness of the hairy surface (in a good solvent) becomes comparable with the particle size. Consequently, the hairy nanoparticles can behave as soft nano-objects. In this context, the term "soft" concerns the possibility of deformations and rearrangements introduced by the polymer chains. Soft nanomaterials are very exciting in the biomedical field, [229] since most of the biological materials form nature (e.g. blood cells, neurons, tissues, etc.) are soft as well. [230] Additionally, soft nanoparticles introduce complexity in the behaviour at the interfaces [200, 231] and even create a new generation of nano-composites. [232]

Fascinatedly, if the ability to rearrange and deform their structure (i.e. softness) is combined with asymmetric properties, soft nanoparticles with amphiphilic character and self-assembly capabilities are obtained. In the subsection 2.1.2.4, an overview of the available fabrication strategies for the synthesis of particles with Janus-like hairy coronas was reported. However, despite the recent development in more reliable immobilization strategies and grafting techniques, to date, only few examples of Janus hairy nanoparticles with core sizes below 100 nm have been published. [110-113, 197, 198] Moreover, all the reported approaches make use of heat and/or toxic metal catalyst for their synthesis. If milder conditions could be applied in the *grafting-from* strategies, such as in photochemical reactions, materials not contaminated by metal catalysts would be obtained and polymerization reactions at room temperature would allow to achieve a better control over the fabrication process. In turn, polymer-grafted Janus nanoparticles could be potentially used in restricting environments where heat-sensitive substrates or active-ingredients are employed.

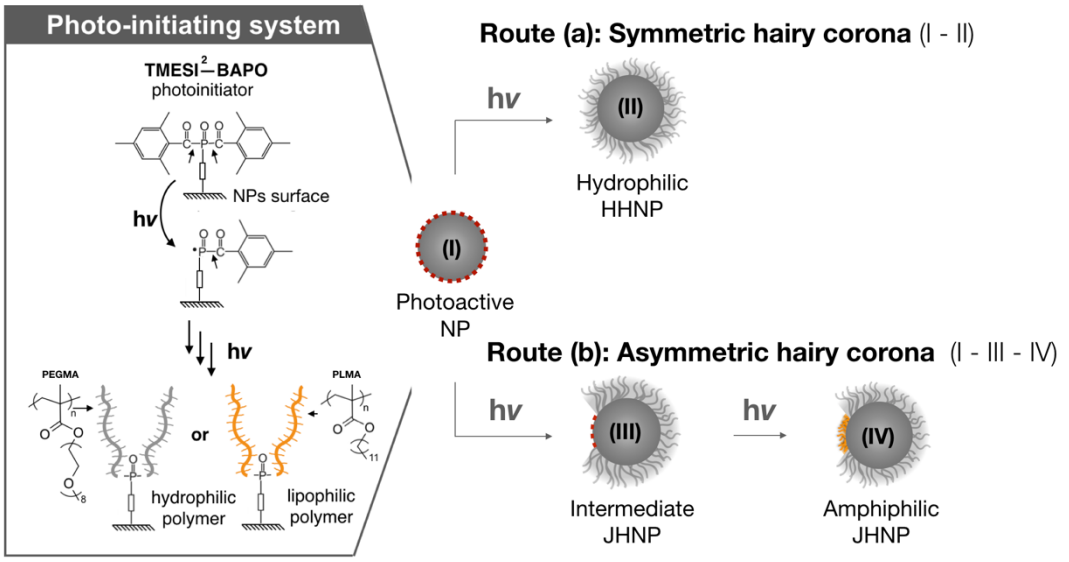


**Figure 5.1**: Schematic representation of the light-triggered synthesis hairy polymer coronas on the surface of silica nanoparticles activated with TMESI²-BAPO (**I**). (Left panel) Photoinitiating system, for the *photografting-from* process, used to generate lipophilic (orange) or hydrophilic (grey) polymer brushes. (Right panel) From nanoparticles functionalized with TMESI²-BAPO (**I**) following the route (a) generation of symmetric hairy coronas (**II**) and following the route (b) of asymmetric corona with amphiphilic character (**IV**) through the fabrication of a hydrophilic intermediate (**III**).

In this chapter, we proposed a novel light-triggered strategy to produce amphiphilic nanoparticles with hairy Janus-like polymer coronas (Figure 5.1). To do so, we activated the surface of small silica nanoparticles (~50 nm in diameter) by surface-anchoring a recently synthetized siloxy-substituted bis (acyl)phosphane oxide photoinitiating system (TMESI²-BAPO).[160] The surface activation with

TMESI²-BAPO allows the photogeneration of a symmetric (homogeneous) hairy corona via a single step *photografting-from* process. Additionally, by exploiting the spatial control of light-induced polymerization, the same photoinitiating system allows synthesis of asymmetric (Janus-like) hairy coronas. This is made possible by the combination a reversible electrostatically mediated immobilization strategy with two photografting steps. Interestingly, this is the first example of fabrication of such systems by employing solely a *grafting-from* strategy.
The mentioned method has been employed to synthetize homogeneous hairy nanoparticles (HHNPs) with hydrophilic character (**II** in Figure 5.1) and Janus hairy nanoparticles (JHNPs) with amphiphilic character (**IV** in Figure 5.1) via the formation of a hydrophilic Janus intermediate (**III** in Figure 5.1). More specifically, the product **II** consist of a homogeneous hairy surface of poly(ethylene glycol) methyl ether methacrylate (PEGMA, in grey in Figure 5.1), whereas the product **IV** consist of a Janus-like hairy corona with a hydrophilic domain of PEGMA and a lipophilic compartment of poly (lauryl methacrylate) (PLMA, in orange in Figure 5.1).

In a comparative investigation, the effect arising from the Janus character have been disclosed in term of self-assembly in water. We provided experimental evidences of the assembly behaviour in near-realistic conditions by using both consolidated techniques (such as small angle X-ray scattering and cryogenic transmission electron microscopy) and emerging ones (such as liquid phase transmission electron microscopy). Part of this work has been already published and it is available at the reference [233].

## 5.2 Materials

Uranyl acetate (2 wt% in deionized water), Ammonium hydroxide ($NH_4OH$, Acros Organics, 30–32% solution, unless stated otherwise), Ethanol absolute (EtOH, VWR, 99.9%). 3-amino- propyltriethoxysilane (TESI-AP, 99%), Tetraethylorthosilicate (TEOS, 99%), Toluene (99.8%), Acetonitrile (99.5%), Dichloromethane ($CH_2Cl_2$, 99.8%), Acetone (ACS reagent), Hydrochloric acid (HCl, ACS reagent 37%), Potassium hydroxide (KOH, pellets), Poly (ethylene glycol) methyl ether methacrylate (PEGMA, Mn 500), Lauryl methacrylate (LMA) were purchased from Sigma Aldrich. Silicon dioxide microparticles (1.0 micron, 99.9%) were purchased from Alfa Aesar. Deionized water was obtained from Milli-Q purification system (Millipore). 3-(trimethoxysilyl) propyl 3-[bis(2,4,6-trimethyl- benzoyl) phosphinyl]-2-methyl-propionate (TMESI²-BAPO) was synthetized via a stable bis(mesitoyl)phosphane intermediate as reported elsewhere.[160]

## 5.3 Experimental procedures

### 5.3.1 Synthesis of TMESI²-BAPO

The synthesis of the 3-(trimethoxysilyl) propyl 3-[bis(2,4,6-trimethyl-benzoyl) phosphinyl]-2-methyl-propionate (TMESI²-BAPO) was made possible thanks to an crucial collaboration with Gruetzmacher's group (ETH, Switzerland). Even though the synthesis was not performed as part of this work, for the sake of clarity a brief description of the synthetic protocol is reported herein. In general, the synthesis of bis(acyl) phosphane oxide derivatives is conceivable via Phospha-Michael addition from a stable bis(mesitoyl) phosphanes. Indeed, as reported in Figure 5.2, 3-(trimethoxysilyl) propyl methacrylate (2) is added to a starting solution of bis(mesitoyl) phosphane (1) and 1,1,3,3-tetramethylguanidine (TMG) in dimethoxyethane (DME). At this stage, a Phospha-Michael addition occurs between the bis(mesitoyl) phosphanes and the methyl acrylate (from 2), catalysed by amines (TMG). After stirring the solution for 18 hours at 60 °C, the solvent is removed under reduced pressure leading to the formation of (3) as a yellow oily product. Then, the product 3 is dissolved in toluene and *tert*-butyl hydroperoxide is added dropwise at 0 °C. After 4 hours of stirring, the solvent is removed under reduced pressure leading to the formation of the final product (4) called TMESI²-BAPO.

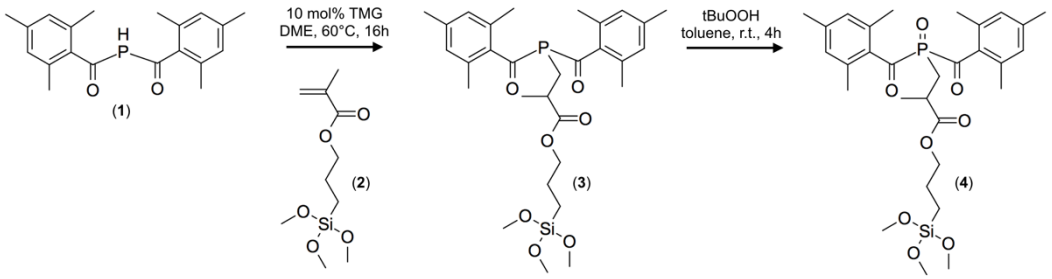


**Figure 5.2**: Scheme of the synthesis of TMESI²-BAPO from a stable bis(mesitoyl) phosphane. Where (**1**) is bis(mesitoyl) phosphane, (**2**) 3-(trimethoxysilyl) propyl methacrylate, (**3**) reaction intermediate, (**4**) 3-(trimethoxysilyl) propyl 3-[bis(2,4,6-trimethyl- benzoyl) phosphinyl]-2-methyl-propionate (TMESI²-BAPO).

### 5.3.2 Synthesis of silica nanoparticle cores

Monodisperse 50nm-sized silica nanoparticles were synthetized using a one-pot hydrolysis-condensation procedure of TEOS in ethanol with ammonia hydroxide as catalyst based on a modified Stöber approach. [234] In a typical procedure 145 ml of absolute ethanol and 10 ml of ammonia solution are added in 250 ml round-bottom flask. The flask is sealed with a silicone septum and heated to 60 °C. When the temperature is stable 5 ml of TEOS are added and the

solution is kept at to 60 °C under continuous stirring at 700 rpm overnight. After hydrolysis-condensation, the obtained nanoparticles are washed 5 times with absolute ethanol by centrifugation/redispersion cycles. For each step, the particles were collected after 30 minutes of centrifugation at a relative centrifugal force of 15400 g. At each vial, containing about 60 mg of nanoparticles, 30 ml of washing solvent were added to redisperse the particles. Finally, the purified particles can be dried in a vacuum oven under reduced pressure at 60 °C.

### 5.3.3 Functionalization of silica nanoparticle with TMESI²-BAPO: photoactive nanoparticles (I)

Purified and dried 50nm-sized silica nanoparticles were dispersed in 125 ml of toluene by sonication (final concentration 17.5 g/l). Then, 0.2 ml of TMESI²-BAPO were added to the reaction mixture. The colloidal suspension was transferred in a round-bottom flask and sealed. After 48 hours of stirring at room temperature, the particles were collected by centrifugation and washed four times in toluene, two times in acetone by centrifugation/redispersion cycles. For each step, the particles were collected after 30 minutes of centrifugation at a relative centrifugal force of 15400 g. At each vial, containing about 60 mg of nanoparticles, 30 ml of washing solvent were added to redisperse the particles. After purification, the particles were dried under reduced pressure. Finally, the functionalized photoactive nanoparticles were dispersed and stored in acetonitrile with a concentration of 15 g/l. Please note that all the steps were conducted in a UV-protected environment. The functionalization of the nanoparticles with TMESI²-BAPO was evaluated via UV-Visible spectroscopy. The spectrometer used and the conditions adopted were the same as reported in the section 4.4.3.

### 5.3.4 Functionalization of silica microscaffolds with TESI-AP: $NH_2$-SMSs

Commercially available silica microparticles (1μm in diameter) were cleaned with wet chemical treatment (RCA-SC1) to remove contaminants and activate the silanols on the silica surface. Silica microparticles (1 g) were added to 100 ml hydrogen peroxide (30%), 100 ml ammonia hydroxide (28-30%) and 100 ml deionize water. The mixture was sonicated and stirred for 1 hour at 70 °C in an open round-bottom flask. The particles were then collected by centrifugation and washed 5 times with absolute ethanol by centrifugation/redispersion cycles. Afterwards, TESI-AP was added to the cleaned particles (500mg) in 30 ml of absolute ethanol in a sealed flask (5 vol% of in ethanol). The mixture was stirred at room temperature for 24 hours. TESI-AP functionalized particles ($NH_2$-MSs) were collected by centrifugation, washed 5 times with absolute ethanol by

centrifugation/redispersion cycles. For each step, the particles were collected after 10 minutes of centrifugation at a relative centrifugal force of 5000 g. At each vial, containing about 500 mg of nanoparticles, 30 ml of washing solvent were added to redisperse the particles. After purification, the particles were dried under reduced pressure.

### 5.3.5 Symmetric hairy surface: synthesis of the hydrophilic homogeneous hairy nanoparticles (II)

In a typical procedure, 5 mL of BAPO functionalized silica nanoparticles in acetonitrile (~ 65 mg) are dispersed in water/PEGMA solution (5 vol %), sonicated and transferred in a lab-made UV-reactor. It consists of a round-bottom flask with three necks for argon inlet and outlet and optical fiber connection through the main neck. The optical fiber is adjusted at 3 cm from the level of the liquid and connected to a light source (LC8 Lightning cure, Hamamatsu Photonics, Hamamatsu, Japan equipped with a Mercury-Xenon lamp with a spectral range distribution from a wavelength of 250 nm to visible light). The flask was covered with aluminum foil and immersed in a bath of water at room temperature to prevent any overheating. The mixture was purged with argon for 20 min under gentle stirring prior light exposure. Then, the light source was activated with an intensity of 120 $mWcm^{-2}$ (UVA) for 1 hour to induce the photopolymerization. Finally, the polymer-grafted nanoparticles were collected by centrifugation, washed seven times with ethanol. For each step, the particles were collected after 30 minutes of centrifugation at a relative centrifugal force of 15400 g. At each vial, containing about 60 mg of nanoparticles, 30 ml of washing solvent were added to redisperse the particles. After purification, the particles were dried under reduced pressure.

### 5.3.6 Asymmetric hairy surface: synthesis of the amphiphilic Janus hairy nanoparticles (IV)

In a typical procedure, 5 mL of BAPO functionalized silica nanoparticles in acetonitrile (~ 65 mg) were added in 20 mL of deionized water containing 3 g of amino functionalized silica microscaffolds ($NH_2$-SMSs)). The pH of the mixture was adjusted to 5 with few µl of HCl ($10^{-2}$ M) sonicated and stirred for 1 hour to promote the nanoparticle assembly on the positively charged microscaffolds. Then, the mixture was centrifuged at low speed (5000 g for 10 minutes) to collect the nanoparticles-microscaffold assembly and remove the unattached nanoparticles (which were removed as supernatant and replaced with the same amount of water a pH of 5). The collected assemblies were transferred in 25 ml of deionized water/PEGMA solution and adjusting the pH to 5. The mixture was transferred in the abovementioned UV-reactor and purged with argon for 20 min.

The mixture was light irradiated to promote the *grafting-from* of PEGMA under the same condition of the homogeneous nanoparticles synthesis. After 1 hour, few μl of KOH ($10^{-2}$ M) were added and the mixture was sonicated to promote disassembly of the nanoparticle-microscaffold structures. The microscaffolds were removed by low speed centrifugation (5000 g for 10 minutes) and partially grafted nanoparticles (intermediate Janus hairy nanoparticles, III) were collected in the supernatant liquid. The intermediate Janus hairy nanoparticles were purified by centrifugation/redispersion cycles with water, acetonitrile. For each step, the particles were collected after 30 minutes of centrifugation at a relative centrifugal force of 15400 g. At each vial, containing about 60 mg of nanoparticles, 30 ml of washing solvent were added to redisperse the particles. After purification, the particles were redispersed in 25 ml $CH_2Cl_2$. The nanoparticles in $CH_2Cl_2$ were transferred in the UV-reactor with 2.5 vol% of LMA monomer. The UV-reactor was immerged in a water bath with a small amount of ice to keep the mixture below room temperature and avoid $CH_2Cl_2$ evaporation. Similarly to the first grafting, the mixture purged with argon and light-irradiated for 1 hour. The amphiphilic Janus particles (IV) were washed seven times by centrifugation/redispersion cycles with $CH_2Cl_2$. For each step, the particles were collected after 30 minutes of centrifugation at a relative centrifugal force of 15400 g. At each vial, containing about 60 mg of nanoparticles, 30 ml of washing solvent were added to redisperse the particles. After purification, the particles were dried under reduced pressure.

## 5.4 Characterization techniques

### 5.4.1 Evaluation of polymer grafting yields

Thermogravimetric analyses were used to evaluate the grafting yields in terms of mass of grafted polymer per nanoparticle surface unit. All the experiments were conducted on a thermal analyzer STA 449 F1 Jupiter (NETZSCH GmbH & Co) with few mg of sample loaded in alumina crucible and heated from room temperature to 700 °C with a heating rate of 10 K $min^{-1}$ under inert helium atmosphere. To promote the oxidation and, thus, the volatilization of carbon residues, at 700 °C the atmosphere was switched from helium to oxygen. However, no weight change was detected after in oxidative condition. The polymer fractions were evaluated by subtracting the total mass loss of BAPO functionalized nanoparticles to the total mass loss of the grafted particles (mass losses were evaluated between 140 and 550 °C). These polymer fractions along with the remaining masses at high temperature were used to evaluate the average polymer per unit area in mg of polymer per $m^2$ of nanoparticles surface as described elsewhere. [235]

### 5.4.2 Morphological investigation in dry state

Herein, contrarily to the work of Chapter 4, the dimensions at stake are too small to allow a suitable analysis by using SEM. Therefore, nanoparticle size and morphologies of the hairy polymer coronas were investigated by using transmission electron microscopy (TEM). Similarly to other electron microscopy techniques, TEM uses an electron beam, however for this technique, the electrons transmitted after interacting with the sample are responsible of reconstructing the image of the specimen in image plane. In conventional vacuum TEM techniques (CTEM) when dealing with non-crystalline samples (as in our case), the contrast of the transmitted image is primarily affected by the mass and thickness of the specimen, and therefore it is defined as mass-thickness contrast. [236] The mass-thickness contrast allows to clearly identify and analyze silica nanoparticles deposited on carbon coated TEM grids. However, in most of the case the organic material, such as those of the hairy polymer coronas, do not have enough contrast and the visualization of such systems becomes very challenging. To overcome this limits we adopted staining techniques. In general, staining techniques use heavy metal ions to increase the sample mass contrast. Both negative and positive staining methods are available. In negative stain, the heavy ions do not interact with the sample and therefore they will surround the sample by creating a thin stain layer. This generate an image of the sample with high contrast surroundings, which emphasize the sample edges. On the other hand, in positive staining methods, the actual sample structure is directly stained. In this case the heavy ions interact with the sample and thus directly increasing the contrast of the organic material. Therefore, it is not the staining agent itself to determine whether the stain is positive or negative, but rather the sample-agent interactions. Common staining agents include anionic agents such as phosphotungstic acid and ammonium molybdate, and cationic such as uranyl acetate, and uranyl formate. [237] Uranyl acetate is surely of one the most convenient because the staining ions $UO_2^{2+}$ impart very high contrast (due to the extremely high atomic number of uranium atoms, 92) and guarantees a good resolution (the uranyl cations are approximately 0.4-0.5 nm in size).[238] An alternative to heavy ion staining involves the use of gold nanoparticles which can selectively bind to specific functional groups. However, in the case of Au NPs labelling, the resolution is limited to the size of the gold nanoparticles which is generally of few nanometers.[239]

All transmission electron microscopy investigations were conducted on JEOL 2010 FEG (JEOL Ltd.) with an acceleration voltage of 200 kV. The images were acquired with an ORIUS SC 200 (2k x 2k) camera. Samples for negative stain CTEM were prepared by depositing a drop of colloid (3 mg $ml^{-1}$) on carbon coated TEM grids (glow discharged for 30 sec with a current of 25 mA). After 1 minute, the liquid in excess was blotted with filter paper. Immediately after, the grid was washed twice with deionized water by rapidly

blotting the water drop from the grid. Then the sample was stained with a drop of uranyl acetate solution (2 wt%). After 30 seconds, the liquid in excess was blotted away with filter paper and washed twice with deionized water as above. Finally, another drop of uranyl acetate solution was deposited on the grid. After 30 seconds the liquid was blotted and the grid was dried under a flux of nitrogen.

### 5.4.3 Morphological investigation and particle-particle interactions in water

The morphology and behavior of hairy polymer coronas as well as the particle-particle interactions in water were investigated by using both direct and indirect techniques. Although techniques such as cryogenic TEM (cryo-TEM) and liquid phase TEM (LP-TEM) give access to a direct visualization of the colloidal system they are limited by the number of particles that can be visualized for each experiment. On the other hand, indirect techniques such as dynamic light scattering (DLS) and small angle X-ray scattering (SAXS) provide information for a more statistically relevant number of particles.

#### Direct visualization

Cryo-TEM involves the investigation of a thin vitrified film of colloidal solution in which all dynamics are arrested by plunge freezing in an appropriate cooling agent. During plunge freezing, the nanoparticles under investigation become embedded in an amorphous thin film of water. The electron transparency of the vitrified thin film is guaranteed by its thickness (usually in the order of 100-200 nm). To do so a liquid thin layer is generated via blotting technique and then plunged into a cooling agent liquid such as ethane (at a temperature of about –183 °C). Attention shall be paid to the film drying before vitrification by performing the film formation in a water-saturated atmosphere. The plunging allows an extremely high cooling rate (10,000–100,000 °C $s^{-1}$), which results in the formation of an amorphous vitrified water embedding the nanoparticles. Both the vitrified water matrix and the nanoparticles under investigation are affected by electron beam damage. The achievable resolution depends on both sample contrast and the electron dose reachable before beam-induced damage becomes visible. Therefore, the achieved resolution is generally relatively low because of the intrinsically low contrast of the sample (made of atoms with low atomic number) and the low dose conditions required. Additionally, because the sample is embedded in a solid vitrified matrix, any dynamic is suppressed. However, when investigating sample morphology of very low contrast materials (e.g. polymeric hairy coronas), the immobilization can be an advantage. Indeed, the absence of dynamics allow longer exposure time at low dose, without introducing any artifacts, which allows in turn the visualization of the morphologies in water with

a better resolution. [240-241] Samples for cryogenic TEM were prepared by depositing a drop of colloid (3 mg $ml^{-1}$) on 200 mesh holey-carbon-coated grids. The grids were blotted with filter paper and frozen by rapidly plunging into liquid ethane. By doing so, a thin film (few hundreds nm) of amorphous ice embedding the nanoparticles was generated. The grids were mounted in a nitrogen-cooled sample holder Gatan 626 and inserted in the microscope by using a dedicated cooled transfer station. All observations were carried out at a temperature of about -180 °C in low dose conditions.

When investigating particle-particle interactions, sample dynamics should not be suppressed to have a better understanding of the system and avoid introduction of artifacts. To do so, LP-TEM was adopted in this study. In this technique, conventional transmission electron microscopes are used in combination with liquid phase sample holder. A schematic design of the sample holder used in this study is reported in Figure 5.3.

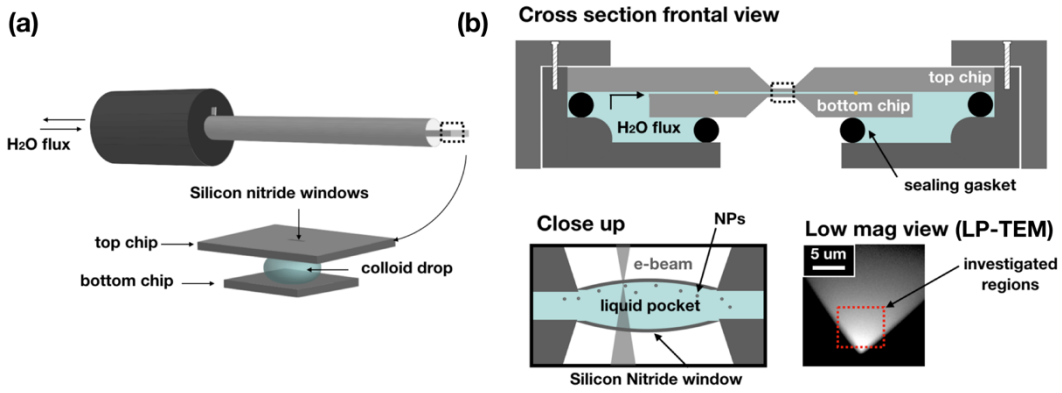


**Figure 5.3**: Liquid phase transmission electron microscopy analysis: (a) Sample holder design which isolate the sample from the vacuum, equipped with flow system connected to a microfabricated liquid cell, (b) cross section and close-up of the liquid-cell embedding the liquid sample.

LP-TEM allow to access sample behavior in water by direct visualization on liquid water. This is possible by embedding the liquid sample in a microfabricated cell composed of two silicon chips with electron transparent $Si_3N_4$ windows separated by 50-500 nm gold spacers (Figure 5.3b). The $Si_3N_4$ windows are surrounded by a liquid reservoir which connected to a flow system embedded in a dedicated sample holder (Figure 5.3a). The whole microfabricated device can be inserted inside the microscope thanks to a vacuum isolation using O-ring seals. In LP-TEM, the thicknesses of both fluid and the $Si_3N_4$ windows are the main factor influencing the achievable resolution.[240] The silicon nitride windows thickness is well known from the microfabrication process. On the other hand, although the nominal thickness of the liquid layer is given by the spacers separating the top and bottom chips, a bulging effect is always present due to the

difference in pressure between the liquid and the vacuum of the column. [242] Consequently, the actual liquid thickness is higher than the nominal one. To reduce the effect of the liquid thickness on the resolution, relatively small $Si_3N_4$ windows are used. To further improve the resolution, the investigated region is limited to the area close to the edges of the liquid cell, i.e. where the liquid layer is thinner. Another aspect to consider is that liquid phase microscopy is affected by beam-induced effects. Contrarily to cryo-TEM where the beam-induced effects are always related to damage, in LP-TEM beam-induced effects can be range from artifacts to severe damage. Indeed, the electron beam collides with the water molecules causing molecule ionization and the ejected electrons decompose the nearby water molecules into radical and molecular species. These includes solvated electrons $e_h^-$, hydrogen radicals $H^\bullet$, hydroxyl radical $OH^\bullet$and following equation:

$$H_2O \rightarrow e_h^- + H^\bullet + OH^\bullet + H_2 + H_2O_2 + H_3O^+ + HO_2^\bullet \quad (6)$$

These species, within few μs, evolve in more stable molecular species which have practical effects on the LP-TEM investigation process. [243] These includes $H_2$ bubble formation, changes in pH, reactions induced by hydrated electrons. [244] Therefore, it is fundamental to consider the beam-induce effects and limit them in order to avoid the introduction of any artefacts. Since water radiolysis is electron-dose dependent, a first measure to reduce such effects is to work with relatively low dose. Additionally, by working with a built-in flow-system, it is possible to replace the liquid affected by the electron beam reducing even more the radiolysis effects. LP- TEM experiments were performed in a Poseidon 210 liquid flow sample holder (Protochips Inc.) loaded with microfabricated E-chips with thin silicon nitride amorphous windows. The E-chips (EPB 55 DM – bottom chip; EPT 55 W – top chip) were rinsed in acetone first and then ethanol (2 min each) to remove the protective coating layers. After being dried with a gas duster, the E-chips were plasma cleaned for 1 minute to enhance the silicon nitride membrane hydrophilicity and to remove any organic contaminants. After having loaded the bottom E-chip inside the sample holder, a drop of the colloidal solution was deposited on it. Then, the system was sealed with the top E-Chip with the silicon nitride windows facing the colloid. After the assembly, the vacuum seal was tested with a turbo pumping station (Pfeiffer Vacuum Technology AG, Germany). During the LP-TEM analysis, low electron dose conditions were used along with a flux deionized water (300 μl $h^{-1}$) by means of a programmable syringe pump (Harvard Apparatus, USA). The image processing was carried out using Gatan Microscopy Suite (GMS3) and ImageJ software.

Both cryo-TEM and LP-TEM investigations were conducted on JEOL 2010 FEG (JEOL Ltd.) with an acceleration voltage of 200 kV. The images were acquired with a Gatan UltraScan 4000 (4k x 4k) camera for low electron dose imaging (below 15 e-/$Å^2$).

## Indirect investigations

Dynamic light scattering allows to indirectly evaluate the particles size in terms of hydrodynamic size. This is possible by shining a monochromatic light beam onto the colloidal solution with nanoparticles in Brownian motion. This causes a Doppler shift (i.e. change frequency of incoming light and the frequency of scattered light) when the light hits the moving nanoparticle. This change is related to the size of the particle, which can be computed as size distribution of objects assumed to be spherical by measuring the diffusion coefficient of the particle and using the autocorrelation function. [245] A Zetasizer Nano ZS (Malvern Instruments, UK) was used for the determination of the hydrodynamic diameters using plastic cells for aqueous suspensions. The device is equipped with a 633 nm laser and with non-invasive backscatter (NIBS) technology to increase the particle size sensitivity. For each sample, three experiments (100 measurements each experiment) were run. For each collection of date, the poly dispersity index (PDI) is herein defined as the square of the ratio between the standard deviation and the mean hydrodynamic diameter.

In DLS analysis, the hydrodynamic size is easily obtained without applying models to describe the experimental data, which means the structural data are obtained under severe approximations. For instance, DLS does not allow to distinguish if an object consist either of a single particle or an agglomerate/assembly of particles. Therefore, the experimental information from a DLS analysis should not be trusted without a comparison with more robust techniques. On the other hand, techniques like small angle X-ray scattering allow a more detailed characterization of nanoscale systems in terms of nanoparticle structural information and nanoparticle assemblies. However, the higher level of details and reliability are counterbalanced by a more complex modeling process to analyze the experimental data. SAXS characterizations on polymer-grafted nanoparticles have been reported previously. [246] For these systems, similarly to LP-TEM, X-ray scattering enables to interrogate the nanoparticles in realist environments such as in water. This is possible in a nondestructive manner and at the same time providing more statistically meaningful information since scattering intensities are averaged over macroscopic sample volumes (i.e. millions of particles). SAXS uses of electron density variations of a sample to generate contrast. [247] More specifically, when the X-ray beam (with a wavelength, $\lambda$) hits the sample, it is elastically scattered of a scattering vector $q = (4\pi \sin(\theta))/\lambda$ with the incoming beam being deflected of $2\theta$. In our study, SAXS measurements were run on both hydrophilic HHNPs (II) and amphiphilic JHNPs (IV) with concentration ranging from 0.2-3.0 mg ml$^{-1}$ by using a Xeuss 2.0 HR laboratory beamline from Xenocs at the Laboratoire Léon Brillouin (LLB, France). For all spectra, a non-linear minimization of the objective function $\chi^2 = \frac{1}{N}\sum_{i=1}^{N}((S_i - S_{ci})/\Delta S_i)^2$ was employed, where $S_i$ and $S_{ci}$ are the measured and computed values

of the *i*th data point. For all the spectra, the $S_{ci}$ values (Equation 7) are computed using the scattering function $P_1(q)$ of one particle made of a spherical core surrounded by a homogeneous spherical corona (Equation 8):

$$S_{\mathrm{ci}}(q) = S_{c\to 0} \times \frac{1}{P_1(0)} \int P_1(k)\mathcal{R}(q,k)dk \qquad (7)$$

$$P_1(q) = \iint \left[ \left(\tilde{b}_{H_2O} - \tilde{b}_c\right)(r+\epsilon)^3 \mathcal{A}\left(q(r+\epsilon)\right) - \left(\tilde{b}_c - \tilde{b}_{SiO_2}\right) r^3 \mathcal{A}(qr) \right]^2 p(r, \bar{r}, \sigma_r) p(\epsilon, \bar{\epsilon}, \sigma_\epsilon) dr d\epsilon \qquad (8)$$

where $\mathcal{R}(q,k)$ is the resolution function of the apparatus, $\mathcal{A}(x) = 3j_1(x)/x$ with $j_1(x)$ as the spherical Bessel function of the 1st kind of order 1, $r$ the radius of the core, $\epsilon$ the thickness of the corona, $p(x, \bar{x}, \sigma_x)$ the Gaussian distribution function centered on $\bar{x}$ with standard deviation $\sigma_x$ and $\tilde{b}_{H_2O}$, $\tilde{b}_c$, $\tilde{b}_{\mathrm{SiO_2}}$ the scattering length densities of solvent, polymer corona and core, respectively (Table 2). Data fitting was fulfilled by fixing values for $\tilde{b}_{H_2O}$ and for $\tilde{b}_{\mathrm{SiO_2}}$. Also, $\sigma_r/r$ and $\sigma_\epsilon/\epsilon$ were kept equal. Using this model, minimum values of $\chi^2$ less than 1 are obtained for all spectra, although higher values are obtained for Janus than for homogeneous particles. This means that the theoretical curve passes through all data points within error bars and that, as far as the minimum of $\chi^2$ is concerned, an alternative model could not be better.

**Table 2.** Physical constants for the different chemical species, $\tilde{b}_X$ is the scattering length density for X-ray (http://sld-calculator.appspot.com); $\rho$ is the mass density.

| Component (Chemical species) | $\tilde{b}_X$ ($10^{10}$cm$^{-2}$) | $\rho$ (nm) |
|---|---|---|
| Solvent ($H_2O$) | 9.47 | 1.0 |
| NP Core ($SiO_2$) | 16.30 | 1.90 |
| Hydrophilic polymer (PEGMA) | 10.67 | 1.15 |
| Hydrophobic polymer (PLMA) | 8.55 | 0.9 |

## 5.4.4 Investigation of the surface potential

The surface potential for native nanoparticles, TMESI²-BAPO functionalized nanoparticles and aminated microscaffolds ($NH_2$-SMSs) was evaluated in terms of zeta potential, which is the electric potential in the interfacial double layer of the particles at the slipping plane. The zeta potentials were calculated from electrokinetic measurements. Indeed, when an electric field

is applied across an electrolyte solution, charged particles suspended in the electrolyte are attracted towards the electrode of opposite charge. Viscous forces begin acting on the particles tending to oppose the movement. Once equilibrium is reached between these two opposing forces, the particles move with constant velocity. This velocity, besides being dependent on the strength of electric field, the dielectric constant of the medium, the viscosity of the medium, it is dependent the zeta potential. [248] The pH-dependent electrokinetic measurements via electrophoresis of the particles in dispersion were carried out with a Zetasizer Nano ZS from Malvern Instruments Ltd. and an MPT-2 autotitrator. For the measurements, the particles were suspended in a solution of $10^{-3}$ M KCl in water (0.42 mg $ml^{-1}$). The pH of the prepared suspensions was controlled by adding either 0.1 M KOH or HCl aqueous solutions. Three measurements were recorded for each sample at each pH value

## 5.5 Results and discussion

### 5.5.1 Synthetic strategies and surface morphologies

### Synthesis of the photoactive nanoparticles

In order to develop photochemical strategies to generate homogeneous and Janus-like soft surfaces at the nanoscale, we first developed a protocol to synthetize monodisperse small nanoparticles to be used as starting material. First, silica nanoparticles were obtained from silica precursors and ammonia as a catalyst by using modified Stöber method, as described in the experimental section. Both scanning (Figure 5.4a) and transmission (Figure 5.4b) electron microscopies showed monodisperse nanoparticles with a spherical shape. More detailed data on nanoparticle size were obtained from a statistical analysis of the intensity profiles from TEM analysis, which gave an average radius of 21.3 ± 7.6 nm. Similarly, dynamic light scattering measurements of the nanoparticles (Figure 5.4c-d) showed an average hydrodynamic size (comparable to the nanoparticle diameter) of 51 nm with a polydispersity index (PDI) of 0.06. These nanoparticles were functionalized with a photoinitiating system via a surface-anchoring of the TMESI²-BAPO by condensation of its methoxy silyl functionalities with the hydroxyl groups of the nanoparticle surface (product II in Figure 5.1). The dried nanoparticles after the functionalization with the BAPO initiating system acquired a light-yellow coloration. The surface-anchoring of TMESI²-BAPO was also confirmed by UV-Visible spectroscopy (Figure 5.4e) which confirmed the presence of light-absorbing moieties in the nanocolloid. On the other hand, we did not observe any variation in size consequently to the surface functionalization. This indicates the formation of a thin layer of TMESI²-BAPO coherently with the anhydrous conditions adopted for the silanization reactions. [249]

## Grafting and immobilization strategies

From the BAPO functionalized nanoparticles (herein defined as 'photoactive'), hydrophilic and amphiphilic hairy polymer surfaces were photochemically grown.

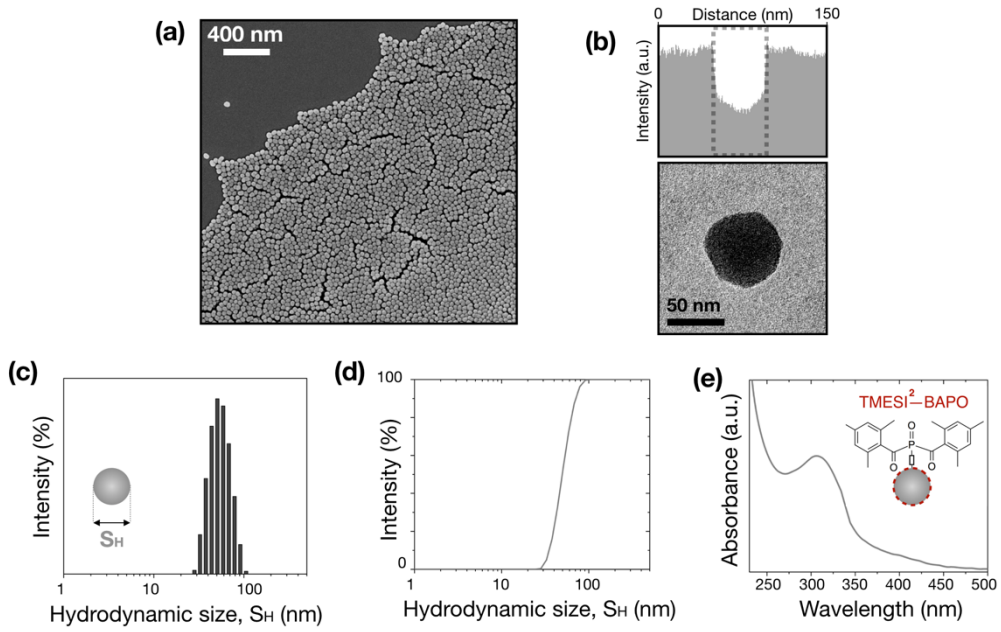


**Figure 5.4**: SEM image of dried cake of native silica particles (a). TEM image of a single native silica nanoparticle and its corresponding transmitted electron intensity profile (b). Hydrodynamic size distribution determined by dynamic light scattering for native silica nanoparticles (c), and its respective cumulative distributions (d). UV-Vis spectrum of photoactive silica nanoparticles functionalized with TMESI$^2$-BAPO initiating system. The spectrum was collected in acetonitrile with a particle concentration of 0.15 mg ml$^{-1}$ (e).

As it is known from previous studies,[156,157,159,160] the photoactivity of the immobilized TMESI$^2$-BAPOs should be comparable to that of free BAPOs. Therefore, when the nanoparticle surface is exposed to light, two surface-anchored phosphinoyl radicals are generated. If acrylic or methacrylic monomers are available, phosphinoyl radicals rapidly add to the available monomer via surface-initiated photopolymerization (*photografting-from* method). Consecutively, ideally, two polymer chains will be developed attached to each single photoactive site. When this protocol is performed in the presence of a hydrophilic monomer and photoactive nanoparticles (I), without any immobilization, homogeneous hydrophilic hairy polymer corona can be generated onto the nanoparticle surface (route (a) in Figure 5.1). For this work, poly (ethylene glycol) methyl ether methacrylate (PEGMA) was selected as hydrophilic monomer. It generates polymer chains with a methacrylic backbone and poly (ethylene glycol) (PEG) side chains on the whole nanoparticle surface (product III in Figure 5.1).

The same *photografting-from* method was used to synthetize amphiphilic Janus-like hairy coronas by a two-step grafting process. The asymmetric character is introduced through the generation of a Janus intermediate (III) as illustrated in the route (b) of Figure 5.1. This Janus intermediate consists of a nanoparticle with two surface-domains: one grafted with a hydrophilic polymer corona and the other one with photoactive functionalities still available. From this intermediate product, the final amphiphilic hairy corona is generated by grafting the photoactive domain with a lipophilic polymer. Therefore, the key aspect in the whole process is the synthesis of the Janus intermediate, which is possible by exploiting the spatial control of photoinitiated processes. More specifically, by immobilizing a monolayer of photoactive nanoparticles (I) on a suitable scaffold, it is possible to initiated the photografting of the hydrophilic polymer chains only from the exposed nanoparticle surface. The other side (in contact with the silica microscaffold) will instead preserve the bis(acyl)phosphane oxide groups thanks to a synergic effect of the (i) suppressed/reduced light penetration through the photoactive nanoparticle and (ii) a solvent cage effect which promote recombination of the involuntarily generated radicals. [250] Indeed, since the first grafting step is performed in water, the hydrophobic escaping radicals (2,4,6-trimethylbenzoyl radicals) are 'locked' between the nanoparticle and scaffold surfaces. This is likely to enhances the probability of having recombination of the escaping radicals with the surface-anchored phosphinoyl radicals.

The immobilization of a monolayer of photoactive nanoparticles on the scaffolds surface should occur in good solvent for the monomer and should be reversible, so that after the partial grafting the nanoparticles can be released. To do so, we developed an immobilization protocol relying on the electrostatic interactions between the photoactive nanoparticle and microscaffolds with a pH-dependent surface charge. More in detail, micrometric silica particles modified with amino functionalities ($NH_2$-SMSs) have been used as scaffolds for the nanoparticle immobilization. The $NH_2$-SMSs are expected to be positively charged in a given range of pH as a consequence of the amine protonation and, thus they can electrostatically attract onto their surface the negatively charged photoactive nanoparticles. The optimal conditions for the electrostatic immobilization were obtained by analyzing the electrophoretic mobility at different pH and therefore the zeta potential for native nanoparticles, photoactive nanoparticles (I) and aminated scaffolds ($NH_2$-SMSs). Results are reported in Figure 5.5a. As expected, the native NPs posses a negative zeta potential profile. [251] Similar negative zeta potential profile is observed for the photoactive nanoparticles, although a slight difference is observed for low pH values. In contrast, $NH_2$-SMSs present a zeta potential profile that strongly depends on the pH with an isoelectric point (IEP) close to 8. Indeed, below the IEP, the positively charged protonated amino groups confer to the $NH_2$-SMSs system a significant positive charge, whereas above the IEP, zeta potential value becomes negative. Thus, by simply playing with the pH of the colloidal solution, it is

possible to modify the charge state of the scaffolds and thus to favor either the nanoparticle attachment (when the scaffolds are positively charged as in Figure 5.5b) or the detachment (when the scaffolds are negatively charged, Figure 5.5c).

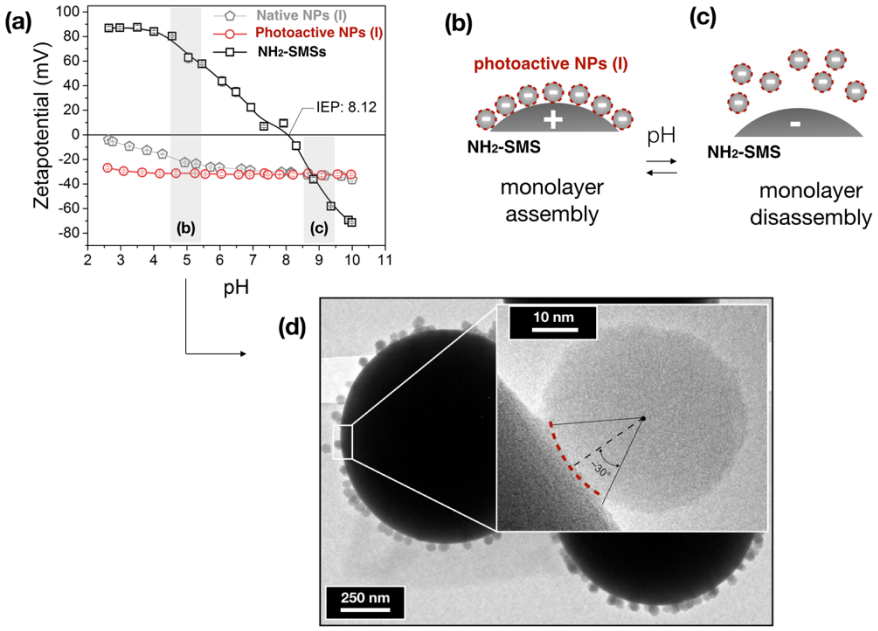


**Figure 5.5**: Zeta potential measurements on silica nanoparticles before and after the functionalization with TMESI²-BAPO compared with the aminated microscaffolds $NH_2$-SMSs (a). Cartoons of attractive regime with monolayer assembly (b) and repulsive regime with monolayer disassembly (c) for the reversible nanoparticle immobilization. TEM image oh photoactive nanoparticles assembled onto the surface of aminated microscaffolds under attractive regime. The inset shows a magnification of a single particle immobilization with the red dashed line indicating the preserved region of photoactive sites.

From what mentioned above, attractive electrostatic interactions between microscaffolds and photoactive NPs are promoted by adjusting the pH of the colloidal suspension to about 5. The result is shown in Figure 5.5d where monolayers of photoactive NPs are assembled on aminated microscaffolds. Under attractive regime, the hydrophilic hairy domain is photogenerated from the exposed surface, which leads to the formation of the Janus intermediate (III). Afterwards, the intermediate products III can be released by adjusting the pH to a repulsive regime (pH = 9). Under repulsive regime, the zeta-potential value of the microscaffolds is negative (-40 mV) and induces the electrostatic repulsion of the attached Janus intermediate. At this point the intermediates III can be collected and a lipophilic domain of poly(lauryl methacrylate) can be grown from the remaining photoactive domain via *photografting-from* method. This last grafting step leads to the formation of the final amphiphilic Janus hairy nanoparticles (product IV in Figure 5.1).

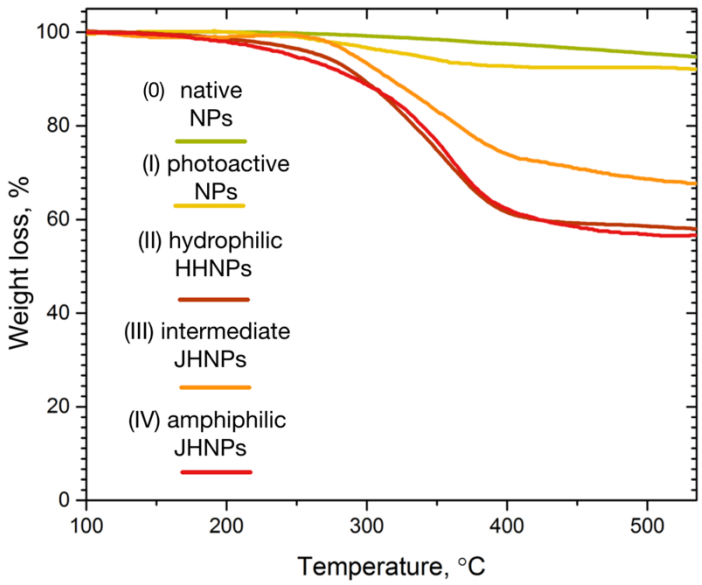


**Figure 5.6**: Thermogravimetric analysis curves for the different particle systems: native nanoparticles (0), photoactive nanoparticles (I), hydrophilic HHNPs (II), intermediate JHNPs (III) and final amphiphilic JHNPs (IV).

**Table 3.** Summary of weight loss percentage from thermogravimetric analysis for the final amphiphilic JHNPs, hydrophilic HHNPs and any other intermediate particle system.

| | Weight loss % | | | |
|---|---|---|---|---|
| **Particle system** | **Total** | **Polymer** | **PEGMA** | **PLMA** |
| Native NPs (0) | 5.0 | n/a | n/a | n/a |
| Photoactive NPs (I) | 8.0 | n/a | n/a | n/a |
| Hydrophilic HHNPs (II) | 41.9 | 33.9 | 33.9 | n/a |
| Intermediate JHNPs (III) | 31.4 | 23.4 | 23.4 | n/a |
| Amphiphilic JHNPs (IV) | 42.9 | 34.9 | 23.4 | 11.5 |

Thermogravimetric analyses (TGA) were performed to determine the grafting. The results are reported in Figure 5.6a. The mass fraction corresponding to each hairy polymer domain (either PEGMA or PLMA) of the different synthetized products are summarized in Table 3. For the hydrophilic HHNPs we found a PEGMA mass fraction of about 34 wt%. On the other hand, for the amphiphilic JHNPs, a mass fraction of PEGMA in the order of 23.5 wt% and of 11.5 wt% for the PLMA mass fraction was found. The mass fraction of the PLMA domain was evaluated by comparing the mass losses of amphiphilic JHNPs and of the intermediate hydrophilic JHNPs. For both homogeneous and Janus hairy nanoparticles, we found an average polymer per unit area between 7.2-10 mg $m^{-2}$,

values which are in good agreement with other *grafting-from* approaches. [251] Interestingly, the SAXS measurements performed on the hydrophilic HHNPs and amphiphilic JHNPs allowed us to confirm the PEGMA/PLMA ratios obtained from the thermogravimetric analyses (vide infra)

## Morphologies of the hairy coronas dry and in water

The morphology of the hairy polymer corona is not clearly visible when conventional TEM is used because of the low contrast of the organic material. Thus, negative stain method with uranyl acetate was selected to increase the contrast allowing in turn to visualize the polymer corona. This has been done for three hairy polymer morphologies hydrophilic HHNPs (II), intermediate JHNPs (III), and amphiphilic JHNPs (IV). The results are shown in Figure 5.7. Negative stained hydrophilic HHNPs (Figure 5.7a) clearly show a dry (not swollen) homogeneous hairy polymer corona of PEGMA with a thickness of 14 ± 3 nm. The intermediate JHNPs (Figure 5.7b) displayed a partial polymer domain (PEGMA) with a thickness of 15 ± 4 nm and, as indicated by the intensity profile, a non-grafted domain. The latter is associated to the remaining photoactive domain. In other words, it corresponds the portion of the nanoparticle originally attached to the aminated microscaffold and protected during the first grafting step. Finally, after the second polymer grafting with the lipophilic polymer, the intensity profile for amphiphilic JHNPs (Figure 5.7c) revealed two features: a photogenerated corona with a morphology and thickness equivalent to that of the intermediate configuration and a thin polymer layer with a thickness of 5 ± 1 nm. As the latter was absent in the intermediate configuration and its extension corresponds exactly to the masked region, it gives the first experimental indication of the existence of Janus nanoparticles with a PLMA hairy polymer corona. Additionally, this observation was further supported by thermogravimetric results which showed differences in polymer mass loss between the intermediate and the final amphiphilic nanoparticles JHNPs.

Hairy polymer surfaces are characterized by the ability to change their morphologies in the presence of a good/bad solvent for the polymer chains. For the systems under investigation, when dispersed in water, the PEGMA domain is expected to be swollen because of its hydrophilicity, whereas the PLMA domain is expected be collapsed onto the NPs surface because of its hydrophobicity. Cryo-TEM is used to investigate morphologies of the hairy polymer coronas in water. The technique allowed us also to get first insights in the interaction patterns, However, it is uncertain to draw conclusions solely from cryo-TEM analysis since the dynamics is suppressed and it is not possible to distinguish between an instantaneous spatial configuration from a configuration of equilibrium. Figure 5.8a shows that hydrophilic HHNPs are well separated.

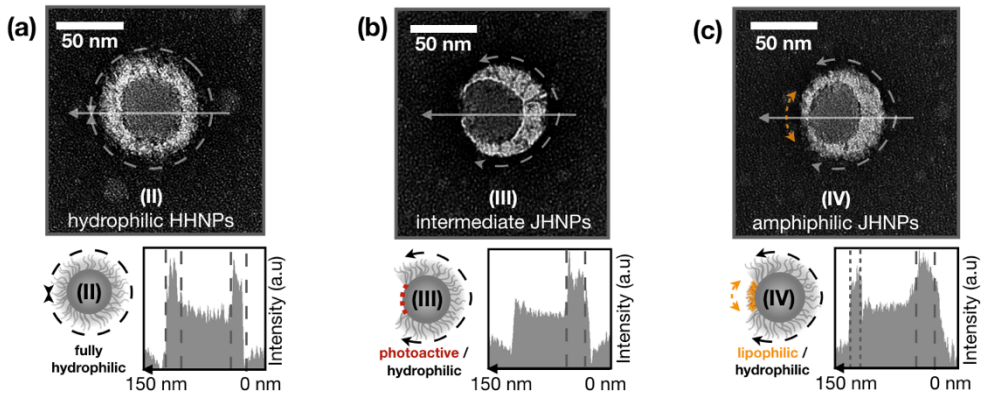


**Figure 5.7**: Morphology of the photogenerated hairy polymer coronas in dry state. Representative TEM images of (a) hydrophilic HHNPs, (b) intermediate JHNPs and (c) final amphiphilic JHNPs along with transmitted electron intensity profiles with schematic representation of the nanoparticles. Images collected after negative stain with uranyl acetate.

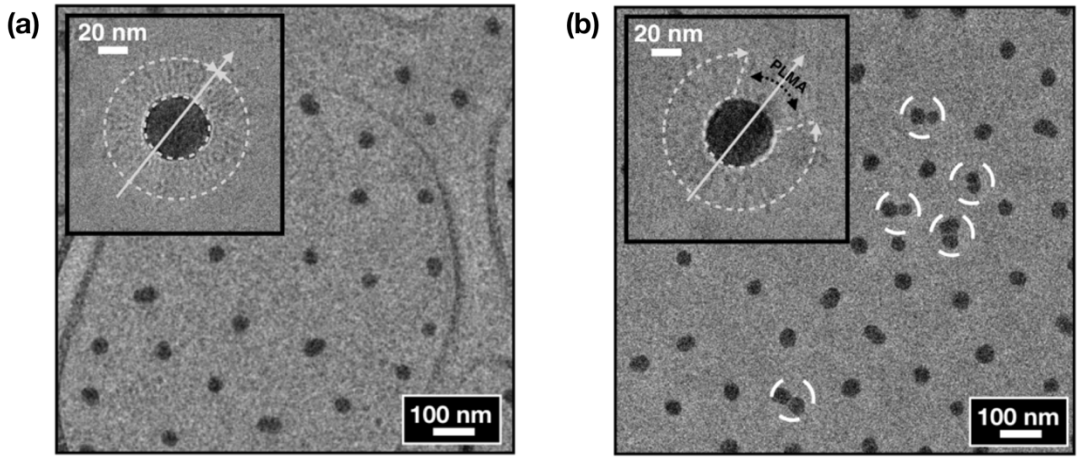


**Figure 5.8**: Cryo-TEM micrographs showing the spatial distribution of (a) hydrophilic HHNPs, (b) amphiphilic JHNPs. The insets show magnifications of the hairy polymer morphology of the in water. In (b), the white circles highlight particles assembled in dimers, whereas the black dashed-line in the inset highlights a domain of higher contrast attributable to a surface-collapsed PLMA domain.

This not interacting distribution is characteristic of sterically stabilized colloids. [252] The close-up of a single homogeneous hairy nanoparticle is shown as inset of Figure 5.8a. Stretched polymeric chains of PEGMA are visible, even though the contrast is low (the C and O from the PEGMA and the O from the amorphous ice generate a very similar mass contrast). In water, the hydrophilic PEGMA hairy interface has a thickness of 23 ± 2 nm, thus the swollen polymer corona is about 1.5 larger than that measured in dry state. The same analysis was performed on the amphiphilic JHNPs as reported in Figure 5.8b. In this case, aggregation is observed with several particles assembled in dimers and, less often, in trimers.

This can be ascribed to the attractive hydrophobic interaction between PLMA polymer domains in water (which is a bad solvent for PLMA). The swollen polymer morphology for the Janus hairy nanoparticles is reported in the inset of Figure 5.8b. We observe both a swollen hydrophilic polymeric interface of PEGMA with a thickness of 24 ± 4 nm, comparable to that of the homogeneous particles, and a smaller non-swollen domain attributed to the PLMA hydrophobic domain.

The thicknesses of the swollen hairy polymer coronas, both for hydrophilic HHNPs and amphiphilic JHNPs, were confirmed by SAXS analyses. Small angle X-ray scattering analyses were conducted on both hydrophilic HHNPs (II) and amphiphilic JHNPs (IV) dispersed in water with concentrations ranging from 0.2-3.0 mg $ml^{-1}$. All the measured spectra were computed by employing the scattering function $P_1(q)$ of one particle made of a spherical core (of radius, $r$) surrounded by a spherical corona (of thickness, $\epsilon$) considered as homogeneous as it was shown in Equation 8 of section 5.4.3. Therefore, from the data treatment and modelling, it is possible to obtain the thickness of the swollen hairy PEGMA for the hydrophilic HHNPs in water. On the other hand, for the amphiphilic JHNPs, the asymmetric compartmentalization of the hydrophilic PEGMA and hydrophobic PLMA hairy domains cannot be directly included in the adopted modelling. For them, the corona is considered to be constituted of both PEGMA and PLMA. At the level of the scattering function $P_1(q)$, this is done by considering a scattering length for the corona ($\tilde{b}_c$) that is accounting for both PLMA and PEGMA (this is reasonable since the scattering lengths are averaged over many amphiphilic particles i.e macroscopic volumes). Consequently, the corona thickness $\epsilon$ for the amphiphilic JHNPs, is an equivalent thickness of a homogeneous corona with the same scattering length. Results are reported in Table 4 and 5 for hydrophilic HHNPs and amphiphilic JHNPs, respectively. Please note that the concentration, within this range, does not play a role in the determined structural information such as nanoparticle radius, $r$ and polymer corona thickness, $\epsilon$. On the other hand, the concentration plays a role in the particle-particle interactions by affecting the scattering $S$ at small $q$ values (these aspects will be clarified in the next section). From structural point of view, having different concentration values helped us to have a better statistic. In this regard, the results for hydrophilic HHNPs and amphiphilic JHNPs are summarized in terms of average values (over the different concentration values) in Table 6. As reported in Table 6, we found nanoparticles cores radius slightly smaller than 25 nm. Similarly, the thickness of the swollen polymeric corona was found to be 23.6 ± 6 nm for the hydrophilic HHNPs and 23.8 ± 9 nm for the amphiphilic JHNPs. Interestingly, these values are very close to those a swollen PEGMA corona found from cryogenic TEM.

**Table 4.** Results from data-fitting using scattering function $P_1(q)$ for the hydrophilic HHNPs at different concentrations. (Confidence intervals on parameters are smaller than 1%)

| C (mg cm$^{-3}$) | $S_{q\to 0}$ (cm$^{-1}$) | $r$ (nm) | $\epsilon$ (nm) | $\sigma_r/r = \sigma_\epsilon/\epsilon$ (-) | $\tilde{b}_c$ (cm$^{-2}$) | $\chi^2$ (-) |
|---|---|---|---|---|---|---|
| **0.2** | 28.4 | 24.5 | 24.3 | 0.116 | 9.71 | 0.29 |
| **0.9** | 109 | 24.7 | 24.3 | 0.113 | 9.70 | 0.40 |
| **1.6** | 191 | 24.6 | 23.6 | 0.116 | 9.71 | 0.48 |
| **2.3** | 280 | 23.2 | 23.2 | 0.117 | 9.71 | 0.50 |
| **3.0** | 352 | 23.0 | 23.0 | 0.116 | 0.69 | 0.49 |

**Table 5.** Results from data-fitting using scattering function $P_1(q)$ for the amphiphilic JHNPs at different concentrations. (Confidence intervals on parameters are smaller than 1%)

| C (mg cm$^{-3}$) | $S_{q\to 0}$ (cm$^{-1}$) | $r$ (nm) | $\epsilon$ (nm) | $\sigma_r/r = \sigma_\epsilon/\epsilon$ (-) | $\tilde{b}_c$ (cm$^{-2}$) | $\chi^2$ (-) |
|---|---|---|---|---|---|---|
| **0.2** | 53.5 | 24.5 | 24.3 | 0.124 | 9.68 | 0.32 |
| **0.9** | 198 | 24.8 | 22.7 | 0.116 | 9.64 | 0.39 |
| **1.6** | 355 | 24.8 | 23.0 | 0.117 | 9.64 | 0.57 |
| **2.3** | 528 | 24.7 | 24.6 | 0.118 | 9.67 | 0.80 |
| **3.0** | 700 | 24.7 | 24.5 | 0.117 | 9.67 | 1.03 |

**Table 6.** Average results from data-fitting using scattering function $P_1(q)$ for hydrophilic HHNPs and amphiphilic JHNPs. (Confidence intervals on parameters are smaller than 1%)

| | Hydrophilic HHNPs | Amphiphilic JHNPs |
|---|---|---|
| $r$ (nm) | 24.6 ± 1 | 24.7 ± 1.5 |
| $\epsilon$ (nm) | 23.6 ± 6 | 23.8 ± 9 |
| $\sigma_r/r = \sigma_\epsilon/\epsilon$ | 0.115 ± 0.001 | 0.118 ± 0.003 |
| $\tilde{b}_c$ (cm$^{-2}$) | 9.70 ± 0.01 | 9.66 ± 0.016 |

Further analysis of SAXS data can be done using with those obtained from thermogravimetric analysis (TGA). Basically, this technique gives access to the weight fraction $w_i$ of each chemical species $i$ (e.g. PEGMA, PLMA and the silica core). Let us denote $x_i$ and $\rho_i$ the volume fraction and mass density, respectively. Then, the system of linear equations: $\rho = \sum_i x_i\rho_i$, $w_i\rho = x_i\rho_i$, $\sum x_i = 1$ provides

volume fractions $x_i$ of each chemical species, the average mass density $\rho$ of the particles. The employed scattering function $P_1(q)$ considers that an 'average polymer' participates to the polymer corona. This polymer is PEGMA for homogeneous nanoparticles, but for Janus nanoparticles it is averaged between PEGMA and PLMA. Therefore, it is possible to write: $w_{pol} = \sum_j w_j$, $x_{pol} = \sum_j x_j$, $k_j = x_j / \sum_j x_j$, $\rho_{pol} = \sum_j k_j \rho_j$, $\tilde{b}_{pol} = \sum_j k_j \tilde{b}_j$ where the subscript "pol" is for the average polymer and "j" for the a given polymer species. Furthermore, the calculated scattering lengths of the corona $\tilde{b}_c$, account for the average polymer and the embedded solvent. That is, $\tilde{b}_c = \tilde{b}_{pol}\phi_{pol} + \tilde{b}_c(1 - \phi_{pol})$, where $\phi_{pol}$ is the volume fraction occupied by the average polymer inside the swollen corona. Thus, from the scattering density of the corona, it is possible to calculate the $\phi_{pol}$ for the homogeneous ($\phi_{pol}^{HHNPs-II}$ of 0.192 ± 0.001) and Janus ($\phi_{pol}^{JHNPs-IV}$ of 0.5 ± 0.01) hairy nanoparticles. Even before calculating the exact value of $\phi_{pol}^{JHNPs-IV}$, we expect that: the $\phi_{pol}^{JHNPs-IV}$ for Janus should lie between 0.192 (corresponding to the swollen PEGMA corona of homogeneous nanoparticles) and 1 (corresponding to bulk polymer), since Janus nanoparticles have a polymer corona partially made of swollen PEGMA and of collapsed PLMA. Therefore, the value of 0.5 ± 0.01 found for Janus nanoparticles is coherent with the morphology of the system. Additionally, if our methodology is correct, we should be able to calculate the $\phi_{pol}^{JHNPs-IV}$ for Janus particles using only the TGA measurements and the $\phi_{pol}^{HHNPs-II}$ for homogeneous particles. Indeed, accordingly to our assumptions, $\phi_{pol}^{JHNPs-IV} = \phi_{pol}^{HHNPs-II} \times k_{PEGMA} + 1 \times k_{PLMA}$ is equal to 0.508 and therefore it is in good agreement with the value determined from the SAXS contrast of the corona for Janus nanoparticles (i.e. 0.5 ± 0.01).

## Particle-particle interactions in water

In this section the self-assembly (or the lack of it) of both hydrophilic HHNPs and amphiphilic JHNPs will be presented through direct and indirect analyses. In the previous section, a preliminary direct visualization of the nanoparticle behaviour in water was reported from cryogenic TEM studies. However, we pointed out how the suppressed dynamic of the analysed system can lead to erroneous interpretations. That is why, LP-TEM is used in a complementary manner to cryo-TEM. Figure 5.9a is representative of how nanoparticles are observed during a LP-TEM experiment. The low contrast is due to the thickness of the liquid layer. However, the hairy polymer coronas can be visualized if the pixel values of the image are represented false colour instead of grey-scale as shown in Figure 5.9b. In doing this, the core of the nanoparticles comes out to be blue-to-green while the polymeric corona orange-to-red. Using false colour rendering, statistical analyses were performed on several hundreds of particles for each system (hydrophilic HHNPs and amphiphilic JHNPs). In

estimating the inter-particle distance $D_{IP}$ was estimated with a maximum distance (cut off) set up to be 200 nm. From the morphological investigations of the polymer coronas, we determined the minimum distance, from the NPs surface, at which two particles are not interacting: this distance was defined as steric limit, $S_L$. Two completely different configurations are observed in liquid phase TEM for homogeneous and Janus nanoparticles, respectively. For the hydrophilic HHNPs, the lack of aggregation unveiled a steric stabilization effect (Figures 5.10a and 5.11b-c). Because of the steric hindrance of the swollen PEGMA corona, the only possible configuration is that of isolated particles (Figure 5.10b).

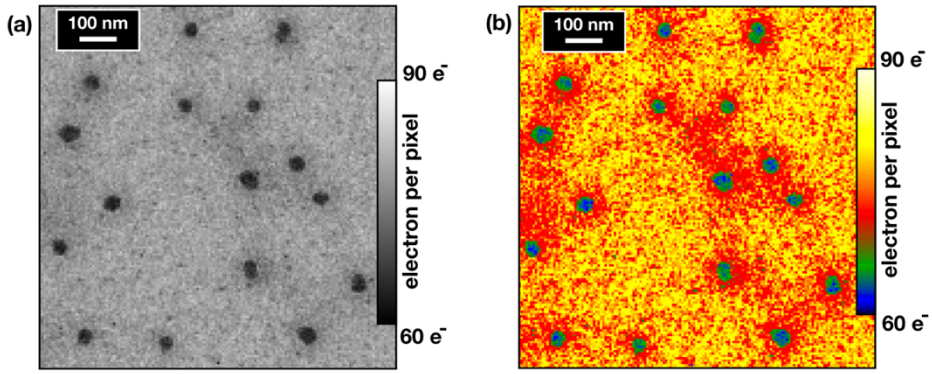


**Figure 5.9**: Typical contrast from direct visualization of liquid sample (hydrophilic HHNPs in water) through LP-TEM: Transmitted electrons represented in (a) grey scale and (b) false colour highlighting the hairy polymer coronas.

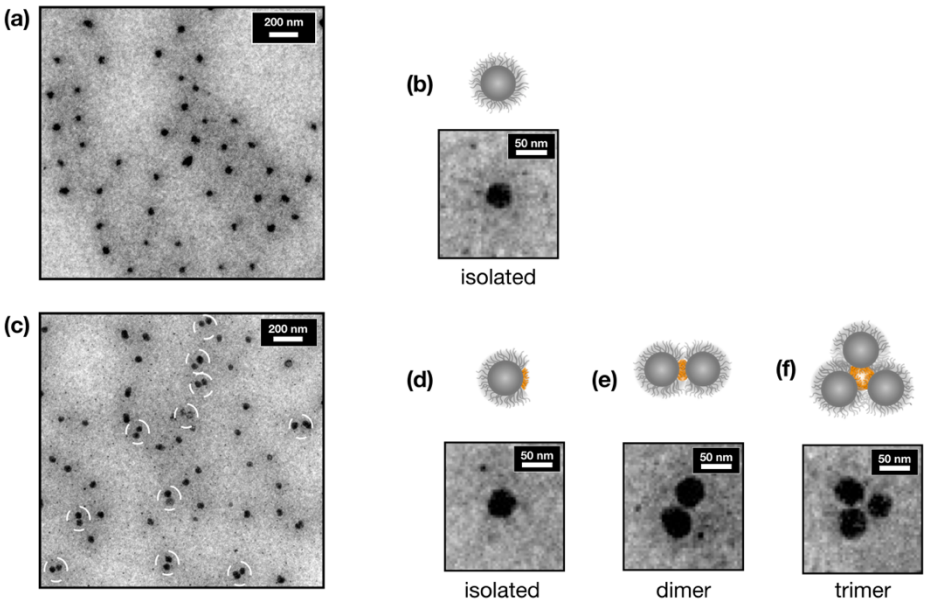


**Figure 5.10**: LP-TEM analyses to investigate particle-particle interactions and the resulting assemblies: (a) exemplificative spatial distribution for hydrophilic HHNPs with equilibrium configuration of (b) isolated particles; (c) exemplificative spatial distribution for amphiphilic JHNPs with equilibrium configuration of (d) isolated particles, (e) dimers and more rarely (f) trimers.

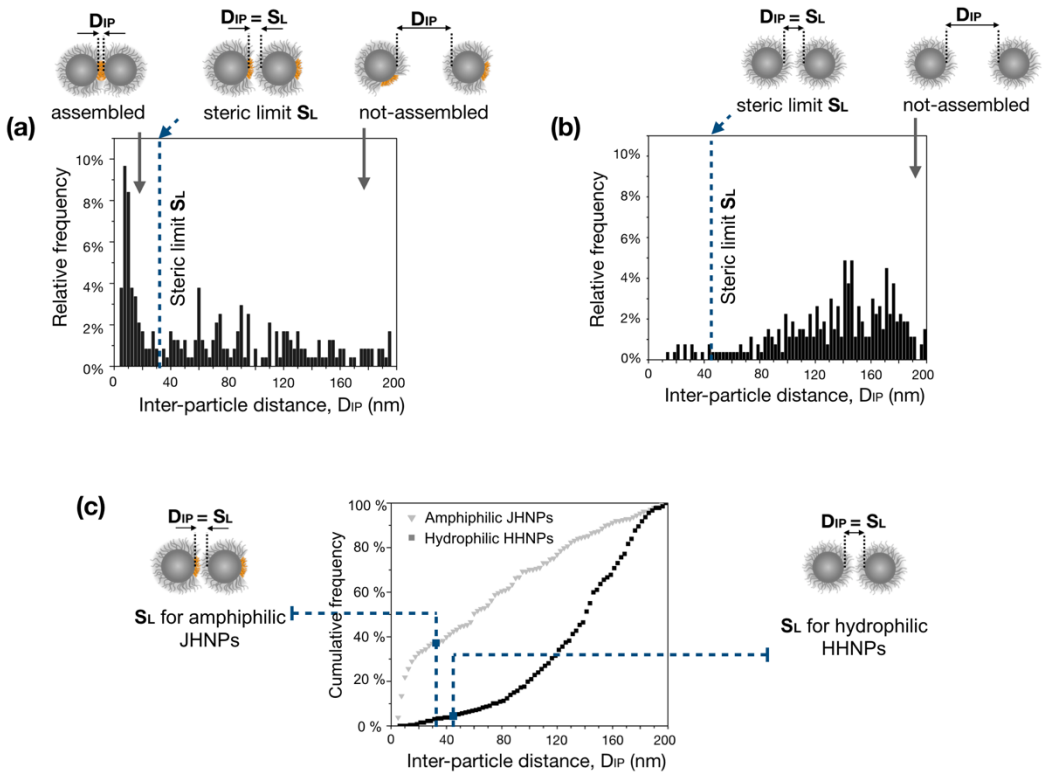


**Figure 5.11**: Statistical analyses of the interparticle distance $D_{IP}$ (with a cut-off of 200 nm) in terms of relative frequency distribution for (a) amphiphilic JHNPs, (b) hydrophilic HHNPs and (c) cumulative frequency distribution comparing the two systems.

Conversely, for Janus nanoparticles (amphiphilic JHNPs), the LP-TEM investigations (Figures 5.10c and 5.11a-c) corroborated the preliminary results of patterns of spatial distribution from cryo-TEM. More specifically, along with isolated particles (Figure 5.10d) we observe a distinguished self-assembly behaviour with formation of mainly dimers (Figure 5.10e) and more rarely trimers (Figure 5.10f). When a Janus nanoparticle approach another (due to its Brownian motion) solvophobic attractive interactions between the PLMA hairy domains can occur (if the orientation is suitable), which will result in self-assembly phenomena. Indeed, the hydrophobic nature of the PLMA domain minimizes the interactions with water by assembling with other particles to an extend that is allowed by the possible geometrical arrangements. Therefore, due to the hindrance of the swollen hairy PEGMA domains, only dimers are likely to be formed. Regarding the self-assembled structure, the average interparticle distance of the interacting amphiphilic was found to be 12 ± 6 nm, which is in good agreement with the thicknesses of the hydrophobic polymer domains.

A better understanding of the self-assembly process was accessed by indirect scattering techniques such as dynamic light scattering and small-angle X-ray scattering. Dynamic light scattering (DLS) measurements were performed on the hydrophilic HHNPs (Figure 5.12a-b) and amphiphilic JHNPs (Figure 5.12c-d). The hydrophilic HHNPs exhibited a hydrodynamic size of 115 nm with PDI of 0.05. This value is consistent with the size of a single nanoparticle core with twice the thickness of the PEGMA hairy corona in the swollen state. On the

other hand, the size obtained for amphiphilic JHNPs (153 nm) suggested that the evaluated hydrodynamic size is likely referring to the size of dimers or trimers rather than the primary size of amphiphilic JHNPs. Indeed, the average hydrodynamic size found for the amphiphilic JHNPs is very close to twice the nanoparticle core size, twice the thickness of swollen PEGMA domain, plus the interparticle distance due to the interacting PLMA domains as for the LP-TEM statistical analysis. In confirmation of that, for amphiphilic JHNPs we found a PDI of 0.12, suggesting thus a much more polydisperse system compared to a PDI of 0.05 for hydrophilic HHNPs. This higher polydispersity is in good agreement with the coexistence of different self-assembled structures as highlighted through LP-TEM (e.g. isolated particle, dimers and trimers).

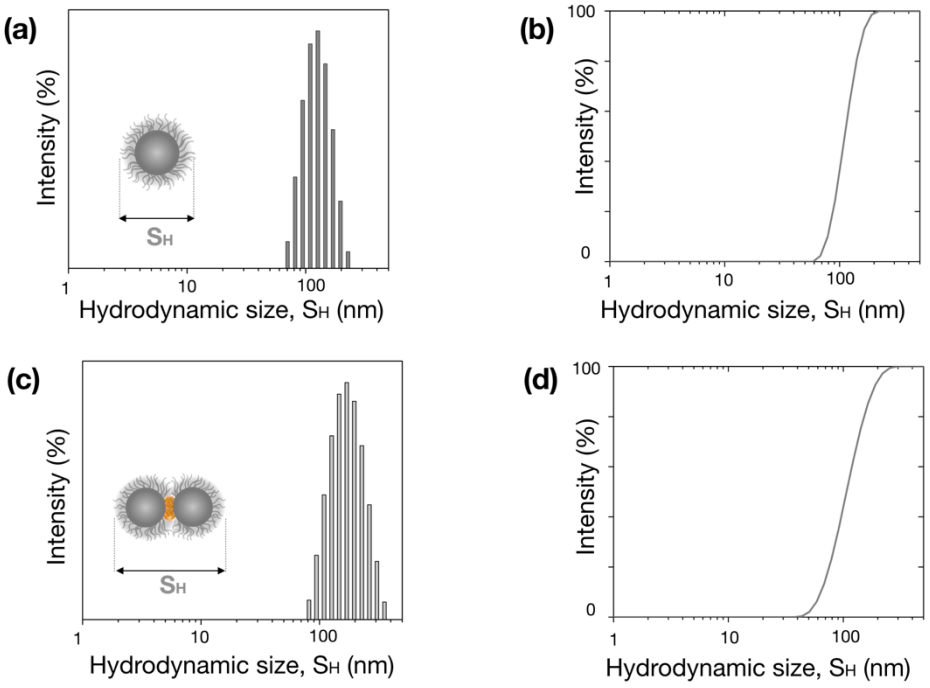


**Figure 5.12**: Statistical analyses of the interparticle distance $D_{IP}$ (with a cut-off of 200 nm) in terms of relative frequency distribution for (a) amphiphilic JHNPs, (b) hydrophilic HHNPs and (c) cumulative frequency distribution comparing the two systems.

In the previous sections, small angle X-ray scattering has been already used to investigate the structural information from a statistically relevant number of particles (either hydrophilic or amphiphilic hairy nanoparticles). The same technique allowed us to investigate particle-particle interaction by looking at scattering cross sections $S$ at small $q$. Indeed, although the coherent differential scattering section $S$ as function of the scattering vector $q$ has a similar shape for the hydrophilic HHNPs and amphiphilic JHNPs at a given sample concentration, the $S$ values at small $q$ are different (Figure 5.13a). This is also numerically reported in Tables 3-4 in terms of $S_{q\to 0}$. These values contain useful information. In fact, the $S_{q\to 0}$ value is related to the osmotic compressibility of the solution. [253]

In the dilute regime, the coherent differential scattering cross section $S_{q\to 0}$ is a virial expansion of the concentration $C$, as reported in Equation 9:

$$S_{q\to 0} = K^2 C \times m(1 - 2mA_2 C + \cdots) \quad (9)$$

where $m$ is the molar weight of particles, $mA_2$ the 2nd virial coefficient, i.e. the two-body interaction in terms of osmotic compressibility ($mA_2$ is positive or negative for repulsive and attractive interactions, respectively) and $K^2$ the contrast factor. In Figure 5.13b, $S_{q\to 0}/K^2 C$ is plotted as a function of particles concentration. For the two sets of data, the concentration dependence of $S_{q\to 0}/K^2 C$ is weak but consistent with the linear behavior expected from Equation 9. It is possible to calculate the contrast factor $K^2$ is from the scattering densities $\tilde{b}_i$ of the ith chemical species as shown in Equation 10:

$$K^2 = \left(\frac{\sum_i \tilde{b}_i - \tilde{b}_{H_2O}}{\sum_i x_i \rho_i}\right)^2 \quad (10)$$

$K^2$ was found to be (7.4 ± 0.1) × $10^{20}$ $cm^2$ $g^{-2}$ and (6.1 ± 0.1) × $10^{20}$ $cm^2$ $g^{-2}$ for hydrophilic HHNPs and amphiphilic JHNPs, respectively. The behaviour of hydrophilic HHNPs and amphiphilic JHNPs requires different comments. On one hand, the $S_{q\to 0}/K^2 C$ values for the hydrophilic HHNPs clearly showed a decreasing trend. In Figure 5.13b, both mean values (dotted line) and linear fit (full line) are reported for the hydrophilic HHNPs data points. The linear fit of the data points represents a virial expansion of the concentration where the vertical intercept and slope lead to molecular weight $m$ and 2nd virial coefficient $mA_2$ of the particles. We found a molecular weight of (1.10 ± 0.05) × $10^8$ g $mol^{-1}$ and second virial coefficient (48 ± 25) μg $cm^{-3}$. The positive value of 2nd virial coefficients found for hydrophilic HHNPs indicate repulsive interaction. This is in good agreement with 2nd virial coefficients with literature for sterically stabilized colloids. [254] On the other hand, for amphiphilic JHNPs the lowest concentration data point seems to separate from the tendency of the others and therefore it was ignored for the linear fitting. We found a molecular weight of (2.1 ± 0.1) × $10^8$ g $mol^{-1}$ and a 2nd virial coefficient of -(33 ± 5) μg $cm^{-3}$. This negative value of 2nd virial coefficient would indicate attractive interactions between the amphiphilic JHNPs. However, we are cautious with this finding since it remains unclear if a system with nanoparticles mainly associated in dimers would still feel, on average, attractive interactions (since two particles associated in a dimer will be stable in water). A better understanding of this could be found by including the first data point (lowest concentration) in the model. Nevertheless, a simple virial expansion at the second coefficient may not be sufficient in this case.
Besides the nature of interactions, the molecular weight of particles found for the amphiphilic JHNPs is almost double of that found for the non-assembled

hydrophilic HHNPs. This undoubtedly indicate the association of Janus nanoparticles in dimers and therefore confirms our previous observations by means of *in situ* LP-TEM and cryo-TEM from a statistically relevant number of particles.

## 5.6 Conclusions

In this chapter, we demonstrated that from surface-immobilized Norrish type I photoinitiator molecules (TMESI²-BAPO) it is possible to photochemically generate soft hairy coronas on the surface of small nanometric particles (~ 25 nm of radius). Upon light exposure, up to two phosphoryl radicals are generated for each initiator site, which can initiate a *photografting-from* growth of polymer chains in mild conditions (i.e. at room temperature and without using any catalyst). First, this photochemically strategy was demonstrated to be suitable to generate homogenous hairy nanoparticles (HHNPs, II). Second, by exploiting the spatial control of the light-induced process along with a reversible nanoparticle protection, through a two-step grafting protocol, we synthetized Janus hairy nanoparticles (JHNPs, IV) via the formation of a photoactive intermediate (III). On one hand, the HHNPs (II) were designed with a hydrophilic hairy corona of PEGMA, whereas the JHNPs (IV) were designed with a compartmentalized amphiphilic Janus-like corona characterized by a hydrophilic PEGMA domain and a lipophilic PLMA domain.

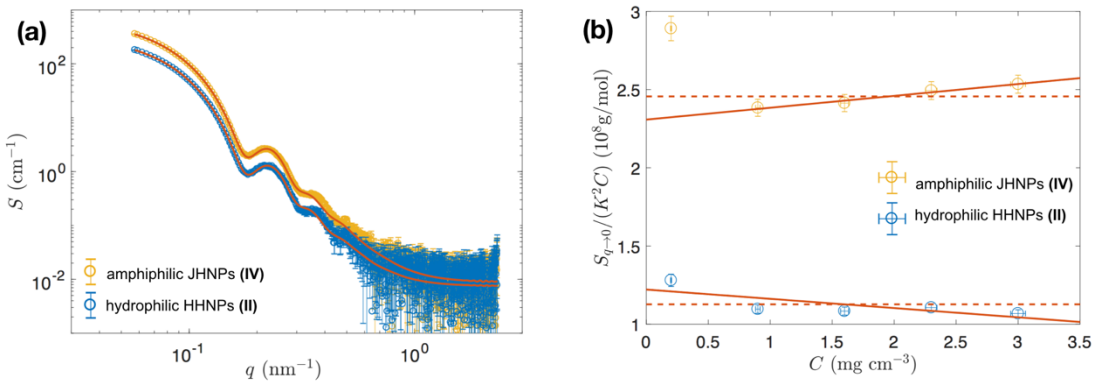


**Figure 5.13**: (a) Small angle X-ray scattering results for hydrophilic HHNPs (blue points) and amphiphilic JHNPs (orange points) in water at concentration equal to 3 mg cm$^{-3}$: coherent differential scattering cross section, $S$, vs. scattering vector $q$ and corresponding best fit using Equation 7 (full lines). (b) Coherent differential scattering cross section at $q \to 0$ per concentration and contrast unit, $S_{q\to0}/(K^2C)$, versus particles concentration for the two series of samples, hydrophilic HHNPs (blue points) and amphiphilic JHNPs (orange points). Full lines correspond to best linear fits of data points, dashed lines to mean values. (Note that the data point for amphiphilic JHNPs at the lowest concentrations has not been used for the linear fit)

The morphologies of the hairy coronas were characterized in both dry state and swollen/collapsed states in water via negative stain protocols and cryogenic TEM. The interaction behaviour of hydrophilic HHNPs and amphiphilic JHNPs in liquid environments were directly visualized by using *in situ* LP-TEM under nearly realistic conditions by avoiding any artefact from drying or indirect visualization techniques. A sterically stabilized system was observed for the hydrophilic HHNPs, with nanoparticles isolated one from the other. On the other hand, the amphiphilic JHNPs shows well-defined self-assembly phenomena with and particle association in dimers and more rarely trimers via hydrophobic interaction. The particle-particle interaction in water were further investigated by using SAXS measurements. This scattering technique granted a deeper understanding underling the self-assembly process from a statistically relevant number of particles. From SAXS measurement, second viral coefficients were derived allowing us to confirm the steric stabilization for hydrophilic HHNPs and the attractive nature of the hydrophobic interactions for the amphiphilic JHNPs. The presence of dimers (the most common assembly-structure) for amphiphilic JHNPs was further supported by the evaluation of the molecular weight from the viral expansion. Specifically, the molecular weight of particles found for the amphiphilic JHNPs was almost double of that found for the non-assembled hydrophilic HHNPs.

To the best of our knowledge, the nanoparticles synthesized in this work are the smallest examples of Janus particle obtained with a *grafting-from* strategy and the first truly nanometric hairy nanoparticles obtained via a photochemical approach. Our synthesis based on a surface photoactivation offers several advantages with respect to conventional thermally-induced polymerizations. Specifically, the synthesis of JHNPs become atom-efficient at low temperatures and does not require any further catalyst. Furthermore, thanks to the temporal and topological control provided by the photopolymerization techniques, our strategy allows to produce sub-100 nm structures.

# 6

# Responsive soft hairy nanoparticles with Janus-like surface heterogeneity for controlled interaction with lipid membranes

## 6.1 Motivation and specific introduction

Cell membranes are ubiquitous in any living being from simplest bacteria to complex biological system like humans. Mainly composed of phospholipid bilayers and proteins, cell membranes play fundamental functions such as cell protection, cell compartmentalization, signaling, selective permeation and transport of ions and molecules. [255] Besides their biological functions, there is an ongoing interest to understand interactions between cell membrane and nanomaterial (in most of the cases as nanoparticles, NPs). [256-257] As a matter of fact, understanding such interactions is crucial in many fields such as drug and gene delivery, [258] imaging and photothermal therapy. [259] Additionally, understanding these interactions allows even to comprehend and predict toxicity of nanomaterials [22] and to develop reproducible cellular uptake behaviors. [260] The interaction between cell membranes and nanomaterials can be either specific or nonspecific. The latter case is characterized by interactions that do not involve specific cell receptors but they only involve molecular interactions mediated by the chemistry of both particle surface and lipid bilayer. [133] Since the chemistry of the lipid bilayer is fixed by the membrane composition, the only way to tune and design this interaction relies on the surface chemistry of the NPs. Scientists have successfully designed nanoparticles with controlled cell membrane – NPs interaction by playing on particle size and shape, surface charge, presence of

functional groups, hydrophobicity/hydrophilicity, etc. [21] More recently, few studies demonstrated that surface heterogeneity has also a role in such interactions. For example, Bishop group showed that gold nanoparticles coated with hydrophobic and hydrophilic ligands in a random arrangement can stabilize the open edge of lipid membranes. [261] In a different work, Stellacci's group demonstrated that gold nanoparticles coated with hydrophobic and hydrophilic ligands arranged in striped domains can penetrate lipid membranes more easily than NPs with random ligand arrangement. [262-263] However, despite the recent efforts in investigating the role of surface heterogeneity, when this heterogeneity has a Janus character (i.e. two distinct surface compartments), its effect on the interactions with cell membrane remains still unclear. Indeed, as it was discussed in Chapter 2 (see subsection 2.2.2.2), the literature on this topic is practically missing. Only very recently, it was observed that Janus-like segregation of hydrophobic ligands on hard silica nanoparticles (100 nm in diameter) remarkably change the interaction with lipid membranes. It was found out that amphiphilic Janus nanoparticles disrupt supported membrane of zwitterionic lipids at pM concentrations. [57] Nevertheless, that study only showed disruptive membrane – NPs interaction which could be detected after the formation of micrometric in size defects. Additionally, supported planer lipid membranes (i.e. deposited on substrates) were adopted as membrane models, whereas results for more realistic systems such as unsupported lipid membranes and liposomes were not provided.

In this chapter, we exploited the versatility of light-induce reaction to generate amphiphilic Janus nanoparticles with soft and pH-responsible hairy surfaces. This was possible by copolymerizing two monomers from the nanoparticle surface: (i) one bearing clickable functionalities (yne) and (ii) the other bearing functionalities tailorable by playing on the pH (tertiary amine as reported in Figure 6.1c). This process was carried out from photoactive nanoparticles via *photografting-from* technique in a similar fashion of Chapter 5. From the clickable system, two toposelective post-polymerization modifications via thiol-yne click reactions allowed us to photogenerate the final nanoparticle. These nanoparticles have two defined domains with hydrophilic and hydrophobic functionalities segregated in a Janus manner and a net positive charge which can be adjusted by playing on the pH (Figure 6.1a). We hypothesized that this "smart" nano-platform can be used to investigate cell membrane – NPs interaction and, in turn, to exploit Janus-like surface heterogeneity and tailorable charge. After a thoughtful characterization, we explored the interaction between the fabricated amphiphilic nanoparticles and cell membranes as both free-standing planar lipid bilayer and liposome (lipid bilayer and lipid chemical structure reported in Figure 6.1a-b). These interactions were examined in a range of pH from 5.8 to 7.8 by using electrical characterization of free-standing planar lipid bilayer as cell membrane model. Within this pH range, it is possible to adjust the degree of protonation of the tertiary amines (with a pKa of 7.4) and therefore the overall positive charged of the hairy particles (Figure 6.1c). A direct visualization

of such interactions was made possible by using liposomes as membrane models in negative stain TEM mode, whereas the interaction dynamic was revealed by LP-TEM.

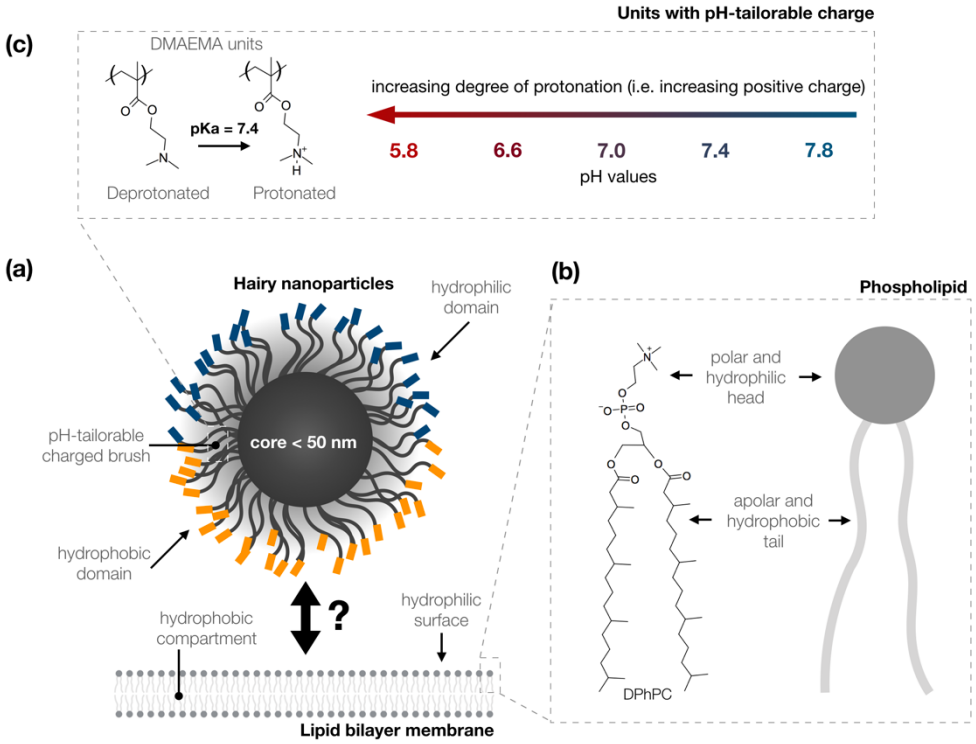


**Figure 6.1**: (a) Schematic illustration of an amphiphilic soft nanoparticle questioning the nonspecific interaction fate toward lipid bilayer membranes depending Janus-like surface heterogeneity and charge. (b) Magnification of DPhPC phospholipid (*1,2-diphytanoyl-sn-glycero-3-phosphocholine*) showing polar head and apolar tail. Tailoring the cationic charge by pH-responsive blocks, (c) exemplification of how the degree of protonation (i.e. cationic charge) can be adjusted by playing on the pH.

## 6.2 Materials

Uranyl acetate (2 wt% in deionized water), Phosphotungstic acid hydrate (Reagent grade solubilized at 2 wt% in deionized water), Ammonium hydroxide ($NH_4OH$, ACS reagent, 28–30% solution), Ethanol abs. (EtOH, VWR, 99.9%), Tetraethylorthosilicate (TEOS, 99%), Toluene (99.8%), Acetonitrile (99.5%), Dichloromethane ($CH_2Cl_2$, 99.8%), Acetone (ACS reagent), N,N-Dimethylformamide (DMF, anhydrous 99.8%), Decane (anhydrous ≥99%), Hydrochloric acid (HCl, ACS reagent 37%), Potassium hydroxide (KOH, pellets), Sodium phosphate monobasic, Disodium hydrogen phosphate, Potassium chloride (KCl),2-(Dimethylamino) ethyl methacrylate (DMAEMA, contains 700-1000 ppm monomethyl ether hydroquinone as inhibitor, 98%), Propargyl acrylate (PA, 98%), Poly(ethylene glycol) methyl ether thiol (PEG-T, average $M_n$ 5000), 1-Hexadecanethiol (HD-T, ≥ 95%), were purchased from

Sigma Aldrich. Silicon dioxide microparticles (1.0 micron, 99.9%) were purchased from Alfa Aesar. 1,2-Diphytanoyl-sn-glycero-3-phosphocholine (DPhPC, 4ME 16:0 PC) was purchased from Avanti Polar. Deionized water was obtained from Milli-Q purification system (Millipore). 3-(trimethoxysilyl) propyl 3-[bis(2,4,6-trimethyl- benzoyl) phosphinyl]-2-methyl-propionate (TMESI²-BAPO) was synthetized via a stable bis(mesitoyl)phosphane intermediate as reported elsewhere.[160]

## 6.3 Experimental procedures

### 6.3.1 Synthesis of TMESI²-BAPO

The procedure has already been reported in the previous pages, please see subsection 5.3.1.

### 6.3.2 Synthesis of silica nanoparticle cores

Monodisperse silica nanoparticles were synthetized using a one-pot hydrolysis-condensation procedure of TEOS in ethanol with ammonia hydroxide as catalyst based on a modified Stöber approach. [234] The adopted procedure was the same reported in subsection 5.3.2, except for having employed a lower amount of ammonia. More specifically, the volume of ammonia solution used was kept the same, as for subsection 5.3.2, but its concentration was reduced from 30-32% to 28-30%. This was done with the aim of slightly reducing the nanoparticles size in accordance to previous studies. [264]

### 6.3.3 Preparation of negatively charged silica microscaffolds: OH-SMSs

Commercially available silica microparticles (1 μm in diameter) were cleaned with wet chemical treatment (RCA-SC1) to remove contaminants and activate the silanols on the silica surface. Silica microparticles (1 g) were added to 100 ml hydrogen peroxide (30%), 100 ml ammonia hydroxide (28-30%) and 100 ml deionize water. The mixture was sonicated and stirred for 1 hour at 70 °C in an open round-bottom flask. The particles were then collected by centrifugation and washed 5 times with absolute ethanol by centrifugation/redispersion cycles.

### 6.3.4 Functionalization of silica nanoparticle with TMESI²-BAPO: photoactive nanoparticles (I)

The adopted experimental procedure is the same reported in subsection 5.3.3.

### 6.3.5 Synthesis of yne(+HNPs) grafted nanoparticles (II) with pH-responsive and clickable hairy surfaces

In a typical procedure, 900 mg of BAPO functionalized silica nanoparticles are added to 210 ml of DMF and sonicated for 30-45 min until the particles are properly dispersed. Then, 12.04 mg of DMAEMA and 1.96 of PA are added to the colloid under stirring (90% : 10%, molar ratio). The whole system is then transferred to a lab-made UV-reactor. It consists of a round-bottom flask with three necks for argon inlet and outlet and optical fiber connection through the main neck. The optical fiber is adjusted at 5 cm from the level of the liquid and connected to a light source (LC8 Lightning cure, Hamamatsu Photonics, Hamamatsu, Japan equipped with a Mercury-Xenon lamp with a spectral range distribution from a wavelength of 250 nm to visible light). The flask was covered with aluminum foil and immersed in a bath of water at room temperature to prevent any overheating. The mixture was purged with argon for 20 min under gentle stirring prior light exposure. Then, the light source was activated with an intensity of 60 $mWcm^{-2}$ (UVA) for 1 hour to induce the photopolymerization. Finally, the polymer-grafted nanoparticles were collected by centrifugation and washed eight times with DMF (x2), acetone (x2), ethanol (x2) and finally acid water (x2). For each step, the particles were collected after 30 minutes of centrifugation at a relative centrifugal force of 15400 g. At each vial, containing about 60 mg of nanoparticles, 30 ml of washing solvent were added to redisperse the particles. After the washing steps, the particles were dialyzed against ultrapure water for 96 hours and changing the dialysate each 4 hours (dialysis tubing of regenerated cellulose M.W. > 12,000 Da, from Spectrum Labs). The synthetic route is schematically reported in step 1 of Figure 6.2.

### 6.3.6 Synthesis of hydrophilic yne/hydro(+HNPs ) intermediate Janus (III) and hydro/hydro(+HNPs) homogeneous (V) nanoparticles

The designed procedure for the synthesis of the intermediate Janus nanoparticles is based on electrostatic immobilization of yne(+HNPs) onto negatively-charged silica microscaffolds (OH-SMPs) in a similar fashion to the protocol of subsection 5.3.6. The immobilization is followed by toposelective click reactions. In a typical procedure, 50 ml of yne(+HNPs) at a concentration of 2.5 mg $ml^{-1}$ were added dropwise to 20 ml of (OH-SMSs) at a concentration of 200 mg $ml^{-1}$. The colloids ware let interact at a pH of 5.5 for 1 hour under gentle stirring. These quantities were calculated to have an excess of microscaffolds and, thus, to ensure the immobilization of all the yne(+HNPs). After the incubation time, the colloids were diluted to reach a total volume of 120 ml of water at a pH of 5. At this point, 4550 μl of polymer solution (PEG-T in water, 40 mg $ml^{-1}$) and photoinitiator solution (I2959 in 2 : 1 MeOH : water solution, 160 mg $ml^{-1}$).

After 30 min of incubation, the whole colloid was transferred in the above-mentioned UV-reactor and irradiated for 50 minutes with an intensity of 60

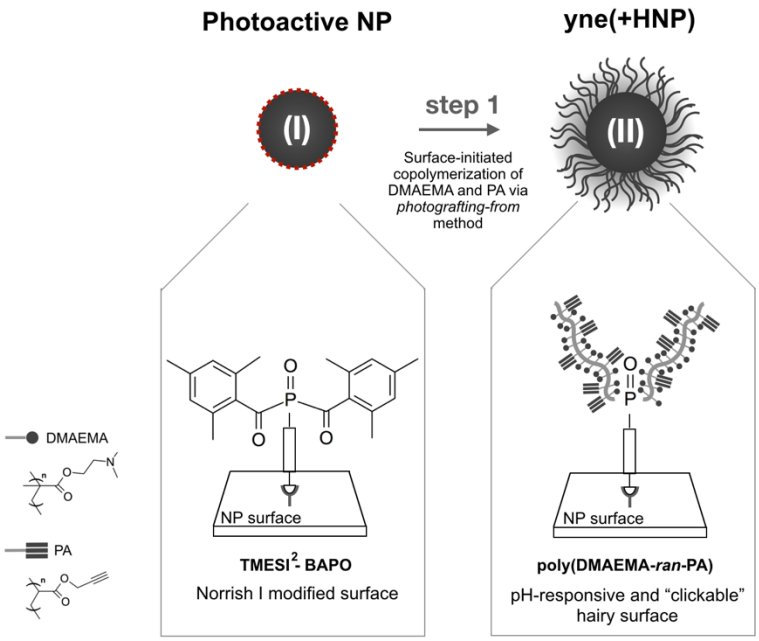


**Figure 6.2**: Schematic representation of the fabrication process via *photografting-from* and light-induced thiol-yne click reactions. (Step 1) Synthesis of yne(+HNPs) from photoactive nanoparticles via photogeneration of poly(DMAEMA-ran-PA) pH responsive and clickable surfaces through *photografting-from* method. The tabs below each product report the schematic structure of the surface in each specific step.

$mWcm^{-2}$ (UVA). After irradiation, 1 ml of $H_2O_2$ solution was added to oxidize the unreacted thiol end-groups of PEG-T and avoid click reaction after the disassembly of nanoparticles. After 10 min of extra irradiation the presence of $H_2O_2$, the pH of the colloid was adjusted to 2 by adding few drops of HCl, 4 ml of KCl solution (3 M) were added to help increasing the ionic strength of the solution and the whole system was sonicated for 30 minutes to promote the disassembly. After sonication, the nanoparticles were collected by vacuum filtration through track-etched polycarbonate membranes (1 μm pore size, Whatman® Nuclepore). The vacuum filtration was repeated at least three times. Finally, the partially PEGylated yne/hydro(+HNPs) were purified via centrifugation and redispersion cycles repeated 5 times with acetone. Finally, the intermediate Janus yne/hydro(+HNPs) were dried by using a rotary evaporator at 45 °C for 4 hours. The synthetic route is schematically reported in the step 2 of Figure 6.4. Similarly, homogeneous hydrophilic particles were obtained by using the above-mentioned strategy but without the immobilization of yne(+HNPs) onto negatively-charged silica microscaffolds (OH-SMPs). In this case, the yne(+HNPs) were homogeneously modified with PEG-T leading to the

formation of so-called hydro/hydro(+HNPs). The synthetic route is schematically reported in the step 2' of Figure 6.3.

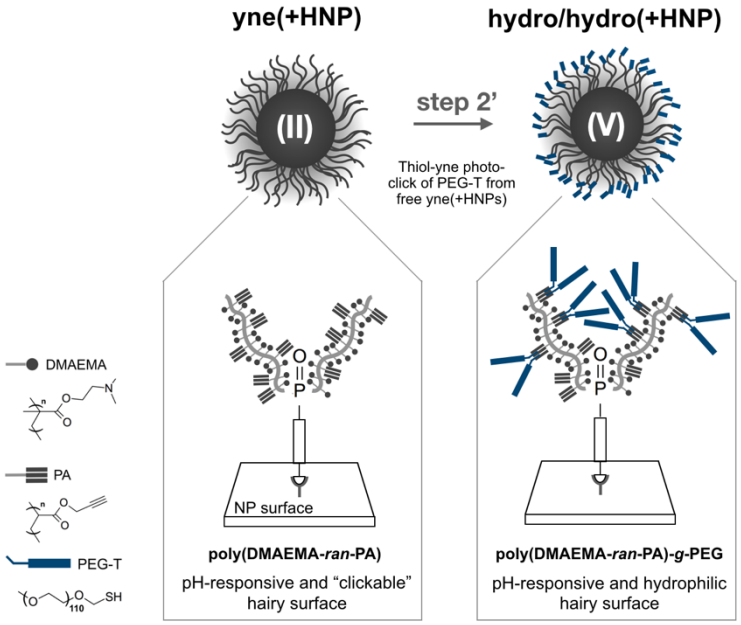


**Figure 6.3**: Schematic representation of the fabrication process of uniformly PEGylated hairy nanoparticles hydro/hydro(+HNPs) via light-induced post-polymerization modification with PEG-T. (Step 2'). The tabs below each product report the schematic structure of the hairy surface photogenerated in each specific step.

## 6.3.7 Synthesis of lipo/hydro(+HNPs ) amphiphilic Janus nanoparticles (IV)

In a typical procedure, 70 mg of partially PEGylated nanoparticles yne/hydro(+HNPs) were added to 30 ml of $CH_2Cl_2$ and sonicated in ice bath until a suitable dispersion was obtained. Then, 132 µl HD-T solution (2.3 mg $ml^{-1}$ in $CH_2Cl_2$) and 236 mg of I-2959 were added to the colloid and sonicated for few minutes. The whole system was then transferred to the above-mentioned UV-reactor and immersed in an ice bath. After 50 minutes of irradiation with an intensity of 60 $mWcm^{-2}$ (UVA), the $CH_2Cl_2$ was evaporated by using a rotary evaporator. Finally, the so produced amphiphilic lipo/hydro(+HNPs) were purified via centrifugation and redispersion cycles repeated 5 times with acetone. The synthetic route is schematically reported in the step 3 of Figure 6.4.

## 6.3.8 Preparation of nanoparticles colloidal dispersion

Stock dispersion of nanoparticles were prepared for both homogeneous hydrophilic hydro/hydro(+HNPs) and Janus amphiphilic lipo/hydro(+HNPs) by

dispersing the nanoparticles at a concentration of 10 mg $ml^{-1}$ in ultrapure deionized water via probe sonication and stored at 4 °C. Prior their use in the different experiments, the nanoparticles were diluted in phosphate buffer at a concentration of 1.5 mg $ml^{-1}$. The buffers were prepared from a combination of monosodium phosphate and disodium phosphate with an overall concentration of 50 mM, with a pH tailored accordingly to the Henderson–Hasselbalch equation. We selected a range of pH from 5.8 to 7.8 with steps of 0.4, since these values can be tracked back to reasonable biological conditions. [265] The dilution in those buffers was done just few hours before the actual use to improve the nanoparticle stability.

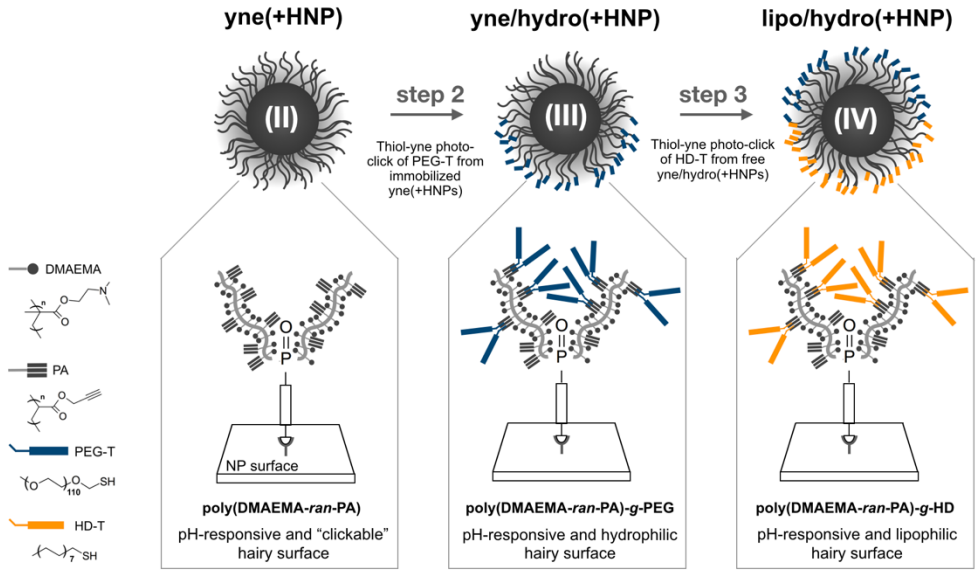


**Figure 6.4**: Schematic representation of the fabrication process of partially PEGylated hairy nanoparticles yne/hydro(+HNPs) via toposelective light-induced post-polymerization modification with PEG-T. (Step 2) Synthesis of amphiphilic Janus-like hairy nanoparticles lipo/hydro(+HNPs) via light-induced post-polymerization modification with HD-T (step 3). The tabs below each product report the schematic structure of the hairy surface photogenerated in each specific step.

## 6.3.9 Preparation of liposomes

Large liposomes were prepared by extrusion. In a typical procedure, 4 mg of lyophilized DPhPC lipids were dissolved in 250 µl $CH_2Cl_2$ and transferred in a 2 ml round-bottom flask. The $CH_2Cl_2$ was evaporated by gentle argon flux while rotating the flask. After solvent evaporation, the flask was placed for 2 hours in high vacuum chamber (0.5 mbar) to further boost the residual solvent removal. The so obtained lipid cake was then hydrated in 1 ml phosphate buffer with a pH of interest (prepared as described in subsection 6.3.9). The hydration was carried out for 2 hours alternated each 30 min by short mixing with a vortex mixer. Then, the hydrated lipid suspension was subjected to 5 freeze-thaw cycles by

alternatively placing the vial first in a cooling acetone - liquid nitrogen bath and then in a warm water bath. The lipid suspension was den extruded by using an extrude set equipped with two 1 ml syringes separated by an extrusion block containing two single-use polycarbonate membranes (Mini-Extruder from Avanti® Polar Lipids, Inc.). Prior extrusion, the syringes were wetted with the buffer of interest to limit the dead volumes and facilitate extrusion. The lipid suspension was first passed 11 times through 0.4 μm polycarbonate membranes and finally collecting the liquid in the initially-empty syringe. This allow to avoid contamination from foreigner materials. The extruded suspension was then extruded additional 11 times through 0.1 μm polycarbonate membranes to finally obtain large unilamellar vesicles. The liposome suspension was stored at 4 °C for a maximum of 3 days.

## 6.4 Characterization techniques

### 6.4.1 Evaluation of polymer grafting yields

The adopted experimental procedure is the same reported in subsection 5.4.1. Experiments were performed in confirmation of the synthesis of lipo/hydro(+HNPs) and each product of the intermediate synesthetic steps i.e. and BAPO functionalized NPs, yne(+HNPs), and yne/hydro(+HNPs).

### 6.4.2 Chemical characterization

Infrared spectroscopy FTIR in transmission mode was to check the presence of "clickable" functionalities after the light-induce surface-initiated co-polymerization of DMAEMA and PA. To do so, we compared the FTIR spectra for native silica nanoparticles and for yne(+HNPs). In a typical sample preparation, 3 mg of dried sample was mixed with 97 mg of KBr. The two components were mixed by using a agate laboratory mortar and pestle. The mixed powder was transferred into 70 mm pellet die and pellets were fabricated by using a laboratory bench top hydraulic press while connecting the die to a vacuum pump. The procedure was repeated 4-5 types till pellet optical clarity was obtained. Spectra were collected by using a Nicolet iS50 FTIR spectrometer. Spectra were recorded in absorbance mode with a resolution of 4 $cm^{-1}$ and a wavelength ranging from 1400 to 4000 $cm^{-1}$, averaging 10 scans for each spectrum.

### 6.4.3 Morphological investigation in dry state

In this Chapter, conventional TEM, with or without stain, was used to study nanoparticles size and polymer corona morphologies. All transmission electron microscopy investigations were conducted on JEOL 2010 FEG (JEOL Ltd.) with an acceleration voltage of 200 kV. The images were acquired with an ORIUS SC 200 (2k x 2k) camera. Samples of yne(+HNPs) for positive stain CTEM were prepared by depositing a drop of colloid (2.5 mg $ml^{-1}$) on carbon coated TEM grids (glow discharged for 30 sec with a current of 25 mA). After 1 minute, the liquid in excess was blotted with filter paper. Immediately after, the grid was washed twice with deionized water by rapidly blotting the water drop from the grid. Then the sample was stained with a drop of phosphotungstic acid solution (PTA, 2 wt% in ultrapure water and buffered to the pH of interest by using sodium hydroxide). After 30 seconds, the liquid in excess was blotted away with filter paper and washed twice with deionized water as above. Finally, another drop of phosphotungstic acid solution was deposited on the grid. After 30 seconds the liquid was blotted and the grid was dried under a flux of nitrogen. However, PTA staining agent do not allow to identify the Janus morphology after the post-polymerization modification. To do so, Au nanoparticles (5 nm, citrate-capped) were incubated with yne(+HNPs) and yne/hydro(+HNPs) to highlight the different Au NPs stain after partial PEGylation via post-polymerization modification. In a typical procedure, 200 µl Au NPs (at a concentration of 5.5 x $10^{13}$ particles/ml) were added to 100 µl of hairy colloid (either yne(+HNPs) or yne/hydro(+HNPs) at a concentration of 2.5 mg $ml^{-1}$) and let interact for 30 min. Then, the hairy nanoparticles were purified from unbound Au NPs by centrifugation. Subsequently, a drop of hairy nanoparticles stained with Au NPs was deposited on carbon coated TEM grids (glow discharged for 30 sec with a current of 25 mA). After 1 minute, the liquid in excess was blotted with filter paper. Finally, the grid was dried under a flux of nitrogen and analyzed under the conditions reported above.

### 6.4.4 Investigation of the surface potential

The experimental conditions were the same as reported in subsection 5.4.4 for yne(+HNPs). Conversely, for OH-SMSs the zeta potential was evaluated only for pH values of interest (i.e. those used to promote NP immobilization or detachment on the SMPs).

### 6.4.5 Particles – Lipid membrane interactions

#### Direct investigation

The interactions with lipid membranes were investigated for two particles system: hydro/hydro(+HNPs) and lipo/hydro(+HNPs) colloidal dispersions

prepared as described in subsection 6.3.8. In a typical procedure, 10 μl of either hydro/hydro(+HNPs) and lipo/hydro(+HNPs) dispersion were let interact with 100 μl of LUVs suspension for 30 min and then analyzed by using negative stain CTEM. Uranyl acetate was chosen as stain agent following the same staining protocol described in subsection 5.4.2. It is important to note that although the nanoparticles were incubated in a specific buffer condition, prior staining the deposited samples was thoughtfully washed with ultrapure water. This step is necessary for two reasons: (i) phosphate residues can crystallize during the drying process, contaminating the sample; (ii) phosphate ions can interact with uranyl ions to produce a fine crystalline precipitate that obscure the sample. Despite its rapidity, the washing step changes pH and ionic strength and subsequently the interacting conditions. Therefore, it is not possible to rely on this technique to distinguish different behaviors depending on the pH value. However, this rapid technique allows to visualize whether interactions between nanoparticles and lipid membranes occurred.

A better understanding was gained from LP-TEM analysis, which was used to directly visualize, *in situ*, the interaction between nanoparticles and liposomes. The adopted experimental procedure was the same as for subsection 5.4.3.1. However, in this case the sample preparation and flux arrangement were adapted to the specific needs. After having loaded the bottom E-chip inside the sample holder, a drop of the liposome suspension was deposited on it. Then, the system was sealed with the top E-Chip with the silicon nitride windows facing the liquid. Once a liposome is identified, the flux is turned on (300 μl $h^{-1}$) by means of a programmable syringe pump (Harvard Apparatus, USA). The flux contains lipo/hydro(+HNPs) in 6.6 pH buffer. The view is kept on the liposomes, which are visualized waiting for the nanoparticles to arrive. When the nanoparticles reach the liposomes, the flux is turned off and the interactions start to be recorded. It is important to note that an acidic buffer was selected because, anyway the beam induces an acidification of the irradiated liquid environment. Although working with low electron doses, this effect is still important since, in this case, there is no water flux to remove the radiolysis products. To have an idea of this effect, studies have demonstrated that under beam irradiation the entire liquid cell will have an increased $H_3O^+$ concentration and thus a reduced pH. For instance, starting from pure water initially at pH 7, after being exposed to a 1 μm radius beam of 1 nA at 300 kV its pH will eventually drop to ~4.9 within the irradiated region and ~6.1 outside. [266] This effect cannot even be compensated by increasing the buffer concentration because such increase in concentration could only introduce additional artefacts due to salt precipitation within the liquid cell. To achieve a better contrast, energy filter TEM (EFTEM) was used by collecting only zero-loss electrons with a GIF Tridiem (Gatan GmbH) post-column energy filter used in image mode.

## Indirect investigation

Interactions between nanoparticle and cell membrane were investigated by using free-standing planar unsupported bilayer lipid membranes (p-BLMs) as cell membrane model. Planar bilayer lipid membranes generate from the self-assembly of individual phospholipids so that the polar head groups are oriented outward to an aqueous solution whereas the hydrophobic aliphatic tails assemble facing each other inward with respect of the aqueous solution. Because of this assembly, p-BLMs are electrically insulating with a behavior that recall a capacitor in parallel with a resistance. This capacitive character arises from the fact that ions accumulate on the membrane surface. When an electric potential is applied between the two membrane sides, the formed layers of opposite charge are separated by a very small distance (less than 10 nm) by a high dielectric constant region (i.e. assembled aliphatic tails). The electrical behavior of a BLMs is affected by the formation of ion channels, as well as proteins, genetic material and nanoparticles interacting with the membranes, as previously reported. [267-269] Therefore, by performing electrical measurement of p-BLMs, before and after nanoparticle addition, it is possible to probe NPs – membrane interactions. Moreover, this technique allows to determine whether the interactions preserve the membrane or leads to membrane rupture. In a typical electrophysiology experiment (electrical measurement on p-BLMs), a membrane-forming solution was prepared by adding DPhPC phospholipids in n-decane at a concentration of 10 mg $ml^{-1}$ and stored at -20 °C when not in use. The adopted experiment configuration is schematically reported in Figure 6.5. The cell is a two-part system consisting of a black Delrin chamber (*trans*) and a removable cuvette (*cis*) with a 150 μm in diameter hole, both from Warner Instruments. The p-BLM is formed over a hole separating the two cis/trans chambers. To do so, 0.5 μl of membrane-forming solution are painted on and around the hole by using a long gel-loading pipet tip and let it dry in air for at least 30 min. This step allows acts as surface pre-treatment which will help the actual membrane formation in the following steps. Once the lipid primer-coating is applied, the two chambers are filled with 750 μl buffer solution at a specific pH.

At this point, the two Ag/AgCl electrodes are inserted in the solution and connected to a waveform generator (33500B Series, Keysight Technologies). A voltage of 50 mV is applied with a sinusoidal waveform and a frequency of 10 kHz. During the experiments, the ionic current (values in the order of pA) was measured. To do so, the resulting ionic current was amplified by using Axopatch 200B amplifier. The amplified current was digitized with a 16 bits analog-digital oscilloscope (PicoScope®, Pico Technologies). To reduce the noise, the whole cell system was closed inside a Faraday copper cage and placed on an anti-vibration marble table. The data acquisition was handled by using dedicated Matlab macros. From the ionic current and voltage, the complex impedance $Zm^*$ of the

system could be estimated in terms of real (*Rm*, resistance) and imaginary (*Xm*, capacitive reactance) parts.

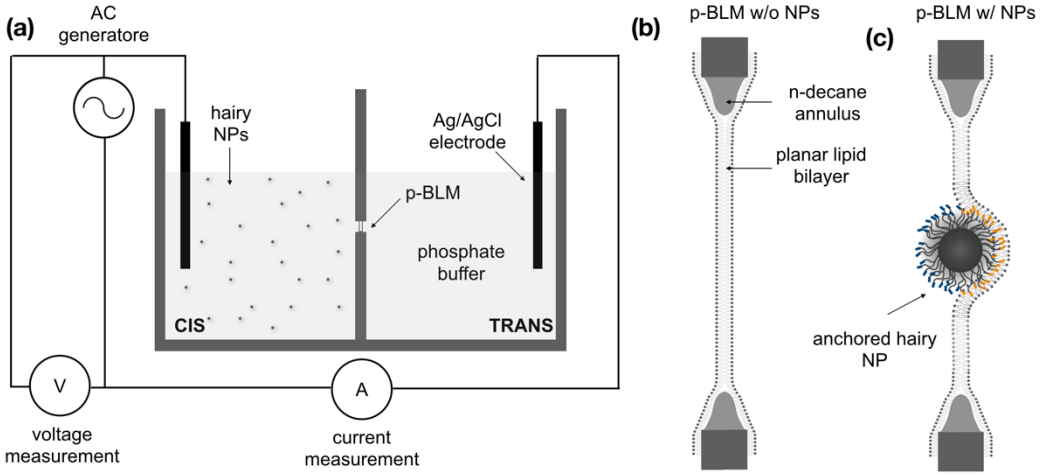


**Figure 6.5**: Electrophysiology of p-BLM. (a) Simplified measurement design with two compartments (*cis* and *trans*) filled with electrolyte solution (phosphate buffer) and connected to an AC power generator via two Ag/AgCl electrodes. The two compartments are separated by a small hole with circular shape and with a diameter of 150 μm. The p-BLM in painted on the that hole and afterwards current and voltage are monitored to calculate the membrane complex impedance overtime. To probe NP-membrane interactions, nanoparticles are added in the cis compartment and the complex impedance is monitored overtime. Nanoparticle that anchor at the lipid bilayer are responsible of decreasing the imaginary component of the complex impedance (capacitive reactance). Illustrations (not drawn to scale) of unsupported lipid membranes (p-BLMs) in (b) pristine condition and (c) with an anchored nanoparticle.

The p-BLM is formed by painting the immersed hole with additional 0.5 μl of membrane-forming solution with a long gel-loading pipet. Its formation could be detected electrically by the change in the measured ionic current and, consequently, by the change in complex impedance. In terms of impedance, once the membrane is formed, the mainly-resistive system becomes mainly-capacitive because of membrane formation. The formation of a p-BLM could be identified and distinguished from an amorphous lipid film by looking at the capacitance values. Only p-BLMs with a capacitance (calculated from *Xm*) lying between 50 and 70 pF were accepted for the actual measurements. The quality of the formed membranes was also evaluated optically by means a 2000x digital camera. Good quality p-BLMs showed a dark central spot (the actual lipid bilayer) surrounded by a solvent annulus with toroidal shape. After the membrane formation, the power supply was turned-off for 10 minutes, allowing the n-decane to evaporate. Then, after a further optical inspection, the impedance of the p-BLM started being measured overtime with averaged acquisition each 10 period for a total acquisition time of 10 minutes. Depending on their quality, membrane may evolve, more or less rapidly, overtime. This innate evolution primarily affects the imaginary component of the complex impedance. In this study, if the imaginary

component *Xm* of the complex impedance varied overtime less than 0.5 % $min^{-1}$, the membrane was used for the actual experiment, and discarded otherwise. This criterion is fundamental to achieve good signal to noise ratio, otherwise we might encounter misleading the interpretation of the electrical properties of the membrane after nanoparticles additions. In all experiments, the complex impedance was measured at room temperature. After about 3 minutes, few μl of nanoparticle were added to the *cis* chamber, whereas an equivalent volume of buffer solution was added to the trans chamber to compensate the volume additions. The nanoparticle addition was so that an average concentration of 230 pM was reached in the *cis* chamber (concentration calculated assuming a nanoparticle radius equal to the average one). Note that during just before the NP addition, the measurement was paused in order to freely open the Faraday cage and close it afterwards. The whole NP addition step required about 10-15 seconds. The electrical measurement was carried out for 7 minutes in total. No reliable information could be obtained from longer measurement time because of membrane instability developed overtime. Control tests were performed by using only buffer additions in both chambers (same volume as for nanoparticle experiments) to check the presence of artefacts from the volume addition. After each experiment the cell was thoughtfully washed with a dilute solution of sodium hydroxide, ultrapure water and ethanol in the reported order. Then, it was let dry completely in an oven at 50 °C. When not in use the Ag/AgCl electrodes were stored in dilute sodium hypochlorite solution and thoughtfully washed with ultrapure water before their use.

## 6.5 Results and discussion

### 6.5.1 Synthetic strategies and surface morphologies

#### General synthetic protocol

The synthetic strategy adopted in this chapter, as it will be shown, is partially an extension of the *photografting-from* approach developed in Chapter 5. This new protocol consists of three main steps. (**Step 1**): A *photografting-from* process involving the copolymerization of 2-(dimethylamino) ethyl methacrylate (DMAEMA) and propargyl acrylate (PA) from photoactive silica nanoparticles (functionalized with $TMESI^2$-BAPO); this step leads to the formation of a product called yne(+HNPs). (**Step 2**): A toposelective post-polymerization modification of poly(DMAEMA-*ran*-PA) hairy surface with thiol-terminated poly(ethylene glycol) chains (PEG-T) via thiol-yne (and -ene) click reactions performed with the yne(+HNPs) immobilized on negatively charged microscaffolds; this step leads to the formation of a product called yne/hydro(+HNPs). (**Step 3**): Final post-polymerization modification of available 'clickable' domains of yne/hydro(+HNPs) via thiol-yne (and -ene) by using 1-hexadecanethiol (HD-T); this step leads to the formation of a product called

amphiphilic lipo/hydro(+HNPs) with Janus-like surface heterogeneity. The products resulting from the three mentioned steps are reported in Figure 6.2 and 6.4.

## Synthesis and characterization of yne(+HNPs)

To begin with, silica nanoparticles were synthetized by following a Stöber method, like that adopted in Chapter 5, adjusted to slightly decrease nanoparticle size. After having modified the surface of nanoparticles with TMESI²-BAPO, the NP size was evaluated by conventional TEM. From the analysis, an average diameter of 38.9 nm was found with a standard deviation of 5 nm. Upon light-exposure, two phosphoryl radicals are generated for each initiator site which can initiate the polymerization of the available monomer. For this study, surface-anchored copolymers were photogenerated containing both tertiary amines (from DMAEMA) to introduce the pH-adjustable positive charge upon amine protonation, and acetylene groups (from the PA) to introduce 'clickable' moieties. We selected DMAEMA as pH-responsive monomer because of the large availability of studies in biological environment and because its polymer has a pKa which lies in a pH range interesting for biological environment. [265, 270-271] On the other hand, propargyl acrylate was selected because it allows to introduce 'clickable' functionalities into polymers via copolymerization strategies. [272] However, in most of the cases it is necessary to protect and then deprotect the acetylene of propargyl acrylate with an alkylsilyl, before and after the polymerization, respectively. [273-274] This is needed in order to avoid the formation of gelled (i.e. cross-linked) systems, which would result in large agglomerates when dealing with nanoparticle grafting.

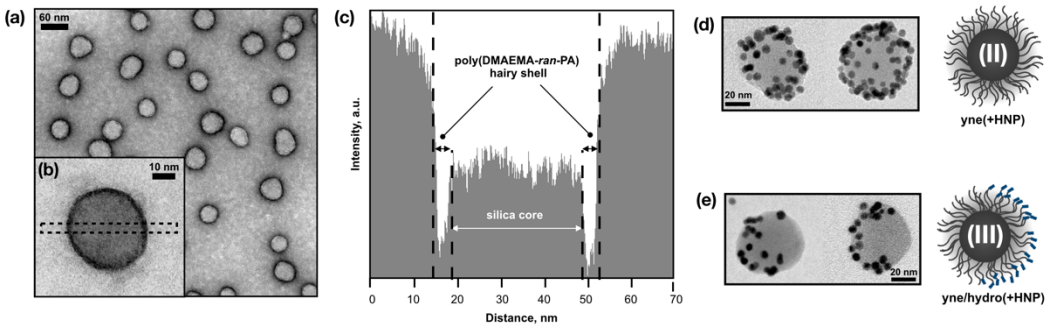


**Figure 6.6**: (a) TEM micrograph of yne(+HNPs) after positive stain with PTA along with (b) a magnification of single stained nanoparticle. (c)Example of intensity profile of a positive stained yne(+HNPs) to estimate the silica core size and poly(DMAEMA-*ran*-PA) polymer shell thickness. (d) yne(+HNPs) and (e) yne/hydro(+HNPs) after incubation with gold nanoparticles to highlight the toposelective modification with PEG-T.

Nevertheless, by light-initiating the polymerization with phosphoryl radicals, PA can be copolymerized with other monomers without the use of any protection for

the acetylene groups. In doing so, previous studies demonstrated that most of the acetylene groups are maintained and only a small degree of branching may be observed. [275] The reasons for that can be found in the relative reactivity of phosphoryl radicals toward various π-bonds, such as triple bond (acetylene) and the double bound (acrylic) of PA and double bound (methacrylic) of the copolymerizing monomer. Electron paramagnetic resonance studies, on phosphoryl radicals, have shown that the quenching rate constants toward triple bond of the acetylene is significantly lower (more than an order of magnitude) than toward the acrylic double bond of PA [275] or to a methacrylic double bond. [276] In this study, the surface-anchored phosphoryl radicals lead to the formation of brushes with pH-responsive and clickable character. The thickness of such polymer corona on the NP surface was evaluated via TEM after positive stain with PTA (Figure 6.6a-b). A thickness of 4.3 ± 0.7 nm, in dry state, was measured by analyzing the transmitted electron intensity profiles (Figure 6.6c) of several hundreds of nanoparticles.

**Table 7.** Summary of weight loss percentage from thermogravimetric analysis for the final Janus-like amphiphilic nanoparticles lipo/hydro(+HNPs) and any other intermediate particle system.

| | Weight loss % | | | | |
|---|---|---|---|---|---|
| **Particle system** | **Total** | **Polymer** | **P(DMAEMA-r-PA)** | **PEG-T** | **HD-T** |
| Photoactive NPs (I) | 12.5 | n/a | n/a | n/a | n/a |
| Homogeneous yne(+HNPs) (II) | 43.0 | 30.5 | 30.5 | n/a | n/a |
| Hydrophilic yne/hydro(+HNPs) (III) | 49.2 | 36.7 | 30.5 | 6.2 | n/a |
| Amphiphilic lipo/hydro(+HNPs) (IV) | 53.4 | 40.9 | 30.5 | 6.2 | 4.2 |

The thermal stability of the yne(+HNPs) was evaluated by TGA. Within the evaluation window in inert conditions (100 - 600 °C), we observe a two-step decomposition profile as reported Figure 6.7a-b. Although, no literature is available on the thermal behavior of poly(DMAEMA-*ran*-PA) copolymers, the multi-step decomposition profile seems to be a common feature of copolymer containing DMAEMA blocks. [277] Additionally, TGA allowed us to estimate the polymer grafting yield by looking at the total mass loss in comparison with the loss of TMESI²-BAPO functionalized nanoparticles. The total mass loss was estimated after switching the atmosphere from helium to oxygen at 600 °C. This was done because of the tendency of DMAEMA-base copolymers to form solid carbonization products which can be removed by using an oxidizing atmosphere (e.g. containing oxygen). We found that the grafted polymer accounts for the

30.5% of the total nanoparticle weight. Additionally, by considering the nanoparticles size, we calculated an average polymer per unit area of 13.5 ± 2.5 mg $m^{-2}$.

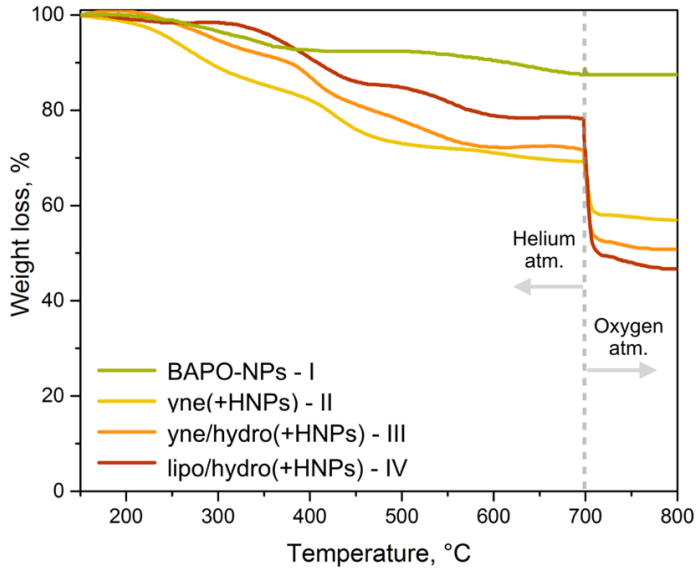


**Figure 6.7**: Thermogravimetric analysis curves for each particle system: photoactive nanoparticles (I), hairy nanoparticles after the first *photografting-from* process yne(+HNPs) (II), intermediate hairy nanoparticles yne/hydro(+HNPs) (III) after the first thiol-yne modification with PEG-T, and final amphiphilic lipo/hydro(+HNPs) (IV) after the second thiol-yne modification with HD-T.

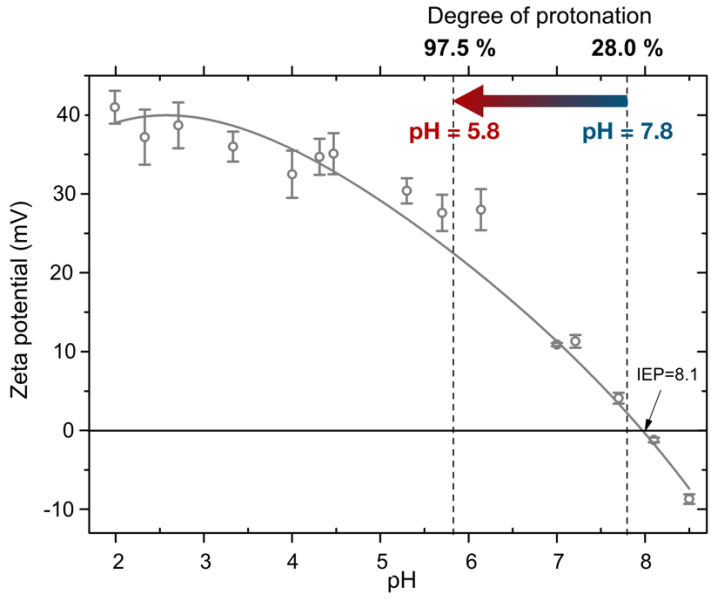


**Figure 6.8**: Zeta potential values at different pH values and the corresponding polynomial fit for polymer grafted yne(+HNPs). The dotted lined highlight the pH range of interest for the interactions with lipid membranes.

For the yne(+HNPs) particle system, and consequently the respective derivatives (e.g. yne/hydro(+HNPs) and lipo/hydro(+HNPs)), it is possible to adjust the

surface positive charge by acting on the degree of protonation via pH changes. Indeed, DMAEMA blocks, with a pKa of about 7.4, increase their degree of protonation when the pH is lowered. Considering the Henderson-Hasselbalch equation, it is possible to evaluate the degree of protonation at a given pH value (i.e. equal to $1 / (1 + 10^{pH-pKa})$). Therefore, ranging the pH from 2 to 9 means ranging the degree of protonation from > 99% to < 0.1 %. This pH responsiveness was indirectly evaluated by measuring the zeta potential of the yne(+HNPs) particle system from a pH of 2 to a pH of 9. The results are reported in Figure 6.8. Interestingly, a pH-dependent zeta potential profile was observed. As expected, most of the changes in surface potential occur for pH values close to the pKa of the polymer. In Figure 6.8, the pH range of interest for the investigations with lipid membranes is highlighted.

From a chemical viewpoint, the photografting of poly(DMAEMA-*ran*-PA) from the photoactivated nanoparticles was evaluated by comparing the FTIR spectrum of yne(+HNPs) with that of the native nanoparticles before any surface-modification. The native NPs (Figure 6.9a-b) showed a broad and intense peak located at 3420 $cm^{-1}$ which correspond to the OH stretching vibration of the silica surface. A typical feature of the silica can be found looking at the shoulder at low wavenumbers corresponding to the shoulder of an intense peak located at 1090 $cm^{-1}$ and corresponding to the Si-O-Si stretching vibration of the silica network. These vibrations are characterized by a very intense peak which can be an issue when trying to identify organic molecules on inorganic silica cores. That is why the spectrum has been recorded up to 1400 $cm^{-1}$. Smaller peaks can be identified at 2290 $cm^{-1}$ corresponding to $CH_3$ typical of partially non-hydrolyzed TEOS molecules and at 1630 $cm^{-1}$ from H-O-H bending vibration of water molecules. More interestingly, the yne(+HNPs) showed a much richer spectrum due to the presence of the hairy poly(DMAEMA-*ran*-PA) polymer shell, Figure 6.9c. A small peak located at 2950 $cm^{-1}$ indicated the presence of C-H stretching from $CH_2$, largely present in the of the poly(DMAEMA-*ran*-PA) shell. This is furtherly confirmed by another peak located at 1470 $cm^{-1}$ and due to C-H bending from $CH_2$. A clear confirmation of the presence of PA blocks in the copolymer structure is indicated by the small peak located at 2125 $cm^{-1}$ (better visible in the magnification in Figure 6.9d). This peak of the alkyne is due to acetylene-hydrogen stretching C≡C-H and clearly shows the presence of 'clickable' functionalities in the system. [275] Moving toward smaller wavenumbers, two sharp peaks located at 1730 and 1660 $cm^{-1}$ can be identified. These are ascribed to C=O stretching vibration and to C=C alkenyl stretching, respectively. The C=O stretching vibration is typical of polymers originating from acrylic and methacrylic monomers, whereas the C=C alkenyl stretching is likely indicating the presence of some degree of branching due to the acetylene functionalities of PA (as described above).

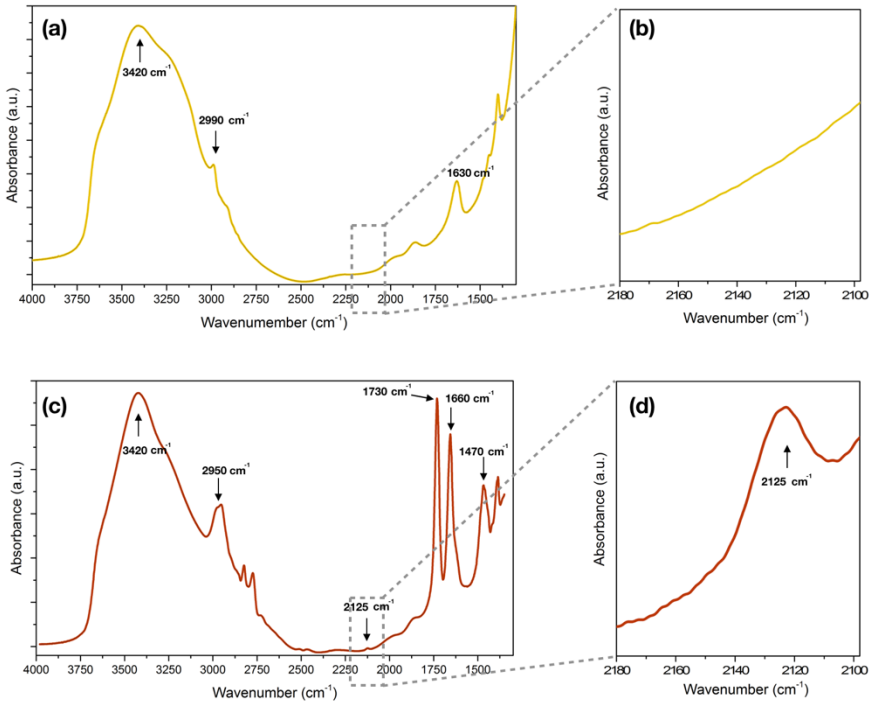


**Figure 6.9**: FTIR spectra of native nanoparticle and (a) and polymer grafted yne(+HNPs) (b). The presence/absence of clickable functionalities is highlighted by the magnification between 2100 and 2180 $cm^{-1}$ in (b) for native nanoparticles and (d) for yne(+HNPs).

## Synthesis and characterization of amphiphilic lipo/hydro(+HNPs)

The so-synthetized yne(+HNPs) were used as starting material to fabricate the final amphiphilic Janus lipo/hydro(+HNPs) passing by the formation of an intermediate yne/hydro(+HNPs). The toposelective post-polymerization modification exploited the synergic combination of yne(+HNPs) immobilization on microscaffold and thiol-yne(ene) light-induced click reactions. Herein, we refer to yne(ene) to consider the presence of both acetylenic (from propargyl acrylate) and ethylenic (from partial branching of propargyl acrylate) functionalities. To begin with, yne(+HNPs) were immobilized on the surface of silica microscaffolds in water at a pH of 5.5. Under this condition, the zeta potential was evaluated via electrophoretic experiments. A positive zeta potential of + 30.4 ± 1.6 mV was found for yne(+HNPs), whereas the OH-SMSs showed a negative potential of– 31.4 ± 0.25 mV. These values are translated in electrostatic interactions which lead to the formation of assemble structures. Under this condition, light-induced thiol-yne(ene) reactions are carried out in the presence of PEG-T and the assembled structures. This modification step allows the formation of the intermediate yne/hydro(+HNPs) which can be detached from the microscaffolds by lowering the pH. These detachment condition were optimized by performing zeta potential measurements at different pH. Eventually, it was observed that, by lowering the pH to 2, the zeta potential for

the hairy nanoparticles remains still high and positive (+ 41.0 ± 2.1 mV) whereas for OH-SMSs it changed dramatically (+ 2 ± 0.5 mV). These conditions, along with the addition of KCl to help screening the charge allowed to detach and collect the yne/hydro(+HNPs). After purification, the available clickable domain of yne/hydro(+HNPs) was modified light-induced thiol-yne(ene) reactions with HD-T chains to impart Janus-like amphiphilic character to the system. The toposelectivity of the first post-polymerization modification reaction with PEG-T was evaluated by comparing yne/hydro(+HNPs) with yne(+HNPs). To do so, the hairy nanoparticles were incubated with gold nanoparticles and the resulting morphology was evaluated via conventional TEM by looking at the Au NPs bound with the poly(DMAEMA-*ran*-PA) hairy shell because of the amino groups. As reported in Figure 6.6d, gold nanoparticles bind uniformly on the surface of yne(+HNPs). On the other hand, because of the presence of PEG chains, gold nanoparticles bind only the unmodified domain of yne/hydro(+HNPs) as reported in Figure 6.6e. This clearly support the toposelective nature of the first modification step. The yields of the post-polymerization reactions can be calculated from the total weight loss of TGA for yne/hydro(+HNPs) and lipo/hydro(+HNPs) in comparison with that of yne(+HNPs). It is possible to ascribe the 6.2 % of the total particle weight, for yne/hydro(+HNPs), to the introduced PEG-T. Similarly, for lipo/hydro(+HNPs) 4.2 % of the total nanoparticle weight could be ascribed to the introduced HD-T chains.

### 6.5.2 Particles – lipid membrane interactions

To understand the physiochemical mechanisms underlying nanoparticle – cell interactions attention should be paid to the nanoparticles size. [141] In very simplistic terms, we can distinguish two cases: (i) nanoparticle size comparable to the lipid bilayer thickness (i.e. smaller than 5-10 nm), (ii) nanoparticle size higher than the lipid bilayer thickness (i.e. bigger than 5-10 nm). This last case fits the systems under investigation in this study. For these sizes, although nanoparticles cannot insert exactly within the lipid bilayer, other interaction pathways are possible. The key factor in these cases is the occurrence of adhesion forces between the nanoparticle and the lipid bilayer once the nanoparticle (due to its Brownian motion) encounter the bilayer. [142] These adhesion forces can originate either from specific interactions (via cell surface receptors) or nonspecific interactions (like in this case). The presence of adhesion forces can cause membrane to wrap around the nanoparticle. This process necessitates to curve the lipid membrane and therefore it requires the membrane bending from its intrinsic spontaneous curvature. The energy required for the membrane bending and stretching must be paid with the adhesion energy resulting from the nanoparticle – membrane interactions. [279-279] From this consideration, a very small particle would require a very high energy for the membrane bending and stretching,

whereas this energy requirement would be lower for higher nanoparticles sizes. Focusing on nanoparticle sizes for which the membrane bending is energetically possible, three different scenarios can occur: (i) non-interacting, (ii) interacting with partial wrapping (i.e. NP is anchored at the cell membrane), (iii) interacting with complete wrapping (i.e. endocytosis pathway, which leads to NP uptake from the cell). The first scenario may occur when adhesion forces with lipid membrane are absent. On the other hand, the discriminant factor between a partial and a total membrane wrapping (i.e. membrane anchoring or uptake) is the energy balance between membrane bending rigidity and nonspecific adhesion strength. [280] Although these considerations are valid for nanoparticles with homogeneous surface properties, different settings occur for nanoparticles with Janus-like surface heterogeneity. As a matter of fact, it has been demonstrated that nanoparticles with Janus-like surface heterogeneity, characterized by adhesive and non-adhesive distinct domains, are always partially engulfed (i.e. partially wrapped) by cell membranes. Indeed, regardless the specific membrane bending rigidity and adhesion strength, after the partial wrapping of the adhesive domain there is no energetic gain in wrapping the non-adhesive domain to compensate membrane bending and stretching. [140] This last scenario is what is expected to observe for our amphiphilic lipo/hydro(+HNPs) Janus-like system.

## Indirectly probing interaction with planar lipid membranes

The interactions of nanoparticles with membranes were evaluated at different pH values (within a range of interest for biological system, 5.8 - 7.8) by using electrophysiology measurements on unsupported planer lipid membranes used as a model. After nanoparticle addition in the *cis* compartment (final concentration of 230 pM) of the electrophysiology system reported in Figure 6.5, the interactions were evaluated by looking at the measured complex membrane impedance $Zm^* = Rm + i\,Xm$. The two components of the measured complex membrane impedance represent the resistance of the membrane ($Rm$) and its reactance ($Xm$, negative because capacitive). The effect on the membrane capacitive reactance are calculated in terms of ratio between $Xm^{NPs}$ (i.e. after NPs addition) and $Xm^0$ (i.e. before NPs addition). Electrophysiology experiments were conducted Janus-like amphiphilic lipo/hydro(+HNPs) (expected to have an adhesive and a non-adhesive domain) in comparison with the hydrophilic homogeneous hydro/hydro(+HNPs) (expected to have a homogeneously non-adhesive surface, because of the PEGylation). A summary of the effect of nanoparticle addition for the homogeneous hydro/hydro(+HNPs) is reported in Figure 6.10a. Interestingly, as expected, no interactions were detected for the homogeneous hydrophilic hydro/hydro(+HNPs). For all the investigated pH, the addition of hydro/hydro(+HNPs) to the system did not cause any effect on both $Xm$ and $Rm$.

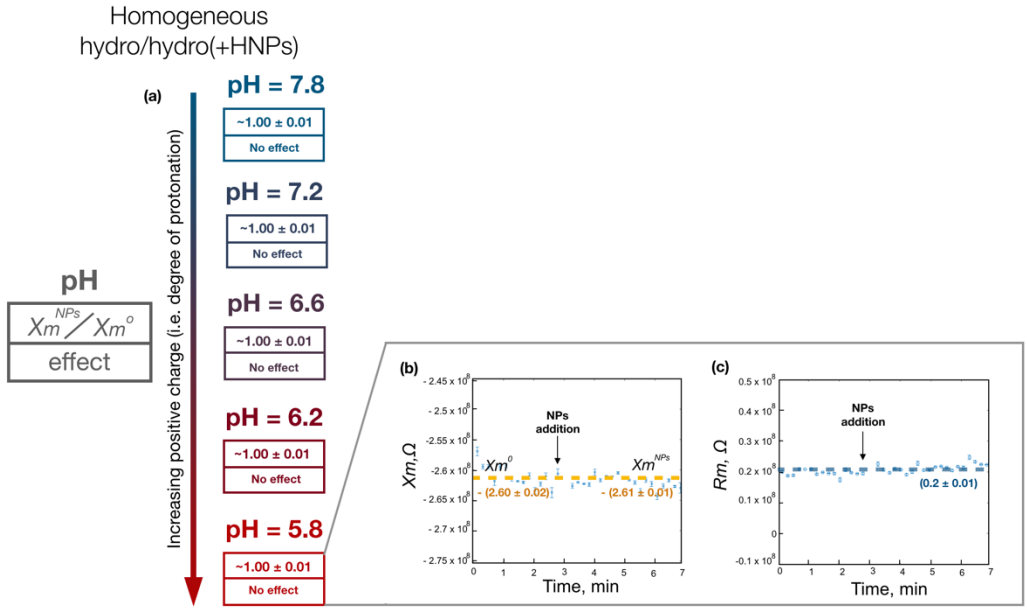


**Figure 6.10**: (a) Schematic summary of the effect of nanoparticles addition on capacitive reactance *Xm* (imaginary part of *Zm**) from electrophysiology measurements on p-BLM for hydrophilic homogeneous hydro/hydro(+HNPs). Effects on *Xm* reported in terms of ratio between $Xm^{NPs}$ (after nanoparticles addition) and $Xm^{0}$ (before nanoparticles addition). Representative examples of the encountered behaviours are reported for a pH=5.8 (b-c). The electrical answer was the same within the pH range of 5.8-7.8. A final average concentration of 230pM was used in all the experiments.

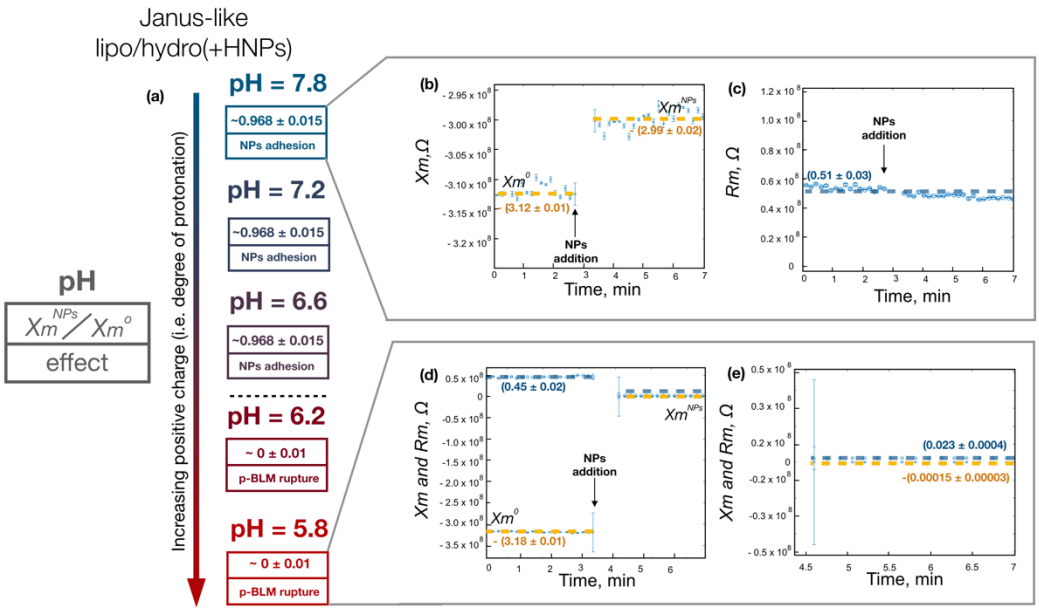


**Figure 6.11**: (a) Schematic summary of the effect of nanoparticles addition on capacitive reactance *Xm* (imaginary part of *Zm**) from electrophysiology measurements on p-BLM for amphiphilic Janus-like lipo/hydro(+HNPs). Effects on *Xm* reported in terms of ratio between $Xm^{NPs}$ (after nanoparticles addition) and $Xm^{0}$ (before nanoparticles addition). Representative examples of the encountered behaviours are reported for a pH=5.8 (b-c) and for 7.8 (d-e). The electrical answer was the same within the pH range of 6.6-7.8 (as for b-c) and 5.8-6.2 (as for d-e). A final average concentration of 230pM was used in all the experiments.

This translates in a $Xm^{NPs}/Xm^0$ ratio of about 1.00 ± 0.01. An example of the impedance measurement on hydro/hydro(+HNPs) at a pH of 5.8 is reported for both imaginary *Xm* (Figure 6.10b) and real *Rm* (Figure 6.10c) components. It is evident that the addition of NPs does not affect the electrical properties of the membrane, since no electrical events are revealed. Therefore, no adhesion of hydro/hydro(+HNPs) on the lipid membrane can be detected. Since the hydro/hydro(+HNPs) did not affected the membrane electrical properties at any of the pH investigated, we concluded that no nanoparticles adhesion occurs for the homogeneous system. Conversely, a pH depended behavior was observed for the amphiphilic lipo/hydro(+HNPs) as schematically summarized in Figure 6.11a. To understand the different behaviors, it is important to note that by decreasing the pH, the positive charge of the DMAEMA blocks increases as a consequence of amine protonation. [281] From 7.8 up to 6.6 as pH values, we clearly detected electrical events upon nanoparticle addition in terms of variation of membrane capacitive reactance, which leads to a decrease of *Xm* and consequently to an increase of the membrane capacity *(Cm = (- 1) / (2π f Xm))*. After several measurements to confirm the reproducibility of the results, an average $Xm^{NPs}/Xm^0$ ratio of 0.968 ± 0.015 was calculated. We found that the *Xm* variation, after nanoparticle addition, does not depend either on the specific pH value (within the 6.6-7.8 range) or the initial membrane electrical properties (i.e. $Xm^0$ and $Rm^0$). An example of electrophysiology measurement at a pH = 7.8, reporting *Xm* and *Rm* overtime before and after addition of the amphiphilic lipo/hydro(+HNPs), is reported in Figure 6.11b-c. In this specific case, the average value of *Xm* decreased of about 3.9 % after lipo/hydro(+HNPs) addition, whereas the membrane resistance *Rm* remained practically unchanged overtime. These findings are in good agreement with to previous electrophysiology studies probing nanoparticle – membrane interactions. [269] Interestingly, for lower pH values (below 6.2), the addition of lipo/hydro(+HNPs) caused the almost immediate membrane rupture. In these cases, the $Xm^{NPs}/Xm^0$ ratio was $(0.45 \pm 3)\ 10^{-4}$ and therefore very close to zero since the membrane reactance decreased of orders of magnitude and not of few percentage. This effect is easily visible in Figures 6.11d-e which report an example of the measure of *Xm* and *Rm* before and after the addition of nanoparticles at a pH of 5.8. The membrane reactance, from its initial value $Xm^0$ decreased of 4 order of magnitude as a consequence of nanoparticle addition. Interestingly, in this case, the membrane resistance *Rm* decreased upon nanoparticle addition. Overall, the membrane complex impedance *Zm** decreased from $(0.45 - i\ 3.18)\ 10^8\ \Omega$ to $(2.3 - i\ 0.015)\ 10^6\ \Omega$, after the nanoparticles addition. This not only indicates a decrease in the system complex impedance, but it also denoted a shift from a mainly capacitive system to a mainly resistive one, as indicated by the different magnitude of variation for the resistive and capacitive components, upon nanoparticles additions. The same findings were observed for all the experiments conducted on lipo/hydro(+HNPs) for pH lower than 6.2. It is

important to note that in these cases the $Xm^{NPs}$ final values do not refer to the capacitive reactance of a lipid membrane since the p-BLM was broken due to nanoparticle addition (the rupture was confirmed by optical inspection of the hole). Therefore, in the case of membrane rupture the $Xm^{NPs}$ values should be interpreted as an equivalent capacitive reactance of the electrophysiology cell. Since we have already observed notable changes in surface charge (in terms of surface potential) close to a pH of 6.2-6.6 (see Figure 6.8), we hypothesized that the membrane rupture is caused by the increasing cationic charge as the pH decreases. Although, the phospholipid membranes used in this study are globally neutral, they expose outward a positively charged surface (i.e. choline). So, when nanoparticles approach the membrane (due to their Brownian motion) if their net charge is too high (at pH<6.2, and zeta>20mV), the overall system (membrane and nanoparticles) cannot find a thermodynamic equilibrium that preserve the membrane integrity. Conversely, if the net charge of nanoparticles is small enough (pH>6.6 and zeta<10mV) the perturbation of the membrane that occurs when particles approach is small enough to allow particle adsorption (or inclusion). The system find a thermodynamic equilibrium that preserve the membrane integrity. Indeed, previous studies showed that short-distance interactions take place in the headgroup region in phosphatidylcholine membranes involving charge associations (i.e. charge pairs). Since these interactions contribute to the stability of the system, it is likely that the introduction of nanoparticle-borne positive charge in the proximity of the headgroup region promote the formation of defects, which in turn may lead to membrane rupture. [282-284]

## Directly visualizing interactions with lipid liposomes

To achieve a deeper understanding of the interaction between lipid membrane and amphiphilic lipo/hydro(+HNPs), we adopted TEM-based analyses by using liposomes as membrane model. Negative stain technique was used to visualize those interactions. Thanks to the higher stability of liposomes in comparison with p-BLM, it was possible to let the NPs interact for longer time with the lipid membranes compared with electrophysiology experiments. A representative example on amphiphilic lipo/hydro(+HNPs) interacting with a liposome are reported in Figures 6.12a-b. In false-color representation, the lipo/hydro(+HNPs) are reported in yellow-to-green color. The nanoparticles clearly interact with lipid bilayer since many of them are anchored on the liposome surface. From the magnification in Figure 6.12b it is evident that the nanoparticles – membrane interactions are driven by adhesion forces as it is demonstrated by the membrane wrapping around each interaction site. The membrane wrapping is schematically illustrated in Figure 6.12c. From the Janus-like surface heterogeneity it is possible to distinguish two distinct domains: a non-adhesive hydrophilic domain due to the hydrophilic PEG-T chains (particle

domain I), and an adhesive domain via insertion of hydrophobic HD-T chains in hydrophobic tails compartment of the membrane (particle domain II). Similarly, it is possible to discriminate two different regimes for the membrane: unaffected membrane region characterized by its natural curvature (membrane region I), and bended membrane region because of the adhesive forces (membrane region II).

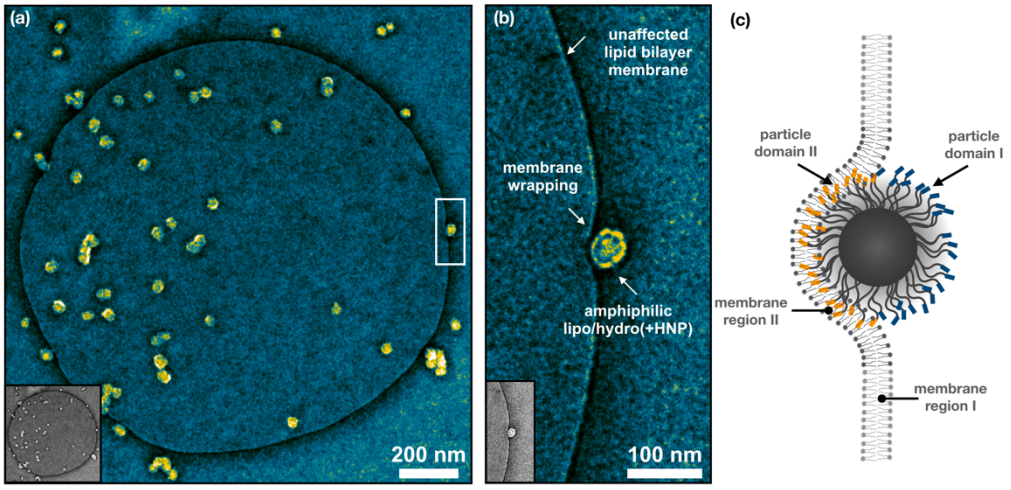


**Figure 6.12**: (a) Representative image of lipo/hydro(+HNPs) amphiphilic hairy nanoparticle interacting with a liposome after 30 min of incubation (pH = 6.6.) followed by negative stain with Uranyl acetate. (b) Magnification of a single interacting nanoparticle anchored at the lipid membrane. Both (a) and (b) clearly show the membrane wrapping due to the hydrophobic and adhesive domain of the lipo/hydro(+HNPs). The images are reported in false-color to help the eyes in distinguishing liposomes and nanoparticles, an inset reporting the original image in grey-scale is included for each micrograph in bottom-left corner. (c) Schematic illustration of lipo/hydro(+HNPs) – membrane wrapping: (particle domain I) non-adhesive hydrophilic domain; (particle domain II) nonspecific adhesive domain via insertion of hydrophobic HD-T chains in hydrophobic tails compartment of the membrane; (membrane region I) unaffected membrane region; (membrane region II) bended membrane region because of the adhesive forces.

The electrophysiology experiments on lipo/hydro(+HNPs) showed that the adhesion of nanoparticles below 6.2 of pH value causes the rupture of the lipid bilayer. With the aim of directly visualizing the NPs-membrane interactions and the membrane rupture we employed *in situ* LP-TEM experiments. In these experiments the liposome suspension is embedded in a microfluidic cell and visualized through two silicon nitride windows by using a transmission electron microscope. The liposome suspension contained lipid vesicles ranging from 100 nm to few μm. For small liposomes, although adhesion occurs, it might be not directly visible in terms of wrapping. Indeed, in this case, membrane wrapping in the points of adhesion may be limited by the initial membrane curvature for a given nanoparticle size. [278] Thus, ideally speaking, liposomes of larger size are a better model (for our nanoparticle size) to easily visualize the phenomena. In Chapter 5, the typical bulging effect that occurs inside such microfluidic systems - because of the pressure difference - was already mentioned as a limiting factor of

this technique. So, although large liposomes would be a better model for our system, we are limited in investigating smaller liposomes next to the windows edges, where the bulging is limited. Indeed, in the cell centre cell (i.e. where larger liposomes distribute) the liquid thickness is too high to visualize low contrast material. Considering all these experimental constrains, in a typical experiment we focused our attention to liposomes close to the window-edges (phase I). Once the liposome was identified, the nanoparticles were introduced by using an external flux of colloid. The flux was stopped when the nanoparticles reached the field of view. At this point the interactions were visualized (phase II). As a consequence of the beam (still using low electron dose rate), the pH of the liquid environment decreased and the NP-membrane interaction at low pH were investigated (phase III). In Figure 6.13a, representative frames of each mentioned phase are reported in false-colour representation to guide the eyes. These frames were selected from a video recording of the camera image view with a frame each 0.4 second (Figure 6.13b). In the frame of the phase I, a liposome with diameter of 126 nm is clearly visible in red colour in the proximity of the window-edge. This moment is defined as the $t_0$ and it corresponds to a state in which the NPs were still not introduced. In the frame of phase II, the nanoparticles reach the liposome and anchor to the bilayer. This moment corresponds to the time $t_i$ from which the evolution of the membrane – because of the interactions with the NPs - started being monitored. It is important to note that this time does not correspond exactly to the instant at which the NPs reached the liposome. Indeed, there is an experimental delay of few seconds due to the focus adjustments needed to correctly visualize the nanoparticle. From the phase III frame of Figure 6.13a, it is directly visible the effect of the acidification of liquid environment. As a matter of fact, within seconds the liposome membrane start being altered near the anchored nanoparticles. The induced defects grow, till the lipid membrane is completely damaged. The membrane rupture is coupled with a translocation of the nanoparticles toward the interior of the vesicle structure. Interestingly, the regions of the membrane clear from anchored nanoparticles seems to remain unaffected by the acidification of the liquid.

## 6.6 Conclusions

In this chapter, we demonstrated that from surface-immobilized Norrish type I photoinitiator molecules (TMESI²-BAPO) it is possible to photochemically generate soft hairy coronas with pH-responsive and clickable functionalities. This is done on the surface of nanometric silica via *photografting-from* approach, leading to the formation of yne(+HNPs). From the hairy nanoparticles, we showed how to generate amphiphilic nanoparticles with Janus-like surface heterogeneity via click reactions. Specifically, thiol-yne reactions promoted by light-irradiation were employed to covalently immobilize hydrophilic or lipophilic thiol-terminated chains. By masking the yne(+HNPs) with micrometric scaffolds

via reversible electrostatic immobilization, it was possible to toposelectively carry out thiol-yne reactions to partially modify the hairy corona with thiol-terminated poly(ethylene glycol) (PEG-T) chains leading to the formation of the Janus intermediate yne/hydro(+HNPs). Another step of thiol-yne reactions was then carried out on the yne/hydro(+HNPs) by employing hexadecanethiol (HD-T) chains. This last post-polymerization modification led to the synthesis of the final amphiphilic hairy nanoparticles lipo/hydro(+HNPs) characterized by a Janus-like surface heterogeneity.

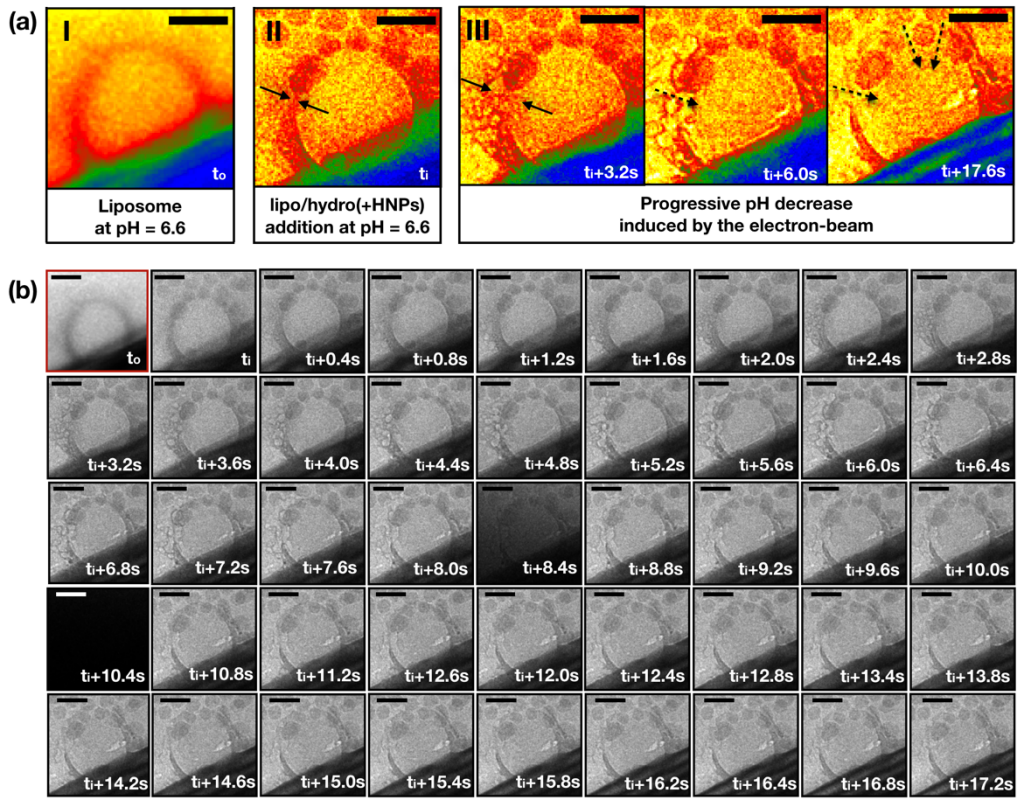


**Figure 6.13**: *In situ* LP-TEM direct visualization of the interactions between lipid membrane and lipo/hydro(+HNPs) using liposomes as model. Liquid environment with an initial pH of 6.6. (a) Selected frames reported in false-color representation and representing the different experiment phases: (Phase I) initial configuration of a liposome before nanoparticles addition, (Phase II) nanoparticles arrive and anchored at the lipid membrane of the liposome. (Phase III) progressive evolution of the liposome because of pH decrease with anchored nanoparticles on the membrane. (b) complete sequence of collected frames. Note that the temporary darkening of field of view (e.g. $t_i$+8.4s and $t_i$+10.4s) was caused by formed bobbles in liquid because of beam irradiation.

The synthetic protocol was thoughtfully characterized from different viewpoints. The presence of clickable functionalities was confirmed from infrared spectroscopy and grafting yields of each modification step was calculated from thermogravimetric analyses coupled with differ stain technique to estimate the thickness of the hairy corona and the toposelectivity of the modification reactions.

The interactions between the synthetized system and cell membrane at different pH values were also investigated. Lipid bilayer were adopted as membrane model in a comparative study between the hydrophilic homogeneous hydro/hydro(+HNPs) and the amphiphilic Janus lipo/hydro(+HNPs). From electrophysiology measurements on unsupported planar lipid membrane, it has been possible to conclude that the presence of a lipophilic domain is required to observe interaction between NPs and lipid bilayers. Indeed, for pH-responsive hairy nanoparticles with homogeneous hydrophilic surface hydro/hydro(+HNPs) no electrical events were detected at any of the pH values investigated, meaning that the values of membrane impedance remain unchanged upon nanoparticle addition. Conversely, the amphiphilic Janus lipo/hydro(+HNPs) showed the ability to anchor at the lipid membrane with a pH-dependant conservative or destructive effect on the membrane stability. More specifically, above a pH of 6.6 (zeta < 10mV), the lipo/hydro(+HNPs) led to an increase of membrane capacitance which was related to adsorption phenomena of the nanoparticles on the lipid membrane. On the other hand, below a pH of 6.2 (zeta > 20mV), the lipo/hydro(+HNPs) system led to the membrane rupture. In confirmation of the electrophysiology findings, we directly visualize the conservative nanoparticles adsorption by using liposomes as membrane model. The nonspecific adhesion forces were indirectly observed in terms of membrane wrapping around the adhesive domains of the lipo/hydro(+HNPs). We hypothesized that for pH lower than 6.2, the interactions are destructive because of the increasing cationic charge due to the progressive protonation of the tertiary amine of the hairy shell which destabilize the assembly of the lipid bilayer. This hypothesis was confirmed by *in situ* liquid phase TEM experiments, which also allowed to reveal and directly visualize the process dynamic.

The photochemical protocol proposed in this work is the first strategy to generate Janus-like surface heterogeneity exploiting the combination of a *photografting-from* approach and toposelective light-induced click reactions. By doing so, it is possible to fabricate nanometric platforms with a synergic combination of different properties (e.g. responsiveness to pH, Janus-like amphiphilicity) which can be used to study the interaction of nanomaterials with cell membranes. Interestingly, the main ideas behind our findings are of general validity since they rely merely on surface properties. Therefore, the same strategy could be extended to any other nanometric objects to create smart cargo/delivery/imaging platforms for biological applications.

# General conclusions

Throughout this manuscript, novel methods for the generation of Janus-like heterogeneity have been designed by exploiting the spatial and temporal control of light-induced reactions in an entirely photochemical manner. In all the experimental contributions, the Janus character was introduced in terms of Janus-like surface heterogeneity. This enabled the introduction of Janus character, to a given system, without the constrains of thermodynamically driven approaches (e.g. built upon phase segregation or heterogeneous nucleation), and thus paving the way for more complex systems with the possibility of broad material combinations.

In the first experimental contribution, the use of surface-anchored organothiols and UV-light were demonstrated to be a winning combination for the synthesis of Janus-like hybrid particles with polymer brush and metal nanostructured distinct domains. After providing evidences of the organothiols modification (of 500 nm in radius silica particles) via X-ray photoelectron spectroscopy, we showed the feasibility of physical immobilization and partial protection of the so-modified particles by using wax/water Pickering emulsion. As a consequence of the physical immobilization, it was possible to photogenerate - from the organothiols - thiyl radicals only on the exposed particle domains. This, in turn, allowed the toposelectively modification of the particles with polymer bushes via *grafting-from* method initiated from the surface-bound thiyl radicals. The remaining thiolated particle domains were then used as nucleation sites in a nanostructuration step with gold nanoparticle. These gold nanoparticles were generated from metal ions by a Norrish I photoinitiator used as photo-reducing agent. We demonstrated that by changing the ratio between available metal ions and organothiols it is conceivable to generate nanostructure surfaces with gold nanoparticles with different sizes (from 12.7 ± 3.7 nm to 22.5 ± 9.8 nm) and consequently of hybrid Janus-like particles with different optical absorption properties.

In the second experimental contribution, a recently synthetize alkoxy-modified Norrish I photoinitiator (TMESI$^2$-BAPO) was employed to photoactivate the surface of small silica particles (21.3 ± 7.6 nm in radius from TEM). We showed how these photoactive particles can be immobilized in monolayers on micrometric scaffolds via reversible electrostatic interactions. The conditions for particle immobilization and release were investigated by means of zeta potential

measurements at different pH values. The particles immobilization allowed to synthetize hydrophilic Janus intermediates by carrying out the *photografting-from* reactions on photoactive nanoparticles after physical immobilization. The final amphiphilic Janus particles were synthetized performing a second step of *photografting-from* reactions from the intermediate Janus in presence of a hydrophobic monomer. After having characterized the hairy Janus-like nanoparticles in both dry and swollen conditions, the self-assembly conditions were directly visualized in water by means of liquid phase TEM. We observe the association of particles in dimers and more rarely in trimers. These assembly patters were linked to directional hydrophobic interactions between the lipophilic domains of the nanoparticles. The findings were confirmed by means of different techniques such as cryogenic TEM and dynamic light scattering. Small angle X-ray scattering (SAXS) was also adopted to obtain more statistically relevant data. In this regard, SAXS measurements allowed to identify the dimerization process (self-assembly in dimers) for the amphiphilic Janus hairy nanoparticles in terms of average molecular weight in comparison with that of hydrophilic uniform hairy nanoparticles, used as reference. The same technique made possible a better understanding of the interaction patterns in matter of second virial coefficients.
In the last experimental contribution, the mentioned alkoxy-modified Norrish I photoinitiator (TMESI[2]-BAPO) was employed to photoactivate the surface of small silica particles (19.9 ± 2.5 nm in radius from TEM). This time, the photoactive particles were uniformly modified by a light-induced surface-initiated copolymerization reaction of two monomers, one bearing a protonable group and the other bearing a clickable group. In a second step, amphiphilic Janus-like nanoparticles were obtained via toposelective thiol-yne click reaction. This was achievable by using modified version of the above-mentioned electrostatic reversible particle immobilization and thanks to the availability of clickable functionalities in the polymer bushes. After having characterized the so-synthetized particle from physical and chemical viewpoints, their interaction with cell membrane, namely lipid bilayers, were explored. Indeed, as a consequence of their chemistry, these Janus-like nanoparticles possess distinct "adhesive" (modified with alkyl chains with a length comparable to that of the hydrophobic tails of phospholipids) and "non-adhesive" (modified with long poly (ethylene glycol) chains) domains with respect of lipid bilayers. Negative stain TEM showed nanoparticles anchoring at the lipid membrane likely due to the "adhesive" lipophilic patches. As a matter of fact, uniform "non-adhesive" particles, used as reference, did not showed any interaction pattern with lipid bilayer structures. Planar lipid membrane electrophysiology analyses allowed to investigate such interactions at different pH values, ranging from 5.8 to 7.8, and therefore to question the effect of the nanoparticle-borne cationic charge on the membrane stability. We observed that if their net charge is too high (at pH<6.2, and zeta>20mV), the nanoparticles leads to the membrane rupture. Conversely, if the net charge of nanoparticles is small enough (pH>6.6 and zeta<10mV), the

nanoparticles can anchor at the lipid membranes preserving their stability. In confirmation of these findings, the charge-induced membrane rupture was also directly observed in dynamic conditions by means of in situ liquid phase transmission electron microscopy.

Throughout this manuscript, we demonstrated how and to what extend photochemical methods can be used to impart Janus character to particles ranging from the micro to the nanoscale. This was done at a surface level via surface modification techniques (such as, in situ generation of metal nanoparticles, polymer brush via *grafting-from* techniques and click chemistry) and therefore, proposing versatile approaches of general validity. Along with the design of new synthetic light-driven protocols, we demonstrated how, from the newly introduced Janus-like character, unique properties originate which are impossible to achieve otherwise with non-compartmentalized surface properties (e.g. uniform or mixed).

# Appendices

## A.1 List of figure

### Chapter 1

**Figure 1.1**: (a) rightward bent of the wrybill plover (*Anarhynchus frontalis*) beak; (b) example of asymmetric tree growth; (c) asymmetric carbon generating chiral molecules, dextrorotatory for the top and laevorotatory for the bottom; (d) example of asymmetric particle with amphiphilic properties showing, so called, Janus character.

**Figure 1.2**: Janus morphologies and architectures for two materials/properties (in orange and light grey): spherical (a), capsules or vesicles (b), and ellipsoidal (c) geometries. (d-f) Various kinds of dumbbell-shaped Janus particles with symmetric appearance (d), attached nodes (e) or snowman character (f). Disk shaped (g) and cylindrical (h) Janus particles. Janus character from core-compartmentalization (i) and from surface-compartmentalization (l).

**Figure 1.3**: Number of articles published in peer-reviewed journals each year in the field of "Janus Particles" from 1991 to 2017. The data were obtained from the citation indexing service Web of Science®.

### Chapter 2

**Figure 2.1**: Common synthetic routes for the synthesis inorganic Janus heterostructures composed of a combination of two materials (indicated as $M_1$ and $M_2$) via (a) heterogeneous nucleation, (b) synthesis at liquid-liquid interface, (c) decomposition of an initial core-shell structure into dumbbell-structure. Example of different material combination such as: (d) metal - metal oxide Au-Fe3O4, (e) metal – semiconductor Au-CdSe, (f) metal oxide – semiconductor Fe2O3-ZnS, (g) semiconductor – semiconductor CdSe-PbSe. Adapted from the references [44-47].

**Figure 2.2**: Phase inversion for the preparation of organic Janus particles made from poly(styrene) and poly(isoprene) with a volume ratio of both sides depends on the polymer feed composition (a). Preparation of nanoparticles via phase-separation of block-copolymers. Evolution of the structures as function of molecular weight and the $D/L_0$ ratio, where D and $L_0$ correspond to the particle diameter and the period of lamellar structure (b). Adapted from the references [53, 54].

**Figure 2.3**: Schematic representation of Janus particles fabrication via particles immobilization by controlled sinking in P(S-r-AA), gold nanoparticles self-assembly and thermal annealing (a). Janus particles fabrication through particle physical entrapment in polymeric fiber mats and toposelective nanoparticles labelling, scale bar is 100 nm(b).[59, 60]

**Figure 2.4**: Organic Janus micelles via stepwise transformation of mixed shell micelles of two diblock-copolymers AB and BC. Chemical transformation scheme (a) and the resulting Janus micelles self-assemble into tubular structures, which, upon sonication, disassembly into half-discs (b). Adapted from reference [72].

**Figure 2.5**: Synthesis of organic Janus particles via crosslinking of the B block-assembly (black) within multi-compartment micelle (MCM) based on ABC triblock-copolymers. (A) Directed self-assembly of ABC triblock-copolymer into clover-shaped MCMs with three B knots. Scheme of crosslinking of the micelles and Janus particles formation after redispersion in a good solvent for block A and C. (B) TEM images of "clover" MCMs structure (top) and organic Janus particles after crosslinking and redispersion (bottom) after stain with $OsO_4$ (scale bars are 200 and 25 nm in inset). Adapted from reference [79].

**Figure 2.6**: Synthesis of organic Janus particles with different architectures prepared via the selective crosslinking of the middle block of polybutadiene of triblock-copolymer (polystyrene-b -polybutadiene-b -poly(methyl methacrylate), SBM) assembled in microphase-segregated bulk structure and subsequent dissolution. On the left: Phase diagram of SBM. On the right: Synthetic protocols to target Janus micelles, Janus cylinders, or Janus discs. Adapted from [82, 84, 88].

**Figure 2.7**: Schematic representation of the preparation of Janus gold (a) and iron oxide nanoparticles (b) with amphiphilic character by ligand-exchange at toluene/water interface. Reproduced and adapted from reference [97].

**Figure 2.8**: Mesoscale simulations of nanoparticles coated with different mixtures of two immiscible ligands. In (a) effect of different ligand structures at a constant sphere radius: (A) Length ratio 4:4, equal bulkiness. (B) Length ratio 6:6 with one ligand (yellow) having a bulkier tail group. (C–E) Length ratios 4:6, 4:7, and 4:13, respectively, with equal bulkiness of the tail. In (b) Effect of surface curvature from high to zero (A–D) for a ligand pair with length ratio of 4:7. In (c-d) schematic illustration of how the presence of shorter ligands allows longer ones to have a larger free volume; and hence, gain conformational entropy. The free volume is indicated as cone structure for the longer ligand. Two sub-cones can be identified: one whose angle is determined by the packing of the molecules and the other due to this interfacial free volume. As the radius of curvature decreases, the first cone becomes the dominant, and make the second one irrelevant which is related to the formation of a Janus-like segregation. Reproduced and adapted from [100, 101].

**Figure 2.9**: Schematic representation of the synthesis of polymer-grafted stimuli-responsive Janus particles by combining *grafting-from* and grafting-to approaches in the following order: (i) modification of silica particles with organo-amine functionalities; (ii) toposelective modification of such functionalities into ATRP-initiator functionalities on the surface of particles immobilized at wax colloidosomes; (iii) *Grafting-from* via ATRP process and grafting-to by using carboxyl-terminated polymers. Reproduced from the reference [105].

**Figure 2.10**: Schematic representation of the synthesis of polymer-grafted magnetic nanoparticles: (a) electrostatic immobilization of aminated nanoparticles onto mica substrates; (b) toposelective modification of amino functionalities to ATRP-initiator groups; (c) partial *grafting-from* of PNIPAm from the nanoparticle exposed surface; (d) nanoparticle release; (e) modification of available amino functionalities to ATRP-initiator groups; (f) *grafting-from* of PMAA. Reproduced from the reference [197].

**Figure 2.11**: Schematic representation of the synthesis of polymer-grafted gold Janus nanoparticles via a combination of *grafting-from* and solid-state grafting-to (a). TEM images of the polymer-grafted nanoparticles (b-d) with asymmetric morphology identified by labelling the grafted PAA domain (grown via *grafting-from*) with platinum nanoparticles (yellow – AuNPs, blue - Pt NPs, red - PEO). Reproduced and adapted from the reference [111].

**Figure 2.12**: Schematic representation of polymer-grafted Janus nanoparticles via grafting from and grafting-to of single chain: (a) grafting-to of single chain of anionic polystyrene onto the surface of chloromethylphenyl-capped nanoparticles by a rapid elimination of Cl from the NP surface with Li anion of the polymer (b); *grafting-from* of PNIPAm on the remaining particle surface (c). Reproduced from the reference [198].

**Figure 2.13**: Mesoscale simulations for the self-assembly of soft amphiphilic Janus particles. (a) structure of the soft Janus particles; (b) Phase diagram of soft Janus particles in the G– β plane. Snapshots of typical equilibrium self-assembled structures (marked by star symbols in the phase diagram) (c-n). Reproduced and adapted from the reference [285].

**Figure 2.14**: Simulation of Self-assembly of amphiphilic particles with uncharged hydrophobic domain on one side and charged hydrophilic domain on the other. Results from Granick group: (a) Region of permitted tilt angles between two charged hemispheres plotted as a function of the concentration of a monovalent salt. (b) Geometric representation of helix growth by face-sharing tetrahedral as the salt concentration increases. (c) Observed reaction pathways and kinetics of cluster formation of amphiphilic Janus particles at low salt concentration. Results from Sciortino *et al.*: Phase diagram in the temperature – density (d) and pressure - temperature (e) planes. Snapshot of an equilibrium typical configuration for a 5000 particles system (f). Typycal shape of particle aggregates as micelles (g) and vesicles (h). Reproduced and adapted from references [16, 127-128].

**Figure 2.15**: Schematic clustering of amphiphilic Janus particles (Janus-like surface) in dependence of the corona size in chloroform and water at pH 10 (a). Here also, PS is gray, PMAA is orange and the sore is black. TEM images of nanoparticle self-assembly at concentration of 0.05, 0.5 and 5 g/L in alkaline water (b) and chloroform (c). Images collected after stain with OsO4. Scale bars are 100 and 50 nm in insets. Reproduced and adapted from reference [79].

**Figure 2.16:** Effect of pH on the cluster/particles size in terms of average hydrodynamic diameter of PAA/PSSNa Janus particles (indicated with JN, with different polymer types as reported in the enclosed table) as compared to uniformly grafted nanoparticles with PAA or PSSNa (a). Monte Carlo simulation based on a hydrophobic surface equal to 14.9% at a pH of 2 (b). Cryo-TEM of Janus nanoparticle (JN3) with 90.8kDa PSSNa molecular weight (c). Reproduced and adapted from reference [110].

**Figure 2.17**: Self-assembly of polymer-grafted PMMA/PEO Janus nanoparticles (Janus-like surface) in acetone-dioxane solvent solution: (a) Schematic representation of the clustering phenomena for Janus (top) and mixed (bottom) morphology. TEM micrographs of polymer-grafted particles with Janus (b–f) and mixed (g) morphology in dioxane after various incubation times. Reproduced and adapted from reference [129].

**Figure 2.18**: Surface activity of Janus nanoparticles: (a) Interfacial tension isotherms (hexane/water interface) for the adsorption of pristine Fe3O4 nanoparticles and DDT-coated Au nanoparticles in comparison to dumbbell Au/$Fe_3O_4$ Janus nanoparticles (Janus-like core), in which the Au-

domain is coated with different thiols, DDT and ODT. (b) Interfacial tension isotherms of deionized water against PS/PMMA Janus particles (Janus-like surface) in toluene solution at different concentrations. (c) Droplet after the interfacial tension reaches quasi-equilibrium and droplets with interfacial area reduction with wrinkling formation at aging time of 6000 sec and 12 hours. Reproduced from references [199, 200].

## Chapter 3

**Figure 3.1**: Electronic states and transitions between them represented as Jablonski diagram for a photoinitiator molecule. Radical formation pathways for type I and II photoinitiators from the excited triplet following a cleavage process and hydrogen abstraction, respectively.

**Figure 3.2**: Photoscission following an α-cleavage of benzyl chromophore derivatives (type I) for different substitution scenario: (a) benzyl ketals, (b) hydroxyalkyl phenyl ketones, (c) dialkoxy acetophenones, (d) mono(acyl)phosphine oxides, (e) bis(acyl)phosphine oxides.

**Figure 3.3**: Generation of polymeric surface via grafting-to approach (a), i.e. reaction between surface-bound group and end-group from preformed polymer chain, and *grafting-from* approach (b), i.e. surface-initiated polymerization from a monomer. The initial stages of the grafting processes are reported in red.

**Figure 3.4**: Representation of scaling laws for different regimes of neutral polymer surfaces. Scenarios at different grafting densities are reported in terms of distance between two chain, D and radius of gyration of the free polymer, Rg. (a) Low grafting density (D > 2Rg), mushroom regime. (b) Medium grafting density (D < Rg), semi-diluted brush regime. (c) High grafting density (D << Rg), concentrated brush regime.

**Figure 3.5**: *Photografting-from* via type I initiating system. Immobilization of BAPO-derivative on a given substrate (this step depends on the available surface functionalities). Photoscission of the anchored initiator with generation of one acyl radical (low reactive), released in the medium and a surface-anchored phosphoryl radical (highly reactive). Polymerization initiation from the phosphoryl radical and subsequent photoscission of the remaining acyl group. Polymerization initiation from the freshly generated phosphoryl radical. Note that the photogeneration of phosphoryl radicals has been reported in two separate steps for clarity. However, depending on the irradiation condition, the two steps can be virtually simultaneous.

**Figure 3.6**: *Photografting-from* via type II initiating system. Schematic representation of the BP excitation process, leading to the formation of BP molecules in their excited triplet [BP]T. Abstraction by [BP]T of hydrogens available on the substrate surface with rapidly radical coupling of the surface radical and the generated semipinacol $[BPH]^{T}$. Upon subsequent light-exposure, the surface radicals, formed from the coupling products, initiate a polymerization from the surface.

**Figure 3.7**: (a) Reduction of metal ions by ketyl radicals leading to the formation of metal nanoparticles, acetone and protons. (b) Photoscission process via α-cleavage of I-2959 (type I initiator) with formation of a ketyl radical and a benzoyl radical. (c) Air induced oxidation of benzoyl radical to the corresponding substituted benzoic acid.

## Chapter 4

**Figure 4.1**: (a) Graphical illustration of localized surface plasmons in gold nanoparticles excited by light propagating in free space. Schematic representation of a cross section of (sub)-micrometric particle (b) homogeneously and (c) asymmetrically nanostructured with Au NPs.

**Figure 4.2**: (a) Graphical illustration of a colloidosome structure with thiolated particles immobilized and partially masked by the solidified wax. (b) Partially grafted particle with PEG brushes resulting from the *photografting-from* process. (c) Final particle consisting of two distinct domains: one with polymer brushes and the other nanostructured with photogenerated Au NPs. (Step I) Scheme of the *photografting-from* process from the surface-bound thiyl radical generated upon UV exposure. (Step II) Scheme of the gold nanostructuration through gold ions photoreduction process by ketyl radicals. Note that, for the sake of simplicity, in the step II the photogeneration of thiyl radicals was omitted.

**Figure 4.3**: Survey (a) and S2p high-resolution XPS spectra (b) of organothiol-modified silica particles (SH-MPs). The high-resolution spectrum reports original (filled circle) and fitted (–) data along with peaks deconvolutions S(1) and S(2).

**Figure 4.4**: Representative FE-SEM micrographs of the emulsion-assisted masking. (a) Overall view of the collected wax droplets stabilized by thiolated particles after wax solidification (colloidosomes) (b)-(c) Magnification of colloidosome of different size. (d) Magnification of the colloidosome surface highlighting the masking balance. The black arrows are pointing toward the protected side.

**Figure 4.5**: Survey (a) and O1s (b), C1s (c) and Au4f (d) high-resolution XPS spectra of PEG grafted and Au nanostructured Janus microparticles (AuNP/PEG-JMPs synthetized with a PEG-JMPs : $HAuCl_4$ ratio of 10:1). The high-resolution spectra report original (filled circle) and fitted (–) data along with peaks deconvolutions.

**Figure 4.6**: Representative FE-SEM micrographs of AuNP/PEG-JMPs fabricated by photochemical route. The dashed lines show the division between the two domains of each particles. The arrows are pointing toward the gold nanostructured sides of the Janus particles. Systems synthetized by using a PEG-JMPs : $HAuCl_4$ mass ratio of either 10:1 (a) or 10:1 (c) along with their respective size distributions (b) and (d). All the scale bars are 200 nm.

**Figure 4.7**: Energy-dispersive X-ray spectroscopy for particle surface area centred in the Au nanostructured domain (spectrum S(a)) and in the polymer-grafted domain (spectrum S(b)) for AuNP/PEG-JMPs synthesized by using a PEG-JMPs : $HAuCl_4$ mass ratio of 10:1. On the left panel the atomic percentages for silicon, oxygen and gold are reported.

**Figure 4.8**: Absorbance from UV-Visible spectroscopy of (a) gold precursor photoinitiator solution before irradiation (i.e. gold ions $Au^{3+}$) and of colloid of Janus AuNP/PEG-JMPs after gold ions photoreduction by using either a PEG-JMPs : $HAuCl_4$ mass ratio of 10:1 (b) or 10:3 (c). On the left panel, the optical appearances of the solutions/colloids are reported.

## Chapter 5

**Figure 5.1**: Schematic representation of the light-triggered synthesis hairy polymer coronas on the surface of silica nanoparticles activated with TMESI$^2$-BAPO (**I**). (Left panel) Photoinitiating system, for the *photografting-from* process, used to generate lipophilic (orange) or hydrophilic (grey) polymer brushes. (Right panel) From nanoparticles functionalized with TMESI$^2$-BAPO (**I**)

following the route (a) generation of symmetric hairy coronas (**II**) and following the route (b) of asymmetric corona with amphiphilic character (**IV**) through the fabrication of a hydrophilic intermediate (**III**).

**Figure 5.2**: Scheme of the synthesis of TMESI²-BAPO from a stable bis(mesitoyl) phosphane. Where (**1**) is bis(mesitoyl) phosphane, (**2**) 3-(trimethoxysilyl) propyl methacrylate, (**3**) reaction intermediate, (**4**) 3-(trimethoxysilyl) propyl 3-[bis(2,4,6-trimethyl- benzoyl) phosphinyl]-2-methyl-propionate (TMESI²-BAPO).

**Figure 5.3**: Liquid phase transmission electron microscopy analysis: (a) Sample holder design which isolate the sample from the vacuum, equipped with flow system connected to a microfabricated liquid cell, (b) cross section and close-up of the liquid-cell embedding the liquid sample.

**Figure 5.4**: SEM image of dried cake of native silica particles (a). TEM image of a single native silica nanoparticle and its corresponding transmitted electron intensity profile (b). Hydrodynamic size distribution determined by dynamic light scattering for native silica nanoparticles (c), and its respective cumulative distributions (d). UV-Vis spectrum of photoactive silica nanoparticles functionalized with TMESI²-BAPO initiating system. The spectrum was collected in acetonitrile with a particle concentration of 0.15 mg $ml^{-1}$ (e).

**Figure 5.5**: Zeta potential measurements on silica nanoparticles before and after the functionalization with TMESI²-BAPO compared with the aminated microscaffolds $NH_2$-SMSs (a). Cartoons of attractive regime with monolayer assembly (b) and repulsive regime with monolayer disassembly (c) for the reversible nanoparticle immobilization. TEM image oh photoactive nanoparticles assembled onto the surface of aminated microscaffolds under attractive regime. The inset shows a magnification of a single particle immobilization with the red dashed line indicating the preserved region of photoactive sites.

**Figure 5.6:** Thermogravimetric analysis curves for the different particle systems: native nanoparticles (0), photoactive nanoparticles (I), hydrophilic HHNPs (II), intermediate JHNPs (III) and final amphiphilic JHNPs (IV).

**Figure 5.7**: Morphology of the photogenerated hairy polymer coronas in dry state. Representative TEM images of (a) hydrophilic HHNPs, (b) intermediate JHNPs and (c) final amphiphilic JHNPs along with transmitted electron intensity profiles with schematic representation of the nanoparticles. Images collected after negative stain with uranyl acetate.

**Figure 5.8**: Cryo-TEM micrographs showing the spatial distribution of (a) hydrophilic HHNPs, (b) amphiphilic JHNPs. The insets show magnifications of the hairy polymer morphology of the in water. In (b), the white circles highlight particles assembled in dimers, whereas the black dashed-line in the inset highlights a domain of higher contrast attributable to a surface-collapsed PLMA domain.

**Figure 5.9**: Typical contrast from direct visualization of liquid sample (hydrophilic HHNPs in water) through LP-TEM: Transmitted electrons represented in (a) grey scale and (b) false colour highlighting the hairy polymer coronas.

**Figure 5.10**: LP-TEM analyses to investigate particle-particle interactions and the resulting assemblies: (a) exemplificative spatial distribution for hydrophilic HHNPs with equilibrium

configuration of (b) isolated particles; (c) exemplificative spatial distribution for amphiphilic JHNPs with equilibrium configuration of (d) isolated particles, (e) dimers and more rarely (f) trimers.

**Figure 5.11**: Statistical analyses of the interparticle distance $D_{IP}$ (with a cut-off of 200 nm) in terms of relative frequency distribution for (a) amphiphilic JHNPs, (b) hydrophilic HHNPs and (c) cumulative frequency distribution comparing the two systems.

**Figure 5.12**: Statistical analyses of the interparticle distance $D_{IP}$ (with a cut-off of 200 nm) in terms of relative frequency distribution for (a) amphiphilic JHNPs, (b) hydrophilic HHNPs and (c) cumulative frequency distribution comparing the two systems.

**Figure 5.13**: (a) Small angle X-ray scattering results for hydrophilic HHNPs (blue points) and amphiphilic JHNPs (orange points) in water at concentration equal to 3 mg $cm^{-3}$: coherent differential scattering cross section, $S$, vs. scattering vector $q$ and corresponding best fit using Equation 7 (full lines). (b) Coherent differential scattering cross section at $q \to 0$ per concentration and contrast unit, $S_{q\to 0}/(K^2C)$, versus particles concentration for the two series of samples, hydrophilic HHNPs (blue points) and amphiphilic JHNPs (orange points). Full lines correspond to best linear fits of data points, dashed lines to mean values. (Note that the data point for amphiphilic JHNPs at the lowest concentrations has not been used for the linear fit).

## Chapter 6

**Figure 6.1**: (a) Schematic illustration of an amphiphilic soft nanoparticle questioning the nonspecific interaction fate toward lipid bilayer membranes depending Janus-like surface heterogeneity and charge. (b) Magnification of DPhPC phospholipid (*1,2-diphytanoyl-sn-glycero-3-phosphocholine*) showing polar head and apolar tail. Tailoring the cationic charge by pH-responsive blocks, (c) exemplification of how the degree of protonation (i.e. cationic charge) can be adjusted by playing on the pH.

**Figure 6.2**: Schematic representation of the fabrication process via *photografting-from* and light-induced thiol-yne click reactions. (Step 1) Synthesis of yne(+HNPs) from photoactive nanoparticles via photogeneration of poly(DMAEMA-ran-PA) pH responsive and clickable surfaces through *photografting-from* method. The tabs below each product report the schematic structure of the surface in each specific step.

**Figure 6.3**: Schematic representation of the fabrication process of uniformly PEGylated hairy nanoparticles hydro/hydro(+HNPs) via light-induced post-polymerization modification with PEG-T. (Step 2'). The tabs below each product report the schematic structure of the hairy surface photogenerated in each specific step.

**Figure 6.4**: Schematic representation of the fabrication process of partially PEGylated hairy nanoparticles yne/hydro(+HNPs) via toposelective light-induced post-polymerization modification with PEG-T. (Step 2) Synthesis of amphiphilic Janus-like hairy nanoparticles lipo/hydro(+HNPs) via light-induced post-polymerization modification with HD-T (step 3). The tabs below each product report the schematic structure of the hairy surface photogenerated in each specific step.

**Figure 6.5**: Electrophysiology of p-BLM. (a) Simplified measurement design with two compartments (*cis* and *trans*) filled with electrolyte solution (phosphate buffer) and connected to an AC power generator via two Ag/AgCl electrodes. The two compartments are separated by a

small hole with circular shape and with a diameter of 150 μm. The p-BLM in painted on the that hole and afterwards current and voltage are monitored to calculate the membrane complex impedance overtime. To probe NP-membrane interactions, nanoparticles are added in the cis compartment and the complex impedance is monitored overtime. Nanoparticle that anchor at the lipid bilayer are responsible of decreasing the imaginary component of the complex impedance (capacitive reactance). Illustrations (not drawn to scale) of unsupported lipid membranes (p-BLMs) in (b) pristine condition and (c) with an anchored nanoparticle.

**Figure 6.6**: (a) TEM micrograph of yne(+HNPs) after positive stain with PTA along with (b) a magnification of single stained nanoparticle. (c)Example of intensity profile of a positive stained yne(+HNPs) to estimate the silica core size and poly(DMAEMA-*ran*-PA) polymer shell thickness. (d) yne(+HNPs) and (e) yne/hydro(+HNPs) after incubation with gold nanoparticles to highlight the toposelective modification with PEG-T.

**Figure 6.7**: Thermogravimetric analysis curves for each particle system: photoactive nanoparticles (I), hairy nanoparticles after the first *photografting-from* process yne(+HNPs) (II), intermediate hairy nanoparticles yne/hydro(+HNPs) (III) after the first thiol-yne modification with PEG-T, and final amphiphilic lipo/hydro(+HNPs) (IV) after the second thiol-yne modification with HD-T.

**Figure 6.8**: Zeta potential values at different pH values and the corresponding polynomial fit for polymer grafted yne(+HNPs). The dotted lined highlight the pH range of interest for the interactions with lipid membranes.

**Figure 6.9**: FTIR spectra of native nanoparticle and (a) and polymer grafted yne(+HNPs) (b). The presence/absence of clickable functionalities is highlighted by the magnification between 2100 and 2180 $cm^{-1}$ in (b) for native nanoparticles and (d) for yne(+HNPs).

**Figure 6.10**: (a) Schematic summary of the effect of nanoparticles addition on capacitive reactance *Xm* (imaginary part of *Zm**) from electrophysiology measurements on p-BLM for hydrophilic homogeneous hydro/hydro(+HNPs). Effects on *Xm* reported in terms of ratio between $Xm^{NPs}$ (after nanoparticles addition) and $Xm^{0}$ (before nanoparticles addition). Representative examples of the encountered behaviours are reported for a pH=5.8 (b-c). The electrical answer was the same within the pH range of 5.8-7.8. A final average concentration of 230pM was used in all the experiments.

**Figure 6.11**: (a) Schematic summary of the effect of nanoparticles addition on capacitive reactance *Xm* (imaginary part of *Zm**) from electrophysiology measurements on p-BLM for amphiphilic Janus-like lipo/hydro(+HNPs). Effects on *Xm* reported in terms of ratio between $Xm^{NPs}$ (after nanoparticles addition) and $Xm^{0}$ (before nanoparticles addition). Representative examples of the encountered behaviours are reported for a pH=5.8 (b-c) and for 7.8 (d-e). The electrical answer was the same within the pH range of 6.6-7.8 (as for b-c) and 5.8-6.2 (as for d-e). A final average concentration of 230pM was used in all the experiments

**Figure 6.12**: (a) Representative image of lipo/hydro(+HNPs) amphiphilic hairy nanoparticle interacting with a liposome after 30 min of incubation (pH = 6.6.) followed by negative stain with Uranyl acetate. (b) Magnification of a single interacting nanoparticle anchored at the lipid membrane. Both (a) and (b) clearly show the membrane wrapping due to the hydrophobic and adhesive domain of the lipo/hydro(+HNPs). The images are reported in false-color to help the eyes in distinguishing liposomes and nanoparticles, an inset reporting the original image in grey-

scale is included for each micrograph in bottom-left corner. (c) Schematic illustration of lipo/hydro(+HNPs) – membrane wrapping: (particle domain I) non-adhesive hydrophilic domain; (particle domain II) nonspecific adhesive domain via insertion of hydrophobic HD-T chains in hydrophobic tails compartment of the membrane; (membrane region I) unaffected membrane region; (membrane region II) bended membrane region because of the adhesive forces.

**Figure 6.13**: *In situ* LP-TEM direct visualization of the interactions between lipid membrane and lipo/hydro(+HNPs) using liposomes as model. Liquid environment with an initial pH of 6.6. (a) Selected frames reported in false-color representation and representing the different experiment phases: (Phase I) initial configuration of a liposome before nanoparticles addition, (Phase II) nanoparticles arrive and anchored at the lipid membrane of the liposome. (Phase III) progressive evolution of the liposome because of pH decrease with anchored nanoparticles on the membrane. (b) complete sequence of collected frames. Note that the temporary darkening of field of view (e.g. $t_i$+8.4s and $t_i$+10.4s) was caused by formed bobbles in liquid because of beam irradiation.

# A.2 List of table

## Chapter 4

**Table 1**: Atomic concentration (%) from the X-Ray photoelectron spectroscopy survey spectra for thiol-modified silica microparticles (SH-MPs) and Janus silica microparticles with polyethylene(glycol) brushes and Au nanoparticles (AuNP/PEG-JMPs) .

## Chapter 5

**Table 2.** Physical constants for the different chemical species, $\tilde{b}_X$ is the scattering length density for X-ray (http://sld-calculator.appspot.com); $\rho$ is the mass density.

**Table 3.** Summary of weight loss percentage from thermogravimetric analysis for the final amphiphilic JHNPs, hydrophilic HHNPs and any other intermediate particle system.

**Table 4.** Results from data-fitting using scattering function $P_1(q)$ for the hydrophilic HHNPs at different concentrations. (Confidence intervals on parameters are smaller than 1%)

**Table 5.** Results from data-fitting using scattering function $P_1(q)$ for the amphiphilic JHNPs at different concentrations. (Confidence intervals on parameters are smaller than 1%)

**Table 6.** Average results from data-fitting using scattering function $P_1(q)$ for hydrophilic HHNPs and amphiphilic JHNPs. (Confidence intervals on parameters are smaller than 1%)

## Chapter 6

**Table 7.** Summary of weight loss percentage from thermogravimetric analysis for the final Janus-like amphiphilic nanoparticles lipo/hydro(+HNPs) and any other intermediate particle system.

# A.3 List of conference proceedings and peer-reviewed publications from the author

## Related to the PhD research topic

- Sangermano, M., **Razza, N.**, Light induced grafting-from strategies as powerful tool for surface modification. Express Polymer Letters (2019), 13(2): 135-145

- **Razza N.**, Rizza G., Coulon P. E., Lairez D., Fadda G. C., Voit B., Synytska A., Grützmacher H., Sangermano M., Enabling the Synthesis of Homogeneous or Janus Hairy Nanoparticles through Surface Photoactivation - Nanoscale (2018) – 10(30), 14492-14498

- **Razza N.**, Castellino M., and Sangermano M., Fabrication of Janus particles via a "photografting-from" method and gold photoreduction, Journal of Materials Science 52.23 (2017): 13444-13454.

- *Synthesis and Behavior of Janus Hairy Nanoparticles via Photografting-from Strategy by Exploiting the Use of Anchored Type I Photoinitiator*, Oral presentation at the V European Symposium of Photopolymer Science, Mulhouse, France, September 03-06, 2018. – Best oral presentation award.

- *Thiol and UV-light for rapid Janus particles fabrication via photografting-from method and gold photoreduction*, Oral resentation at the XXVI International Materials Research Congress,Cancun, Mexico, August 20-25, 2017.

- *UV-triggered decoration of Janus micro/nano particles*, Oral presentation at the 253rd American Chemical Society National Meeting San Francisco, CA, April 2-6, 2017.

- *When Janus Meets Helios: Janus (Sub)-Micrometric Particles Made by UV-Light*, Poster presentation at the IV European Symposium of Photopolymer Science, Leipzig, Germany, September 11-14, 2016 – Best poster presentation award.

## Related to side research topics

- Brännström S., Finnveden M., **Razza N.**, Martinelle M., Malmström E., Sangermano M., Johansson M., *Tailoring Thermo-Mechanical Properties of Cationically UV-Cured Systems by a Rational Design of Vinyl Ether Ester Monomers using Enzyme Catalysis*, Macromolecular Chemistry and Physics, 219 (21), 1800335

- Sangermano M., **Razza N.**, Graham G., Barandiaran I., Kortaberria G., *Electrical Insulating Polymeric Nanocomposites with Enhanced Thermal Conductivity by Visible-light Curing of Epoxy–BNNTs Formulations*, Polymer International, (2017), 66(12), 1935-1939.

- **Razza N.**, Blanchet B., Lamberti A., Pirri F-C., Tulliani J-M., Bozano L-D., Sangermano M., *UV-Printable and Flexible Humidity Sensors Based on Conducting/Insulating Semi-Interpenetrated Polymer Networks*, Macromolecular Materials and Engineering, (2017), 302(10).

- Sautrot-Ba P., Contreras A., Abbad Andaloussi S., Coradin T., Hélary C., **Razza N.**, Sangermano M., Mazeran P-E., Malval J-P., Versace D-L., *Eosin-mediated synthesis of polymer coatings combining photodynamic inactivation and antimicrobial properties*, Journal of Materials Chemistry B, (2017) 5.37, 7572-7582.

- Sangermano M., Vitale A., **Razza N.**, Favetto A., Paleari M., Ariano P., *Multilayer UV-cured organic capacitors*, Polymer, (2015), 56, 131-134.

# References


1. Palmer, S.E., 1985. *The role of symmetry in shape perception*. Acta Psychologica, 59(1), pp.67-90.

2. Little, A.C. and Jones, B.C., 2003. *Evidence against perceptual bias views for symmetry preferences in human faces*. Proceedings of the Royal Society of London B: Biological Sciences, 270(1526), pp.1759-1763.

3. Compagnucci, C., Fish, J. and Depew, M.J., 2014. *Left–right asymmetry of the gnathostome skull: Its evolutionary, developmental, and functional aspects.* genesis, 52(6), pp.515-527.

4. Getzin, S. and Wiegand, K., 2007. *Asymmetric tree growth at the stand level: random crown patterns and the response to slope*. Forest Ecology and Management, 242(2-3), pp.165-174.

5. Salam, A., 1991. *The role of chirality in the origin of life.* Journal of Molecular Evolution, 33(2), pp.105-113.

6. Bonner, W.A., 1995. *Chirality and life*. Origins of Life and Evolution of the Biosphere, 25(1-3), pp.175-190.

7. De Gennes, P.G., 1992. *Soft matter.* Reviews of modern physics, 64(3), p.645.

8. Yi, Y., Sanchez, L., Gao, Y., Lee, K. and Yu, Y., 2017. *Interrogating Cellular Functions with Designer Janus Particles*. Chemistry of Materials, 29(4), pp.1448-1460.

9. Lee, K., Yi, Y. and Yu, Y., 2016. *Remote control of T cell activation using magnetic Janus particles*. Angewandte Chemie, 128(26), pp.7510-7513.

10. Gao, Y. and Yu, Y., 2015. Macrophage uptake of Janus particles depends upon Janus balance. Langmuir, 31(9), pp.2833-2838.

11. Chen, B., Jia, Y., Gao, Y., Sanchez, L., Anthony, S.M. and Yu, Y., 2014. *Janus particles as artificial antigen-presenting cells for T cell activation*. ACS applied materials & interfaces, 6(21), pp.18435-18439.

12. Sanchez, L., Yi, Y. and Yu, Y., 2017. *Effect of partial PEGylation on particle uptake by macrophages*. Nanoscale, 9(1), pp.288-297.

13. Aveyard, R., 2012. *Can Janus particles give thermodynamically stable Pickering emulsions?*. Soft Matter, 8(19), pp.5233-5240.

14. Tu, F., Park, B.J. and Lee, D., 2013. *Thermodynamically stable emulsions using Janus dumbbells as colloid surfactants*. Langmuir, 29(41), pp.12679-12687.

15. Xu, Q., Kang, X., Bogomolni, R.A. and Chen, S., 2010. *Controlled assembly of Janus nanoparticles*. Langmuir, 26(18), pp.14923-14928.

16. Hong, L., Cacciuto, A., Luijten, E. and Granick, S., 2008. *Clusters of amphiphilic colloidal spheres*. Langmuir, 24(3), pp.621-625.

17. Jiang, S., Chen, Q., Tripathy, M., Luijten, E., Schweizer, K.S. and Granick, S., 2010. *Janus particle synthesis and assembly*.Advanced materials,22(10), pp.1060-1071.

18. Walther, A. and Müller, A.H., 2013. *Janus particles: synthesis, self-assembly, physical properties, and applications*. Chemical reviews, 113(7), pp.5194-5261.

19. Klabunde, K.J. and Richards, R.M. eds., 2009. *Nanoscale materials in chemistry*. John Wiley & Sons.

20. Hiemenz, P.C. and Rajagopalan, R., 1997. *Principles of Colloid and Surface Chemistry, revised and expanded*. CRC press.

21. Verma, A. and Stellacci, F., 2010. *Effect of surface properties on nanoparticle–cell interactions*. Small, 6(1), pp.12-21.

22. Nel, A., Xia, T., Mädler, L. and Li, N., 2006. *Toxic potential of materials at the nanolevel*. Science, 311(5761), pp.622-627.

23. Lundqvist, M., Stigler, J., Elia, G., Lynch, I., Cedervall, T. and Dawson, K.A., 2008. *Nanoparticle size and surface properties determine the protein corona with possible implications for biological impacts*. Proceedings of the National Academy of Sciences.

24. Casagrande, C., Fabre, P., Raphael, E. and Veyssié, M., 1989. *"Janus beads": realization and behaviour at water/oil interfaces.* EPL (Europhysics Letters), 9(3), p.251.

25. Zoppe, J.O., Ataman, N.C., Mocny, P., Wang, J., Moraes, J. and Klok, H.A., 2017. *Surface-initiated controlled radical polymerization: state-of-the-art, opportunities, and challenges in surface and interface engineering with polymer brushes.* Chemical reviews, 117(3), pp.1105-1318.

26. Kango, S., Kalia, S., Celli, A., Njuguna, J., Habibi, Y. and Kumar, R., 2013. *Surface modification of inorganic nanoparticles for development of organic–inorganic nanocomposites—a review*. Progress in Polymer Science, 38(8), pp.1232-1261.

27. Chen, M., Zhong, M. and Johnson, J.A., 2016. *Light-controlled radical polymerization: Mechanisms, methods, and applications*. Chemical reviews, 116(17), pp.10167-10211.

28. Sangermano, M., Razza, N., 2019. *Light induced grafting-from strategies as powerful tool for surface modification*. Express Polymer Letters, 13(2), pp.135-145.

29. Decker, C., 1998. *The use of UV irradiation in polymerization*. Polymer International, 45(2), pp.133-141.

30. Dietlin, C., Schweizer, S., Xiao, P., Zhang, J., Morlet-Savary, F., Graff, B., Fouassier, J.P. and Lalevée, J., 2015. *Photopolymerization upon LEDs: new photoinitiating systems and strategies*. Polymer Chemistry, 6(21), pp.3895-3912.

31. Wu, B., Zhang, H., Chen, C., Lin, S. and Zheng, N., 2009. *Interfacial activation of catalytically inert Au (6.7 nm)-Fe 3 O 4 dumbbell nanoparticles for CO oxidation*. Nano Research, 2(12), pp.975-983.

32. Schladt, T.D., Graf, T., Köhler, O., Bauer, H., Dietzsch, M., Mertins, J., Branscheid, R., Kolb, U. and Tremel, W., 2012. *Synthesis and magnetic properties of FePt@ MnO nano-heteroparticles*. Chemistry of Materials, 24(3), pp.525-535.

33. Pineider, F., de Julián Fernández, C., Videtta, V., Carlino, E., Al Hourani, A., Wilhelm, F., Rogalev, A., Cozzoli, P.D., Ghigna, P. and Sangregorio, C., 2013. *Spin-polarization transfer in colloidal magnetic-plasmonic Au/iron oxide hetero-nanocrystals*. ACS nano, 7(1), pp.857-866.

34. Wang, C., Daimon, H. and Sun, S., 2009. *Dumbbell-like Pt– Fe3O4 nanoparticles and their enhanced catalysis for oxygen reduction reaction*. Nano letters, 9(4), pp.1493-1496.

35. Jang, Y., Chung, J., Kim, S., Jun, S.W., Kim, B.H., Lee, D.W., Kim, B.M. and Hyeon, T., 2011. *Simple synthesis of Pd–Fe 3 O 4 heterodimer nanocrystals and their application as a magnetically recyclable catalyst for Suzuki cross-coupling reactions*. Physical Chemistry Chemical Physics, 13(7), pp.2512-2516.

36. Xu, C., Xie, J., Ho, D., Wang, C., Kohler, N., Walsh, E.G., Morgan, J.R., Chin, Y.E. and Sun, S., 2008. *Au–Fe3O4 dumbbell nanoparticles as dual-functional probes*. Angewandte Chemie International Edition, 47(1), pp.173-176.

37. Lopes, G., Vargas, J.M., Sharma, S.K., Béron, F., Pirota, K.R., Knobel, M., Rettori, C. and Zysler, R.D., 2010. *Ag– Fe3O4 Dimer colloidal nanoparticles: Synthesis and enhancement of magnetic properties*. The Journal of Physical Chemistry C, 114(22), pp.10148-10152.

38. Nakhjavan, B., Tahir, M.N., Natalio, F., Gao, H., Schneider, K., Schladt, T., Ament, I., Branscheid, R., Weber, S., Kolb, U. and Sönnichsen, C., 2011. *Phase separated Cu@ Fe 3 O 4 heterodimer nanoparticles from organometallic reactants*. Journal of Materials Chemistry, 21(24), pp.8605-8611.

39. Schladt, T.D., Shukoor, M.I., Schneider, K., Tahir, M.N., Natalio, F., Ament, I., Becker, J., Jochum, F.D., Weber, S., Köhler, O. and Theato, P., 2010. *Au@ MnO nanoflowers: hybrid nanocomposites for selective dual functionalization and imaging*. Angewandte Chemie International Edition, 49(23), pp.3976-3980.

40. Nakhjavan, B., Tahir, M.N., Panthöfer, M., Gao, H., Gasi, T., Ksenofontov, V., Branscheid, R., Weber, S., Kolb, U., Schreiber, L.M. and Tremel, W., 2011. *Controlling phase formation in solids: rational synthesis of phase separated Co@ Fe 2 O 3 heteroparticles and CoFe 2 O 4 nanoparticles*. Chemical Communications, 47(31), pp.8898-8900.

41. Carbone, L. and Cozzoli, P.D., 2010. *Colloidal heterostructured nanocrystals: Synthesis and growth mechanisms*. Nano Today, 5(5), pp.449-493.

42. Wang, C., Xu, C., Zeng, H. and Sun, S., 2009. *Recent progress in syntheses and applications of dumbbell-like nanoparticles*. Advanced materials, 21(30), pp.3045-3052.

43. Heitsch, A.T., Hessel, C.M., Akhavan, V.A. and Korgel, B.A., 2009. *Colloidal silicon nanorod synthesis*. Nano letters, 9(8), pp.3042-3047.

44. Kwon, K.W. and Shim, M., 2005. *γ-Fe2O3/II– VI sulfide nanocrystal heterojunctions*. Journal of the American Chemical Society, 127(29), pp.10269-10275.

45. Grodzińska, D., Pietra, F., van Huis, M.A., Vanmaekelbergh, D. and de Mello Donegá, C., 2011. *Thermally induced atomic reconstruction of PbSe/CdSe core/shell quantum dots into PbSe/CdSe bi-hemisphere hetero-nanocrystals*. Journal of Materials Chemistry, 21(31), pp.11556-11565.

46. Yu, H., Chen, M., Rice, P.M., Wang, S.X., White, R.L. and Sun, S., 2005. *Dumbbell-like bifunctional Au- Fe3O4 nanoparticles*. Nano letters, 5(2), pp.379-382.

47. Mokari, T., Rothenberg, E., Popov, I., Costi, R. and Banin, U., 2004. *Selective growth of metal tips onto semiconductor quantum rods and tetrapods*. Science, 304(5678), pp.1787-1790.

48. Zhang, L., Zhang, F., Dong, W.F., Song, J.F., Huo, Q.S. and Sun, H.B., 2011. *Magnetic-mesoporous Janus nanoparticles*. Chemical Communications, 47(4), pp.1225-1227.

49. Gu, H., Yang, Z., Gao, J., Chang, C.K. and Xu, B., 2005. *Heterodimers of nanoparticles: formation at a liquid- liquid interface and particle-specific surface modification by functional molecules*. Journal of the American Chemical Society, 127(1), pp.34-35.

50. Chen, T., Chen, G., Xing, S., Wu, T. and Chen, H., 2010. *Scalable Routes to Janus Au-SiO2 and Ternary Ag- Au- SiO2 Nanoparticles*. Chemistry of Materials, 22(13), pp.3826-3828.

51. Yabu, H., Higuchi, T., Ijiro, K. and Shimomura, M., 2005. *Spontaneous formation of polymer nanoparticles by good-solvent evaporation as a nonequilibrium process*. Chaos: An Interdisciplinary Journal of Nonlinear Science, 15(4), p.047505.

52. Yabu, H., Koike, K., Motoyoshi, K., Higuchi, T. and Shimomura, M., 2010. *A Novel Route for Fabricating Metal-Polymer Composite Nanoparticles with Phase-Separated Structures*. Macromolecular rapid communications, 31(14), pp.1267-1271.

53. Higuchi, T., Tajima, A., Yabu, H. and Shimomura, M., 2008. *Spontaneous formation of polymer nanoparticles with inner micro-phase separation structures*. Soft Matter, 4(6), pp.1302-1305.

54. Higuchi, T., Tajima, A., Motoyoshi, K., Yabu, H. and Shimomura, M., 2008. *Frustrated phases of block copolymers in nanoparticles*. Angewandte Chemie International Edition, 47(42), pp.8044-8046.

55. Higuchi, T., Yabu, H., Onoue, S., Kunitake, T. and Shimomura, M., 2008. *Preparation of lamella-structured block-copolymer particles and their irreversible lamella-disorder phase*

*transition*. Colloids and Surfaces A: Physicochemical and Engineering Aspects, 313, pp.87-90.

56. Higuchi, T., Tajima, A., Motoyoshi, K., Yabu, H. and Shimomura, M., 2009. *Suprapolymer structures from nanostructured polymer particles*. Angewandte Chemie International Edition, 48(28), pp.5125-5128.

57. Lee, K., Zhang, L., Yi, Y., Wang, X. and Yu, Y., 2018. *Rupture of Lipid Membranes Induced by Amphiphilic Janus Nanoparticles*. ACS nano, 12(4), pp.3646-3657.

58. Ma, X., Hahn, K. and Sanchez, S., 2015. *Catalytic mesoporous Janus nanomotors for active cargo delivery*. Journal of the American Chemical Society, 137(15), pp.4976-4979.

59. McConnell, M.D., Kraeutler, M.J., Yang, S. and Composto, R.J., 2010. *Patchy and multiregion janus particles with tunable optical properties*. Nano letters, 10(2), pp.603-609.

60. Lin, C.C., Liao, C.W., Chao, Y.C. and Kuo, C., 2010. *Fabrication and characterization of asymmetric Janus and ternary particles*. ACS applied materials & interfaces, 2(11), pp.3185-3191.

61. Ho, C.C., Chen, W.S., Shie, T.Y., Lin, J.N. and Kuo, C., 2008. *Novel fabrication of Janus particles from the surfaces of electrospun polymer fibers*. Langmuir, 24(11), pp.5663-5666.

62. Pieranski, P., 1980. *Two-dimensional interfacial colloidal crystals*. Physical Review Letters, 45(7), p.569.

63. Hong, L., Jiang, S. and Granick, S., 2006. *Simple method to produce Janus colloidal particles in large quantity*. Langmuir, 22(23), pp.9495-9499.

64. Panwar, K., Jassal, M. and Agrawal, A.K., 2017. *Ag–SiO2 Janus particles based highly active SERS macroscopic substrates*. Applied Surface Science, 411, pp.368-373.

65. Panwar, K., Jassal, M. and Agrawal, A.K., 2015. *In situ synthesis of Ag–SiO2 Janus particles with epoxy functionality for textile applications*. Particuology, 19, pp.107-112.

66. Panwar, K., Jassal, M. and Agrawal, A.K., 2016. *TiO 2–SiO 2 Janus particles with highly enhanced photocatalytic activity*. RSC Advances, 6(95), pp.92754-92764.

67. Halperin, A., 1988. *Microphase separation in binary polymeric micelles*. Journal de Physique, 49(1), pp.131-137.

68. Charlaganov, M., Borisov, O.V. and Leermakers, F.A., 2008. *Modeling of triblock terpolymer micelles with a segregated corona.* Macromolecules, 41(10), pp.3668-3677.

69. Han, Y. and Jiang, W., 2011. *Self-assembly of the AB/BC diblock copolymer mixture based on hydrogen bonding in a selective solvent: a Monte Carlo study*. The Journal of Physical Chemistry B, 115(10), pp.2167-2172.

70. Palyulin, V.V. and Potemkin, I.I., 2008. *Mixed versus ordinary micelles in the dilute solution of AB and BC diblock copolymers*. Macromolecules, 41(12), pp.4459-4463.

71. Hu, J. and Liu, G., 2005. *Chain Mixing and Segregation in B– C and C– D Diblock Copolymer Micelles.* Macromolecules, 38(19), pp.8058-8065.

72. Cheng, L., Zhang, G., Zhu, L., Chen, D. and Jiang, M., 2008. *Nanoscale tubular and sheetlike superstructures from hierarchical self-assembly of polymeric janus particles*. Angewandte Chemie International Edition, 47(52), pp.10171-10174.

73. Voets, I.K., de Keizer, A., de Waard, P., Frederik, P.M., Bomans, P.H., Schmalz, H., Walther, A., King, S.M., Leermakers, F.A. and Cohen Stuart, M.A., 2006. *Double-Faced Micelles from Water-Soluble Polymers*. Angewandte Chemie International Edition, 45(40), pp.6673-6676.

74. Voets, I.K., Fokkink, R., Hellweg, T., King, S.M., de Waard, P., de Keizer, A. and Stuart, M.A.C., 2009. *Spontaneous symmetry breaking: formation of Janus micelles*. Soft Matter, 5(5), pp.999-1005.

75. Voets, I.K., Fokkink, R., de Keizer, A., May, R.P., de Waard, P. and Cohen Stuart, M.A., 2008. *On the transition between a heterogeneous and homogeneous corona in mixed polymeric micelles*. Langmuir, 4(21), pp.12221-12227.

76. Voets, I.K., de Keizer, A., Cohen Stuart, M.A. and de Waard, P., 2006. *Core and corona structure of mixed polymeric micelles*. Macromolecules, 39(17), pp.5952-5955.

77. Walther, A., Millard, P.E., Goldmann, A.S., Lovestead, T.M., Schacher, F., Barner-Kowollik, C. and Müller, A.H., 2008. *Bis-hydrophilic block terpolymers via RAFT polymerization: toward dynamic micelles with tunable corona properties*. Macromolecules, 41(22), pp.8608-8619.

78. Walther, A., Barner-Kowollik, C. and Müller, A.H., 2010. *Mixed, multicompartment, or Janus micelles? A systematic study of thermoresponsive bis-hydrophilic block terpolymers.* Langmuir, 26(14), pp.12237-12246.

79. Gröschel, A.H., Walther, A., Löbling, T.I., Schmelz, J., Hanisch, A., Schmalz, H. and Müller, A.H., 2012. *Facile, solution-based synthesis of soft, nanoscale Janus particles with tunable Janus balance*. Journal of the American Chemical Society, 134(33), pp.13850-13860.

80. Bates, F.S., Hillmyer, M.A., Lodge, T.P., Bates, C.M., Delaney, K.T. and Fredrickson, G.H., 2012. *Multiblock polymers: panacea or Pandora's box?.* Science, 336(6080), pp.434-440.

81. Erhardt, R., Zhang, M., Böker, A., Zettl, H., Abetz, C., Frederik, P., Krausch, G., Abetz, V. and Müller, A.H., 2003. *Amphiphilic Janus micelles with polystyrene and poly (methacrylic acid) hemispheres.* Journal of the American Chemical Society, 125(11), pp.3260-3267.

82. Erhardt, R., Böker, A., Zettl, H., Kaya, H., Pyckhout-Hintzen, W., Krausch, G., Abetz, V. and Müller, A.H., 2001. *Janus micelles.* Macromolecules, 34(4), pp.1069-1075.

83. Saito, R., Fujita, A., Ichimura, A. and Ishizu, K., 2000. *Synthesis of microspheres with microphase-separated shells*. Journal of Polymer Science Part A: Polymer Chemistry, 38(11), pp.2091-2097.

84. Walther, A., André, X., Drechsler, M., Abetz, V. and Müller, A.H., 2007. *Janus discs*. Journal of the American Chemical Society, 129(19), pp.6187-6198.

85. Walther, A., Göldel, A. and Müller, A.H., 2008. *Controlled crosslinking of polybutadiene containing block terpolymer bulk structures: A facile way towards complex and functional nanostructures*. Polymer, 49(15), pp.3217-3227.

86. Walther, A., Drechsler, M., Rosenfeldt, S., Harnau, L., Ballauff, M., Abetz, V. and Müller, A.H., 2009. *Self-assembly of Janus cylinders into hierarchical superstructures*. Journal of the American Chemical Society, 131(13), pp.4720-4728.

87. Walther, A., Drechsler, M. and Müller, A.H., 2009. *Structures of amphiphilic Janus discs in aqueous media*. Soft Matter, 5(2), pp.385-390.

88. Liu, Y., Abetz, V. and Müller, A.H., 2003. *Janus cylinders.* Macromolecules, 36(21), pp.7894-7898.

89. Wolf, A., Walther, A. and Müller, A.H., 2011. Janus triad: Three types of nonspherical, nanoscale janus particles from one single triblock terpolymer. Macromolecules, 44(23), pp.9221-9229.

90. Bain, C.D., Troughton, E.B., Tao, Y.T., Evall, J., Whitesides, G.M. and Nuzzo, R.G., 1989. *Formation of monolayer films by the spontaneous assembly of organic thiols from solution onto gold*. Journal of the American Chemical Society, 111(1), pp.321-335.

91. Duguet, E., Désert, A., Perro, A. and Ravaine, S., 2011. *Design and elaboration of colloidal molecules: an overview*. Chemical Society Reviews, 40(2), pp.941-960.

92. Walther, A. and Müller, A.H., 2008. *Janus particles*. Soft Matter, 4(4), pp.663-668.

93. Chen, Q., Yan, J., Zhang, J., Bae, S.C. and Granick, S., 2012. *Janus and multiblock colloidal particles*. Langmuir, 28(38), pp.13555-13561.

94. Hu, J., Zhou, S., Sun, Y., Fang, X. and Wu, L., 2012. *Fabrication, properties and applications of Janus particles*. Chemical Society Reviews, 41(11), pp.4356-4378.

95. Wösten, H.A., 2001. *Hydrophobins: multipurpose proteins*. Annual Reviews in Microbiology, 55(1), pp.625-646.

96. Pradhan, S., Xu, L. and Chen, S., 2007. *Janus nanoparticles by interfacial engineering*. Advanced functional materials, 17(14), pp.2385-2392.

97. Andala, D.M., Shin, S.H.R., Lee, H.Y. and Bishop, K.J., 2012. *Templated synthesis of amphiphilic nanoparticles at the liquid–liquid interface*. ACS nano, 6(2), pp.1044-1050.

98. Stranick, S.J., Parikh, A.N., Tao, Y.T., Allara, D.L. and Weiss, P.S., 1994. *Phase separation of mixed-composition self-assembled monolayers into nanometer scale molecular domains*. The Journal of Physical Chemistry, 98(31), pp.7636-7646.

99. Stranick, S.J., Atre, S.V., Parikh, A.N., Wood, M.C., Allara, D.L., Winograd, N. and Weiss, P.S., 1996. *Nanometer-scale phase separation in mixed composition self-assembled monolayers*. Nanotechnology, 7(4), p.438.

100. Kim, H., Carney, R.P., Reguera, J., Ong, Q.K., Liu, X. and Stellacci, F., 2012. *Synthesis and characterization of Janus gold nanoparticles*. Advanced materials, 24(28), pp.3857-3863.

101. Singh, C., Ghorai, P.K., Horsch, M.A., Jackson, A.M., Larson, R.G., Stellacci, F. and Glotzer, S.C., 2007. *Entropy-mediated patterning of surfactant-coated nanoparticles and surfaces*. Physical Review Letters, 99(22), p.226106.

102. Liu, B., Wei, W., Qu, X. and Yang, Z., 2008. *Janus colloids formed by biphasic grafting at a Pickering emulsion interface.* Angewandte Chemie, 120(21), pp.4037-4039.

103. Zhang, J., Jin, J. and Zhao, H., 2009. *Surface-initiated free radical polymerization at the liquid– liquid interface: a one-step approach for the synthesis of amphiphilic Janus silica particles*. Langmuir, 25(11), pp.6431-6437.

104. Zhang, J., Wang, X., Wu, D., Liu, L. and Zhao, H., 2009. *Bioconjugated Janus particles prepared by in situ click chemistry.* Chemistry of Materials, 21(17), pp.4012-4018.

105. Berger, S., Synytska, A., Ionov, L., Eichhorn, K.J. and Stamm, M., 2008. *Stimuli-responsive bicomponent polymer janus particles by "grafting from"/"grafting to" approaches*. Macromolecules, 41(24), pp.9669-9676.

106. Kirillova, A., Marschelke, C., Friedrichs, J., Werner, C. and Synytska, A., 2016. *Hybrid Hairy Janus Particles as Building Blocks for Antibiofouling Surfaces*. ACS applied materials & interfaces, 8(47), pp.32591-32603.

107. Kirillova, A., Stoychev, G. and Synytska, A., 2016. *Programmed assembly of oppositely charged homogeneously decorated and Janus particles*. Faraday discussions, 191, pp.89-104.

108. Kirillova, A., Ionov, L., Roisman, I.V. and Synytska, A., 2016. *Hybrid hairy Janus particles for anti-icing and de-icing surfaces: Synergism of properties and effects*. Chemistry of Materials, 28(19), pp.6995-7005.

109. Kirillova, A., Schliebe, C., Stoychev, G., Jakob, A., Lang, H. and Synytska, A., 2015. *Hybrid hairy Janus particles decorated with metallic nanoparticles for catalytic applications*. ACS applied materials & interfaces, 7(38), pp.21218-21225.

110. Lattuada, M. and Hatton, T.A., 2007. *Preparation and controlled self-assembly of Janus magnetic nanoparticles*. Journal of the American Chemical Society, 129(42), pp.12878-12889.

111. Wang, B., Li, B., Zhao, B. and Li, C.Y., 2008. *Amphiphilic Janus gold nanoparticles via combining "solid-state grafting-to" and "grafting-from" methods.* Journal of the American Chemical Society, 130(35), pp.11594-11595.

112. Wang, B., Dong, B., Li, B., Zhao, B. and Li, C.Y., 2010. *Janus gold nanoparticle with bicompartment polymer brushes templated by polymer single crystals*. Polymer, 51(21), pp.4814-4822.

113. Zhou, T., Wang, B., Dong, B. and Li, C.Y., 2012. *Thermoresponsive amphiphilic Janus silica nanoparticles via combining "polymer single-crystal templating" and "grafting-from" methods.* Macromolecules, 45(21), pp.8780-8789.

114. Whitesides, G.M. and Grzybowski, B., 2002. *Self-assembly at all scales.* Science, 295(5564), pp.2418-2421.

115. Rothemund, P.W., 2006. *Folding DNA to create nanoscale shapes and patterns*. Nature, 440(7082), p.297.

116. Binney, J. and Tremaine, S., 2011. *Galactic dynamics (Vol. 20).* Princeton university press.

117. Smoukov, S.K., Gangwal, S., Marquez, M. and Velev, O.D., 2009. *Reconfigurable responsive structures assembled from magnetic Janus particles*. Soft Matter, 5(6), pp.1285-1292.

118. Isojima, T., Suh, S.K., Vander Sande, J.B. and Hatton, T.A., 2009. *Controlled assembly of nanoparticle structures: spherical and toroidal superlattices and nanoparticle-coated polymeric beads.* Langmuir, 25(14), pp.8292-8298.

119. Sacanna, S., Rossi, L. and Pine, D.J., 2012. *Magnetic click colloidal assembly.* Journal of the American Chemical Society, 134(14), pp.6112-6115.

120. Yuet, K.P., Hwang, D.K., Haghgooie, R. and Doyle, P.S., 2009. *Multifunctional superparamagnetic Janus particles.* Langmuir, 26(6), pp.4281-4287.

121. Gangwal, S., Cayre, O.J. and Velev, O.D., 2008. *Dielectrophoretic assembly of metallodielectric Janus particles in AC electric fields*. Langmuir, 24(23), pp.13312-13320.

122. Gangwal, S., Cayre, O.J., Bazant, M.Z. and Velev, O.D., 2008. *Induced-charge electrophoresis of metallodielectric particles.* Physical review letters, 100(5), p.058302.

123. Yan, J., Bloom, M., Bae, S.C., Luijten, E. and Granick, S., 2012. *Linking synchronization to self-assembly using magnetic Janus colloids*. Nature, 491(7425), p.578.

124. Hong, L., Cacciuto, A., Luijten, E. and Granick, S., 2006. *Clusters of charged Janus spheres*. Nano letters, 6(11), pp.2510-2514.

125. Goyal, A., Hall, C.K. and Velev, O.D., 2008. *Phase diagram for stimulus-responsive materials containing dipolar colloidal particles*. Physical Review E, 77(3), p.031401.

126. Goyal, A., Hall, C.K. and Velev, O.D., 2010. *Bicontinuous gels formed by self-assembly of dipolar colloid particles*. Soft Matter, 6(3), pp.480-484.

127. Chen, Q., Whitmer, J.K., Jiang, S., Bae, S.C., Luijten, E. and Granick, S., 2011. *Supracolloidal reaction kinetics of Janus spheres*. Science, 331(6014), pp.199-202.

128. Sciortino, F., Giacometti, A. and Pastore, G., 2009. *Phase diagram of janus particles*. Physical review letters, 103(23), p.237801.

129. Wang, B., Li, B., Dong, B., Zhao, B. and Li, C.Y., 2010. *Homo-and hetero-particle clusters formed by janus nanoparticles with bicompartment polymer brushes*. Macromolecules, 43(22), pp.9234-9238.

130. Adams, D.J., Adams, S., Melrose, J. and Weaver, A.C., 2008. *Influence of particle surface roughness on the behaviour of Janus particles at interfaces*. Colloids and Surfaces A: Physicochemical and Engineering Aspects, 317(1-3), pp.360-365.

131. Binks, B.P. and Fletcher, P.D.I., 2001. *Particles adsorbed at the oil– water interface: a theoretical comparison between spheres of uniform wettability and "Janus" particles*. Langmuir, 17(16), pp.4708-4710.

132. Hirose, Y., Komura, S. and Nonomura, Y., 2007. *Adsorption of Janus particles to curved interfaces*. The Journal of chemical physics, 127(5), p.054707.

133. Chen, K.L. and Bothun, G.D., 2013. *Nanoparticles meet cell membranes: probing nonspecific interactions using model membranes.*

134. Israelachvili, J.N., Mitchell, D.J. and Ninham, B.W., 1976. *Theory of self-assembly of hydrocarbon amphiphiles into micelles and bilayers*. Journal of the Chemical Society, Faraday Transactions 2: Molecular and Chemical Physics, 72, pp.1525-1568.

135. Seifert, U., 1997. *Configurations of fluid membranes and vesicles*. Advances in physics, 46(1), pp.13-137.

136. Nagle, J.F. and Tristram-Nagle, S., 2000. *Structure of lipid bilayers*. Biochimica et Biophysica Acta (BBA)-Reviews on Biomembranes, 1469(3), pp.159-195.

137. Ding, H.M. and Ma, Y.Q., 2012. *Interactions between Janus particles and membranes*. Nanoscale, 4(4), pp.1116-1122.

138. Arai, N., Yasuoka, K. and Zeng, X.C., 2013. *A vesicle cell under collision with a Janus or homogeneous nanoparticle: translocation dynamics and late-stage morphology*. Nanoscale, 5(19), pp.9089-9100.

139. Alexeev, A., Uspal, W.E. and Balazs, A.C., 2008. *Harnessing Janus nanoparticles to create controllable pores in membranes*. Acs Nano, 2(6), pp.1117-1122.

140. Agudo-Canalejo, J. and Lipowsky, R., 2017. *Uniform and Janus-like nanoparticles in contact with vesicles: energy landscapes and curvature-induced forces.* Soft Matter, 13(11), pp.2155-2173.

141. Agudo-Canalejo, J. and Lipowsky, R., 2015. *Critical particle sizes for the engulfment of nanoparticles by membranes and vesicles with bilayer asymmetry*. ACS nano, 9(4), pp.3704-3720.

142. Agudo-Canalejo, J. and Lipowsky, R., 2015. *Adhesive nanoparticles as local probes of membrane curvature.* Nano letters, 15(10), pp.7168-7173.

143. Galatola, P. and Fournier, J.B., 2014. *Capillary force acting on a colloidal particle floating on a deformed interface.* Soft Matter, 10(13), pp.2197-2212.

144. Sharifi-Mood, N., Liu, I.B. and Stebe, K.J., 2015. *Curvature capillary migration of microspheres.* Soft Matter, 11(34), pp.6768-6779.

145. Emerson, R. and Arnold, W., 1932. *The photochemical reaction in photosynthesis.* The Journal of general physiology, 16(2), pp.191-205.

146. Crivello, J.V. and Dietliker, K., 1998. *Photoinitiators for free radical cationic & anionic photopolymerisation*.

147. Fouassier, J.P. and Lalevée, J., 2012. *Photoinitiators for polymer synthesis: scope, reactivity, and efficiency. John Wiley & Sons.*

148. Alexander, S., 1977. *Adsorption of chain molecules with a polar head a scaling description.* Journal De Physique, 38(8), pp.983-987.

149. De Gennes, P.G., 1976. *Scaling theory of polymer adsorption*. Journal de Physique, 37(12), pp.1445-1452.

150. De Gennes, P., 1980. *Conformations of polymers attached to an interface*. Macromolecules, 13(5), pp.1069-1075.

151. Halperin, A., 1988. *Collapse of grafted chains in poor solvents.* Journal de Physique, 49(3), pp.547-550.

152. Halperin, A. and Zhulina, E.B., 1991. *Stretching polymer brushes in poor solvents*. Macromolecules, 24(19), pp.5393-5397.

153. Schmidt, R., Zhao, T., Green, J.B. and Dyer, D.J., 2002. *Photoinitiated polymerization of styrene from self-assembled monolayers on gold*. Langmuir, 18(4), pp.1281-1287.

154. Fan, X., Xia, C., Fulghum, T., Park, M.K., Locklin, J. and Advincula, R.C., 2003. *Polymer brushes grafted from clay nanoparticles adsorbed on a planar substrate by free radical surface-initiated polymerization*. Langmuir, 19(3), pp.916-923.

155. Vernekar, S.P., Ghatge, N.D. and Wadgaoknar, P.P., 1988. *Decomposition rate studies of azobisnitriles containing functional groups.* Journal of Polymer Science Part A: Polymer Chemistry, 26(3), pp.953-958.

156. Huber, A., Kuschel, A., Ott, T., Santiso-Quinones, G., Stein, D., Bräuer, J., Kissner, R., Krumeich, F., Schönberg, H., Levalois-Grützmacher, J. and Grützmacher, H., 2012. *Phosphorous-Functionalized Bis (acyl) phosphane Oxides for Surface Modification*. Angewandte Chemie, 124(19), pp.4726-4730.

157. Grützmacher, H., Geier, J., Stein, D., Ott, T., Schönberg, H., Sommerlade, R.H., Boulmaaz, S., Wolf, J.P., Murer, P. and Ulrich, T., 2008. *A simple straightforward synthesis of phenylphosphane and the photoinitiator bis (mesitoyl) phenylphosphane oxide (Irgacure 819)*. CHIMIA International Journal for Chemistry, 62(1-2), pp.18-22.

158. P. Murer, J.-P. Wolf, S. Burkhardt, H. Grützmacher, D. Stein, K. Dietliker, PCT Int. Appl. WO 2006056541A1 20060601, 2006.

159. Wang, J., Siqueira, G., Müller, G., Rentsch, D., Huch, A., Tingaut, P., Levalois-Grützmacher, J. and Grützmacher, H., 2016. *Synthesis of new bis (acyl) phosphane oxide*

*photoinitiators for the surface functionalization of cellulose nanocrystals*. Chemical Communications, 52(13), pp.2823-2826.

160. Sangermano, M., Periolatto, M., Castellino, M., Wang, J., Dietliker, K., Grutzmacher, J.L. and Grutzmacher, H., 2016. *A Simple Preparation of Photoactive Glass Surfaces Allowing Coatings via the "Grafting-from" Method*. ACS applied materials & interfaces, 8(30), pp.19764-19771.

161. Mostegel, F.H., Ducker, R.E., Rieger, P.H., El Zubir, O., Xia, S., Radl, S.V., Edler, M., Cartron, M.L., Hunter, C.N., Leggett, G.J. and Griesser, T., 2015. *Versatile thiol-based reactions for micrometer-and nanometer-scale photopatterning of polymers and biomolecules*. Journal of Materials Chemistry B, 3(21), pp.4431-4438.

162. Kilambi, H., Reddy, S.K., Schneidewind, L., Lee, T.Y., Stansbury, J.W. and Bowman, C.N., 2007. *Design, development, and evaluation of monovinyl acrylates characterized by secondary functionalities as reactive diluents to diacrylates*. Macromolecules, 40(17), pp.6112-6118.

163. Wei, H., Li, Q., Ojelade, M., Madbouly, S., Otaigbe, J.U. and Hoyle, C.E., 2007. *Thiol–ene free-radical and vinyl ether cationic hybrid photopolymerization*. Macromolecules, 40(24), pp.8788-8793.

164. Khire, V.S., Lee, T.Y. and Bowman, C.N., 2007. *Surface modification using thiol– acrylate conjugate addition reactions*. Macromolecules, 40(16), pp.5669-5677.

165. Yang, W. and Rånby, B., 1999. *Photoinitiation performance of some ketones in the LDPE–acrylic acid surface photografting system*. European polymer journal, 35(8), pp.1557-1568.

166. Cho, J.D., Kim, S.G. and Hong, J.W., 2006. *Surface modification of polypropylene sheets by UV-radiation grafting polymerization*. Journal of applied polymer science, 99(4), pp.1446-1461.

167. Pan, B., Viswanathan, K., Hoyle, C.E. and Moore, R.B., 2004. *Photoinitiated grafting of maleic anhydride onto polypropylene*. Journal of Polymer Science Part A: Polymer Chemistry, 42(8), pp.1953-1962.

168. Hong, K.H., Liu, N. and Sun, G., 2009. *UV-induced graft polymerization of acrylamide on cellulose by using immobilized benzophenone as a photo-initiator*. European Polymer Journal, 45(8), pp.2443-2449.

169. Ma, H., Davis, R.H. and Bowman, C.N., 2000. *A novel sequential photoinduced living graft polymerization*. Macromolecules, 33(2), pp.331-335.

170. Roppolo, I., Chiappone, A., Bejtka, K., Celasco, E., Chiodoni, A., Giorgis, F., Sangermano, M. and Porro, S., 2014. *A powerful tool for graphene functionalization: Benzophenone mediated UV-grafting*. *Carbon*, *77*, pp.226-235.

171. Luan, S., Zhao, J., Yang, H., Shi, H., Jin, J., Li, X., Liu, J., Wang, J., Yin, J. and Stagnaro, P., 2012. *Surface modification of poly (styrene-b-(ethylene-co-butylene)-b-styrene) elastomer via UV-induced graft polymerization of N-vinyl pyrrolidone*. Colloids and Surfaces B: Biointerfaces, 93, pp.127-134.

172. Sugiura, S., Edahiro, J.I., Sumaru, K. and Kanamori, T., 2008. *Surface modification of polydimethylsiloxane with photo-grafted poly (ethylene glycol) for micropatterned protein adsorption and cell adhesion*. Colloids and Surfaces B: Biointerfaces, 63(2), pp.301-305.

173. Schneider, M.H., Willaime, H., Tran, Y., Rezgui, F. and Tabeling, P., 2010. *Wettability patterning by UV-initiated graft polymerization of poly (acrylic acid) in closed microfluidic systems of complex geometry.* Analytical chemistry, 82(21), pp.8848-8855.

174. Goda, T., Matsuno, R., Konno, T., Takai, M. and Ishihara, K., 2008. *Photografting of 2-methacryloyloxyethyl phosphorylcholine from polydimethylsiloxane: tunable protein repellency and lubrication property.* Colloids and Surfaces B: Biointerfaces, 63(1), pp.64-72.

175. Feng, Y., Zhao, H., Behl, M., Lendlein, A., Guo, J. and Yang, D., 2013. *Grafting of poly (ethylene glycol) monoacrylates on polycarbonateurethane by UV initiated polymerization for improving hemocompatibility.* Journal of Materials Science: Materials in Medicine, 24(1), pp.61-70.

176. Jia, X., Jiang, X., Liu, R. and Yin, J., 2009. *Poly (N-isopropylacrylamide) Brush Fabricated by Surface-Initiated Photopolymerization and its Response to Temperature.* Macromolecular Chemistry and Physics, 210(21), pp.1876-1882.

177. Chen, F., Jiang, X., Liu, R. and Yin, J., 2010. *Well-defined PMMA brush on silica particles fabricated by surface-initiated photopolymerization (SIPP).* ACS applied materials & interfaces, 2(4), pp.1031-1037.

178. Deng, J.P. and Yang, W.T., 2001. *Self-initiating performance of maleic anhydride on surface photografting polymerization*. Journal of Polymer Science Part A: Polymer Chemistry, 39(19), pp.3246-3249.

179. Taniguchi, M., Pieracci, J., Samsonoff, W.A. and Belfort, G., 2003. *UV-assisted graft polymerization of synthetic membranes: mechanistic studies.* Chemistry of materials, 15(20), pp.3805-3812.

180. Rohr, T., Ogletree, D.F., Svec, F. and Fréchet, J.M., 2003. *Surface functionalization of thermoplastic polymers for the fabrication of microfluidic devices by photoinitiated grafting.* Advanced Functional Materials, 13(4), pp.264-270.

181. Gupta, S., Agrawal, M., Conrad, M., Hutter, N.A., Olk, P., Simon, F., Eng, L.M., Stamm, M. and Jordan, R., 2010. *Poly (2-(dimethylamino) ethyl methacrylate) Brushes with Incorporated Nanoparticles as a SERS Active Sensing Layer*. Advanced Functional Materials, 20(11), pp.1756-1761.

182. Zhang, N., Steenackers, M., Luxenhofer, R. and Jordan, R., 2009. *Bottle-brush brushes: cylindrical molecular brushes of poly (2-oxazoline) on glassy carbon*. Macromolecules, 42(14), pp.5345-5351.

183. Steenackers, M., Sharp, I.D., Larsson, K., Hutter, N.A., Stutzmann, M. and Jordan, R., 2009. *Structured polymer brushes on silicon carbide*. Chemistry of Materials, 22(1), pp.272-278.

184. Steenackers, M., Gigler, A.M., Zhang, N., Deubel, F., Seifert, M., Hess, L.H., Lim, C.H.Y.X., Loh, K.P., Garrido, J.A., Jordan, R. and Stutzmann, M., 2011. *Polymer brushes on graphene*. Journal of the American Chemical Society, 133(27), pp.10490-10498.

185. Shiojima, T., Inoue, Y., Kyomoto, M. and Ishihara, K., 2016. *High-efficiency preparation of poly (2-methacryloyloxyethyl phosphorylcholine) grafting layer on poly (ether ether ketone) by photoinduced and self-initiated graft polymerization in an aqueous solution in the presence of inorganic salt additives*. Acta biomaterialia, 40, pp.38-45.

186. Sheng, W., Li, W., Li, B., Li, C., Xu, Y., Guo, X., Zhou, F. and Jia, X., 2015. *Mussel-Inspired Photografting on Colloidal Spheres: A Generalized Self-Template Route to Stimuli-Responsive Hollow Spheres for Controlled Pesticide Release*. Macromolecular rapid communications, 36(18), pp.1640-1645.

187. Bai, G., Ma, S., Qie, R., Liu, Z., Shi, Y., Li, C., Wang, R., Guo, X., Zhou, F. and Jia, X., 2016. *UV-Triggered Surface-Initiated Polymerization from Colorless Green Tea Polyphenol-Coated Surfaces*. Macromolecular rapid communications, 37(15), pp.1256-1261.

188. Kimling, J., Maier, M., Okenve, B., Kotaidis, V., Ballot, H. and Plech, A., 2006. *Turkevich method for gold nanoparticle synthesis revisited*. The Journal of Physical Chemistry B, 110(32), pp.15700-15707.

189. Grzelczak, M., Pérez-Juste, J., Mulvaney, P. and Liz-Marzán, L.M., 2008. *Shape control in gold nanoparticle synthesis*. Chemical Society Reviews, 37(9), pp.1783-1791.

190. Scaiano, J.C., Stamplecoskie, K.G. and Hallett-Tapley, G.L., 2012. *Photochemical Norrish type I reaction as a tool for metal nanoparticle synthesis: importance of proton coupled electron transfer*. Chemical Communications, 48(40), pp.4798-4808.

191. Marin, M.L., McGilvray, K.L. and Scaiano, J.C., 2008. *Photochemical strategies for the synthesis of gold nanoparticles from Au (III) and Au (I) using photoinduced free radical generation*. Journal of the American Chemical Society, 130(49), pp.16572-16584.

192. Scaiano, J.C., Aliaga, C., Maguire, S. and Wang, D., 2006. *Magnetic field control of photoinduced silver nanoparticle formation*. The Journal of Physical Chemistry B, 110(26), pp.12856-12859.

193. Jockusch, S., Landis, M.S., Freiermuth, B. and Turro, N.J., 2001. *Photochemistry and photophysics of α-hydroxy ketones*. Macromolecules, 34(6), pp.1619-1626.

194. Kim-Thuan, N. and Scaiano, J.C., 1984. *Electron transfer from α-aminoalkyl radicals to methyl viologen*. International journal of chemical kinetics, 16(4), pp.371-377.

195. Scaiano, J.C., 1981. *Photochemical and free-radical processes in benzil-amine systems. Electron-donor properties of. alpha.-aminoalkyl radicals.* The Journal of Physical Chemistry, 85(19), pp.2851-2855.

196. Mirkhalaf, F., Paprotny, J. and Schiffrin, D.J., 2006. *Synthesis of metal nanoparticles stabilized by metal– carbon bonds*. Journal of the American Chemical Society, 128(23), pp.7400-7401.

197. Vasquez, E.S., Chu, I.W. and Walters, K.B., 2014. *Janus magnetic nanoparticles with a bicompartmental polymer brush prepared using electrostatic adsorption to facilitate toposelective surface-initiated ATRP*. Langmuir, 30(23), pp.6858-6866.

198. Yao, X., Jing, J., Liang, F. and Yang, Z., 2016. *Polymer-Fe3O4 Composite Janus Nanoparticles.* Macromolecules, 49(24), pp.9618-9625.

199. Glaser, N., Adams, D.J., Böker, A. and Krausch, G., 2006. *Janus particles at liquid– liquid interfaces*. Langmuir, 22(12), pp.5227-5229.

200. Jiang, Y., Löbling, T.I., Huang, C., Sun, Z., Müller, A.H. and Russell, T.P., 2017. *Interfacial Assembly and Jamming Behavior of Polymeric Janus Particles at Liquid Interfaces*. ACS applied materials & interfaces, 9(38), pp.33327-33332.

201. Amendola, V., Pilot, R., Frasconi, M., Marago, O.M. and Iati, M.A., 2017. *Surface plasmon resonance in gold nanoparticles: a review*. Journal of Physics: Condensed Matter, 29(20), p.203002.

202. ,Petryayeva, E. and Krull, U.J., 2011. *Localized surface plasmon resonance: nanostructures, bioassays and biosensing—a review*. Analytica chimica acta, 706(1), pp.8-24.

203. Hirsch, L.R., Stafford, R.J., Bankson, J.A., Sershen, S.R., Rivera, B., Price, R.E., Hazle, J.D., Halas, N.J. and West, J.L., 2003. *Nanoshell-mediated near-infrared thermal therapy of tumors under magnetic resonance guidance*. Proceedings of the National Academy of Sciences, 100(23), pp.13549-13554.

204. Hu, T., Lin, Y., Yan, J. and Di, J., 2013. *Synthesis of hollow gold nanoparticles on the surface of indium tin oxide glass and their application for plasmonic biosensor.* Spectrochimica Acta Part A: Molecular and Biomolecular Spectroscopy, 110, pp.72-77.

205. Sauerbeck, C., Haderlein, M., Schürer, B., Braunschweig, B., Peukert, W. and Klupp Taylor, R.N., 2014. *Shedding light on the growth of gold nanoshells*. ACS nano, 8(3), pp.3088-3096.

206. Wu, L.Y., Ross, B.M., Hong, S. and Lee, L.P., 2010. *Bioinspired nanocorals with decoupled cellular targeting and sensing functionality.* Small, 6(4), pp.503-507.

207. Li, X., Hu, H., Li, D., Shen, Z., Xiong, Q., Li, S. and Fan, H.J., 2012. *Ordered array of gold semishells on TiO2 spheres: an ultrasensitive and recyclable SERS substrate*. ACS applied materials & interfaces, 4(4), pp.2180-2185.

208. Choi, J., Zhao, Y., Zhang, D., Chien, S. and Lo, Y.H., 2003. *Patterned fluorescent particles as nanoprobes for the investigation of molecular interactions.* Nano letters, 3(8), pp.995-1000.

209. Jang, S.G., Kim, S.H., Lee, S.Y., Jeong, W.C. and Yang, S.M., 2010. *Facile synthesis of core–shell and Janus particles via 2-D dendritic growth of gold film.* Journal of colloid and interface science, 350(2), pp.387-395.

210. Rodríguez-Fernández, D., Pérez-Juste, J., Pastoriza-Santos, I. and Liz-Marzán, L.M., 2012. *Colloidal synthesis of gold semishells*. ChemistryOpen, 1(2), pp.90-95.

211. Bao, H., Butz, B., Zhou, Z., Spiecker, E., Hartmann, M. and Klupp Taylor, R.N., 2012. *Silver-assisted colloidal synthesis of stable, plasmon resonant gold patches on silica nanospheres*. Langmuir, 28(24), pp.8971-8978.

212. Bao, H., Bihr, T., Smith, A.S. and Taylor, R.N.K., 2014. *Facile colloidal coating of polystyrene nanospheres with tunable gold dendritic patches*. Nanoscale, 6(8), pp.3954-3966.

213. Razza, N., Castellino, M. and Sangermano, M., 2017. *Fabrication of Janus particles via a "photografting-from" method and gold photoreduction*. Journal of Materials Science, 52(23), pp.13444-13454.

214. Goldstein, J.I., Newbury, D.E., Michael, J.R., Ritchie, N.W., Scott, J.H.J. and Joy, D.C., 2017. *Scanning electron microscopy and X-ray microanalysis*. Springer.

215. Shindo, D. and Oikawa, T., 2002. *Energy dispersive x-ray spectroscopy. In Analytical Electron Microscopy for Materials Science* (pp. 81-102). Springer, Tokyo.

216. Tasumi, M., 2014. *Introduction to experimental infrared spectroscopy: Fundamentals and practical methods*. John Wiley & Sons.

217. Hüfner, S., 2013. *Photoelectron spectroscopy: principles and applications.* Springer Science & Business Media.

218. Denes, F., Pichowicz, M., Povie, G. and Renaud, P., 2014. *Thiyl radicals in organic synthesis*. Chemical reviews, 114(5), pp.2587-2693.

219. Lu, H.B., Campbell, C.T. and Castner, D.G., 2000. *Attachment of functionalized poly (ethylene glycol) films to gold surfaces.* Langmuir, 16(4), pp.1711-1718.

220. Vericat, C., Vela, M.E., Benitez, G.A., Gago, J.M., Torrelles, X. and Salvarezza, R.C., 2006. *Surface characterization of sulfur and alkanethiol self-assembled monolayers on Au (111)*. Journal of Physics: Condensed Matter, 18(48), p.R867.

221. Whitby, C.P., Fornasiero, D. and Ralston, J., 2010. *Structure of oil-in-water emulsions stabilised by silica and hydrophobised titania particles*. Journal of colloid and interface science, 342(1), pp.205-209.

222. B.P. Binks and C.P. Whitby. *Nanoparticle silica-stabilised oil-in-water emulsions: improving emulsion stability.* Colloids Surf. A, 2005, 253, 105–115.

223. Chen, J.J., Struk, K.N. and Brennan, A.B., 2011. *Surface modification of silicate glass using 3-(mercaptopropyl) trimethoxysilane for thiol–ene polymerization.* Langmuir, 27(22), pp.13754-13761.

224. Popat, K.C., Sharma, S. and Desai, T.A., 2004. *Quantitative XPS analysis of PEG-modified silicon surfaces.* The Journal of Physical Chemistry B, 108(17), pp.5185-5188.

225. Casaletto, M.P., Longo, A., Martorana, A., Prestianni, A. and Venezia, A.M., 2006. *XPS study of supported gold catalysts: the role of $Au^0$ and $Au^{\delta+}$ species as active sites.* Surface and Interface Analysis, 38(4), pp.215-218.

226. Kim H-S., Seo Y.S., Kim K., Han J.W., Par Y., Cho S., 2016. *Concentration effect of reducing agents on green synthesis of gold nanoparticles: size, morphology, and growth mechanism.* Nanoscale Research Letters, 11, pp230.

227. Amendola, V. and Meneghetti, M., 2009. *Size evaluation of gold nanoparticles by UV– vis spectroscopy.* The Journal of Physical Chemistry C, 113(11), pp.4277-4285.

228. Barner-Kowollik, C., Goldmann, A.S. and Schacher, F.H., 2016. *Polymer interfaces: synthetic strategies enabling functionality, adaptivity, and spatial Control.* Macromolecules, 49(14), pp.5001-5016.

229. Callejas-Fernández, J., Estelrich, J., Quesada-Pérez, M. and Forcada, J. eds., 2014. *Soft nanoparticles for biomedical applications.* Royal Society of Chemistry.

230. Levental, I., Georges, P.C. and Janmey, P.A., 2007. *Soft biological materials and their impact on cell function.* Soft Matter, 3(3), pp.299-306.

231. Garbin, V., Jenkins, I., Sinno, T., Crocker, J.C. and Stebe, K.J., 2015. *Interactions and stress relaxation in monolayers of soft nanoparticles at fluid-fluid interfaces.* Physical review letters, 114(10), p.108301.

232. Balazs, A.C., Emrick, T. and Russell, T.P., 2006. *Nanoparticle polymer composites: where two small worlds meet*. Science, 314(5802), pp.1107-1110.

233. Razza, N., Rizza, G., Coulon, P.E., Didier, L., Fadda, G.C., Voit, B., Synytska, A., Grützmacher, H. and Sangermano, M., 2018. *Enabling the synthesis of homogeneous or Janus hairy nanoparticles through surface photoactivation.* Nanoscale, 10(30), pp.14492-14498.

234. Berger, S., Ionov, L. and Synytska, A., 2011. *Engineering of Ultra- Hydrophobic Functional Coatings Using Controlled Aggregation of Bicomponent Core/Shell Janus Particles.* Advanced Functional Materials, 21(12), pp.2338-2344.

235. Gann, J.P. and Yan, M., 2008. *A versatile method for grafting polymers on nanoparticles.* Langmuir, 24(10), pp.5319-5323.

236. Williams, D.B., Carter, C.B. and Veyssiere, P., 1998. *Transmission electron microscopy: a textbook for materials science*. New York: Springer.

237. Hayat, M.A., 1981. *Principles and techniques of electron microscopy. Biological applications.* Edward Arnold.

238. Van Bruggen, E.F.J., Wiebenga, E.H. and Gruber, M., 1960. *Negative-staining electron microscopy of proteins at pH values below their isoelectric points. Its application to hemocyanin*. Biochimica et Biophysica Acta, 42, pp.171-172.

239. Mayhew, T.M., Mühlfeld, C., Vanhecke, D. and Ochs, M., 2009. *A review of recent methods for efficiently quantifying immunogold and other nanoparticles using TEM sections through cells, tissues and organs*. Annals of Anatomy-Anatomischer Anzeiger, 191(2), pp.153-170.

240. De Yoreo, J.J. and Sommerdijk, N.A., 2016. *Investigating materials formation with liquid-phase and cryogenic TEM.* Nature Reviews Materials, 1(8), p.16035.

241. Kuntsche, J., Horst, J.C. and Bunjes, H., 2011. *Cryogenic transmission electron microscopy (cryo-TEM) for studying the morphology of colloidal drug delivery systems.* International journal of pharmaceutics, 417(1-2), pp.120-137.

242. Yang, J. and Paul, O., 2002. *Fracture properties of LPCVD silicon nitride thin films from the load–deflection of long membranes.* Sensors and Actuators A: Physical, 97, pp.520-526.

243. Hill, M.A. and Smith, F.A., 1994. *Calculation of initial and primary yields in the radiolysis of water.* Radiation Physics and Chemistry, 43(3), pp.265-280.

244. Ross, F.M., 2016. *Liquid Cell Electron Microscopy*. Cambridge University Press.

245. Goldburg, W.I., 1999. *Dynamic light scattering.* American Journal of Physics, 67(12), pp.1152-1160.

246. Grünewald, T., Lassenberger, A., van Oostrum, P., Rennhofer, H., Zirbs, R., Capone, B., Vonderhaid, I., Amenitsch, H., Lichtenegger, H. and Reimhult, E., 2015. *Core–Shell Structure of Monodisperse Poly(ethylene glycol)-Grafted Iron Oxide Nanoparticles Studied by Small-Angle X-ray Scattering*. Chemistry of materials, 27(13), pp.4763-4771.

247. Li, T., Senesi, A. J., and Lee, B., 2016. *Small angle X-ray scattering for nanoparticle research.* Chemical reviews, 116(18), pp.11128-11180.

248. Hunter, R.J., 2013. *Zeta potential in colloid science: principles and applications* (Vol. 2). Academic press.

249. Krasnoslobodtsev, A.V. and Smirnov, S.N., 2002. *Effect of water on silanization of silica by trimethoxysilanes.* Langmuir, 18(8), pp.3181-3184.

250. Kolczak, U., Rist, G., Dietliker, K. and Wirz, J., 1996. *Reaction mechanism of monoacyl- and bisacylphosphine oxide photoinitiators studied by $^{31}$P-, $^{13}$C-, and $^{1}$H-CIDNP and ESR.* Journal of the American Chemical Society, 118(27), pp.6477-6489.

251. Liao, W.P. and Kuhl, T.L., 2012. *Steric forces of tethered polymer chains as a function of grafting density: Studies with a single diblock molecular weight.* Macromolecules, 45(14), pp.5766-5772.

252. Crassous, J.J., Ballauff, M., Drechsler, M., Schmidt, J. and Talmon, Y., 2006. *Imaging the volume transition in thermosensitive core– shell particles by cryo-transmission electron microscopy*. Langmuir, 22(6), pp.2403-2406.

253. Zimm, B.H., 1948. *The scattering of light and the radial distribution function of high polymer solutions*. The Journal of Chemical Physics, 16(12), pp.1093-1099.

254. Dutta, N., Egorov, S. and Green, D., 2013. *Quantification of nanoparticle interactions in pure solvents and a concentrated PDMS solution as a function of solvent quality.* Langmuir, 29(32), pp.9991-10000.

255. Lodish, H., Berk, A., Zipursky, S.L., Matsudaira, P., Baltimore, D. and Darnell, J., 1995. *Molecular cell biology* (Vol. 3). New York: WH Freeman.

256. Mailander, V. and Landfester, K., 2009. *Interaction of nanoparticles with cells.* Biomacromolecules, 10(9), pp.2379-2400.

257. Cheng, L.C., Jiang, X., Wang, J., Chen, C. and Liu, R.S., 2013. *Nano–bio effects: interaction of nanomaterials with cells*. Nanoscale, 5(9), pp.3547-3569.

258. Farokhzad, O.C. and Langer, R., 2009. *Impact of nanotechnology on drug delivery.* ACS nano, 3(1), pp.16-20.

259. Huang, X., El-Sayed, I.H., Qian, W. and El-Sayed, M.A., 2006. *Cancer cell imaging and photothermal therapy in the near-infrared region by using gold nanorods.* Journal of the American Chemical Society, 128(6), pp.2115-2120.

260. Massignani, M., LoPresti, C., Blanazs, A., Madsen, J., Armes, S.P., Lewis, A.L. and Battaglia, G., 2009. *Controlling cellular uptake by surface chemistry, size, and surface topology at the nanoscale*. Small, 5(21), pp.2424-2432.

261. Shin, S.H.R., Lee, H.Y. and Bishop, K.J., 2015. *Amphiphilic nanoparticles control the growth and stability of lipid bilayers with open edges*. Angewandte Chemie, 127(37), pp.10966-10970.

262. Verma, A., Uzun, O., Hu, Y., Hu, Y., Han, H.S., Watson, N., Chen, S., Irvine, D.J. and Stellacci, F., 2008. *Surface-structure-regulated cell-membrane penetration by monolayer-protected nanoparticles*. Nature materials, 7(7), p.588.

263. Van Lehn, R.C., Atukorale, P.U., Carney, R.P., Yang, Y.S., Stellacci, F., Irvine, D.J. and Alexander-Katz, A., 2013. *Effect of particle diameter and surface composition on the spontaneous fusion of monolayer-protected gold nanoparticles with lipid bilayers.* Nano letters, 13(9), pp.4060-4067.

264. Greasley, S.L., Page, S.J., Sirovica, S., Chen, S., Martin, R.A., Riveiro, A., Hanna, J.V., Porter, A.E. and Jones, J.R., 2016. *Controlling particle size in the Stöber process and incorporation of calcium*. Journal of colloid and interface science, 469, pp.213-223.

265. Scopes, R.K., 2013. *Protein purification: principles and practice*. Springer Science & Business Media.

266. Schneider, N. and Ross, F.M., 2016. *Electron beam effects in liquid cell TEM and STEM. Liquid Cell Electron Microscopy*, p.140.

267. Tien, H. T., 1984, *Cyclic voltammetry of bilayer lipid membranes*. The Journal of Physical Chemistry, 88(15), pp3172-3174.

268. Tong, Y., Han, X., Song, Y., Jiang, J., and Wang, E., 2003. *Characterization and property of DNA incorporated bilayer lipid membranes.* Biophysical chemistry, 105(1), pp1-9.

269. Carney, R.P., Astier, Y., Carney, T.M., Voïtchovsky, K., Jacob Silva, P.H. and Stellacci, F., 2013. *Electrical method to quantify nanoparticle interaction with lipid bilayers*. ACS nano, 7(2), pp.932-942

270. Schmaljohann, D., 2006. *Thermo-and pH-responsive polymers in drug delivery*. Advanced drug delivery reviews, 58(15), pp.1655-1670.

271. Agarwal, S., Zhang, Y., Maji, S. and Greiner, A., 2012. *PDMAEMA based gene delivery materials*. Materials Today, 15(9), pp.388-393.

272. Lowe, A.B., 2014. *Thiol-yne 'click'/coupling chemistry and recent applications in polymer and materials synthesis and modification*. Polymer, 55(22), pp.5517-5549.

273. Wei, X., Chen, W., Chen, X. and Russell, T.P., 2010. *Disorder-to-order transition of diblock copolymers induced by alkyne/azide click chemistry.* Macromolecules, 43(14), pp.6234-6236.

274. Kitaura, T., Tomioka, H., Fukatani, N. and Kitayama, T., 2013. *Anchimeric assistance on sequence regulation in partial modification of isotactic poly (propargyl methacrylate) by click reaction.* Polymer Chemistry, 4(4), pp.887-890.

275. Ciftci, M., Kahveci, M.U., Yagci, Y., Allonas, X., Ley, C. and Tar, H., 2012. *A simple route to synthesis of branched and cross-linked polymers with clickable moieties by photopolymerization*. Chemical Communications, 48(82), pp.10252-10254.

276. Sluggett, G.W., McGarry, P.F., Koptyug, I.V. and Turro, N.J., 1996. L*aser flash photolysis and time-resolved ESR study of phosphinoyl radical structure and reactivity.* Journal of the American Chemical Society, 118(31), pp.7367-7372.

277. Roy, S.G., Bauri, K., Pal, S., Goswami, A., Madras, G. and De, P., 2013. *Synthesis, characterization and thermal degradation of dual temperature-and pH-sensitive RAFT-made copolymers of N, N-(dimethylamino) ethyl methacrylate and methyl methacrylate.* Polymer International, 62(3), pp.463-473.

278. Zhang, S., Gao, H. and Bao, G., 2015. *Physical principles of nanoparticle cellular endocytosis*. ACS nano, 9(9), pp.8655-8671.

279. Chen, K.L. and Bothun, G.D., 2013. *Nanoparticles meet cell membranes: probing nonspecific interactions using model membranes.* Environmental Science & Technology, 48 (2), pp 873–880

280. Yuan, H., Li, J., Bao, G. and Zhang, S., 2010. *Variable nanoparticle-cell adhesion strength regulates cellular uptake.* Physical review letters, 105(13), p.138101.

281. Lee, H., Son, S.H., Sharma, R. and Won, Y.Y., 2011. *A Discussion of the pH-Dependent Protonation Behaviors of Poly (2-(dimethylamino) ethyl methacrylate)(PDMAEMA) and Poly (ethylenimine-ran-2-ethyl-2-oxazoline)(P (EI-r-EOz))*. The Journal of Physical Chemistry B, 115(5), pp.844-860.

282. Creighton, P., 1983. *Structures and Molecular Principles*. WE Freeman and Company, New York.

283. Lounnas, V. and Wade, R.C., 1997. *Exceptionally stable salt bridges in cytochrome P450cam have functional roles*. Biochemistry, 36(18), pp.5402-5417.

284. Pasenkiewicz-Gierula, M., Takaoka, Y., Miyagawa, H., Kitamura, K. and Kusumi, A., 1999. *Charge pairing of headgroups in phosphatidylcholine membranes: a molecular dynamics simulation study*. Biophysical journal, 76(3), pp.1228-1240.

285. Li, Z. W., Lu, Z. Y., Sun, Z. Y., & An, L. J., 2012. *Model, self-assembly structures, and phase diagram of soft Janus particles*. Soft Matter, 8(25), pp.6693-6697.